ΕΘΝΙΚΟ ΜΕΤΣΟΒΙΟ ΠΟΛΥΤΕΧΝΕΙΟ
ΣΧΟΛΗ ΠΟΛΙΤΙΚΩΝ ΜΗΧΑΝΙΚΩΝ
ΤΟΜΕΑΣ ΓΕΩΤΕΧΝΙΚΗΣ

ΔΙΔΑΚΤΟΡΙΚΗ ΔΙΑΤΡΙΒΗ

ΑΝΑΛΥΣΗ ΚΑΙ ΣΧΕΔΙΑΣΜΟΣ ΣΥΣΤΗΜΑΤΩΝ ΘΕΜΕΛΙΩΣΕΩΝ–ΑΝΩΔΟΜΗΣ ΕΝΑΝΤΙ ΜΕΓΑΛΩΝ ΕΔΑΦΙΚΩΝ ΜΕΤΑΚΙΝΗΣΕΩΝ

Αθανάσιος Σ. Ζαφειράκος

Διπλωματούχος Πολιτικός Μηχανικός Ε.Μ.Π.

M.Eng. University of Tokyo

Αθήνα, Ιούνιος 2014

Η παρούσα έρευνα έχει συγχρηματοδοτηθεί από την Ευρωπαϊκή Ένωση (Ευρωπαϊκό Κοινωνικό Ταμείο - ΕΚΤ) και από εθνικούς πόρους μέσω του Επιχειρησιακού Προγράμματος «Εκπαίδευση και Δια Βίου Μάθηση» του Εθνικού Στρατηγικού Πλαισίου Αναφοράς (ΕΣΠΑ) – Ερευνητικό Χρηματοδοτούμενο Έργο: *Ηράκλειτος ΙΙ*. Επένδυση στην κοινωνία της γνώσης μέσω του Ευρωπαϊκού Κοινωνικού Ταμείου.

NATIONAL TECHNICAL UNIVERSITY OF ATHENS
SCHOOL OF CIVIL ENGINEERING
DEPARTMENT OF GEOTECHNICAL ENGINEERING

DOCTORAL DISSERTATION

INELASTIC STATIC AND SEISMIC RESPONSE OF DEEPLY EMBEDDED FOUNDATIONS

Athanasios S. Zafeirakos

Diploma in Civil Engineering N.T.U.A

M.Eng. University of Tokyo

Athens, June 2014

European Union
European Social Fund

OPERATIONAL PROGRAMME
EDUCATION AND LIFELONG LEARNING
investing in knowledge society
MINISTRY OF EDUCATION & RELIGIOUS AFFAIRS
MANAGING AUTHORITY
Co- financed by Greece and the European Union

NSRF 2007-2013
programme for development
EUROPEAN SOCIAL FUND

This research has been co-financed by the European Union (European Social Fund – ESF) and Greek national funds through the Operational Program "Education and Lifelong Learning" of the National Strategic Reference Framework (NSRF) - Research Funding Program: *Heracleitus II*. Investing in knowledge society through the European Social Fund.

ΕΘΝΙΚΟ ΜΕΤΣΟΒΙΟ ΠΟΛΥΤΕΧΝΕΙΟ
ΣΧΟΛΗ ΠΟΛΙΤΙΚΩΝ ΜΗΧΑΝΙΚΩΝ
ΤΟΜΕΑΣ ΓΕΩΤΕΧΝΙΚΗΣ

ΑΝΑΛΥΣΗ ΚΑΙ ΣΧΕΔΙΑΣΜΟΣ ΣΥΣΤΗΜΑΤΩΝ ΘΕΜΕΛΙΩΣΕΩΝ–ΑΝΩΔΟΜΗΣ ΕΝΑΝΤΙ ΜΕΓΑΛΩΝ ΕΔΑΦΙΚΩΝ ΜΕΤΑΚΙΝΗΣΕΩΝ

ΔΙΔΑΚΤΟΡΙΚΗ ΔΙΑΤΡΙΒΗ

Αθανασίου Σ. Ζαφειράκου

Διπλωματούχου Πολιτικού Μηχανικού Ε.Μ.Π.
M.Eng. University of Tokyo

Η διατριβή υποβλήθηκε στη Σχολή Πολιτικών Μηχανικών του Εθνικού Μετσόβιου Πολυτεχνείου προς εκπλήρωση των προϋποθέσεων του τίτλου του *Διδάκτορος Μηχανικού*.

ΤΡΙΜΕΛΗΣ ΣΥΜΒΟΥΛΕΥΤΙΚΗ ΕΠΙΤΡΟΠΗ:

1. Γ. ΓΚΑΖΕΤΑΣ, Καθηγητής Ε.Μ.Π. (Επιβλέπων)
2. Γ. ΜΠΟΥΚΟΒΑΛΑΣ, Καθηγητής Ε.Μ.Π
3. Ν. ΓΕΡΟΛΥΜΟΣ, Επ. Καθηγητής ΕΜΠ

ΕΠΤΑΜΕΛΗΣ ΕΞΕΤΑΣΤΙΚΗ ΕΠΙΤΡΟΠΗ:

1. Γ. ΓΚΑΖΕΤΑΣ, Καθηγητής Ε.Μ.Π. (Επιβλέπων)
2. Γ. ΜΠΟΥΚΟΒΑΛΑΣ, Καθηγητής Ε.Μ.Π.
3. Ν. ΓΕΡΟΛΥΜΟΣ, Επ. Καθηγητής ΕΜΠ
4. Μ. ΚΑΒΒΑΔΑΣ, Αν. Καθηγητής Ε.Μ.Π.
5. Ι. ΑΝΑΣΤΑΣΟΠΟΥΛΟΣ, Καθηγητής University of Dundee
6. Ε. ΣΑΠΟΥΝΤΖΑΚΗΣ, Καθηγητής Ε.Μ.Π.
7. Π. ΝΤΑΚΟΥΛΑΣ, Καθηγητής Παν. Θεσσαλίας

Η παρούσα έρευνα έχει συγχρηματοδοτηθεί από την Ευρωπαϊκή Ένωση (Ευρωπαϊκό Κοινωνικό Ταμείο - ΕΚΤ) και από εθνικούς πόρους μέσω του Επιχειρησιακού Προγράμματος «Εκπαίδευση και Δια Βίου Μάθηση» του Εθνικού Στρατηγικού Πλαισίου Αναφοράς (ΕΣΠΑ) – Ερευνητικό Χρηματοδοτούμενο Έργο: Ηράκλειτος ΙΙ. Επένδυση στην κοινωνία της γνώσης μέσω του Ευρωπαϊκού Κοινωνικού Ταμείου.

NATIONAL TECHNICAL UNIVERSITY OF ATHENS
SCHOOL OF CIVIL ENGINEERING
DEPARTMENT OF GEOTECHNICAL ENGINEERING

INELASTIC STATIC AND SEISMIC RESPONSE OF DEEPLY EMBEDDED FOUNDATIONS

DOCTORAL DISSERTATION

Athanasios S. Zafeirakos

Diploma in Civil Engineering N.T.U.A
M.Eng. University of Tokyo

The thesis is submitted to the School of Civil Engineering of the National Technical University of Athens in fulfilment of the requirements for the *Degree of Doctor of Philosophy*

ADVISORY COMMITTEE:

1. G. GAZETAS, Professor N.T.U.A. (Supervisor)
2. G.BOUCKOVALAS, Professor N.T.U.A.
3. N. GEROLYMOS, Assistant Professor N.T.U.A.

EXAMINATION COMMITTEE:

1. G. GAZETAS, Professor N.T.U.A. (Supervisor)
2. G.BOUCKOVALAS, Professor N.T.U.A.
3. N. GEROLYMOS, Assistant Professor N.T.U.A.
4. M. KAVVADAS, Associate Professor N.T.U.A.
5. I. ANASTASOPOULOS, Professor University of Dundee
6. E. SAPOUNTZAKIS, Professor N.T.U.A.
7. P. DAKOULAS, Professor University of Thessaly

European Union
European Social Fund
OPERATIONAL PROGRAMME EDUCATION AND LIFELONG LEARNING
investing in knowledge society
MINISTRY OF EDUCATION & RELIGIOUS AFFAIRS
MANAGING AUTHORITY
Co- financed by Greece and the European Union
NSRF 2007-2013
EUROPEAN SOCIAL FUND

This research has been co-financed by the European Union (European Social Fund – ESF) and Greek national funds through the Operational Program "Education and Lifelong Learning" of the National Strategic Reference Framework (NSRF) - Research Funding Program: Heracleitus II. Investing in knowledge society through the European Social Fund.

Π ρ ο λ ε γ ό μ ε ν α

ἐὰν μὴ ἔλπηται ανέλπιστον οὐκ ἐξευρήσει,
ανεξερεύνητον ἐὸν καὶ ἄπορον

Ηράκλειτος (544 - 484 π.Χ.)

Πιστεύω ακράδαντα ότι η ρήση αυτή αποτυπώνει με χαρακτηριστική ακρίβεια την όλη πορεία προς την απόκτηση του Ανωτάτου Ακαδημαϊκού Τίτλου, από τα αρχικά κιόλας κίνητρα, στις στιγμές − κατά την διάρκεια − όπου φαινόταν απλά ακατόρθωτο, έως το πέρας. Κύριε Γκαζέτα, υπήρξατε ο Δάσκαλος που συνέβαλε τα μέγιστα στο να ελπίζω στην εξερεύνηση του ανέλπιστου. Από τα χρόνια της διπλωματικής μου ακόμα, όταν με την εγκάρδια καθοδήγησή σας με βοηθήσατε να λάβω αποφάσεις-σταθμούς για την μετέπειτα πορεία μου. Για όλα αυτά, どうも有難うございます先生 (domo arigato gozaimasu, Sensei).

Το να ευχαριστήσω απλά τον Νικο Γερόλυμο για την άψογη συνεργασία μας όλο αυτό το διάστημα, θα ήταν επιεικώς ανεπαρκές. Στα πλαίσια των προλεγομένων, όμως, Νίκο αυτό που μπορώ να κάνω είναι να εκφράσω την απεριόριστη εκτίμηση και την φιλία που τρέφω προς το πρόσωπό σου.

Θα ήθελα να ευχαριστήσω τα μέλη της Επιτροπής μου, κ. Γιώργο Μπουκοβάλα, κ. Μιχαήλ Καββαδά, κ. Ευάγγελο Σαπουντζάκη και κ. Παναγιώτη Ντακούλα, για τις υποδείξεις και την συμβολή τους στην τελική διαμόρφωση της Διατριβής. Το επιστημονικό τους κύρος πιστοποιεί την εγκυρότητα του παρόντος πονήματος.

Ευχαριστώ πολύ τον Γιάννη Αναστασόπουλο, τον οποίον γνωρίζω από την διπλωματική μου και εκτιμώ ιδιαιτέρως, αλλά και όλα τα μέλη της ομάδας Σεισμικής Γεωτεχνικής Μηχανικής, τον Βασίλη Δρόσο, την Ευαγγελία Γαρίνη, τον Ράλλη Κουρκουλή, την Φανή Γελαγώτη, και προφανώς τους στυλοβάτες της ομαλούς διαχείρισης, Μαρία Γεωργιοπούλου και Δώρα Φισελιά.

Ευχαριστώ τους συναδέλφους με τους οποίους μοιράστηκα όλα αυτά τα χρόνια μαζί με τον χώρο εργασίας, και όλα τα άγχη, τις αγωνίες και τις χαρές: (με σειρά εμφανίσεως) τον Σπύρο Γιαννακό, την Κατερίνα Λεοντάρη, την Γιώτα Τασιοπούλου και την Μαριάννα Λώλη. Παιδιά, καλά τα περάσαμε, ε? Εντάξει, είχαμε και τις διακυμάνσεις μας, αλλά ποια οικογένεια δεν τις βιώνει?

Όσον αφορά τώρα στο κλίμα και στους ανθρώπους που συνάντησα στον Τομέα Γεωτεχνικής, είμαι πρόθυμος να στοιχηματίσω ότι τέτοια παρέα είναι σχεδόν

απίθανο να βρει κανείς, είτε σε χώρο εργασίας, είτε αλλού. Το να σας αναφέρω με τα υποκοριστικά, με τα οποία σας ξέρει ο πολύς ο κόσμος, απλά θα αντέβαινε στην σοβαρότητα ενός πανεπιστημιακού πονήματος. Συνεπώς: Δημήτρη Καραμήτρο, Γιάννη Χαλούλο (…), Κωνσταντίνε Τζιβάκο, Ζαφείρη, Παναγιώτη Σιταρένιο, Αλέξανδρε Καλέ, Πέτρο Φορτσάκη, Γιώργο Προυντζόπουλε, Παύλο Αστερίου, Γιάννη Τσιάπα, Βάλια Δημητριάδη, Σμαράγδα Ευθυμίου, Μαρία Κωνσταντίνου, Δημήτρη Λίτσα, Φίλιππε Χόρτη, και φυσικά οι "σειρές" μου: Αλέξανδρε Βαλσαμή, Στέφανε Βαζδέκη, Ιουλία Σοφιανού και Άρτεμις, σας ευχαριστώ για όλες τις όμορφες στιγμές που ζήσαμε παρέα, κι επιφυλάσσομαι για την συνέχεια!

Δεν θα μπορούσα να παραλείψω τους συναδέλφους, πλέον, Χρήστο Σουλιώτη, Χάρη Παρασκευουλάκο, Κωνσταντίνο Καραπιπέρη και Στέλλα Ιωαννίδου, με τους οποίους είχα την χαρά να συνεργαστώ στα πλαίσια της διπλωματικής εργασίας τους.

Ένα μεγάλο ευχαριστώ στην Ελληνική Επιστημονική Εταιρεία Εδαφομηχανικής και Γεωτεχνικής Μηχανικής (ΕΕΕΕΓΜ), και ιδίως τον κ. Ανδρέα Αναγνωστόπουλο και τον κ. Χρήστο Τσατσανίφο, για την μοναδική ευκαιρία που μου έδωσαν να συμμετάσχω στο 22^{ο} Συνέδριο Νέων Γεωτεχνικών Μηχανικών. Ελπίζω να στάθηκα στο άξιος της εμπιστοσύνης τους.

Ευχαριστώ ιδιαιτέρως την Πάτυ Καραγκιοζοπούλου και τον Μανόλη Τσίμα για την άψογη διαχείριση που ασκούν στο Πρόγραμμα *Ηράκλειτος ΙΙ*.

Τέλος, η παρούσα Διατριβή δεν θα ήταν εφικτό να εκπονηθεί δίχως την αμέριστο συμπαράσταση από την Οικογένειά μου, στην οποία και αφιερώνεται.

Εἰρήνη τῷ *ἀναγιγνώσκοντι*

Αθανάσιος Σ. Ζαφειράκος, Αθήνα Ιούνιος 2014

Στην Οικογένειά μου,

Σαράντο, Μαρία και Άξιο

ΔΙΔΑΚΤΟΡΙΚΗ ΔΙΑΤΡΙΒΗ

Αθανασίου Σ. Ζαφειράκου

ΑΝΑΛΥΣΗ ΚΑΙ ΣΧΕΔΙΑΣΜΟΣ ΣΥΣΤΗΜΑΤΩΝ ΘΕΜΕΛΙΩΣΕΩΝ–ΑΝΩΔΟΜΗΣ ΕΝΑΝΤΙ ΜΕΓΑΛΩΝ ΕΔΑΦΙΚΩΝ ΜΕΤΑΚΙΝΗΣΕΩΝ

Εκτενής Περίληψη

Η ανάλυση κρισίμων έργων Πολιτικού Μηχανικού (π.χ. γέφυρες, ανεμογεννήτριες, θαλάσσιες πλατφόρμες αντλήσεως υδρογονανθράκων, κ.α.) τα οποία κατά την διάρκεια της οικονομικής ζωής τους αναμένεται να εκτεθούν σε ισχυρές περιβαλλοντικές φορτίσεις, είτε κλιματολογικής (ισχυροί άνεμοι ή/και θαλάσσιοι κυματισμοί) είτε τεκτονικής (σε σεισμογενείς περιοχές) προελεύσεως, απαιτεί συνυπολογισμό της *μή-γραμμικής* αλληλεπίδρασης εδάφους-θεμελίου-ανωδομής στον τεχνο-οικονομικό σχεδιασμό. Αυτό προϋποθέτει την ανάπτυξη και χρήση μεθόδων ανάλυσης στις οποίες λαμβάνεται υπόψιν, εκτός από την *μή-γραμμική* απόκριση της ανωδομής, και η *μή-γραμμικότητα* στο επίπεδο εδάφους-θεμελίου: κάτι το μη επιτρεπόμενο, βάσει των συγχρόνων Κανονιστικών διατάξεων.

Το φρέαρ είναι ένα άκαμπτο εγκιβωτισμένο στο έδαφος σώμα, με σημαντικές διαστάσεις ύψους και πλάτους. Εφαρμόζεται ευρέως, ως θεμελίωση γεφυρών μεγάλων ανοιγμάτων, σε δυσχερείς γεωμορφολογικά περιοχές (χαράδρες, ολισθαίνοντα πρανή, κ.α.), ή περιοχές με υψηλή σεισμική επικινδυνότητα. Ενδεικτικά αναφέρεται ότι στον αυτοκινητόδρομο της Εγνατίας Οδού, το 20% των γεφυρών είναι θεμελιωμένες με φρέατα. Ως περιπτώσεις ιστορικών τεχνικών έργων θεμελιωμένων με φρέατα αναφέρονται τα εξής: η γέφυρα Tagus στην Λισαβόνα και Golden Gate στο San Francisco, οι γέφυρες Williamsburg και Verrazano Narrows στην Νέα Υόρκη, η Rainbow bridge (στον κόλπο του Τόκυο), τα συστήματα γεφυρών που ενώνουν τα νησιά Honshu-Shikoku (π.χ. η Akashi kaikyo, οι γέφυρες Seto και Nishi-Seto) και οι γέφυρες του Port Island και Nishinomiya-ko, τα ογκώδη φρέατα των οποίων έπαιξαν σημαίνοντα ρόλο στην μή-κατάρρευση των γεφυρών αυτών κατά τον σεισμό του Kobe (1995). Στον Ελλαδικό χώρο, πλήθος σημαντικών

γεφυρών της Εγνατίας και της Αττικής Οδού, αλλά και του ΠΑΘΕ, είναι θεμελιωμένες σε φρέατα. Ενδεικτικά αναφέρουμε τις οδικές γέφυρες του Ισθμού, Βοτονοσίου, Τρουμπέτας, Μετσόβου-Παναγιάς.

Λόγω των διαστάσεων και της δυσκαμψίας τους, η απόκριση των φρεάτων διέπεται από μια πολύπλοκη κατανομή των τάσεων στην διεπιφάνεια εδάφους-φρέατος, καθώς και από την δημιουργία ενεργητικών και παθητικών πρισμάτων στο έδαφος θεμελίωσης. Είναι συνεπώς προφανές ότι το φρέαρ δεν δύναται να αναλυθεί όπως οι πάσσαλοι, η συμπεριφορά των οποίων ορίζεται από την ευκαμψία τους ενώ αγνοείται και η συνεισφορά της βάσης. Διαφέρει δε σημαντικά και από τα συνήθη εγκιβωτισμένα θεμέλια των οποίων η κατακόρυφη διατμητική αντίσταση στην παράπλευρη επιφάνεια είναι, εν γένει, μικρή. Η μή-γραμμική ανελαστική συμπεριφορά του εδάφους και η ανάπτυξη μή-γραμμικών φαινομένων γεωμετρίας στην διεπιφάνεια (ήτοι αποκόλληση και ολίσθηση) αποτελούν επιπλέον παράγοντες που δυσχεραίνουν την επίλυση του προβλήματος. Αξιοσημείωτο δε είναι ότι ενώ υπάρχει εκτενής βιβλιογραφία σχετικά με μεθόδους ανάλυσης επιφανειακών, ελαφρώς εγκιβωτισμένων (D/B ≤ 1) και κοίλων κυλινδρικών φρεάτων (skirted ή bucket foundations), οι λύσεις για βαθιά εγκιβωτισμένες (D/B ≥ 1) άκαμπτες θεμελιώσεις σε μεγάλες παραμορφώσεις βασίζονται ακόμα σε μεθοδολογίες που έχουν αναπτυχθεί για πασσάλους (π.χ. Matlock, 1970; Hansen, 1961).

Βάσει όλων των ανωτέρω, η παρούσα διδακτορική διατριβή αποσκοπεί να συμβάλει στην διερεύνηση της μή-γραμμικής ανελαστικής απόκρισης συστημάτων εδάφους-φρεάτων θεμελίωσης-ανωδομής υπό στατικώς και σεισμικώς επιβαλλόμενες ισχυρές φορτίσεις, έως την αστοχία. Διαρθρώνεται σε τέσσερα σχεδόν αυτοτελή κεφάλαια. Πιο συγκεκριμένα:

Στο δεύτερο κεφάλαιο παρουσιάζεται εκτενής παραμετρική διερεύνηση, μέσω πεπερασμένων στοιχείων σε 3-Δ, της φέρουσας ικανότητας σε συνδυασμένη N-M-Q φόρτιση βαθιών εγκιβωτισμένων θεμελίων (D/B ≥ 1) εντός συνεκτικών και μη-συνεκτικών εδαφών, λαμβάνοντας υπόψιν μή-γραμμικότες (α) υλικού (εδάφους), και (β) διεπιφάνειας, αποσκοπώντας στην κατάρτιση γενικευμένου κριτηρίου αστοχίας.

Στο τρίτο κεφάλαιο αναπτύσσεται μεθοδολογία προκαταρκτικού σεισμικού σχεδιασμού φρεάτων θεμελιώσεως συστημάτων πυλώνα-καταστρώματος γεφυρών. Βάσει αυτής, διαστασιολογείται το φρέαρ λαμβάνοντας υπόψιν την "*υπεραντοχή*" την οποία δύναται να αναπτύξει υπό συγκεκριμένες συνθήκες φόρτισης (λόγος μεταβιβαζομένης ροπής/τέμνουσα M/Q).

Στο τέταρτο και στο πέμπτο κεφάλαιο διερευνάται αριθμητικώς η σεισμική μή-γραμμική αλληλεπίδραση εδάφους–φρέατος θεμελίωσης–ανωδομής, κατά την οποία το έδαφος, το φρέαρ και η κατασκευή προσομοιώνονται με 3-Δ πεπερασμένα στοιχεία. Η έμφαση δίδεται στην απόκριση σεισμικώς *υπό*-διαστασιολογημένων φρεάτων, όπου ενεργοποιούνται μή-γραμμικότητες στο έδαφος (αντοχή σε φέρουσα ικανότητα) και, ιδίως, στις διεπιφάνειες φρέατος-εδάφους (αποκόλληση, ανασήκωμα, ολίσθηση). Οι μεθοδολογίες ανάλυσης που εφαρμόζονται είναι: στο μεν τέταρτο κεφάλαιο, αυτή της φασματικής ταύτισης (με έμφαση στην φυσική του προβλήματος), στο δε πέμπτο της Ανάλυσης Δυναμικής Αντίστασης (Incremental Dynamic Analysis).

Κεφάλαιο 2ο

Γενικευμένη καμπύλη φέρουσας αντοχής βαθιών εγκιβωτισμένων θεμελιώσεων, λαμβάνοντας υπόψιν την μή-γραμμικότητα του εδάφους και της διεπιφάνειας

Στις κλασσικές μεθόδους υπολογισμού φέρουσας ικανότητας θεμελίων (π.χ. Brinch Hansen, Meyerhof), η φέρουσα ικανότητα υπό γενική N-M-Q φόρτιση υπολογίζεται λαμβάνοντας κατάλληλους συντελεστές για την εκκεντρότητα και την κλίση της γενικής φόρτισης. Στις σύγχρονες μεθόδους, όμως, λαμβάνεται υπόψιν η ταυτόχρονη δράση και η αλληλεπίδραση μεταξύ των εντατικών μεγεθών που μεταβιβάζονται στην θεμελίωση, και οι οριακές καταστάσεις αστοχίας, υπό συνδυασμένη N-M-Q φόρτιση, αποτυπώνονται σε μία περιβάλλουσα αστοχίας (ή καμπύλη φέρουσας αντοχής, ή καμπύλη αλληλεπίδρασης). Η μορφή και το σχήμα

των περιβαλλουσών αστοχίας εξαρτάται από την γεωμετρία του θεμελίου, τις εδαφικές συνθήκες και οι συνθήκες διεπιφάνειας εδάφους θεμελίου (π.χ. συνθήκες πλήρους ή ατελούς επαφής). Ενώ υπάρχει εκτενής σχετική βιβλιογραφία, αυτή αφορά μόνο τις περιπτώσεις επιφανειακών και ελαφρώς εγκιβωτισμένων θεμελίων (D/B ≤ 1). Επιπροσθέτως, λόγω της πολυπλοκότητας του σχήματος και της επιρροής τους από τους προαναφερθέντες παράγοντες, λίγες κλειστές αναλυτικές σχέσεις (κριτήρια αστοχίας) για τις περιβάλλουσες έχουν προταθεί, ούτως ώστε να γίνουν άμεσα προσβάσιμες για τον συνήθη σχεδιασμό.

Στην ενότητα αυτή της Διατριβής διερευνάται εκτενώς, μέσω πεπερασμένων στοιχείων σε 3-Δ, η φέρουσα ικανότητα υπο συνδυασμένη N-M-Q φόρτιση βαθιών εγκιβωτισμένων (D/B ≥ 1) άκαμπτων θεμελίων εντός συνεκτικών και μη-συνεκτικών εδαφών, αποσκοπώντας στην ανάπτυξη ενός γενικευμένου κριτηρίου αστοχίας, το οποίο απουσιάζει από την βιβλιογραφία.

Μεθοδολογία ανάλυσης

Αριθμητικό προσομοίωμα

Μελετάται η απόκριση άκαμπτων φρεάτων τετραγωνικής κατόψεως B x B (όπου B = 10m) και βαθμού εγκιβωτισμού D/B = 1, 2 και 3, υποβαλλομένων σε συνδυασμένη N-M-Q φόρτιση στην κεφαλή τους. Η ανάλυση πραγματοποιείται με χρήση του κώδικα ABAQUS version 6.9. Στο **Σχ. 2.1** δίδεται ενδεικτική διακριτοποίηση πεπερασμένων στοιχείων για D/B = 1.

Εξετάζεται η απόκριση των φρεάτων τόσο σε συνεκτικό όσο και σε μή-συνεκτικό έδαφος, ενώ λαμβάνεται υπόψιν η μή-γραμμική ανελαστική συμπεριφορά του εδάφους και της διεπιφάνειας εδάφους-φρέατος.

Για λόγους πληρότητας, εξετάζεται και η περίπτωση φρεάτων σε συνεκτικό έδαφος με θεώρηση διεπιφάνειας πλήρους επαφής.

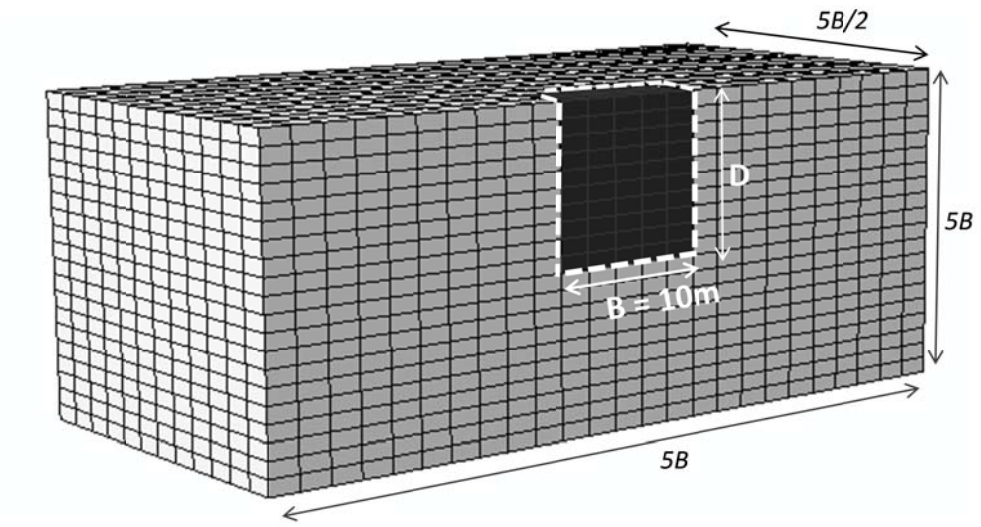

Σχ. 2.1 Προσομοίωμα πεπερασμένων στοιχείων για D/B = 1

Καταστατικό προσομοίωμα για συνεκτικά εδάφη–επαλήθευση

Η συμπεριφορά του συνεκτικού εδάφους περιγράφεται από ένα ελαστο-πλαστικό καταστατικό προσομοίωμα (Gerolymos & Gazetas, 2006), το οποίο αποτελεί επαναδιατύπωση του αρχικώς προταθέντος από τους Armstrong & Frederick (1966), και είναι διαθέσιμο στην βιβλιοθήκη υλικών του ABAQUS. Ακολουθεί το κριτήριο διαρροής Von Mises με μή-γραμμικό κινηματικό νόμο κράτυνσης και συσχετισμένο νόμο πλαστικής ροής. Το συγκεκριμένο καταστατικό προσομοίωμα είναι ικανό να περιγράψει την ανελαστική συμπεριφορά συνεκτικού εδάφους υπό αστράγγιστες συνθήκες, η οποία θεωρείται ανεξάρτητη από την μεταβολή στις ολικές ορθές τάσεις. Οι εδαφικές ιδιότητες που επελέγησαν για την παραμετρική διερεύνηση παρουσιάζονται στο **Σχ. 2.2**.

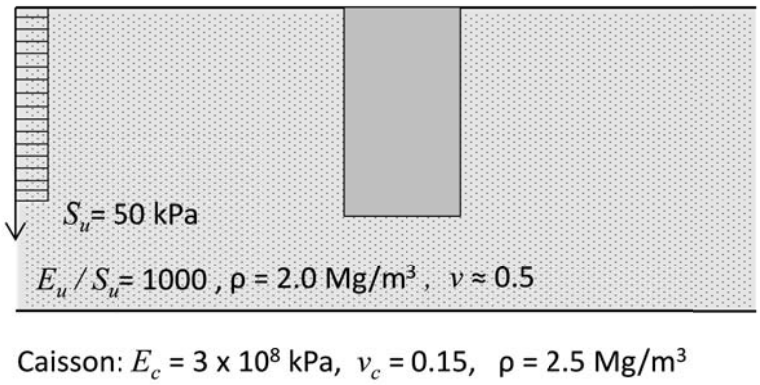

Σχ. 2.2 Το προφίλ του συνεκτικού εδάφους

Η ακρίβεια και η αξιοπιστία του καταστατικού προσομοιώματος επαληθεύεται μέσω σύγκρισης με αποτελέσματα πειραμάτων φυσικής κλίμακας, όπου κοίλα κυλινδρικά φρέατα (suction caissons) σε άργιλο υποβάλλονται σε ανακυκλική φόρτιση (Houlsby et al, 2005). Από την σύγκριση μεταξύ πειραματικών και αριθμητικών αποτελεσμάτων, η οποία δίδεται στο **Σχ. 2.3**, συμπεραίνεται ότι το υιοθετηθέν καταστατικό προσομοίωμα δύναται να αναπαράγει επιτυχώς τα βασικά χαρακτηριστικά της απόκρισης, όπως η μή-γραμμικότητα διεπιφάνειας (αποκόλληση). Σχετικά με τα πειραματικά αποτελέσματα, αξίζει να σημειωθεί σε αυτό το σημείο ότι ο λόγος για την έντονη απομείωση στην δυσκαμψία του φρέατος, η οποία είναι εμφανής μετά τον πρώτο κύκλο φόρτισης συνδέεται άμεσα με τις συνθήκες διεξαγωγής του πειράματος. Πιο συγκεκριμένα, οι ερευνητές σε μεταγενέστερη δημοσίευσή τους (Kelly, Houlsby & Byrne; 2006) ανέφεραν ότι η συμπεριφορά αυτή οφείλεται στην χαλάρωση της αργίλου Bothkennar λόγω συνθηκών μερικής στράγγισης στις οποίες πραγματοποιήθηκε το πείραμα, δεδομένου ότι μεταξύ των κύκλων φόρτισης μεσολαβούσε ένα διόλου ευκαταφρόνητο χρονικό διάστημα (> 20 ημερών),

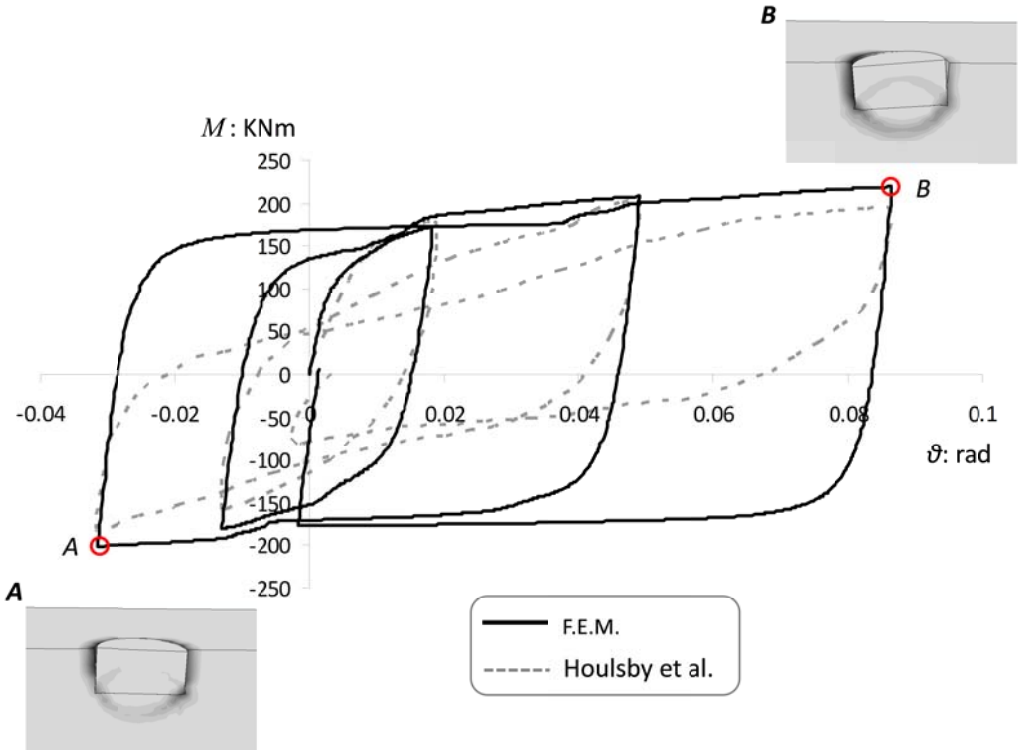

Σχ. 2.3 Επαλήθευση καταστατικού προσομοιώματος για συνεκτικό έδαφος μέσω πειραμάτων φυσικής κλίμακας

Καταστατικό προσομοίωμα για μή-συνεκτικά εδάφη−επαλήθευση

Το καταστατικό προσομοίωμα για το μή-συνεκτικό έδαφος αποτελεί επέκταση του προσομοιώματος που βαθμονομήθηκε από τους Gerolymos & Gazetas (2006) για συνεκτικά υλικά. Το προσομοίωμα χαρακτηρίζεται από έναν μή-γραμμικό νόμο κράτυνσης, μή-συσχετισμένο νόμο πλαστικής ροής, και τροποποιημένο κριτήριο διαρροής Mohr-Coulomb. Οι παράμετροι του καταστατικού προσομοιώματος βαθμονομούνται με στόχο το βέλτιστο συνταίριασμα με το κριτήριο αστοχίας Mohr-Coulomb στο επίπεδο των κυρίων τάσεων. Το προσομοίωμα ενσωματώνεται στον κώδικα πεπερασμένων στοιχείων ABAQUS μέσω υπορουτίνας, η οποία συνδέει τις παραμέτρους του προσομοιώματος με την κατακόρυφη τάση, τις κύριες τάσεις και την γωνία Lode σε κάθε βήμα φόρτισης. Η γωνία Lode επιτρέπει την ακριβέστερη προσομοίωση της απόκρισης του εδάφους σε τρισδιάστατο περιβάλλον.

Το εδαφικό προφίλ που χρησιμοποιήθηκε στις αναλύσεις παρουσιάζεται στο **Σχ. 2.4**.

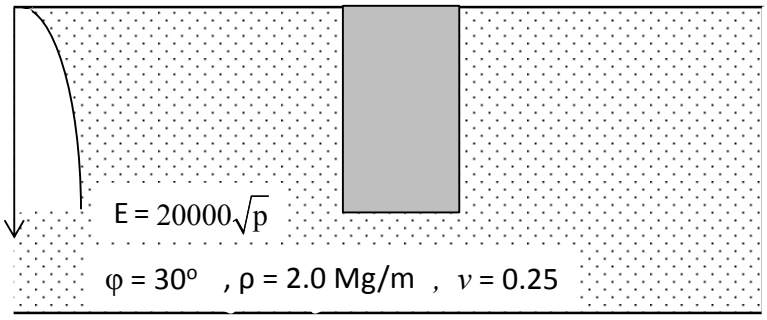

Σχ. 2.4 Το μή-συνεκτικό εδαφικό προφίλ που χρησιμοποιήθηκε για τις αναλύσεις

Το προτεινόμενο καταστατικό προσομοίωμα επαληθεύτηκε από τους Giannakos et al (2012) μέσω σύγκρισης με πειραματικά αποτελέσματα από τρία πειράματα σε φυγοκεντριστή μεμονωμένου πασσάλου σε ξηρή άμμο υπό ανακυκλική εγκάρσια φόρτιση.

Προσομοίωση διεπιφανειών

Η προσομοίωση της διεπιφάνειας φρέατος–συνεκτικού εδάφους γίνεται μέσω ειδικών στοιχείων διεπιφάνειας, όπου επιτρέπεται η ολίσθηση κατά μήκος της διεπιφάνειας και η αποκόλληση του θεμελίου από το έδαφος, ανάλογα με τις συνθήκες φόρτισης. Η ολίσθηση διέπεται από τον νόμο του Coulomb, ο δε συντελεστής τριβής μ της διεπιφάνεια θεμελίου–εδάφους μεταβάλλεται παραμετρικά. Στην περίπτωση φρεάτων σε μή-συνεκτικό έδαφος, το έδαφος λόγω ελλείψεως συνοχής έρχεται να πληρώσει τα κενά που τείνουν να δημιουργηθούν. Συνεπώς, οι μη-γραμμικές συνθήκες διεπιφάνειας αναφέρονται κυρίως στην ολίσθηση κατά μήκος τους, ενώ δεν επιτρέπεται η αποκόλληση.

Αναλύσεις ευαισθησίας

Με γνώμονα τον βέλτιστο συνδυασμό υπολογιστικής ακρίβειας και χαμηλού χρονικού κόστους πραγματοποιήθηκε έλεγχος ευαισθησίας ως προς: (α) τον τύπο των χρησιμοποιούμενων πεπερασμένων στοιχείων, και (β) την πλευρική έκταση του καννάβου. Πιο συγκεκριμένα, ελέγχθηκαν τρείς τύποι οκτακομβικών πεπερασμένων στοιχείων συνεχούς μέσου: C3D8, C3D8R και C3D8H. Από την ανάλυση, κατά την οποία τα φρέατα υπεβλήθησαν σε μονοτονική οριζόντια φόρτιση στην κεφαλή, επελέγησαν τελικώς τα στοιχεία C3D8. Όσον αφορά την

οριζόντια έκταση του προσομοιώματος, εξετάστηκαν δύο περιπτώσεις *L x L* (σε κάτοψη), 5Β *x* 5Β, και 10Β *x* 10Β. Η σχεδόν ταύτιση των αποτελεσμάτων σε όρους Q-u οδήγησε στην επιλογή του οικονομικότερου 5Β *x* 5Β.

Μέθοδος ανάλυσης

Η ανάλυση πραγματοποιείται μέσω (α) επιβαλλομένων δυνάμεων (N-M-Q), και (β) επιβαλλομένων μετακινήσεων (u, ϑ), στην κεφαλή του φρέατος. Το κατακόρυφο φορτίο μεταβάλλεται παραμετρικά συναρτήσει του οριακού φορτίου N_u, έτσι ώστε ο συντελεστής

$\chi = N/N_u$

(ο αντίστροφος του στατικού συντελεστή ασφαλείας έναντι κατακόρυφης αστοχίας, FSv) να παίρνει τιμές σε όλο το φάσμα μεταξύ χ = 0 και χ = 1.

Ως φορτίο αστοχίας ορίζεται το σημείο εκείνο (σε διάγραμμα Q-u ή M-ϑ) όπου η εφαπτομενική δυσκαμψία ισούται με το 1% της αρχικής. Το εύρος των υπολογισθεισών μετακινήσεων, καθ' όλην την αριθμητική διερεύνηση, ήταν μεταξύ 0.20 m – 0.35 m.

Αποτελέσματα

Η περιβάλλουσα αστοχίας

Η γενικευμένη εξίσωση της περιβάλλουσας αστοχίας που αναπτύχθηκε στην παρούσα Διατριβή, δίδεται από ένα ελλειψοειδές της μορφής:

$$f = \left(\frac{Q}{Q_u}\right)^{n_1} + \left(\frac{M}{M_u}\right)^{n_2} + n_3\left(\frac{Q}{Q_u}\right)\left(\frac{M}{M_u}\right) - 1 = 0 \qquad (1)$$

όπου περιγράφεται η αλληλεπίδραση ροπής-τέμνουσας M-Q για ένα συγκεκριμένο κατακόρυφο φορτίο (χ) σε κανονικοποιημένη μορφή. Οι συντελεστές n_1, n_2, n_3 της **Εξ.1** θα εξάγονται κατά περίπτωση, αναλόγως του εδάφους και των συνθηκών διεπιφάνειας.

Φρέατα σε συνεκτικό έδαφος

Από τα αριθμητικά αποτελέσματα, εξήχθησαν κλειστές σχέσεις για την αντοχή σε "καθαρή" τέμνουσα Q_u (άνευ ροπής ανατροπής) και για την αντοχή σε "καθαρή" ροπή M_u (χωρίς τέμνουσα) τόσο για διεπιφάνεια πλήρους επαφής, όσο και ατελούς επαφής. Τα αντίστοιχα γραφήματα παρουσιάζονται στο **Σχ. 2.5** για κάθε έναν από τους εξεταζόμενους βαθμούς εγκιβωτισμού (D/B). Για την μή-γραμμική διεπιφάνεια τα αποτελέσματα είναι για συντελεστή τριβής μ =1.

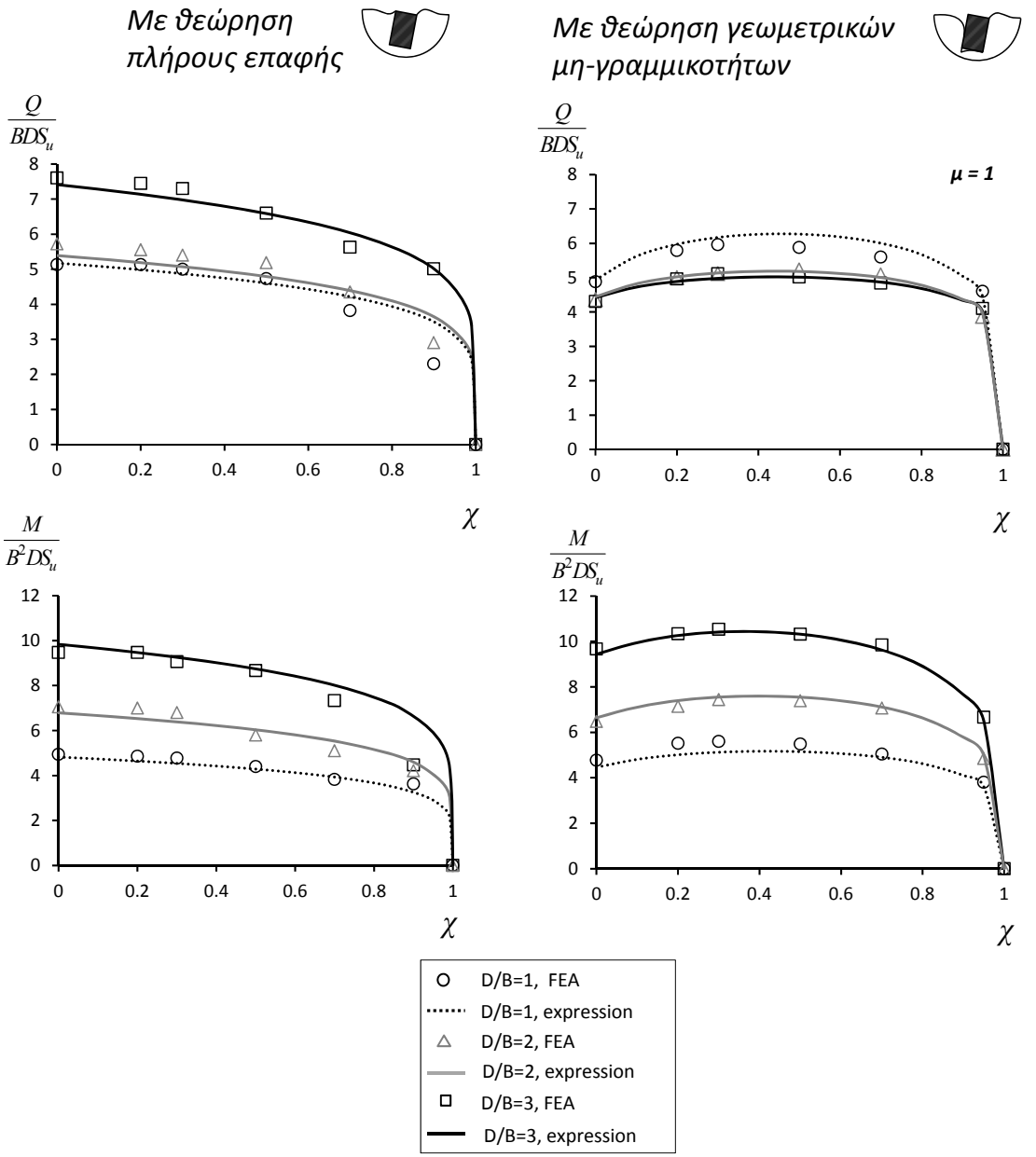

Σχ. 2.5 Διαγράμματα αδιαστατοποιημένης "καθαρής" αντοχής σε τέμνουσα και "καθαρής" αντοχής σε ροπή συναρτήσει του κατακόρυφου φορτίου, για D/B=1-3.

Είναι εμφανές από τα διαγράμματα ότι ενώ στην περίπτωση πλήρους επαφής εδάφους–θεμελίου παρουσιάζεται μείωση της "καθαρής" αντοχής αυξανομένου του κατακορύφου φορτίου, όταν η διεπιφάνεια λαμβάνεται ως μή-γραμμική η συμπεριφορά διαφέρει. Πιο συγκεκριμένα, για μικρές τιμές του χ, έως ≈ 0.5, η αντοχή ελαφρώς αυξάνει λόγω ενεργοποίησης της αντίστασης της βάσης του θεμελίου, ιδίως στα ελαφρώς εγκιβωτισμένα (D/B=1) θεμέλια. Με περαιτέρω αύξηση όμως του χ, όμως, χάνεται η ικανότητα του θεμελίου για αντίσταση τόσο σε τέμνουσα όσο και σε ροπή, λόγω της αυξανομένης πλαστικοποίησεως του εδάφους (αστοχία σε φέρουσα ικανότητα).

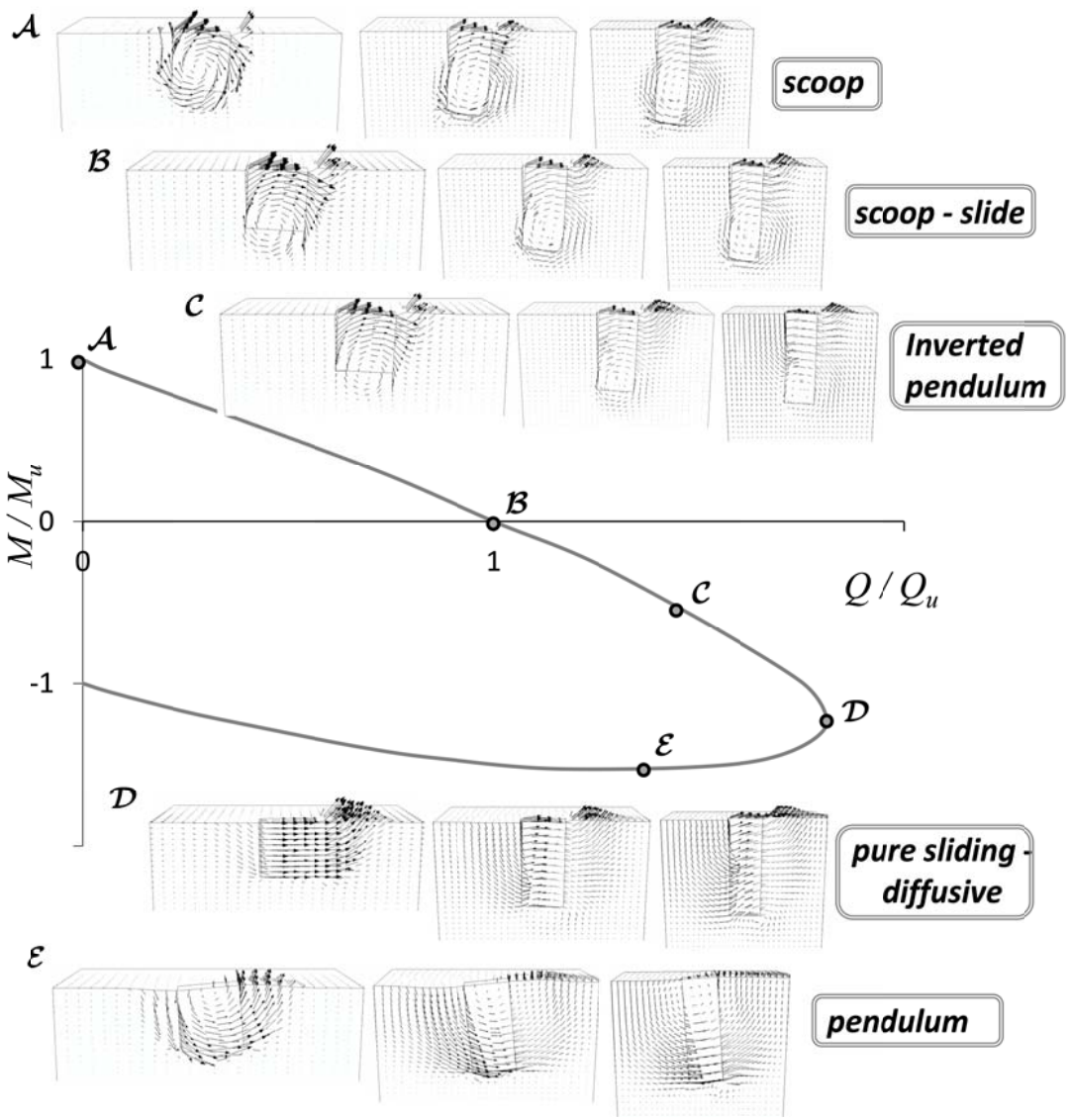

Σχ. 2.6 Μηχανισμοί αστοχίας φρεάτων θεμελίωσης, συναρτήσει του συνδυασμού *M/Q* φόρτισης.

Οι μηχανισμοί αστοχίας φρεάτων σε συνεκτικό έδαφος (για D/B = 1, 2 και 3), όπως αυτοί ταυτοποιήθηκαν κατά την ανάλυση, αποτυπώνονται μέσω των διανυσμάτων των μετακινήσεων στο **Σχ. 2.6**, για μή-γραμμική διεπιφάνεια. Διακρίνονται πέντε βασικοί μηχανισμοί, οι οποίοι αντιστοιχούν στα σημεία $\mathcal{A}$-$\mathcal{E}$ της καμπύλης αστοχίας. Αξίζει να σημειωθεί η ασυμμετρία της καμπύλης, ενδεικτικό της σύζευξης μεταξύ του μετακινησιακού και περιστροφικού βαθμού ελευθερίας. Εμφανίζεται δε "υπεραντοχή" τόσο σε τέμνουσα όσο και σε ροπή, όταν το ζεύγος M-Q που ασκείται στην κεφαλή του φρέατος δρα αντίρροπα ($MQ < 0$). Ο μηχανισμός που διέπει την αστοχία: (i) σε "καθαρή" ροπή είναι αμιγώς περιστροφικός (scoop), (ii) σε "καθαρή" τέμνουσα είναι μικτός περιστροφής-ολίσθησης (scoop-slide), (iii) στην μέγιστη τέμνουσα είναι μηχανισμός ολίσθησης (sliding) και (iv) στην μέγιστη ροπή ενεργοποιείται μηχανισμός εκκρεμούς. Ενδιαμέσως, παρατηρείστε την προοδευτική μετάβαση από τον έναν μηχανισμό (τον προηγούμενο) στον άλλον (στον επόμενο).

Οι τιμές των παραμέτρων της περιβάλλουσας αστοχίας υπολογίσθηκαν με την βοήθεια αλγορίθμου βελτιστοποίησης. Η επαλήθευση των αναλυτικών αποτελεσμάτων παρουσιάζεται στο **Σχ. 2.7** μέσω σύγκρισης με τις αριθμητικώς εξαχθείσες καμπύλες.

Φρέατα σε μή-συνεκτικό έδαφος

Η απόκριση των φρεάτων σε μή-συνεκτικό έδαφος διερευνάται ομοιοτρόπως. Στην περίπτωση αυτή παρατηρείται εντόνως μή-γραμμική εξάρτηση των παραμέτρων αντοχής (**Εξ. 1**) από το βάθος εγκιβωτισμού, τον συντελεστή τριβής διεπιφάνειας και το κατακόρυφο φορτίο, με αποτέλεσμα να μην εξάγονται κλειστές αναλυτικές εκφράσεις. Για τον λόγο αυτόν, χρησιμοποιούνται καταλλήλως εκπαιδευόμενα νευρωνικά δίκτυα. Στο **Σχ. 2.8** παρατίθεται η σύγκριση μεταξύ αριθμητικών και αναλυτικών αποτελεσμάτων για την περιβάλλουσα αστοχίας, σε κανονικοποιημένη μορφή. Όπως και στην περίπτωση των φρεάτων σε συνεκτικό έδαφος, η σύγκριση κρίνεται ως απολύτως ικανοποιητική.

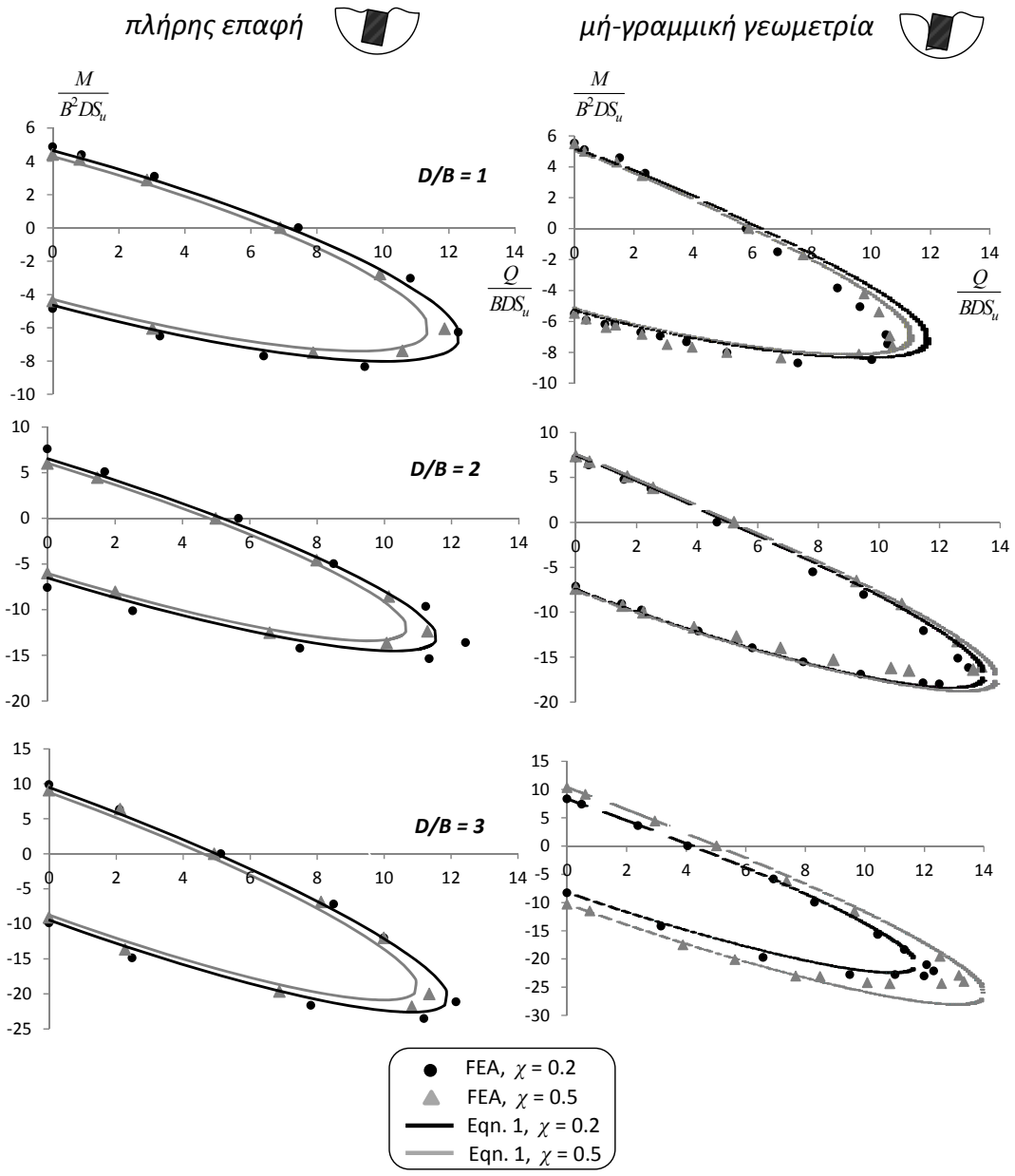

Σχ. 2.7 Σύγκριση μεταξύ των αναλυτικών (Εξ. 1) και των αριθμητικών αποτελεσμάτων: επαλήθευση της μεθοδολογίας για φρέατα σε συνεκτικό έδαφος (αστράγγιστες συνθήκες).

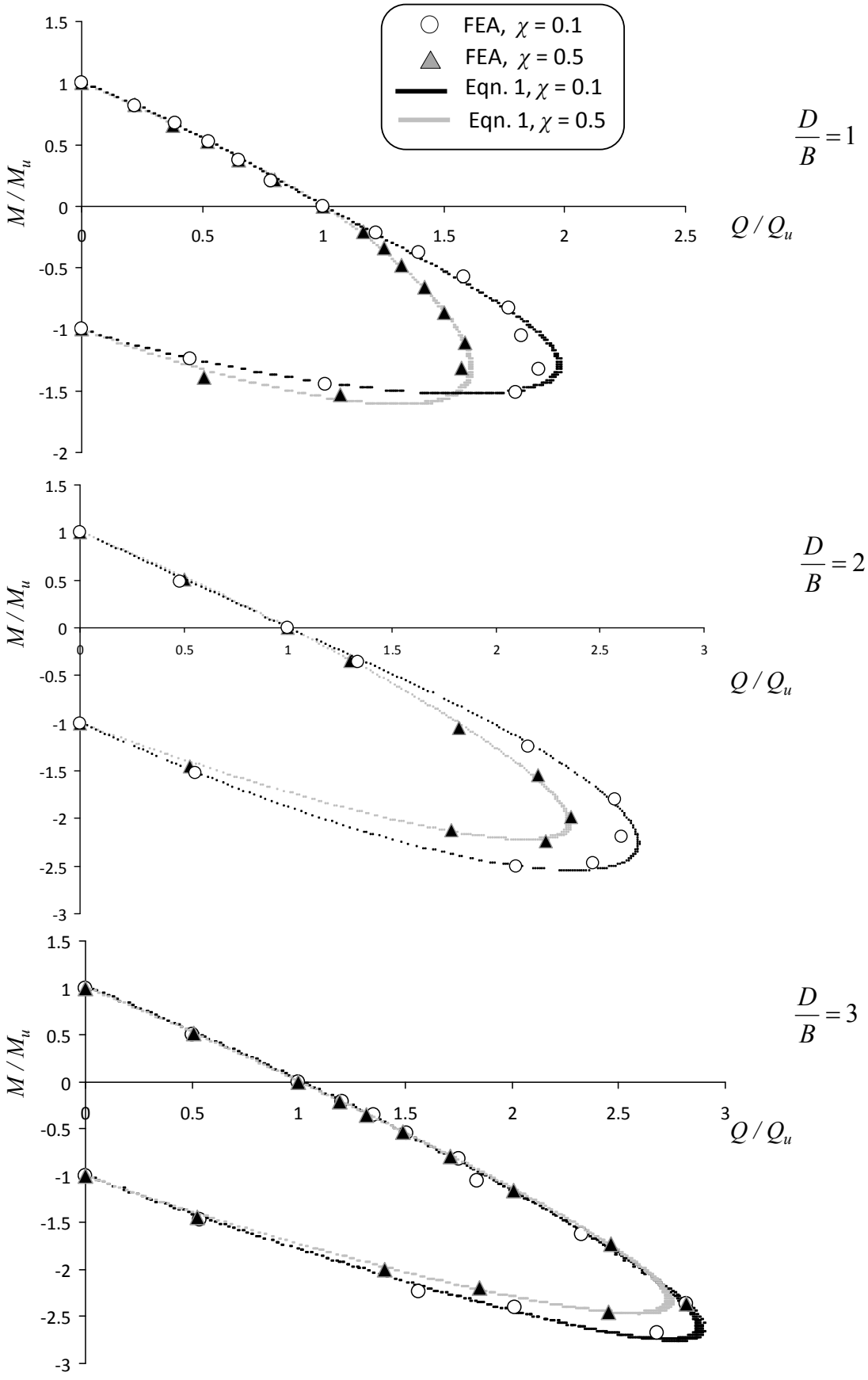

Σχ. 2.8 Σύγκριση μεταξύ των αναλυτικών (Εξ. 1) και των αριθμητικών αποτελεσμάτων: επαλήθευση της μεθοδολογίας για φρέατα σε μή-συνεκτικό έδαφος (συνθήκες πλήρους στραγγίσεως)

Νόμος πλαστικής ροής

Από την ενδελεχή ανάλυση της απόκρισης βαθέων εγκιβωτισμένων άκαμπτων θεμελίων σε συνεκτικό και μή-συνεκτικό έδαφος, υποβαλλομένων σε συνδυασμένη φόρτιση, προτάθηκε ένα γενικευμένο κριτήριο αστοχίας (περιβάλλουσα αστοχίας). Στο πλαίσιο της θεωρίας της πλαστικότητας, η περιβάλλουσα αστοχίας ενός φρέατος (**Εξ. 1**) δύναται να θεωρηθεί και ως καμπύλη διαρροής (yield surface) ενός μακρο-στοιχείου (macroelement). Για τον υπολογισμό των πλαστικών παραμορφώσεων, απαιτείται υιοθέτηση κατάλληλου νόμου πλαστικής ροής (plastic flow rule). Εξετάζεται, λοιπόν, ο νόμος της πλαστικής ροής ο οποίος προκύπτει από τα αριθμητικά "πειράματα".

Καταρχάς, ελέγχεται εάν υποστηρίζεται συζευγμένος νόμος ροής (associated flow rule). Στην περίπτωση αυτή, η καμπύλη διαρροής θα ταυτιζόταν με την καμπύλη πλαστικού δυναμικού (plastic potential function), οπότε ο λόγος των επαυξητικών μετατοπίσεων θα δινόταν από την ακόλουθη σχέση:

$$\frac{\delta u_p}{\delta \vartheta_p} = \frac{\lambda \dfrac{\partial f}{\partial Q}}{\lambda \dfrac{\partial f}{\partial M}} = z_p \tag{2}$$

για το επίπεδο M-Q (όπου και λόγω της ακαμψίας του φρέατος αποδεικνύεται ότι η Εξ.2 δίνει το βάθος του πόλου περιστροφής z_p) και

$$\frac{\delta u_p}{\delta w_p} = \frac{\lambda \dfrac{\partial f}{\partial Q}}{\lambda \dfrac{\partial f}{\partial N}} \tag{3}$$

για το επίπεδο Q-N. Στο **Σχ. 2.9** παρουσιάζεται ενδεικτικά η σύγκριση μεταξύ αριθμητικών και αναλυτικών αποτελεσμάτων για τις περιπτώσεις (α) φρέατος με D/B = 2 σε συνεκτικό έδαφος με μή-γραμμική διεπιφάνεια (μ = 1), και (β) φρέατος με D/B = 1 σε μή-συνεκτικό έδαφος (μ = 1). Εκ των αποτελεσμάτων τεκμαίρεται ότι όντως η υιοθέτηση συζευγμένου νόμου πλαστικής ροής υποστηρίζεται πλήρως από τα αριθμητικά μας δεδομένα.

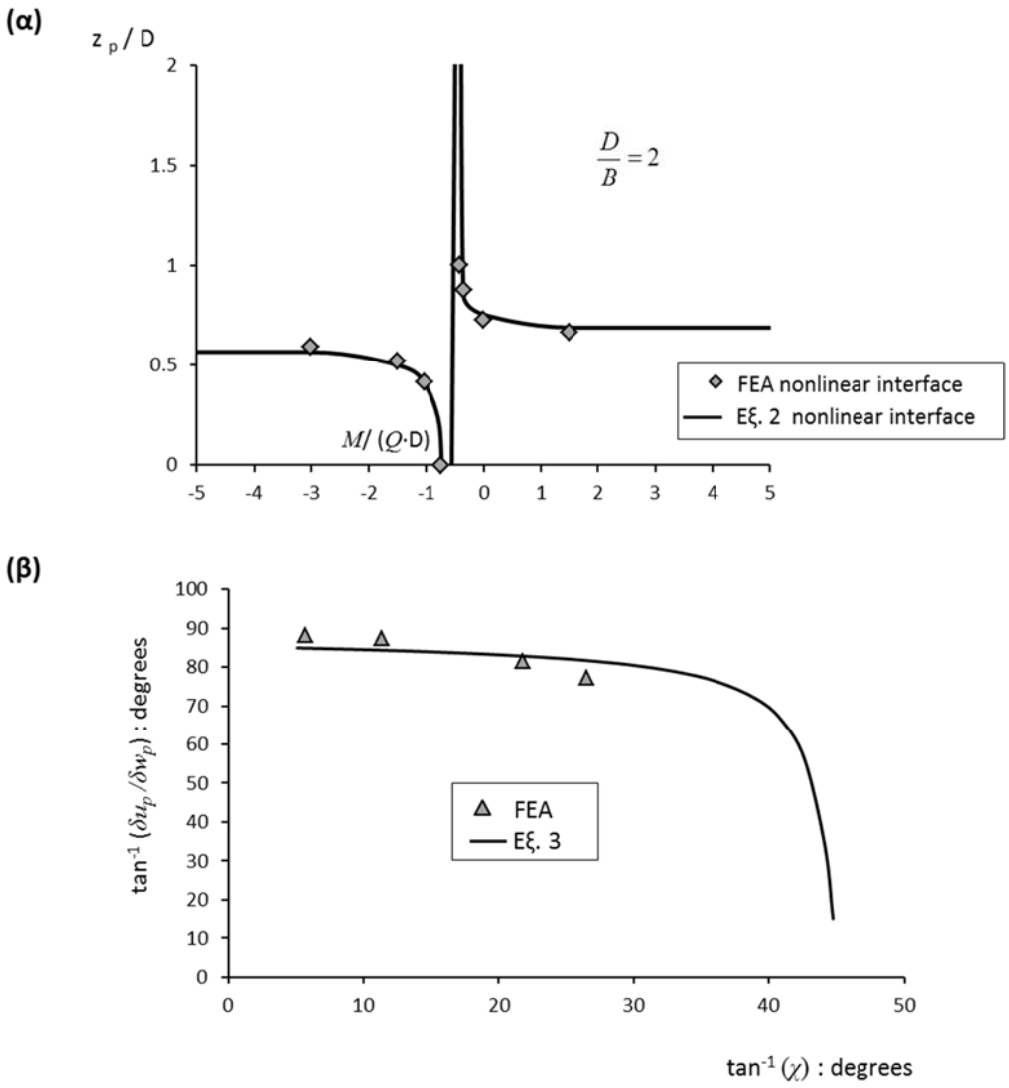

Σχ. 2.9 Σύγκριση μεταξύ αριθμητικών και αναλυτικών (Εξ. 2, 3) αποτελεσμάτων θεωρώντας συζευγμένο νόμο πλαστικής ροής.

Κεφάλαιο 3ο

Μεθοδολογία προκαταρκτικού σεισμικού σχεδιασμού φρεάτων θεμελιώσεως γεφυρών

Κατά τον συνήθη σχεδιασμό των τεχνικών έργων (π.χ. γεφυρών), η αλληλεπίδραση μεταξύ εδάφους−θεμελίωσης−ανωδομής (ήτοι η επίδραση της ενδοσιμότητας του εδάφους στην απόκριση της θεμελίωσης και της ανωδομής) λαμβάνεται υπόψιν αντικαθιστώντας το σύστημα εδάφους-θεμελίωσης μέσω γραμμικών ή μη-γραμμικών, συνήθως ασύζευκτων ελατηρίων. Στην περίπτωση των φρεάτων θεμελιώσεως, όμως, η υιοθέτηση μιας τέτοιας προσέγγισης μπορεί να οδηγήσει σε μη ρεαλιστική εκτίμηση της απόκρισης. Στο **Σχ. 3.1** παρουσιάζεται σχηματικά ένα σύστημα πυλώνα-καταστρώματος γέφυρας, θεμελιωμένη με φρέαρ, η οποία υποβάλλεται σε οριζόντια φόρτιση (Q) στο επίπεδο του καταστρώματος. Η έμφαση δίδεται στην απόκριση της θεμελίωσης με διερεύνηση της επιρροής των συνθηκών σύνδεσης πυλώνα-καταστρώματος. Πιο συγκεκριμένα, εξετάζεται η επίδραση της στροφικής δυσκαμψίας του κόμβου στα εντατικά μεγέθη (ζεύγος M-Q) που μεταβιβάζονται στην θεμελίωση. Η κατάσταση αυτή, ήτοι οι κινηματικοί περιορισμοί (στροφικής φύσεως) που επιβάλλονται από τον κόμβο, προσομοιώνεται μέσω στροφικού ελατηρίου στην κορυφή του πυλώνα, με δυσκαμψία K_R. Η θεμελίωση προσομοιώνεται με δύο διαφορετικές μεθόδους: (α) μέσω μή-γραμμικών αλλά ασύζευκτων ελατηρίων, και (β) μέσω πεπερασμένων στοιχείων, όπου στο ελαστο-πλαστικό μητρώο δυσκαμψίας της θεμελίωσης οι βαθμοί ελευθερίας σε στροφή και μετακίνηση είναι συζευγμένοι. Η σύγκριση της απόκρισης της θεμελίωσης βάσει των δύο ανωτέρω μεθόδων δίδεται, καταρχάς, ποιοτικά σε επίπεδο περιβάλλουσας αστοχίας του φρέατος (βλ. Κεφάλαιο 2^o) σε κανονικοποιημένον χώρο M-Q. Είναι εμφανές ότι η φόρτιση επί του φρέατος με ασύζευκτα ελατήρια ακολουθεί μια όδευση εντός του πρώτου τεταρτημορίου της περιβάλλουσας ($MQ > 0$), καταλήγοντας σε μία μή-αποδεκτή κατάσταση, εκτός αυτής. Η *πραγματική* όμως φόρτιση επί της θεμελίωσης, όπως αυτή αναπαράγεται από την αριθμητική ανάλυση θεωρώντας συζευγμένα ελατήρια, ακολουθεί μια μή-

γραμμική όδευση, η οποία καταλήγει σε αστοχία φέρουσας ικανότητας από συνδυασμό φόρτισης με αρνητικόν μοχλοβραχίονα ($MQ < 0$).

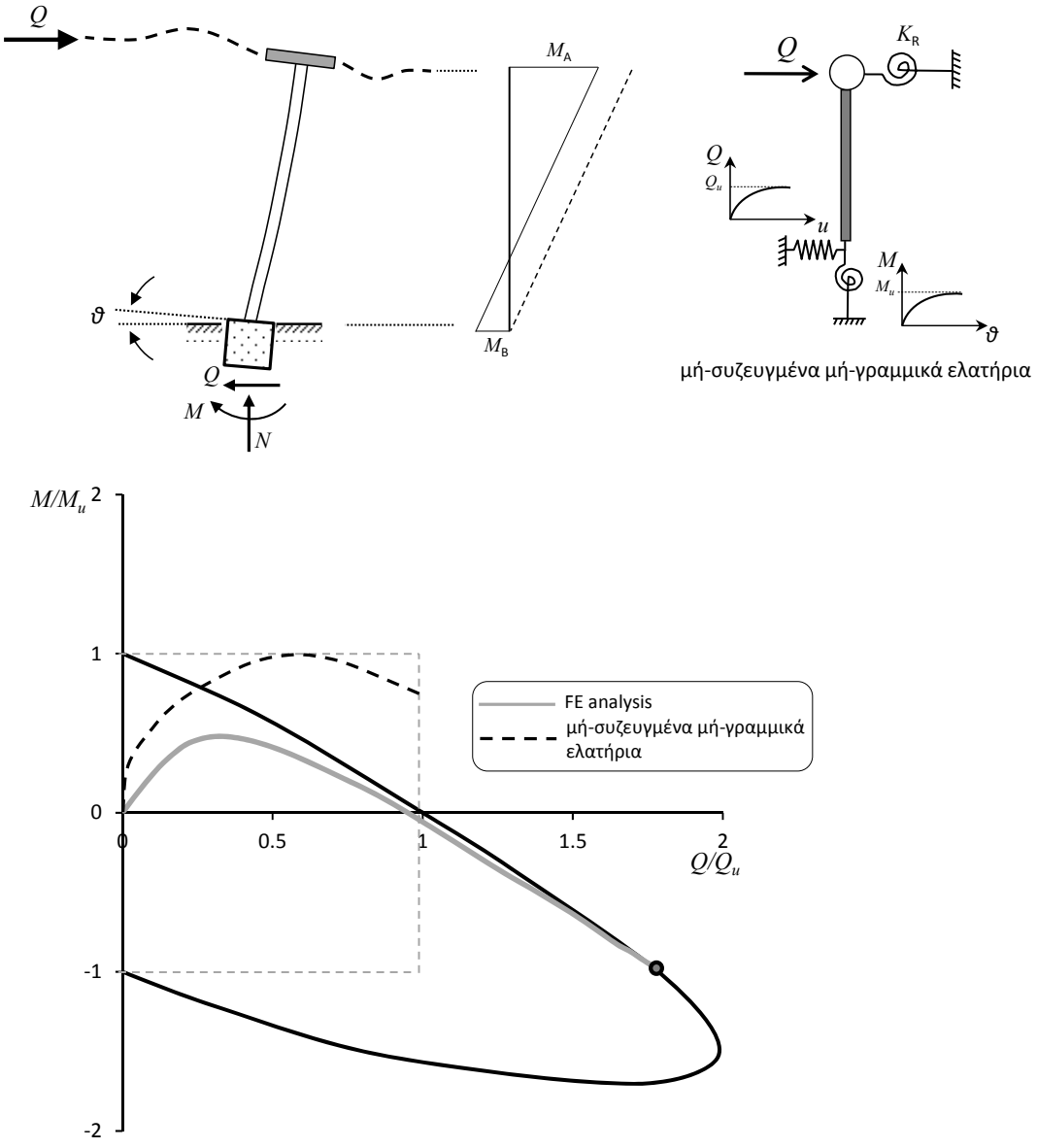

Σχ. 3.1 Σύστημα πυλώνα-καταστρώματος γέφυρας θεμελιωμένο σε φρέαρ, υποβαλλόμενο σε εγκάρσια φόρτιση στο κατάστρωμα. Σύγκριση οδεύσεων φόρτισης επί της κεφαλής φρέατος, προσομοιώνοντας το φρέαρ με (α) μή-συζευγμένα, και (β) συζευγμένα (FE analysis) μή-γραμμικά ελατήρια.

Άξιο αναφοράς αποτελεί η ικανότητα ανάπτυξης "*υπεραντοχής*" σε φέρουσα ικανότητα του φρέατος, με την αντίρροπη δράση τέμνουσας και ροπής επί της κεφαλής του (αρνητικός μοχλοβραχίονας ή *αρνητικό ενεργό ύψος* πυλώνα). Τα ανωτέρω ιδιαιτέρως ενδιαφέροντα ευρήματα καθιστούν σκόπιμη την περεταίρω διερεύνηση του προβλήματος.

Ορισμός του προβλήματος και μέθοδος ανάλυσης

Το πρόβλημα σκιαγραφείται στο **Σχ. 3.2**: φρέαρ κυβικού σχήματος θεμελιώνει σύστημα πυλώνα-καταστρώματος γέφυρας σε δίστρωτον συνεκτικό εδαφικό σχηματισμό. Το όλο σύστημα εδάφους–θεμελίωσης–ανωδομής αναλύεται με πεπερασμένα στοιχεία σε τρείς διαστάσεις (3D) με τον κώδικα ABAQUS. Το έδαφος και η θεμελίωση προσομοιώνονται με οκτακομβικά πεπερασμένα στοιχεία συνεχούς μέσου, το δε βάθρο με στοιχεία δοκού. Η σύνδεση του φρέατος με το έδαφος πραγματοποιείται μέσω στοιχείων διεπιφάνειας, τα οποία προσομοιώνουν ρεαλιστικά τα μή-γραμμικά φαινόμενα γεωμετρίας (αποκόλληση, ολίσθηση, ανασήκωμα). Η μή-γραμμική συμπεριφορά του εδάφους προσομοιώνεται με το καταστατικό προσομοίωμα του Κεφαλαίου 2.

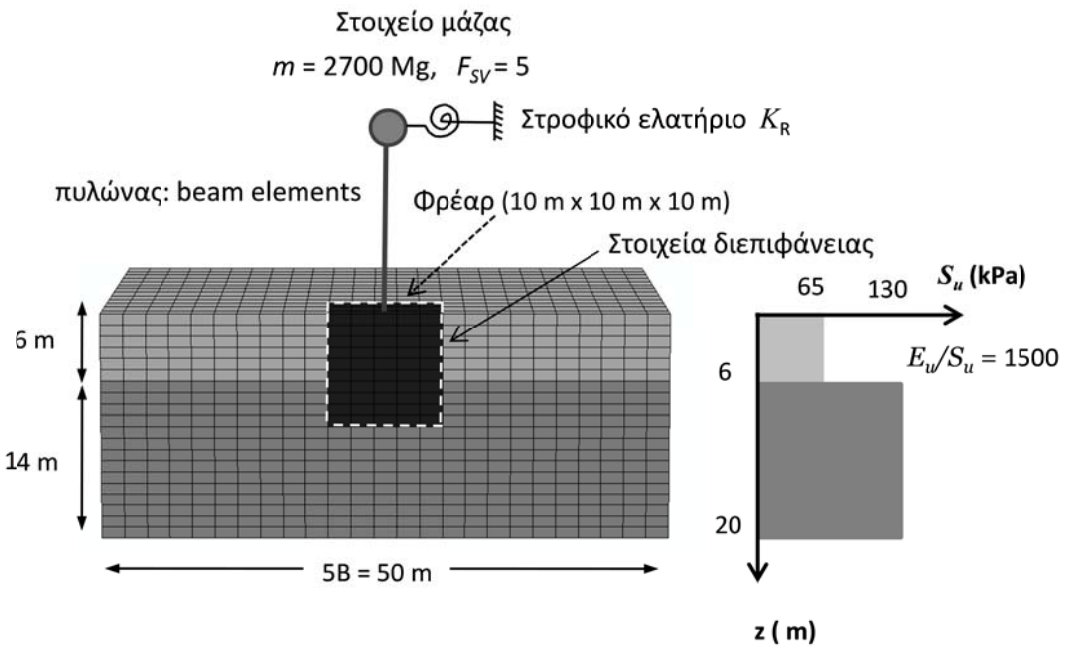

Σχ. 3.2 Το προσομοίωμα πεπερασμένων στοιχείων με τις διερευνούμενες παραμέτρους.

Το κατάστρωμα της γέφυρας προσομοιούμενο ως στοιχείο σημειακής μάζας, και το βάρος του φρέατος αντιστοιχούν σε έναν συντελεστή ασφαλείας έναντι φέρουσας αστοχίας σε κατακόρυφη φόρτιση FS_V = 5.

Οι παράμετροι που εισάγονται στην παρούσα διερεύνηση αφορούν στο ύψος του βάθρου, και στην στροφική δυσκαμψία του καταστρώματος ως προς τον πυλώνα.

Πιο συγκεκριμένα, εξετάζονται τρία ύψη: H = 6 m, 17 m και 55 m, η δε σταθερά του στροφικού ελατηρίου στο επίπεδο του καταστρώματος, K_R, υπολογίζεται έτσι ώστε ο λόγος

$$\kappa_{ratio} = \frac{K_R}{\left(\frac{4E_c I}{H}\right)}$$

όπου ($4EI_c/H$) η καμπτική δυσκαμψία του πυλώνα, να λαμβάνει τις εξής τιμές: κ_{ratio} = 0.1, 0.25, 0.5, 1. Για λόγους πληρότητας εξετάζεται και η περίπτωση του (ελεύθερου) προβόλου (κ_{ratio} = 0). Εάν και ομολογουμένως η προσομοίωση των επιβαλλομένων από το κατάστρωμα κινηματικών περιορισμών μέσω στροφικού ελατηρίου αποτελεί απλούστευση (αγνοούνται τυχόν περιορισμοί μετακινησιακής φύσεως), εντούτοις θεωρείται ότι αποδίδονται ρεαλιστικά οι συνθήκες για γέφυρες όπου το κατάστρωμα εδράζεται στα αντερείσματα μέσω ελαστομερών εφεδράνων ή τριβής.

Το σύστημα εδάφους-φρέατος-ανωδομής υποβάλλεται σε μονοτονική οριζόντια φόρτιση, Q, στο επίπεδο του καταστρώματος και ανιχνεύεται η [κανονικοποιημένη με τις αντίστοιχες "καθαρές" αντοχές σε ροπή (M_u) και σε τέμνουσα (Q_u)], όδευση των δρώντων φορτίων (M-Q) στην κεφαλή του φρέατος, εντός του χώρου που ορίζεται από την περιβάλλουσα αστοχίας του.

Αποτελέσματα

Το **Σχ. 3.3** παρουσιάζει ενδεικτικά αποτελέσματα για την περίπτωση H = 17 m. Παρατηρούμε ότι όσο πιο εύκαμπτη είναι η σύνδεση βάθρου-καταστρώματος (κ_{ratio} → 0.1) τόσο μεγαλύτερη ροπή μεταβιβάζεται στην θεμελίωση. Εξαιρετικό ενδιαφέρον παρουσιάζει η μορφή της όδευσης, η οποία χαρακτηρίζεται από ιδιότητες αναλλοίωτες ως προς την γεωμετρία και την δυσκαμψία του συστήματος εδάφους-θεμελίωσης-ανωδομής.

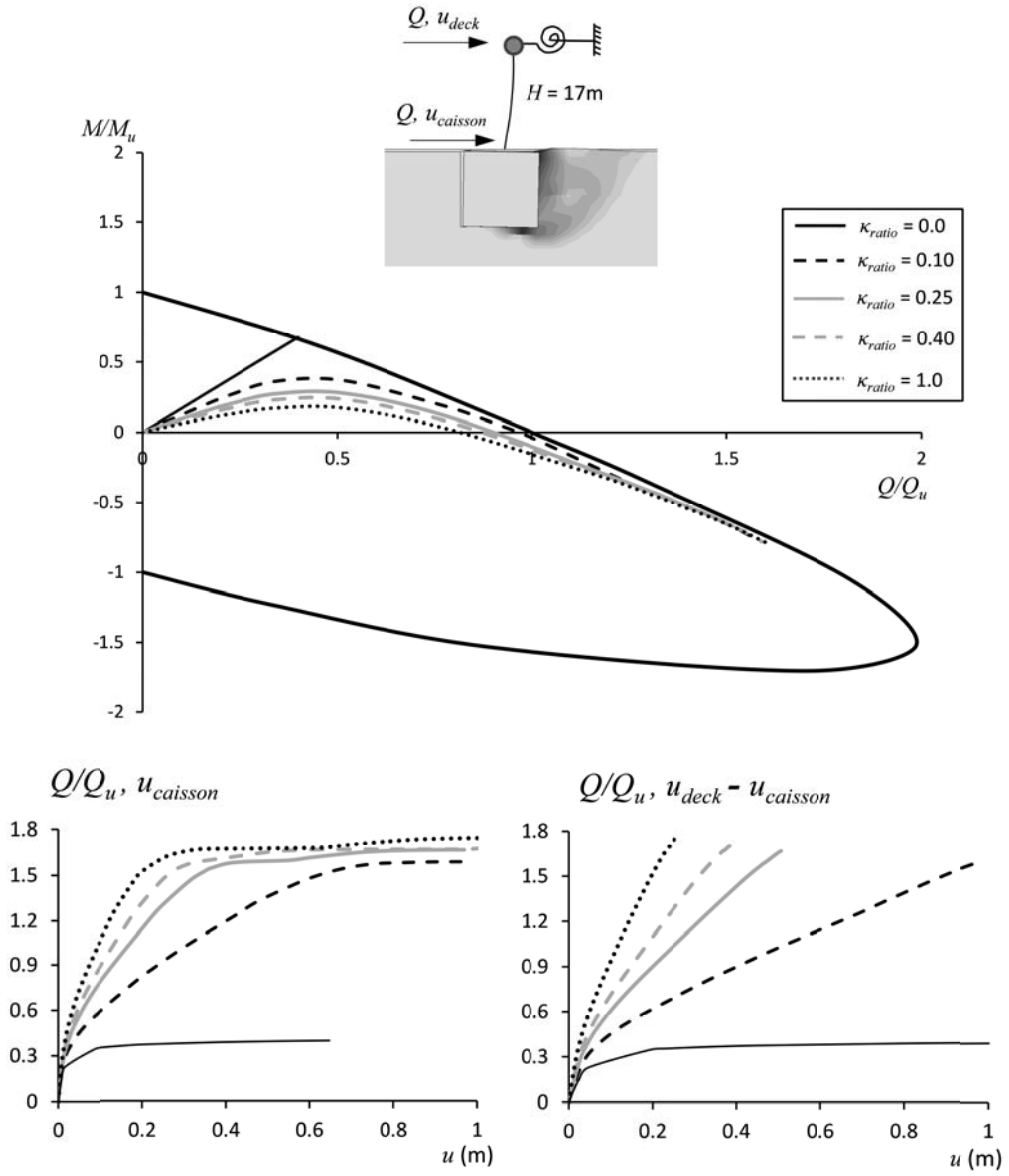

Σχ. 3.3 Καμπύλες όδευσης φόρτισης στην κεφαλή του φρέατος, για πυλώνα ύψους H = 17 m και όλους τους εξεταζόμενους λόγους δυσκαμψίας, κ_{ratio}.

Επί της εν λόγω καμπύλης, δύνανται να ταυτοποιηθούν τρία συγκεκριμένα σημεία τα οποία παρουσιάζονται στο **Σχ. 3.4** μαζί με την συλλογή όλων των οδεύσεων που εξήχθησαν στα πλαίσια της παραμετρικής διερεύνησης, και επιτρέπουν την μαθηματική περιγραφή της:

- Το σημείο C: όλες οι οδεύσεις *κινητοποιούν* μια συγκεκριμένη "υπεραντοχή" στην φέρουσα ικανότητα του φρέατος, η οποία διέπεται από μηχανισμό αστοχίας αναστρόφου εκκρεμούς. Οι αδιαστατοποιημένες συντεταγμένες του σημείου για φρέατα με βάθος εγκιβωτισμού D/B = 1 δίδονται στο σχήμα

(π/2, - 2/3). Σημειώνεται ότι λόγω της διεύρυνσης της περιβάλλουσας αστοχίας με αύξηση του λόγου εγκιβωτισμού (βλ. Κεφάλαιο 2), οι αδιαστατοποιημένες συντεταγμένες του σημείου διαφέρουν για κάθε D/B.

- Το σημείο ***B***: παρατηρείται ότι το μέγιστο (ως προς την ροπή) της καμπύλης όδευσης αποτελεί και το σημείο τομής: της όδευσης, με την ευθεία που ορίζεται από τα σημεία {0.5Q_u , 0} και {Q_f /Q_u , M_f /M_u } (σημείο τομής της όδευσης του εκάστοτε προβόλου με την περιβάλλουσα αστοχίας)
- Το σημείο ***A***: η κλίση της αρχικής εφαπτομένης στην καμπύλη όδευσης αντιστοιχεί στο αρχικό *ενεργό ύψος* του πυλώνα, H_{eff}.

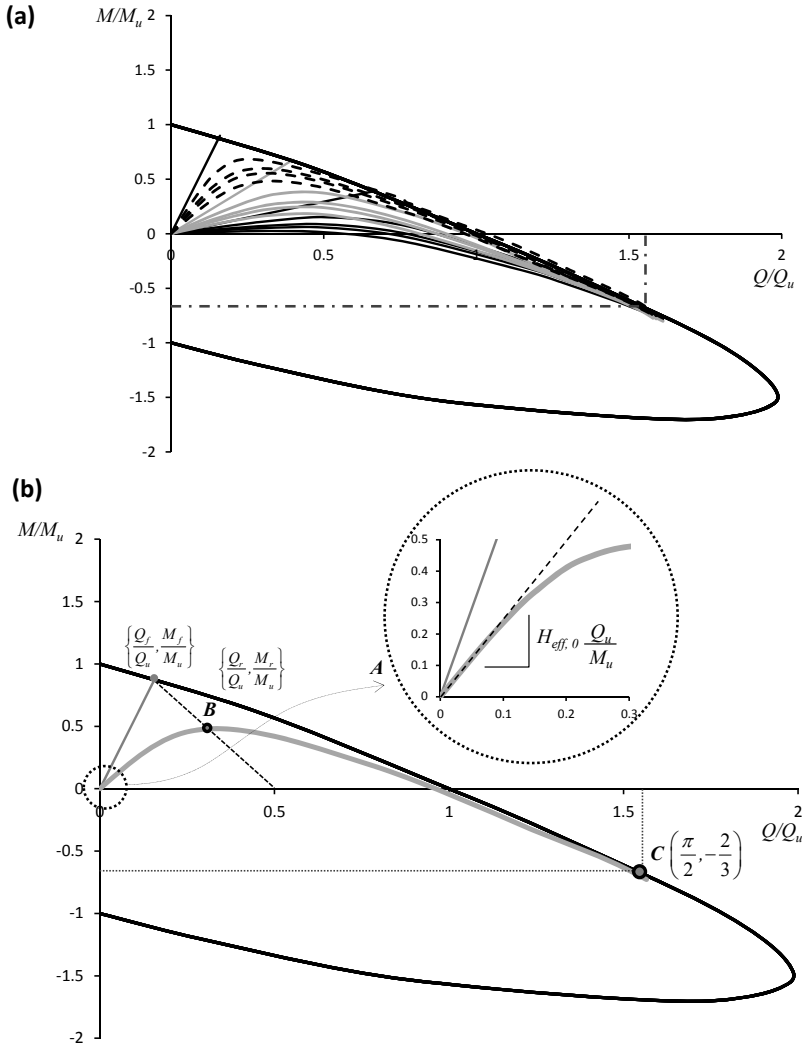

Σχ. 3.4 (α) Συλλογή των οδεύσεων φόρτισης στην κεφαλή του φρέατος, (β) χαρακτηριστικά σημεία επί της καμπύλης της όδευσης, από τα οποία προκύπτει η αναλυτική της διατύπωση

Όσον αφορά το H_{eff}, αυτό προκύπτει βάσει του στατικού συστήματος πυλώνα-καταστρώματος (βλ. **Σχ. 3.5**).

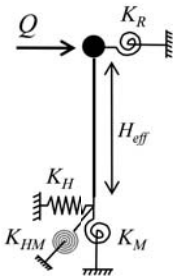

Σχ. 3.5 Στατικό σύστημα πυλώνα-καταστρώματος για τον υπολογισμό του ενεργού του ύψους, αντικαθιστώντας το έδαφος με συζευγμένα μη-γραμμικά ελατήρια

και δίδεται από την σχέση

$$H_{eff} = \frac{2EI_c K_R K_{HM} - 2EI_c K_{HM}^2 H - K_R K_{HM}^2 H^2 + K_R K_H K_M H^2 + 2EI_c K_H K_M H}{2\left(EI_c K_R K_H - K_R K_{HM}^2 H - EI_c K_{HM}^2 + EI_c K_H K_M + K_R K_H K_M H\right)} \quad (1)$$

Για την αναλυτική διατύπωση της όδευσης φορτίσεως προτείνεται η ακόλουθη έκφραση:

$$\frac{M}{M_u} = \gamma\left[(1+\alpha)\left(1-e^{-\beta\frac{Q}{Q_u}}\right)-\alpha\frac{Q}{Q_u}\right] \quad (2)$$

η οποία περιέχει τρείς παραμέτρους (α ,β και γ) που υπολογίζονται από την επίλυση συστήματος των τριών εξισώσεων, όπως αυτές προκύπτουν από τα χαρακτηριστικά σημεία (A, B, C) της καμπύλης. Με κατάλληλη επεξεργασία των αποτελεσμάτων, η σύγκριση μεταξύ των αριθμητικών και των αναλυτικών οδεύσεων παρουσιάζεται στο **Σχ. 3.6**

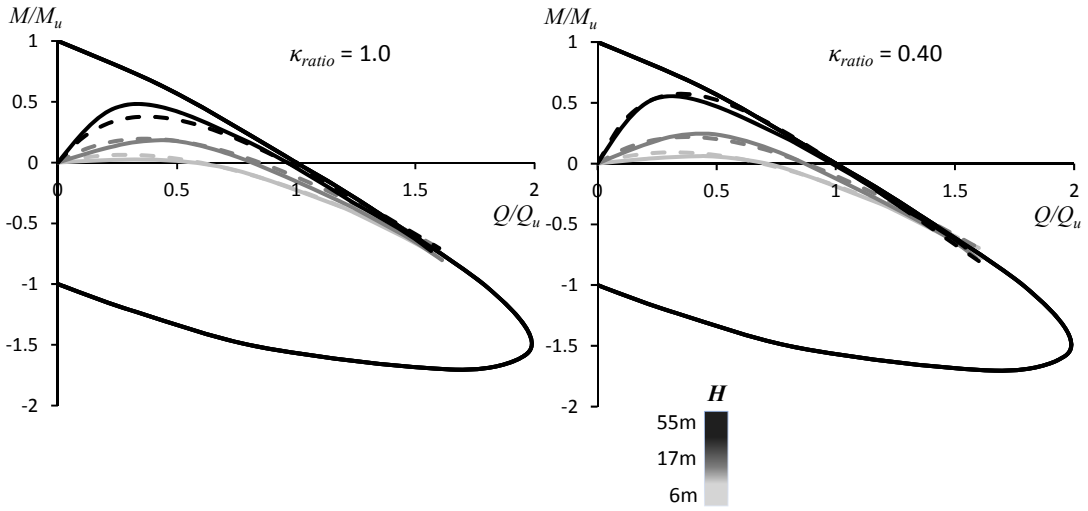

Σχ. 3.6 Σύγκριση μεταξύ αριθμητικών (συμπαγείς γραμμές) και αναλυτικών (διακεκομμένες γραμμές) αποτελεσμάτων για την όδευση της φόρτισης στην θεμελίωση

Μή-γραμμική απόκριση θεμελίωσης-ανωδομής: Πρόταση για τον προκαταρκτικό σεισμικό σχεδιασμό φρεάτων

Στην έως τώρα ανάλυση του προβλήματος, η ανωδομή (δηλαδή το βάθρο και το κατάστρωμα) θεωρήθηκαν ελαστικά. Στην περίπτωση αυτή, οι δυνάμεις που παραλαμβάνονται από τα στοιχεία του συστήματος (θεμελίωση, βάθρο, κόμβος βάθρου-καταστρώματος) δείχνονται σχηματικά στο **Σχ. 3.7**.

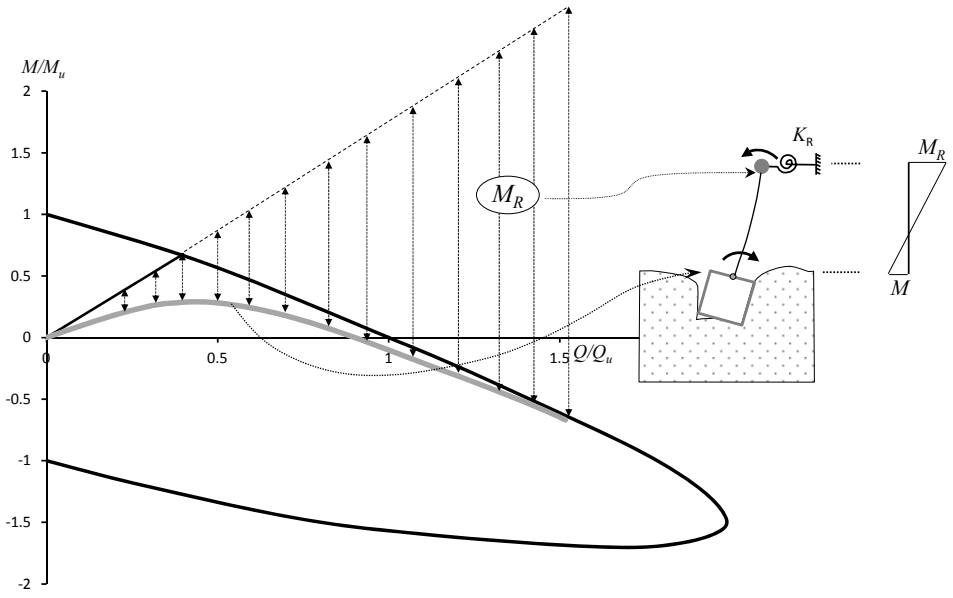

Σχ. 3.7 Κατανομή των φορτίων σε ανωδομή και θεμελίωση

Ως εκ τούτου, η όδευση αντιστοιχεί στην φόρτιση επί της θεμελίωσης αλλά και στην καταπόνηση της βάσης του βάθρου, ενώ M_R η είναι η ροπή που μπορεί να παραλάβει ο κόμβος βάθρου-καταστρώματος. Δεδομένου ότι

(α) κατά τους ισχύοντες κανονισμούς, η ανωδομή σχεδιάζεται για αστοχία στον κόμβο (κρίσιμη περιοχή), ενώ η πλαστική άρθρωση στην βάση αποτρέπεται, και

(β) η διατιθέμενη "υπεραντοχή" του φρέατος μπορεί να αξιοποιηθεί προς επίτευξιν της βέλτιστης τεχνο-οικονομικής λύσης σχεδιασμού της θεμελίωσης,

προτείνεται μεθοδολογία για τον προκαταρκτικό σεισμικό σχεδιασμό των φρεάτων για δεδομένου συστήματος βάθρου-καταστρώματος, η οποία περιλαμβάνει τα εξής βήματα:

(i) Υπολογίζεται η σεισμική δράση στο κατάστρωμα, $Q = S_a\, mg$, όπου S_a η φασματική επιτάχυνση σχεδιασμού.

(ii) Με δεδομένη την σεισμική ικανότητα του κόμβου (αντοχή σε ροπή M, από τον δομοστατικό σχεδιασμό της ανωδομής), γίνεται η παραδοχή ότι αυτή αντιστοιχείται στην συνολική ροπή M_R που καταπονεί τον κόμβο κατά την αστοχία του φρέατος σε φέρουσα ικανότητα. Από το **Σχ. 3.7**, η ροπή για φρέατα με D/B = 1 προκύπτει ως: $M = \left(H \frac{Q_u}{M_u} + \frac{2}{3} \right) M_u$.

(iii) Από τα (i) και (ii) υπολογίζονται οι "καθαρές" αντοχές του φρέατος σε τέμνουσα και σε ροπή (Q_u, M_u), βάσει των οποίων διαστασιολογείται.

(iv) Ελέγχεται ο συντελεστής ασφαλείας σε κατακόρυφη φόρτιση, FS_V. Εάν $FS_V \geq 2$ (ή ο όποιος απαιτούμενος), τότε ολοκληρώνεται η διαδικασία προκαταρκτικού σχεδιασμού. Εάν δεν ικανοποιείται η ανωτέρω συνθήκη, επαναδιαστασιολογείται το φρέαρ (αυξάνοντας τις διαστάσεις) έως ότου η απαίτηση για τον FS_V ικανοποιηθεί. Έπειτα, ελέγχονται οι δράσεις σχεδιασμού (Q, M) στον χώρο της νέας κανονικοποιημένης καμπύλης αστοχίας του φρέατος (η M_R θα βρίσκεται τώρα στα αριστερά της "υπεραντοχής"). Στην περίπτωση που $Q < Q_u$ (χώρος στον οποίον η M

δύναται ναι είναι > M_R) χαράσσεται η καμπύλη όδευσης και ελέγχονται οι δράσεις τόσο στον κόμβο όσο και στην βάση του βάθρου ως προς την ικανότητάς τους.
Είναι προφανές ότι πρόκειται για μία επαναληπτική διαδικασία διαστασιολόγησης του φρέατος, σε όρους αντοχής. Όσον αφορά την τελική διαστασιολόγηση, αυτή πραγματοποιείται σε ύστερο στάδιο, με γνώμονα πλέον τις αναμενόμενες μετακινήσεις, π.χ. σε ένα πλαίσιο σχεδιασμού της γέφυρας με στάθμες επιτελεστικότητας (Performance-Based Design).

Κεφάλαιο 4ο

*Περί της σεισμικής απόκρισης σεισμικώς **υπό**-διαστασιολογημένων φρεάτων θεμελιώσεως*

Οι αρχές του ικανοτικού σχεδιασμού αναφέρονται κατά κύριον λόγο στην ανωδομή, αγνοώντας ή υπο-εκτιμώντας την επιρροή εδάφους και θεμελίωσης. Μάλιστα, οι περισσότεροι αντισεισμικοί κανονισμοί απαιτούν η θεμελίωση να παραμένει οιονεί ελαστική. Παρότι μια τέτοια απαίτηση μπορεί να φαίνεται λογική (αστοχίες στο επίπεδο της θεμελίωσης είναι καί δύσκολα ανιχνεύσιμες καί δύσκολα επιδιορθώσιμες), μπορεί να οδηγήσει σε μη-συντηρητικές υπερ-απλουστεύσεις, ιδίως στην περίπτωση πολύ ισχυρών σεισμικών διεγέρσεων, όπου η ανάπτυξη σημαντικής γεωμετρικής μή-γραμμικότητας, όπως η αποκόλληση και η ολίσθηση, στην θεμελίωση είναι αναπόφευκτες. Επιπλέον, αγνοώντας τα φαινόμενα αυτά μένουν ανεκμετάλλευτοι μηχανισμοί οι οποίοι δύνανται να περιορίσουν την σεισμική ενέργεια που μεταβιβάζεται στην ανωδομή.

Σύμφωνα με τον ισχύοντα–συμβατικό ικανοτικό σχεδιασμό, για την διαστασιολόγηση της θεμελίωσης χρησιμοποιούνται κατάλληλοι συντελεστές ασφαλείας ώστε να περιοριστεί η ανάπτυξη μή-γραμμικών φαινομένων στο επίπεδο της θεμελίωσης κατά την σεισμική φόρτιση, να αποφευχθεί δε πάση θυσία η αστοχία φέρουσας ικανότητας. Δεδομένου ότι η ανάπτυξη πλαστικής άρθρωσης

επιτρέπεται μόνον για τα στοιχεία της ανωδομής, χρησιμοποιούνται κατάλληλοι συντελεστές *υπεραντοχής* προκειμένου να εξασφαλισθεί ότι η φέρουσα ικανότητα της θεμελίωσης θα είναι μεγαλύτερη από την αντοχή της ανωδομής [π.χ. ΕΑΚ, 2000 και EC-8]. Εντούτοις, εξαιτίας του ανακυκλικού και κινηματικού χαρακτήρα της σεισμικής φόρτισης, η ενεργοποίηση της μή-γραμμικής ανελαστικής απόκρισης της θεμελίωσης δεν συνιστά υποχρεωτική αστοχία υπό ισχυρή σεισμική ένταση. Αντιθέτως μάλιστα, πρόσφατες μελέτες καταδεικνύουν την ενδεχομένως ευνοϊκή δράση της, προτείνοντας μέχρι και την ενσωμάτωση σχετικών οδηγιών στους Κανονισμούς [FEMA-356, 2000; Martin and Lam, 2000; Kutter et al., 2003; Gazetas et al., 2003; 2007; Harden and Hutchinson, 2006; Paolucci et al., 2008; Kawashima et al., 2007; Gajan & Kutter, 2008; Chatzigogos et al., 2009; Anastasopoulos et al., 2009]. Ιδίως μάλιστα στην περίπτωση υψίκορμων κατασκευών όπως οι υψηλές γέφυρες, στις θεμελιώσεις των οποίων αναπτύσσονται μεγάλες ροπές, η μή-γραμμική γεωμετρία στην θεμελίωση συμβάλλει στην μείωση της απαιτούμενης πλαστιμότητας της ανωδομής. Βάσει των ανωτέρω θα ήταν ενδεχομένως εφικτή η αναθεώρηση της υφισταμένης φιλοσοφίας, προς μία κατεύθυνση σχεδιασμού που θα επέτρεπε την εκδήλωση των προαναφερθέντων μηχανισμών αστοχίας, εφόσον βέβαια τα αναπτυσσόμενα μετακινησιακά μεγέθη παραμένουν εντός αποδεκτών ορίων.

Στο παρόν κεφάλαιο διερευνάται η αποτελεσματικότητα της εν λόγω προσέγγισης για την περίπτωση των φρεάτων θεμελιώσεως. Στο **Σχ. 4.1** περιγράφεται σχηματικά η απόκριση όταν το φρέαρ (α) ακολουθώντας τις συμβατικές απαιτήσεις, προκύπτει σεισμικώς *υπέρ*-διαστασιολογημένο (ως προς την ανωδομή), και (β) ακολουθώντας μια νέα λογική προκύπτει σεισμικώς *υπό*-διαστασιολογημένο, ευνοώντας ανάπτυξη μή-γραμμικών φαινομένων.

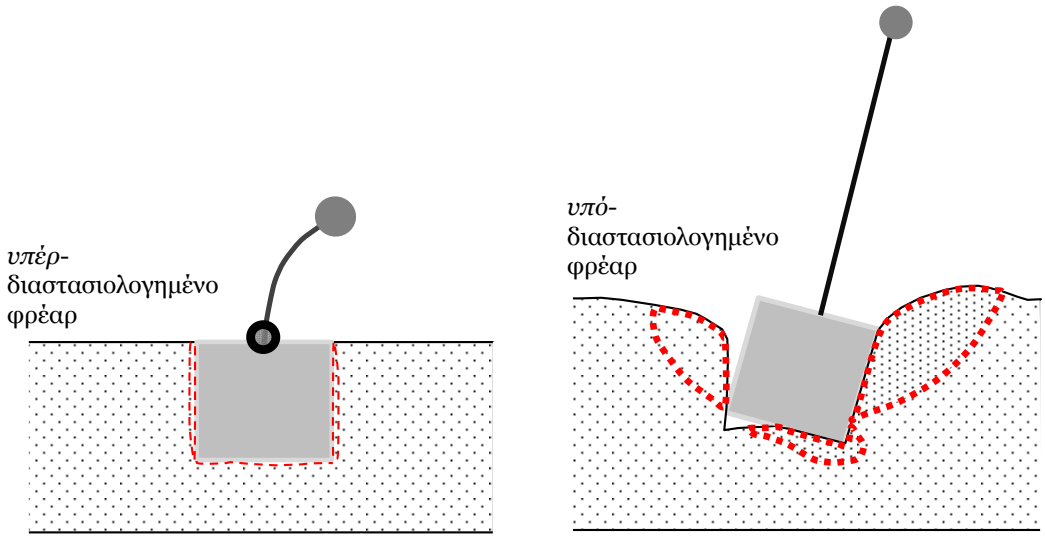

Σχ. 4.1 Απόκριση σεισμικώς *υπέρ*- και σεισμικώς *υπό*- διαστασιολογημένου φρέατος

Ορισμός του προβλήματος και μεθοδολογία ανάλυσης

Το εξεταζόμενο πρόβλημα παρουσιάζεται στο **Σχ. 4.2** και αποτελείται από φρέαρ κυβικού σχήματος με το οποίο θεμελιώνεται βάθρο γέφυρας σε δίστρωτο συνεκτικό εδαφικό σχηματισμό. Οι λεπτομέρειες της αριθμητικής προσομοίωσης παρουσιάζονται στο Κεφάλαιο 3. Στα σύνορα του προσομοιώματος επιβάλλονται κατάλληλοι κινηματικοί περιορισμοί ώστε να προσομοιώνεται η κίνηση ελευθέρου πεδίου. Το ύψος του βάθρου και η μάζα του καταστρώματος μεταβάλλονται παραμετρικά. Συνολικά εξετάζεται η δυναμική συμπεριφορά τεσσάρων (4) προσομοιωμάτων, σχεδιασμένων βάσει του στατικού (FS_V) και του σεισμικού (FS_E) συντελεστή ασφαλείας τους, όπως αυτός έχει προκύψει από την καμπύλη αντοχής του συστήματος εδάφους-φρέατος και μιας ψευδο-στατικώς επιβαλλομένης επιτάχυνσης στην κορυφή της ανωδομής, η οποία μεταφέρεται ως ζεύγος ροπής-τέμνουσας στην κεφαλή του φρέατος (**Σχ. 4.3**): (*α*) ένα "ελαφρώς" φορτιζόμενο (FS_V = 5.0), σεισμικώς *υπό*-διαστασιολογημένο (FS_E < 1) φρέαρ, (*β*) ένα "ελαφρώς" φορτιζόμενο, σεισμικώς *υπέρ*-διαστασιολογημένο (FS_E > 1) φρέαρ, (γ) ένα "βαρέως" φορτιζόμενο (FS_V = 2.5), σεισμικώς *υπό*-διαστασιολογημένο (F_E < 1) φρέαρ, και (δ) ένα "βαρέως" φορτιζόμενο, σεισμικώς *υπέρ*-διαστασιολογημένο φρέαρ.

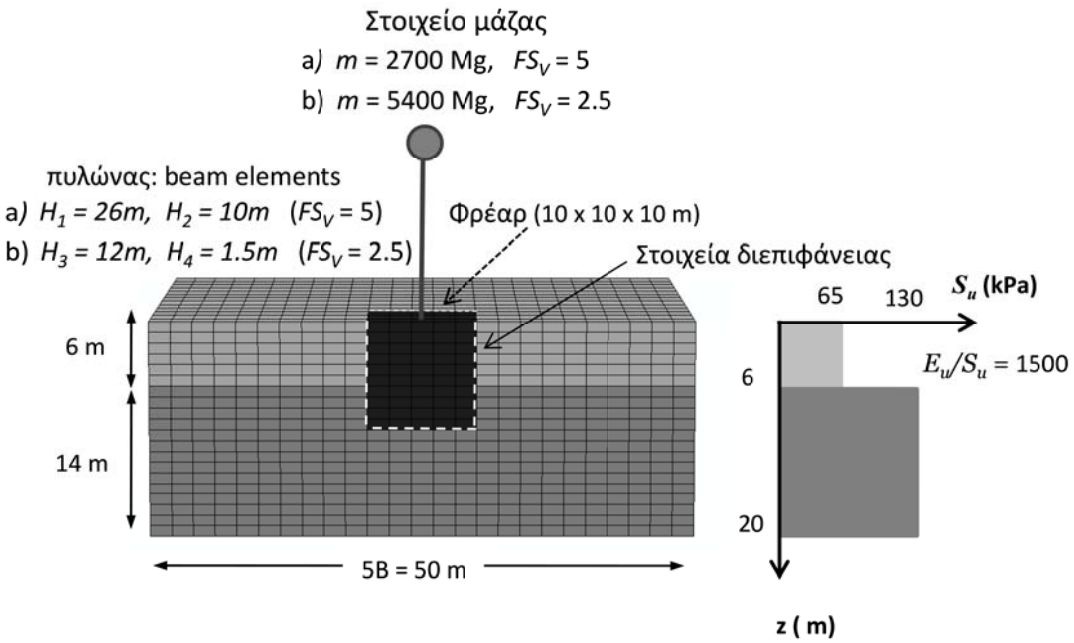

Σχ. 4.2 Το προσομοίωμα πεπερασμένων στοιχείων μαζί με τις παραμέτρους που επελέγησαν για την παραμετρική διερεύνηση

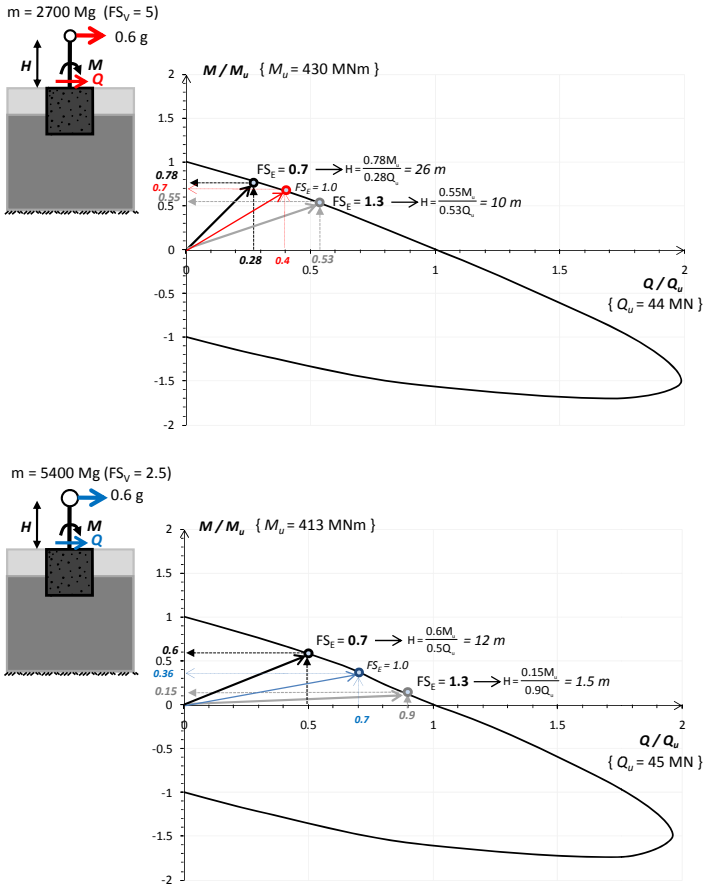

Σχ. 4.3 Υπολογισμός των υψών των βάθρων

Τα γεωμετρικά στοιχεία των ανωδομών επελέγησαν έτσι ώστε η θεμελιώδης ιδιοπερίοδός τους να αντιστοιχεί σε T_{str} = 0.6 sec, η οποία είναι μεγαλύτερη από την αντίστοιχη του εδαφικού σχηματισμού (T_{soil} = 0.41 sec). Με τον τρόπο αυτό δεν απαιτούνται αποσβεστήρες στα όρια του προσομοιώματος (ύπαρξη συχνότητας αποκοπής για την απόσβεση ακτινοβολίας, ίση με την θεμελιώδη ιδιοπερίδο του εδάφους).

Μέθοδος ανάλυσης

Το σύστημα εδάφους-φρέατος-ανωδομής υποβάλλεται σε σεισμική διέγερση στην βάση. Τα διεγείροντα επιταχυνσιογραφήματα προκύπτουν από μία επαναληπτική διαδικασία στην οποία υποβάλλονται τρείς “φυσικές” καταγραφές (Sakarya, JMA, Rinaldi). Κατά την διαδικασία αυτή, η οποία παρουσιάζεται σχηματικά στο **Σχ. 4.4**, οι καταγραφές τροποποιούνται καταλλήλως έως ότου το φάσμα απόκρισής τους να ταυτιστεί με ένα φάσμα “στόχο” (είτε σχεδιασμού είτε αυθαιρέτως θεωρουμένου). Έπειτα, τα τροποποιημένα επιταχυνσιογραφήματα διαδίδονται στην βάση του προσομοιώματος (deconvolution), και τα τελικώς προκύπτοντα από την διαδικασία αυτή, αποτελούν τα διεγείροντα επιταχυνσιογραφήματα.

Μέσω της διαδικασίας αυτής, η σύγκριση της απόκρισης των συστημάτων με έμφαση στην διερεύνηση του ευνοϊκού ή δυσμενούς ρόλου της μή-γραμμικής ανελαστικής αλληλεπίδρασης εδάφους-φρέατος-ανωδομής γίνεται “*επί ίσοις όροις*”, μιας και εξαλείφεται η εξάρτισή της από τα δυναμικά χαρακτηριστικά τόσο της διέγερσης (συχνοτικό περιεχόμενο, αριθμός κύκλων, διαδοχή παλμών) όσο και της ανωδομής (ενεργός ιδιοπερίοδος, T_{SSI}).

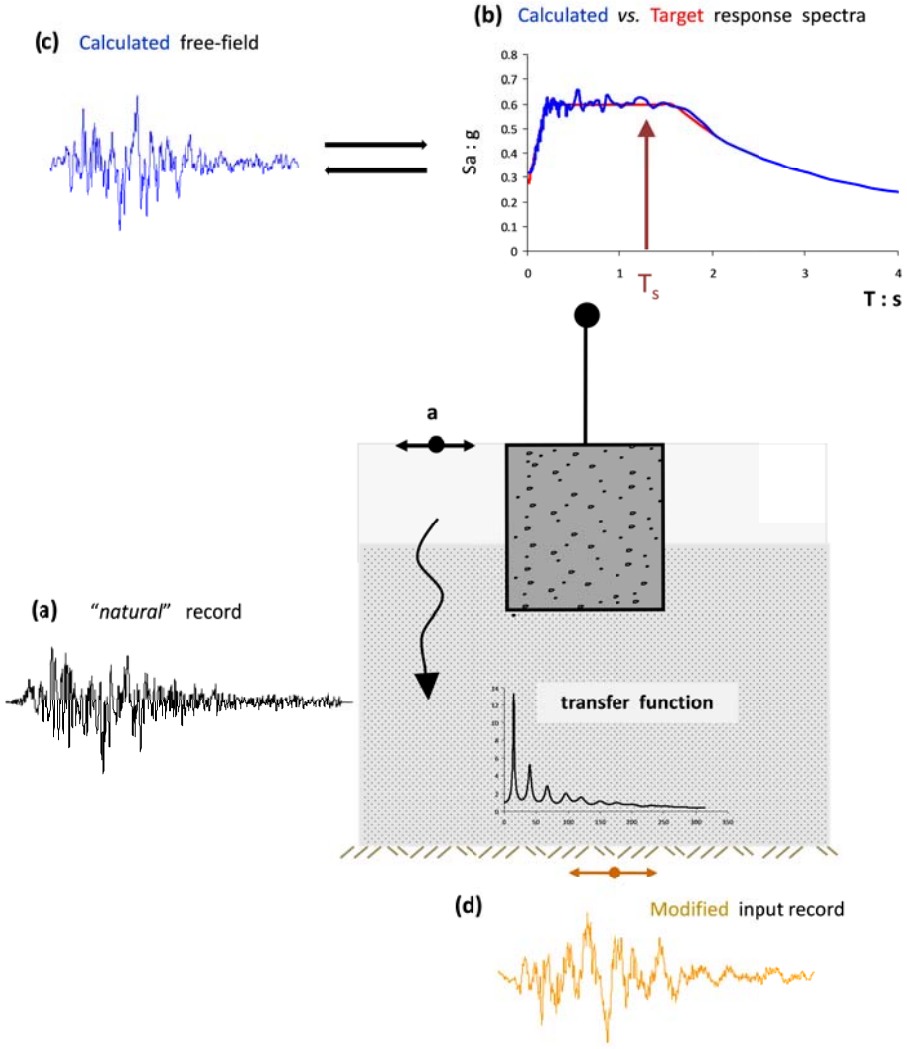

Σχ. 4.4 Επαναληπτική διαδικασία τροποποίησης "φυσικών" καταγραφών ούτως ώστε το φάσμα απόκρισής τους να ταυτιστεί με το φάσμα "στόχο".

Αποτελέσματα

Η σύγκριση της απόκρισης των συστημάτων παρουσιάζεται (ενδεικτικά, για την τροποποιημένη διέγερση Sakarya) στα **Σχ. 4.5-4.7**, σε όρους φασμάτων απόκρισης της κίνησης της μάζας ("floor" response spectra), οριζοντίων μετακινήσεων στο επίπεδο της μάζας, και ροπής-στροφής του φρέατος. Ως αναμενόταν, τα μή-γραμμικά φαινόμενα γεωμετρίας, τα οποία αναπτύσσονται κατά την απόκριση των σεισμικώς *υπό*-διαστασιολογημένων φρεάτων, παρέχουν ένα άνω όριο στις μεταβιβαζόμενες σεισμικές δράσεις στην ανωδομή, με κόστος όμως τις αυξημένες

δυναμικές στροφές του θεμελίου σε σχέση με τα αντίστοιχα σεισμικώς υπέρ-διαστασιολογημένα.

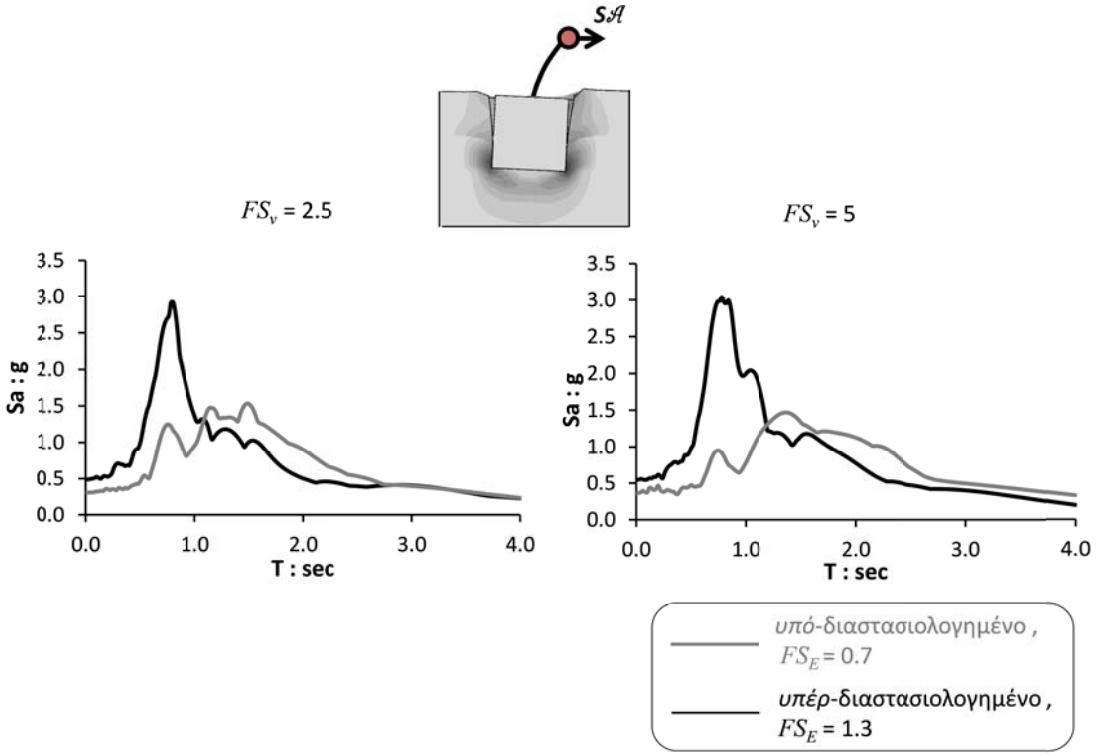

Σχ. 4.5 Φάσματα απόκρισης της κίνησης της μάζας ("floor" response spectra).

Αυτό γίνεται ιδιαιτέρως αντιληπτό από την μορφή των βρόχων ροπής-στροφής του **Σχ. 4.7**, και ιδίως από την απόκριση του ελαφρώς φορτισμένου, εκ των σεισμικώς *υπό*-διαστασιολογημένων θεμελίων, φρέατος. Παρόλα αυτά, χάρις στο σημαντικό βάρος και τον εγκιβωτισμό του φρέατος, τα οποία ασκούν δυνάμεις επαναφοράς κατά την λικνιστική απόκρισή του, η παραμένουσα στροφή και στις δύο περιπτώσεις είναι μηδαμινή.

Αναφορικά με τις αναπτυσσόμενες μετατοπίσεις στο επίπεδο της μάζας, κατά την συμβατική θεώρηση σχεδιασμού (σεισμικώς υπέρ-διαστασιολογημένες θεμελιώσεις) το σημαντικότερο μέρος της συνολικής μετατόπισης U_{tot} οφείλεται στην μετατόπιση λόγω κάμψης U_{flex}. Σε αντίθεση, οι σεισμικώς *υπό*-διαστασιολογημένες θεμελιώσεις αναπτύσσουν μετατόπιση κυρίως λόγω στροφής του θεμελίου U_{rigid} (στροφή στερεού σώματος), με την U_{flex} να είναι αμελητέα. Συνεπώς, σύμφωνα με αυτήν την θεώρηση σχεδιασμού, η καταπόνηση της

ανωδομής (η οποία συνδέεται με την U_{flex}) περιορίζεται σαφώς, αλλά με τίμημα αυξημένες (σχετικά) παραμένουσες μετατοπίσεις.

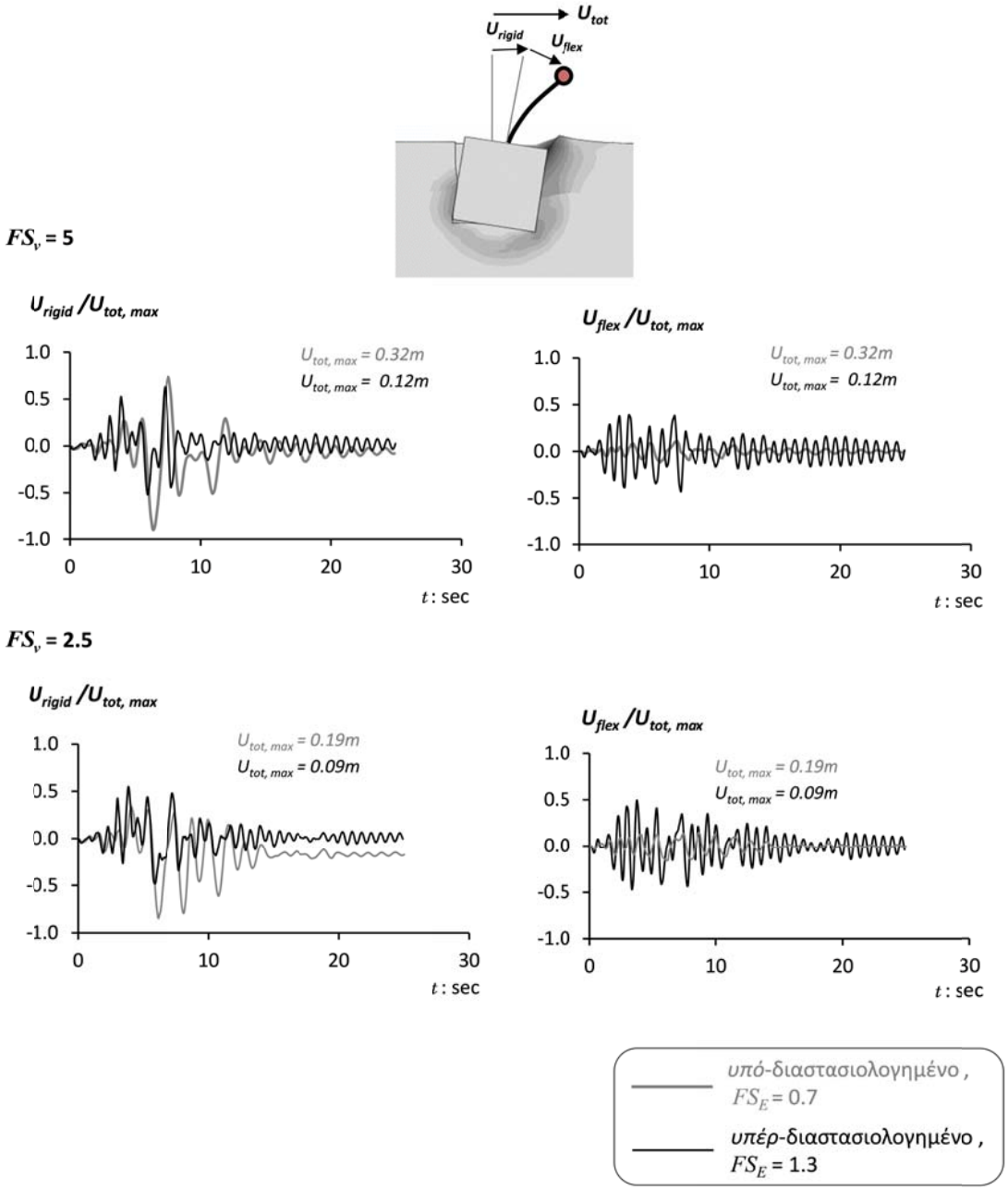

Σχ. 4.6 Κανονικοποιημένες οριζόντιες μετατοπίσεις στο επίπεδο της μάζας, λόγω κίνησης στην βάση (κίνηση στερεού) και λόγω κάμψης.

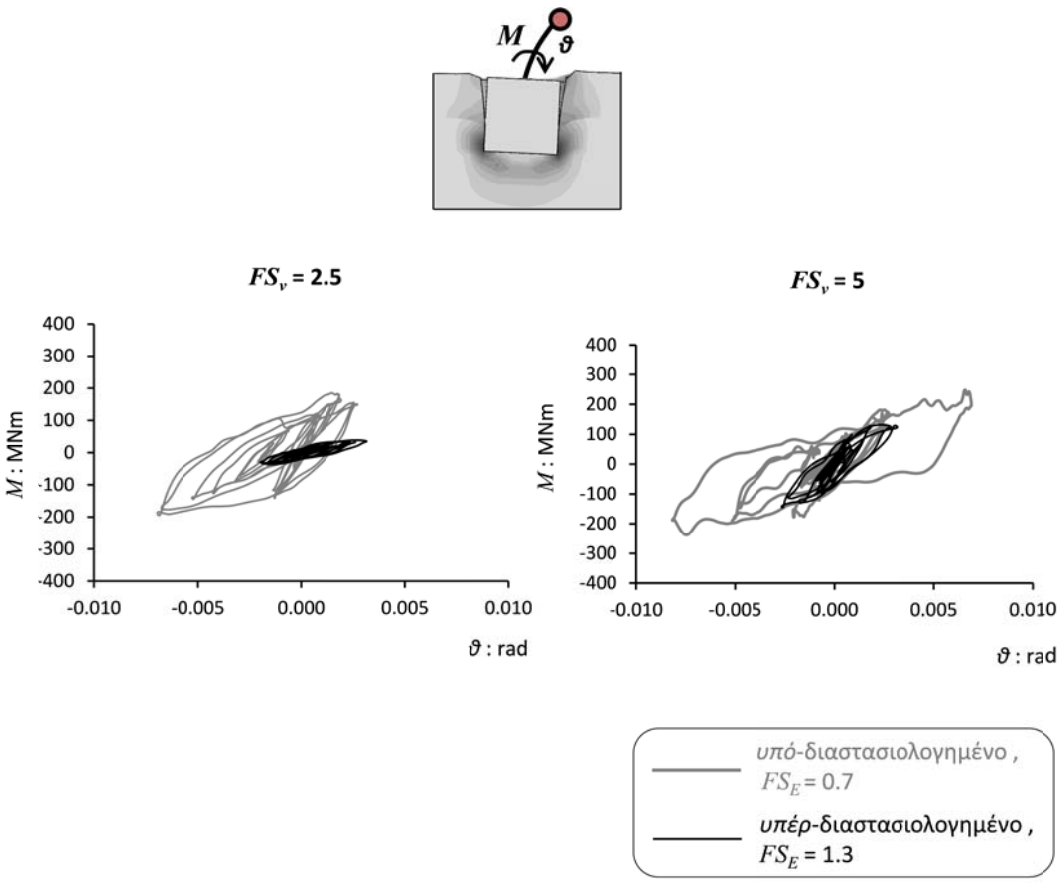

Σχ. 4.7 Εξέλιξη ροπής-στροφής στην κεφαλή του φρέατος

Εν κατακλείδι, τα αποτελέσματα των δυναμικών αναλύσεων, με έμφαση στην φυσική του προβλήματος της σεισμικής μή-γραμμικής αλληλεπίδρασης εδάφους-φρέατος-ανωδομής, αναδεικνύουν σ' αυτήν την περίπτωση την υπεροχή, σε όρους απόκρισης, των ελαφρώς φορτιζομένων σεισμικώς *υπό*-διαστασιολογημένων φρεάτων, τόσο ως προς στην απομείωση των σεισμικών δράσεων που μεταβιβάζονται στην ανωδομή, όσο και ως προς τις παραμένουσες μετακινήσεις. Δύναται ως εκ τούτου το υπόδειγμα αυτό να θεωρηθεί προς υιοθέτηση ως μία οικονομικώς συμφέρουσα τεχνική λύση η οποία ταυτόχρονα δρα εν είδει σεισμικής μόνωσης.

Κεφάλαιο 5ο

Διερεύνηση αλληλεπίδρασης φρεάτων θεμελιώσεως–ανωδομής μέσω Ανάλυσης Δυναμικής Αντίστασης (IDA)

Στο κεφάλαιο αυτό επεκτείνεται η παραμετρική διερεύνηση της σεισμικής μή-γραμμικής ανελαστικής αλληλεπίδρασης εδάφους–φρέατος θεμελίωσης–ανωδομής, η οποία παρουσιάστηκε στην προηγούμενη ενότητα. Για να ληφθεί υπόψιν η αναπόφευκτη αβεβαιότητα των αποτελεσμάτων για διάφορες διεγέρσεις (ως προς την μορφή, την ένταση και τα δυναμικά χαρακτηριστικά), αξιοποιείται η τεχνική της Ανάλυσης Δυναμικής Αντίστασης (Incremental Dynamic Analysis, Vamvatsikos et al. 2002). Γίνονται δηλαδή μή γραμμικές δυναμικές αναλύσεις υπό πολλαπλά επιταχυνσιογραφήματα κλιμακούμενα σε κατάλληλα επίπεδα έντασης, έτσι ώστε να οδηγήσουν την κατασκευή από τη λειτουργικότητα (ελαστική απόκριση) έως την αστοχία σε καθολική δυναμική αστάθεια. Πρόκειται για μια μέθοδο υψηλού χρονικού κόστους, η οποία όμως παρέχει μια πλήρη εικόνα της σεισμικής συμπεριφοράς της κατασκευής και επιτρέπει τη λεπτομερή σύγκριση των παραμέτρων της απόκρισης και της αντοχής των εξεταζομένων συστημάτων, για τις διάφορες παραδοχές σχεδιασμού και προσομοίωσής του.

Τα αποτελέσματα της ΑΔΑ είναι ζεύγη τιμών του Μέτρου Έντασης (ΜΕ) του σεισμού και της προκύπτουσας Παραμέτρου Απόκρισης (ΠΑ) για κάθε ανάλυση. Με κατάλληλη παρεμβολή παρουσιάζονται σε συνεχείς καμπύλες ΑΔΑ, μία για κάθε καταγραφή. Οι καμπύλες αυτές, και η σύνοψή τους σε 16, 50 και 84% καμπύλες ΔΑ (Vamvatsikos 2002), παρουσιάζουν μια πλήρη εικόνα της συμπεριφοράς της κατασκευής, δίνοντας π.χ. το ΜΕ το οποίο πρέπει να έχει η σεισμική διέγερση ώστε να οδηγήσει (με συγκεκριμένη πιθανότητα) την κατασκευή σε ΠΑ ίση με δεδομένη τιμή. Στην παρούσα έρευνα, ως ΜΕ ελήφθη η κορυφαία τιμή της εδαφικής επιτάχυνσης ελευθέρου πεδίου (PGA), ενώ ως ΠΑ τα εξής: η πλαστιμότητα μετακίνησης, η μέγιστη σχετική μετακίνηση της ανωδομής, η μέγιστη δυναμική και η παραμένουσα στροφή του φρέατος.

Το αριθμητικό προσομοίωμα

Το πρόβλημα σκιαγραφείται στο **Σχ. 5.1**: φρέαρ κυβικού σχήματος θεμελιώνει βάθρο γέφυρας σε δίστρωτον συνεκτικό εδαφικό σχηματισμό. Οι λεπτομέρειες της αριθμητικής προσομοίωσης με πεπερασμένα στοιχεία σε τρείς διαστάσεις (3D) ανεπτύχθη στις προηγηθείσες ενότητες.

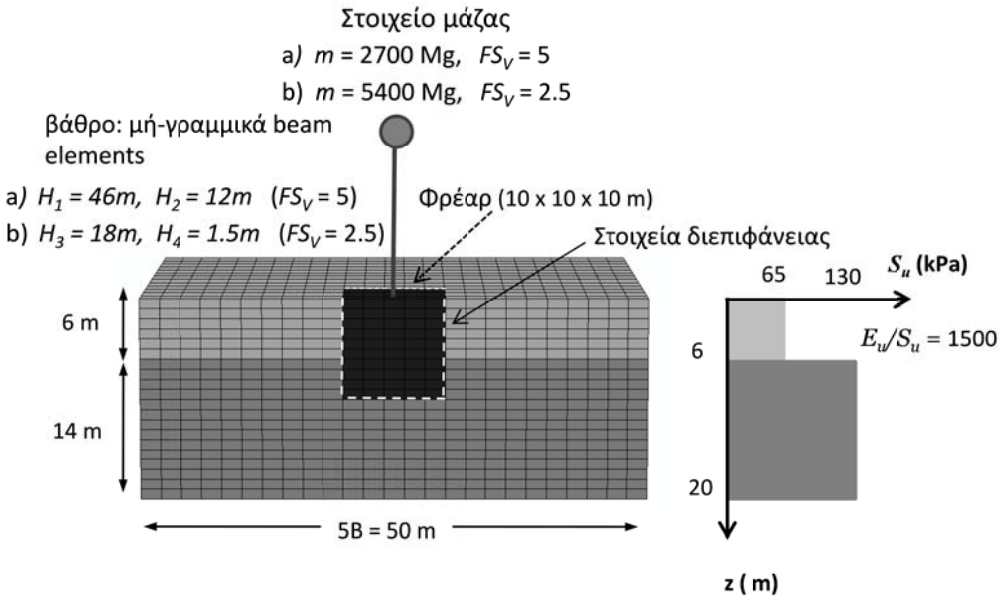

Σχ. 5.1 Το προσομοίωμα πεπερασμένων στοιχείων μαζί με τις παραμέτρους που επελέγησαν για την παραμετρική διερεύνηση

Σύμφωνα με την μεθοδολογία που ακολουθήθηκε στο προηγούμενο κεφάλαιο, το ύψος του βάθρου και η μάζα του καταστρώματος μεταβάλλονται παραμετρικά. Συνολικά εξετάζεται η δυναμική συμπεριφορά τεσσάρων (4) εξιδανικευμένων προσομοιωμάτων, σχεδιασμένων βάσει του στατικού (FS_V) και του σεισμικού (FS_E) συντελεστή ασφαλείας τους, όπως αυτός έχει προκύψει από την καμπύλη αντοχής του συστήματος εδάφους-φρέατος και μιας ψευδο-στατικώς επιβαλλομένης "κρίσιμης" επιτάχυνσης στην κορυφή της ανωδομής, $A_{C,f}$ η οποία οδηγεί την θεμελίωση σε αστοχία φέρουσας ικανότητας. Η ανωδομή σχεδιάζεται με επιτάχυνση διαρροής, $A_{C,str}$ έτσι ώστε κατά την μεν συμβατική θεώρηση σχεδιασμού να επιδιώκεται η αστοχία της έναντι αστοχίας στην θεμελίωση, ή

αλλιώς $\frac{A_{c,f}}{A_{c,str}} > 1$ (υπέρ-διαστασιολογημένη θεμελίωση, ως προς την ανωδομή), κατά την δε μή-συμβατική θεώρηση να ισχύει $\frac{A_{c,f}}{A_{c,str}} < 1$ (*υπό*-διαστασιολογημένη θεμελίωση, ως προς την ανωδομή). Η σύνοψη των χαρακτηριστικών των τεσσάρων προσομοιωμάτων καθώς και οι τιμές για την κρίσιμη επιτάχυνση A_C που ελήφθησαν στην παρούσα εργασία δίδονται στον **Πίνακα 1**.

Η συμπεριφορά του εδάφους προσομοιώνεται με τροποποιημένο μή-γραμμικό καταστατικό προσομοίωμα με κριτήριο διαρροής Von Mises, κινηματικό-ισοτροπικό νόμο κράτυνσης και συσχετισμένο νόμο πλαστικής ροής, όπως παρουσιάστηκε στο 2^{ο} Κεφάλαιο. Οι παράμετροι του προσομοιώματος βαθμονομούνται με βάση τις δημοσιευμένες καμπύλες G–γ της βιβλιογραφίας. Τα πλευρικά όρια έχουν δεσμευτεί με κατάλληλους κινηματικούς περιορισμούς ώστε να ακολουθούν την κίνηση του ελευθέρου πεδίου.

Η μή-γραμμική συμπεριφορά της ανωδομής προσομοιώνεται με έναν υπερβολικό νόμο ροπής (M)−καμπυλότητας (κ) της μορφής:

$$\kappa = \frac{M_y}{EI}\left(\frac{M}{M_y - M}\right) \qquad \text{για } M < M_y$$

όπου *EI* η καμπτική δυσκαμψία της ανωδομής και M_y η ροπή διαρροής, υπολογισθείσα από την εκάστοτε αντιστοιχούσα $A_{C,\,str}$.

Τα γεωμετρικά στοιχεία των ανωδομών επελέγησαν έτσι ώστε η θεμελιώδης ιδιοπερίοδός τους να αντιστοιχεί σε T_{str} = 0.6 sec, η οποία είναι μεγαλύτερη από την αντίστοιχη του εδαφικού σχηματισμού (T_{soil} = 0.41 sec).

Πίνακας 1. Σύνοψη των χαρακτηριστικών για τα τέσσερα εξιδανικευμένα προσομοιώματα.

model	**m (Mg)**	FS_V	**H (m)**	A_c **: κρίσιμη επιτάχυνση**	**Θεμελίωση**
1	2700	5.0	46	*0.3* g (θεμελίωση) 0.8 g (ανωδομή)	***υπό***-διαστασιολογημένη
2	2700	5.0	12	0.8 g (θεμελίωση) *0.3* g (ανωδομή)	*υπέρ*-διαστασιολογημένη
3	5400	2.5	18	*0.3* g (θεμελίωση) 0.8 g (ανωδομή)	***υπό***-διαστασιολογημένη
4	5400	2.5	1.5	0.8 g (θεμελίωση) *0.3* g (ανωδομή)	*υπέρ*-διαστασιολογημένη

Σεισμικές καταγραφές

Για την εκτέλεση των δυναμικών αναλύσεων χρησιμοποιούνται 10 φυσικές σεισμικές καταγραφές, οι οποίες και παρουσιάζονται στο **Σχ. 5.2** με τα αντίστοιχα ελαστικά φάσματα απόκρισής τους. Γίνεται φανερό ότι οι καταγραφές αυτές καλύπτουν μεγάλο εύρος περιόδων και φασματικών τιμών, μερικές δε και επηρεασμένες από φαινόμενα κατευθυντικότητας και αλματικότητας (fling).

Η επικλιμάκια αναγωγή των φυσικών καταγραφών πραγματοποιήθηκε με γνώμονα τον διττό ρόλο του εδάφους στην απόκριση του φρέατος, το οποίο:

(1) λειτουργεί ως μέσον διαδόσεως του σεισμικού κύματος, ενισχύοντας ή εξασθενώντας το. Σε περίπτωση πολύ ισχυρών διεγέρσεων, το έδαφος πιθανόν να αστοχήσει λόγω έντονης μή-γραμμικότητας πριν από οποιαδήποτε ενδεχόμενη αστοχία του συστήματος θεμελίωσης—ανωδομής. Είναι σαφές ότι η περίπτωση αυτή είναι εκτός σκοπού της παρούσας εργασίας.

(2) Παρέχει τους μηχανισμούς αντίστασης που συμβάλλουν στην φέρουσα ικανότητα του συστήματος εδάφους—φρέατος.

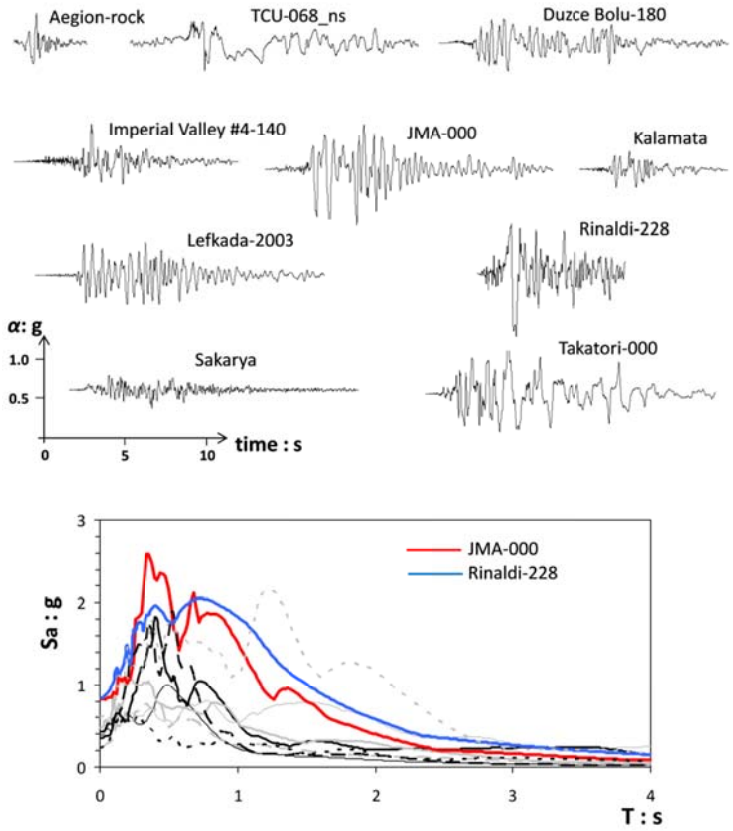

Σχ. 5.2 Οι 10 φυσικές καταγραφές μαζί με τα αντίστοιχα ελαστικά φάσματα απόκρισης.

Σε μια προσπάθεια να μειωθεί ο αριθμός των παραμέτρων που υπεισέρχονται στον υπολογισμό της απόκρισης των συστημάτων, μόνο η δεύτερη "ιδιότητα" του εδάφους λαμβάνεται υπόψιν, ενώ ο ρόλος του εδάφους ως μέσου διαδόσεως σκοπίμως αγνοείται. Πιο συγκεκριμένα, όλα τα διεγείροντα επιταχυνσιογραφήματα υπολογίζονται μέσω αναλύσεων αντιστρόφου συνελίξεως (deconvolution) των φυσικών καταγραφών στην βάση του προσομοιώματος, ούτως ώστε να δίδουν πέντε τιμές-στόχους μέγιστης εδαφικής επιτάχυνσης, PGA, στην κορυφή του ελευθέρου πεδίου, ήτοι 0,1 g, 0.2 g, 0,3 g, 0.4 g και 0.6 g. Παρατηρήθηκε ότι περιορίζοντας την κλιμάκωση των καταγραφών στις συγκεκριμένες πέντε τιμές PGA : (α) το συνολικό υπολογιστικό κόστος μειώνεται σημαντικά, ενώ (β) αποκτάται μια σαφής εικόνα του εξεταζομένου φαινομένου. Συνολικά πραγματοποιήθηκαν 200 δυναμικές αναλύσεις.

Μέτρο Εντάσεως (ΜΕ) και Παράμετροι Αποκρίσεως (ΠΑ)

Το ΜΕ που επελέγη για την παρούσα έρευνα είναι η κορυφαία τιμή της εδαφικής επιτάχυνσης, PGA, στην επιφάνεια του ελευθέρου πεδίου. Το μέγεθος αυτό αποτελεί το πλέον συνηθέστερα χρησιμοποιούμενο διεθνώς.

Η επιλογή των Παραμέτρων Απόκρισης (ΠΑ) εξαρτάται από την φύση του εκάστοτε προβλήματος. Συνολικά επελέγησαν τέσσερις ΠΑ, οι οποίες αφορούν στην απόκριση της ανωδομής και στην δυναμική ευστάθεια στου συστήματος. Θα παρουσιαστούν όμως ενδεικτικά αποτελέσματα για τις δύο πιο χαρακτηριστικές:

- Την πλαστιμότητα μετακίνησης, μ_δ, επηρεασμένη από την αλληλεπίδρασης εδάφους−θεμελίου−ανωδομής, η οποία δίδεται από τον μέγιστο λόγο της καμπτικής παραμόρφωσης της ανωδομής (απαλλαγμένης από την μετακίνηση στερεού σώματος), προς την οριζόντια μετατόπιση διαρροής της ανωδομής, u_y :

$$\mu_\delta = \max\left[\frac{u^{\text{mass}} - (u^{\text{structure base}} + \theta H)}{u_y}\right]$$

  Η u_y με την σειρά της υπολογίζεται για κάθε μία από τις τέσσερις ανωδομές από τις αντίστοιχες καμπύλες pushover, θεωρώντας συνθήκες πάκτωσης στην θεμελίωση.

- Την μέγιστη δυναμική στροφή του φρέατος, θ_{max}.

Αποτελέσματα αναλύσεων και σχολιασμός

Η συγκριτική αξιολόγηση της απόκρισης των συστημάτων εδάφους-φρέατος-ανωδομής, γίνεται στα **Σχ. 5.3-5.4**, μέσω καμπυλών ΑΔΑ για τα δύο πιο αντιπροσωπευτικά συστήματα: το "ελαφρώς" φορτιζόμενο, σεισμικώς *υπό*-διαστασιολογημένο *model 1*, και το "βαρέως" φορτιζόμενο, σεισμικώς *υπέρ*-διαστασιολογημένο *model 4*. Οι καμπύλες ΑΔΑ για την απαίτηση σε πλαστιμότητα μετακίνησης, μ_δ, δίδονται στο **Σχ. 5.3**. Αναμφίβολα, η σεισμικώς *υπό*-

διαστασιολογημένη θεμελίωση, η οποία ευνοεί την ενεργοποίηση μή-γραμμικής απόκρισης, αποδεικνύεται επωφελής για την ανωδομή: απομειώνεται σημαντικά η απαίτηση σε πλαστιμότητα, μ_δ < 0.45, για την πλειονότητα των σεισμικών διεγέρσεων, σε αντίθεση με μ_δ > 3 που αναπτύσσεται όταν το φρέαρ είναι σεισμικώς *υπέρ*-διαστασιολογημένο (*model 4*).

Το **Σχ. 5.4** παρουσιάζει τις καμπύλες ΑΔΑ για την μέγιστη αναπτυχθείσα στροφή στην κεφαλή του φρέατος, θ_{max}. Όπως αναμενόταν, ενώ η απόκριση του σεισμικώς *υπό*-διαστασιολογημένου *model 1* σε όρους επιπόνησης της ανωδομής υπερτερεί συγκριτικά με την αντίστοιχη του *υπέρ*-διαστασιολογημένου *model 4*, οι αναπτυσσόμενες αποκολλήσεις του φρέατος και οι πλαστικές παραμορφώσεις στο περιβάλλον έδαφος αυξάνουν κατά πολύ την στροφή του. Προκαλείται δε αστοχία του συστήματος κατά την σταθμισμένη σε PGA = 7 m/s^2 διέγερση TCU-068 (διπλασιασμένη διέγερση ChiChi, 1999). Παρόλα αυτά, και εξαιρουμένης της προαναφερθείσας λίαν καταστρεπτικής καταγραφής, η απόκριση είναι εντός ανεκτών ορίων. Επιπροσθέτως, πρέπει να τονισθεί ότι η αύξηση της στροφής του θεμελίου και κατά συνέπειαν και της μετατόπισής του, μεταφράζεται σε παραμόρφωση στερεού σώματος για την ανωδομή, η οποία σε αντίθεση με την καμπτική παραμόρφωση που αναπτύσσεται στα συμβατικώς σχεδιασμένα συστήματα με *υπέρ*-διαστασιολογημένη θεμελίωση, δεν προκαλεί ένταση στον φορέα.

Για την πληρέστερη επεξήγηση των αποτελεσμάτων αυτών, στο **Σχ. 5.5** δείχνονται οι ισοϋψείς των πλαστικών παραμορφώσεων για την περίπτωση της διέγερσης JMA-000, υποκλιμακωμένη σε PGA = 0.4 g. Παρατηρείστε την έντονη πλαστικοποίηση του εδάφους κάτω από το φρέαρ, λόγω του μεγάλου κατακόρυφου φορτίου, στο "βαρέως" φορτισμένο *model 4*. Σε αντίθεση, στο "ελαφρώς" φορτισμένο σεισμικώς υπό-διαστασιολογημένο φρέαρ (*model 1*) κυριαρχεί η έντονη μή-γραμμικότητα πέριξ του φρέατος λόγω της αποκόλλησης, ενώ παρατηρείται και ανάπτυξη πρίσματος παθητικών ωθήσεων.

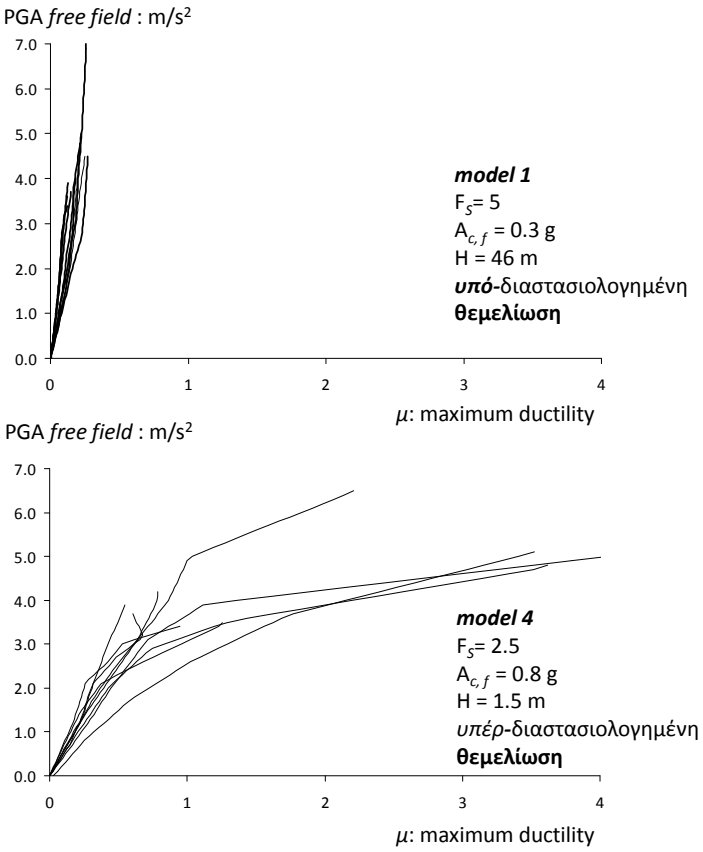

Σχ. 5.3. Καμπύλες ΑΔΑ για ΠΤΑ: μδ, για τα model 1 και model 4.

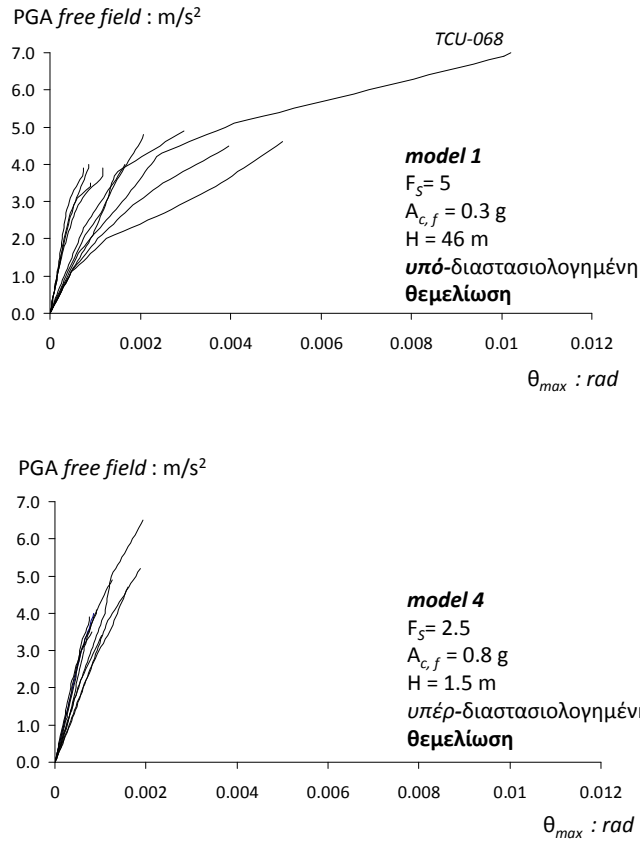

Σχ. 5.4. Καμπύλες ΑΔΑ για ΠΤΑ: θmax, για τα model 1 και model 4.

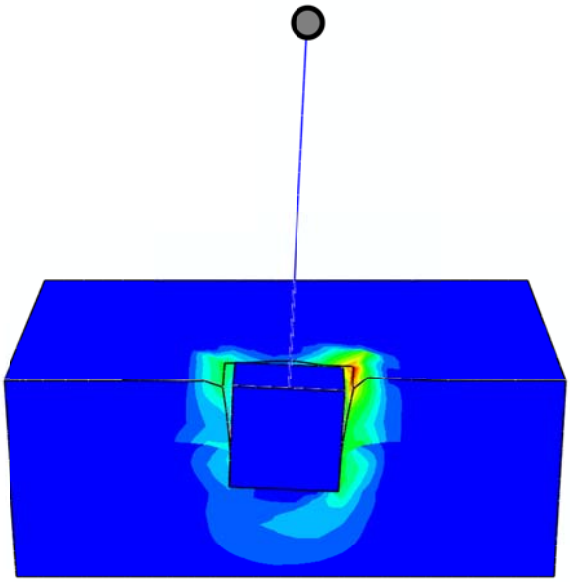

model 1
F_S= 5
$A_{c,f}$ = 0.3 g
H = 46 m
υπό-διαστασιολογημένη
θεμελίωση

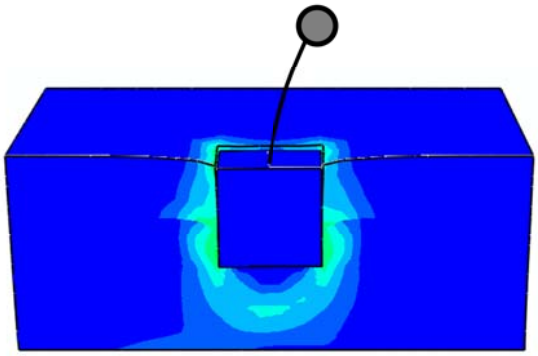

model 4
F_S= 2.5
$A_{c,f}$ = 0.8 g
H = 1.5 m
υπέρ-διαστασιολογημένη
θεμελίωση

Σχ. 5.5. Ισοϋψείς πλαστικών παραμορφώσεων (PEMAG) στο τέλος της σεισμικής εξαίτησης, για τα model 1 και model 4. Καταγραφή: JMA-000, κλιμακούμενο σε PGA = 0.4 g.

Συμπεράσματα

Η παρούσα ενότητα διερευνά την σεισμική μή-γραμμική ανελαστική αλληλεπίδραση εδάφους–φρέατος θεμελίωσης–ανωδομής μέσω ΑΔΑ, όπου λαμβάνεται υπόψιν η 3-D φύση του προβλήματος. Υπό το πρίσμα αυτό, ανεδείχθη η υπεροχή, σε όρους απόκρισης, των “ελαφρώς” φορτιζομένων σεισμικώς *υπό*-

διαστασιολογημένων φρεάτων, τόσο ως προς στην απομείωση των σεισμικών δράσεων που μεταβιβάζονται στην ανωδομή, όσο και ως προς τις πλήρως ανεκτές αναπτυχθείσες παραμένουσες μετατοπίσεις.

Table of Contents

Chapter 1: Introduction

Chapter 2: Generalized bearing strength surface for deeply embedded foundations: Numerical analysis accounting for interface nonlinearities

Chapter 3: Towards a preliminary seismic capacity design of caisson foundations supporting bridge piers

Introduction

1.1 Motivation

Large caissons are often employed as foundations for long bridges spanning over land or water. Owing to their massive dimensions, they constitute the technically feasible solution when the foundation soil has inadequate bearing capacity to support the superstructure on a shallow or piled foundation. They are preferred from piles to support bridge piers in sliding slopes, as they also play the role of a retaining wall. Monumental examples are the Tagus Bridge in Portugal, supported on a 88 m high caisson; the San–Francisco–Oakland Bay Bridge whose major pier is founded on a 75 m high caisson; the Golden State bridge in San Francisco; the Port Island and Nishinomiya–ko bridges in Japan, the massive caissons of which played a major role in the survival of these bridges during the Kobe 1995 earthquake.

Though primarily used to transfer vertical loads (N) safely into soft ground, caissons are also subjected to significant horizontal (Q) and overturning moment (M) loads imposed from severe environmental or seismic events. The response under combined loading involves complex three-dimensional stress distribution along the caisson shaft, shear tractions at the circumference. Moreover, depending on the loading magnitude, the nature of the soil and the caisson-soil interface conditions, the response involves mobilization of a significant amount of the surrounding soil mass, mainly in the form of active and passive wedges. It has thus now become widely accepted that the interaction of these loading components should be explicitly considered when determining the bearing capacity of the foundation. Strikingly, however, although notable work has been published regarding the combined capacity of shallow and skirted foundations, with embedment ratios

(embedment depth, D, to foundation width, B) D / B ≤ 1, the majority of solutions for deeply embedded foundations, with D / B ≥ 1, still rely on simple horizontal reaction concepts developed for piles. It is in this respect that the first part of the present Thesis aims to develop and propose a generalized failure criterion for deeply embedded foundations under combined loading, accounting for material (soil) and caisson-soil interface nonlinearities. The failure criterion will be validated for various soil and interface conditions, and it will be given in terms of, currently the State-of-the-Art in foundation design, three-dimensional N-Q-M failure envelopes.

The next part of the Thesis is motivated by some rather interesting aspects that were revealed from the response of deeply embedded foundations under combined loads, and in particular regarding the "overstrength" that the foundation was shown to exhibit under certain loading combinations; a response that cannot be captured by the conventionally employed analysis methodologies, in which the foundation is substituted with a set of linear, or even nonlinear, usually uncoupled, springs attached at the base of the superstructure. It will be shown that accounting for nonlinear foundation stiffness when *soil–foundation–structure interaction* (*SFSI*) effects are significant is essential for reproducing the accurate response. By means of a numerical study of caisson foundations supporting bridge pier-deck systems subjected to lateral loading, the importance of incorporating nonlinear *SFSI* effects into the geotechnical assessment of foundations will be stressed, aiming to develop a methodology to be used for the preliminary seismic design of caisson foundations.

The last part of the study aspires to shed light on the impact of nonlinear *SFSI* on the seismic response of caisson foundations. The motivation stemmed from recent strong earthquake events (e.g. Kobe 1995), where many caissons, despite their large dimensions, exhibited strong inelastic response, causing thus the supported structures to suffer severe damage.

The concept of "allowing" foundation elements to yield is still relatively new in earthquake engineering practice. Development of nonlinearities below ground surface is forbidden in existing regulations, codes and specifications. According to EC8 (Part 2, § 5.8):

"*…foundations shall not be used as sources of hysteretic energy dissipation, and therefore shall be designed to remain elastic under the design seismic action*."

For the case of deep embedded and caisson foundations, this indicates that nonlinearities of material (soil yielding) and geometric nature, involving separation (gapping) between the caisson shaft and the soil, slippage at the soil–caisson shaft interface and base uplifting, are prohibited. Such a restriction may, at first, appear reasonable, due to the fact that the inspection and rehabilitation of foundation damage after a strong earthquake is not a trivial task. This concept, however, may result in economically unfeasible designs, especially in areas where strong earthquake events are anticipated and soil nonlinearity is unavoidable unless seismically *over*-designed foundations are used. Moreover, neglecting the aforementioned phenomena prohibits the exploitation of strongly non-linear energy dissipating mechanisms in defense of the superstructure. In this study, this notion will be put to the test, by means of powerful numerical techniques (e.g. Incremental Dynamic Analysis). With due consideration to soil and interface nonlinearities, the response of seismically *under*-designed and seismically *over*-designed caisson foundations supporting bridge piers will be thoroughly examined and compared in Performance Based Design terms.

1.2 Structure of Dissertation

The Dissertation is structured in four chapters, each corresponding to an autonomous, self-contained, single journal paper that has either been published in a peer-reviewed journal, or is undergoing review. However, the sequence of the chapters, as presented below, intends to propose an indicative path to the reader, with each chapter appearing motivated or closely related, in logical order, with the preceding ones.

Chapter 2

The Dissertation starts with an extensive parametric investigation of the response of rigid deeply embedded foundations (1 ≤ D / B ≤ 3) to combined vertical (N), horizontal (Q) and moment (M) loading, by means of three-dimensional (3D) finite element (FE) analysis. The analysis is performed for foundations in both cohesive and frictional soils, with due consideration to the caisson–soil contact interface conditions. The goal is to propose a unified failure criterion for deeply embedded foundations, which is missing from the literature. Regarding the results, the ultimate limit states, corresponding to bearing capacity failure of the foundation, are presented by bearing strength surfaces (or failure envelopes) in dimensionless and normalized forms and the effects of the embedment ratio, vertical load and interface friction on the bearing capacity are studied in detail. Particular emphasis is given on the physical and geometrical interpretation of the kinematic mechanisms that accompany failure, with respect to the loading ratio M/Q. Exploiting the numerical results, analytical expressions are derived for the capacities under pure horizontal, moment and vertical loading, for certain conditions. A generalized closed-form expression for the bearing strength surface in M-Q-N space is then proposed and validated for all cases examined. Finally, it is shown that adopting an associated flow rule for predicting the plastic deformations, yields a rather satisfactory comparison with the finite element results, irrespective of: (a) the caisson geometry, (b) the type of soil and its behaviour, and (c) the interface conditions. A simplified geometrical explanation and physical interpretation of the associated flow rule assumption (normality conditions) in M-Q load space is also provided.

Chapter 3

The third Chapter examines, by means of finite element analysis in 3D, the nonlinear response under lateral monotonic and slow-cyclic loading of caisson foundations supporting bridge piers in cohesive soils. The study is performed with respect to the combined moment (M)-horizontal load (Q) on the foundation, and involves similar rigid cubic caissons carrying a column-mass superstructure of varying height (H) and

pier-deck joint rigidity. The latter is simulated by a rotational spring at the deck level with parametrically varying stiffness, relating to the rigidity of the connection. The lateral load is imposed at the deck level, and the resulting M-Q load path on the caisson is mapped within the bounds of the respective failure envelope. The analysis revealed that due to pier-to-deck joint stiffness and the nonlinear coupling between the rotational and translational degrees of freedom at the foundation, triggering the "*negative effective height*" effect, the loading at the caisson follows a nonlinear path. Most interestingly, the load-path displays certain characteristics, such as a particular "overstrength" in bearing capacity that can be mobilized by the foundation, irrespective of the stiffness properties and constraints at the superstructure system. Regarding the response under cyclic loading, the M-Q loops are shown to be well enveloped by the monotonic "backbone" curve for all examined cases. Finally, from the numerical results, a closed-form expression for the load-path is formulated, and a methodology to be used for the preliminary seismic design for caisson foundations is proposed.

Chapter 4

This is the first of the two Chapters that deal with the strongly inelastic response of caisson foundations subjected to extreme seismic loading. More specifically, the seismic behaviour of caisson foundations supporting typical bridge piers is analysed with 3D finite elements, with due consideration to soil and interface nonlinearities. Single-degree-of freedom (SDOF) oscillators of varying mass and height, simulating heavily and lightly loaded bridge piers, founded on similar caissons are studied. Four different combinations of the static (FS_V) and seismic (FS_E) factors of safety are examined: (*a*) a lightly loaded ($FS_V = 5$) seismically *under*-designed ($FS_E < 1$) caisson, (*b*)) a lightly loaded seismically *over*-designed ($FS_E > 1$) caisson, (*c*) a heavily loaded ($FS_V = 2.5$) seismically *under*-designed ($FS_E < 1$) caisson and (*d*) a heavily loaded seismically *over*-designed caisson. The analysis is performed with use of seismic records appropriately modified so that the effective response periods (due to soil-structure-interaction effects) of the studied systems correspond to the same spectral

acceleration, thus allowing their inelastic seismic performance to be compared on a "*fair*" basis. Key performance measures of the systems are then contrasted, such as: accelerations, displacements, rotations and settlements. It is shown that the performance of the lightly loaded seismically *under*-designed caisson is advantageous: not only does it reduce significantly the seismic load to the superstructure, but it also produces minimal residual displacements of the foundation. For heavily loaded foundations, however (FS_V = 2.5), the performance of the two systems (*over* and *under* designed) is similar.

Chapter 5

The final Chapter presents a 3D finite-element Incremental Dynamic Analysis (IDA) study of caisson foundations carrying single-degree-of-freedom (SDOF) structures in clayey soil. The emphasis is given to the interplay between the nonlinearities developed above (superstructure) and, mainly, below ground surface, either of material (soil plasticity) or of geometric (caisson-soil interface gapping and slippage) origin. The study is performed with respect to the static (FS_V) and the seismic (FS_E) safety factor of the foundation and involves SDOF oscillators of varying mass (to account for vertical loading, FS_V) and height (relating to moment loading, FS_E) founded on similar rigid cubic caissons. Structural nonlinearity is now considered by a simplified moment-curvature law, and the yield strength is deliberately chosen so that the following three configurations are obtained: (a) a lightly loaded (FS_V = 5) seismically *under*-designed (as compared to the superstructure) caisson, (b) a lightly loaded seismically *over*-designed caisson, and (c) a heavily loaded (FS_V = 2.5) seismically *under*-designed caisson. The analysis is performed with several earthquake records, each scaled to multiple levels of intensity. IDA curves are then produced for a single intensity measure (peak ground acceleration, PGA), and appropriate engineering demand parameters (EDP) that describe both the maximum and the residual response of the system. The results emphasize a potentially beneficial role of foundation nonlinearities on reducing the seismic demands on the superstructure, but at the cost of residual foundation settlements and rotations.

Generalized bearing strength surface for deeply embedded foundations: Numerical analysis accounting for interface nonlinearities

ABSTRACT

The response of rigid caisson foundations to combined vertical (N), horizontal (Q) and moment (M) loading is investigated parametrically by a series of three-dimensional finite element analyses. The study accounts for foundations in both cohesive and frictional soils, with due consideration to the caisson–soil contact interface conditions. The ultimate limit states are presented by bearing strength surfaces in dimensionless and normalized forms and the effects of the embedment ratio, vertical load and interface friction on the bearing capacity are studied in detail. Particular emphasis is given on the physical and geometrical interpretation of the kinematic mechanisms that accompany failure, with respect to the loading ratio M/Q. Exploiting the numerical results, analytical expressions are derived for the capacities

under pure horizontal, moment and vertical loading, for certain conditions. A generalized closed-form expression for the bearing strength surface in M-Q-N space is then proposed and validated for all cases examined. Finally, it is shown that adopting an associated flow rule for predicting the plastic deformations, yields a rather satisfactory comparison with the finite element results, irrespective of: (a) the caisson geometry, (b) the type of soil and its behaviour, and (c) the interface conditions. A simplified geometrical explanation and physical interpretation of the associated flow rule assumption (normality conditions) in M-Q load space is also provided.

2.1. Introduction

Large caissons are often employed as foundations for long bridges spanning over land or water. Though primarily used to transfer vertical loads safely into soft ground, caissons may also be subjected to significant horizontal and overturning moment loads from severe environmental or seismic events. The response under these loads involves complex three-dimensional stress distribution along the caisson shaft and shear tractions at the circumference [1-5]. Moreover, due to their massive dimensions, as they deform they tend to mobilize a significant amount of the surrounding soil mass, mainly in the form of active and passive wedges, depending on the loading magnitude, the nature of the soil and the caisson-soil interface conditions.

Currently, the State-of-the-Art in foundation design involves expressing the ultimate limit states of a foundation subjected to combined N-Q-M loading by three-dimensional failure envelopes, or bearing strength surfaces. The clear advantages of this method of analysis over the classical bearing capacity solutions have been thoroughly advocated by Gottardi and Butterfield [6], Gourvenec and Randolph [7], Gourvenec and Barnett [8], and others. For the determination of N-Q-M failure envelopes, three main approaches are followed: experimental, analytical and numerical. Owing to the contemporary advances in technical computing, the numerical finite element methods for defining the failure envelope gain increasing

popularity. Interestingly, although notable literature exists regarding the combined capacity of foundations, it exclusively refers to shallow and skirted foundations, with embedment ratios (embedment depth, D, to foundation width, B) D / B ≤ 1 [e.g. 8-14]. Moreover, due to the complexity of the shape of the N-Q-M failure envelopes, stemming from the dependence on the foundation geometry, soil profile, embedment depth and soil-foundation interface conditions, few of these studies propose a closed-form representation of the envelopes for use in routine design. For deeply embedded foundations, with D / B ≥ 1, the majority of solutions still rely on simple horizontal reaction concepts, developed for piles [e.g. 15-17]. To the best of authors' knowledge, a three-dimensional failure envelope for deeply embedded foundations, with D / B ≥ 1, is missing from the literature.

To this end, the novelty of present study lies in the thorough investigation of the response of rigid deeply embedded (caissons) foundations (1 ≤ D / B ≤ 3) under combined N-Q-M loading, by means of an extensive series of finite element analyses in 3-D. The analysis was performed for foundations in both cohesive and cohesionless soil conditions, with due consideration to material (soil) and soil-foundation interface nonlinearities. A generalized failure criterion (bearing strength surface) in the N-Q-M space is then proposed, expressed in terms of classical geotechnical strength parameters (e.g. undrained shear strength, S_u, and friction angle, φ). Closed–form expressions are also proposed for the ultimate uniaxial capacities, for certain cases. Furthermore, the paper provides a detailed analysis of the kinematic mechanisms that accompany failure of the foundation under combined loading. Finally, from the perspective of macroelement modeling, the strength surface is shown to provide a full description of a yield surface, supporting an associated plastic flow rule for the cases examined.

2.2. Finite Element modeling

For the analyses, it was assumed that the caissons were simply "wished into place" and the construction process was not simulated. Although relevant studies revealed that, following this assumption, the soil softening phenomena associated with the

installation processes [e.g. 18, 19] are neglected, appropriate modifications in the soil strength and stiffness profile can be made to account for these effects when applying the results of this study. Small-strain finite element analyses could therefore be employed, since it has been shown that once installed into the ground the mobilization of the bearing capacity of a foundation requires only relatively small displacement excursions [20, 21]. The numerical investigation was performed with the commercially available finite element code ABAQUS version 6.9 [22].

2.2.1. Caisson model and soil properties

The study considers rigid, square (in plan view) caissons of width B and embedment depth D (Fig. 1). The width is kept constant B = 10 m in all analyses, whereas the embedment depth varies parametrically, so that three embedment ratios are obtained, namely D/B = 1, 2 and 3. The analysis is conducted considering both cohesive and frictional soils, taking account for material (in the soil) and geometric (soil-caisson interface) nonlinearities. For reasons of completeness, the special case of a caisson founded in cohesive soil with fully-bonded caisson-soil interface is also presented. The caissons are modeled as rigid bodies, with loads and displacements relating to a single load reference point, as will be shown in the sequel. The caisson material was modeled as isotropic linear elastic with Young's modulus E_c = of 3 x 10^8 kPa, Poisson's ratio vc = 0.15 and with a material density of ρ = 2.5 Mg/m^3.

2.2.1.1. Cohesive soil properties

Soil behavior is described through an elasto-plastic constitutive model [1], which is a reformulation of that originally developed by Armstrong and Frederick [23].The model is available in the material library of ABAQUS. It uses the Von Mises failure criterion along with a nonlinear combined kinematic—isotropic hardening law and an associative plastic flow rule. This study considers a uniform shear stress soil profile of S_u = 50 kPa. The soil has a modulus of elasticity of E_u = 50 MPa, leading to a stiffness-to-strength ratio of E_u / S_u = 1000. A Poisson's ratio of $\nu \approx 0.5$ (= 0.475 to avoid numerical instabilities) was assumed for the soil to approximate the constant volume response of the soil under undrained conditions. The cohesive soil conditions are also schematically illustrated in Fig. 2b.

The authors in [24] validated the constitutive model employed herein for the nonlinear response of embedded and caisson foundations against field tests of suction caissons [25]. From the validation process, it was deduced that the model is capable of capturing the response observed in the trials with satisfactory agreement, in both small and large amplitude lateral loading, including the development of caisson-soil interface nonlinearities (gapping).

2.2.1.2. Frictional soil properties

The plasticity model used in for the frictional soil is an extension of the model used by Gerolymos and Gazetas [1] for cohesive soils. Soil behavior is modeled through a constitutive model with kinematic hardening and non-associated plastic flow rule (the dilatancy angle is zero). A comprehensive review of the constitutive model formulation, which is imported to the FE code through a user subroutine, is provided in [26]. In essence, the module relates the model parameters (namely, the kinematic hardening parameters C and γ) to the principal stresses and the Lode angle. The yield surface of the constitutive model is determined to fit the Mohr–Coulomb failure response in a triaxial loading test for both compression and extension conditions assuming linear interpolation for the intermediate stress states. The constitutive model parameters are calibrated to match the Coulomb failure criterion on the principal stresses plane for every apex of the hexagon with the smooth envelope [26]. Regarding the parameters adopted in our study, a soil with a mass density of ρ = 2 Mg/m^3, friction angle of $\varphi = 30^o$ and Poisson's ratio of ν = 0.25 is considered. The small-strain Modulus of elasticity, E, distribution varies according to $E = 20000\sqrt{p}$, where $\boldsymbol{p}$ is the 1st stress invariant. A schematic illustration of the frictional soil profile along with the model parameters is presented in Fig. 2c. The capability of the constitutive model to reproduce soil behaviour has been validated against centrifuge experiments of static and cyclic response of a single pile and a 2 x 1 group of piles in dry sand [26].

2.2.2. Contact modeling

Throughout relevant literature, the interface between deep foundations and the surrounding soil is treated mainly as "fully-bonded", thus preventing the development of any possible geometric nonlinearities (e.g. gapping and sliding along the interfaces). In this study, even though such interface conditions are also examined, as a special case of caissons in cohesive soil, the main attention is devoted to a more realistic contact simulation, stemming from the nature of each particular case examined. More specifically, for the caissons in cohesive soil with nonlinear caisson-soil interface, where the undrained response of the soil justifies the detachment of the caisson as an admissible state, the surface-to-surface contact interaction is modeled by exponential (“softened”) pressure-overclosure relationship through the direct constraint enforcement method that makes use of Lagrange multipliers. The slippage of the caissons along the interfaces is governed by Coulomb's friction law, by appropriately assigning a friction coefficient μ. For more details on the contact interaction algorithm the reader may refer to ABAQUS manual [22].

Regarding laterally loaded caissons founded in frictional soil, a proper interface modeling should take into account that when the soil reaches the active state, it collapses and flows with the caisson and, thus, no gap is formed. Complying with this condition in the numerical analysis, the caisson-soil interface is treated as purely frictional without allowing separation. It should be noted that this study examines the effect of the interface conditions on the final N-Q-M capacity of the foundations, by parametrically varying the friction coefficient in all relevant cases.

2.2.3. Sensitivity analysis of the boundary conditions and element performance

A typical finite element mesh used in this study, for both cohesive and frictional soil conditions, is shown in Fig. 1. It represents a half-caisson cut through one of the orthogonal planes of symmetry for D/B = 1, and consists of approximately 12.500 3D 8-noded brick elements. To gain confidence in the employed numerical methodology, two types of sensitivity analysis were performed, prior to embarking to the

numerical experiments; an analysis regarding the element type, and an analysis with respect to the extent (Width x Length) of the FE discretized field. The former analysis type was performed in order to assess the *vulnerability* of our model to numerical modeling errors, such as volumetric locking, shear locking and hourglass. Three element types were used, available in the library of ABAQUS [22]: the first order full-integration C3D8, the reduced-integration C3D8R, and the hybrid, constant pressure, C3D8H. Fig. 1b compares the computed response in terms of Q-u pushover curves at the top of the foundation, for a caisson with D/B = 2 in cohesive soil with nonlinear interface. The performance is identical when C3D8 and C3D8H were used, whereas a slight difference can be observed for the case of C3D8R. Weighing carefully the accuracy and the computational cost, the C3D8 type of element was finally chosen for all analyses.

The sensitivity analysis with respect to the extent of the FE field involved two width x length (L x L) configurations, for all D/B cases examined, namely 5B × 5B and 10B × 10B, while the depth of the mesh was kept 5B. The authors in [24] provide the comparison from static pushover tests, in the form of horizontal force (P) - horizontal displacement (u), of caissons with D/B = 1 founded in cohesive soils with nonlinear interface. What is more, Fig. 3 portrays the respective results for caissons with D/B = 1 in frictional soil. More specifically, Q-u pushover curves, referring to the top of the caisson, are plotted, considering (a) χ = 0, μ = 1, and (b) χ = 0, μ = 0.5. The results overall confirm the already known from the literature, that under monotonic loading the lateral boundaries can be placed fairly close to the foundation (just outside the “pressure bulb”). With due consideration to the computational cost, a finite element mesh size of 5B x 5B x 5B was therefore adopted for all numerical analyses.

2.3. Numerical analysis methodology

2.3.1 Sign convention and nomenclature

The sign convention for displacements and loads adopted in this paper, shown in Fig. 2a, obeys a right-handed axes and clockwise positive convention, as proposed by

Butterfield et al [27]. The lateral capacities for pure loading are denoted by the subscript "*u*" (e.g. $Q = M = 0$ for $N = N_u$), whereas the maximum attained loads are subscripted with "*max*". Table 1 summarizes the respective notations for cohesive and frictional soils.

Table 1 Summary of notation for loads and displacements

	Vertical (***N***)		Horizontal (***Q***)		Moment (***M***)	
	cohesive	*frictional*	*cohesive*	*frictional*	*cohesive*	*frictional*
Ultimate load	N_u	N_u	Q_u	Q_u	M_u	M_u
Dimensionless load	N/AS_u	$N/\gamma DB^2$	Q/AS_u	$Q/\gamma DB^2$	M/ABS_u	$M/\gamma DB^3$
Dimensionless ultimate load	N_u/AS_u	$N_u/\gamma DB^2$	Q_u/AS_u	$Q_u/k_p\gamma DB^2$	M_u/ABS_u	$M_u/k_p\gamma DB^3$
Normalised load	N/N_u	N/N_u	Q/Q_u	Q/Q_u	M/M_u	M/M_u
Displacement	*w*	*w*	*u*	*u*	ϑ	ϑ

Note: A = B^2 = 100 m^2 = bearing area of the caisson; S_u= soil undrained shear strength, k_p = $\tan^2(45+\phi/2)$: passive earth pressure coefficient

2.3.2. Load paths

The steps followed in our numerical analyses simulate the actual field conditions. The soil undergoes geostatic loading and then a part of the soil is replaced by the foundation. Then, a vertical load is applied at the caisson head, monotonically increasing till a specified value of the inverse factor of safety $\chi = 1 / FS_v$ (= N / N_u) is reached. Afterwards, the vertical load is kept constant and the caisson is subjected to a combined load of overturning moment and horizontal force under a constant M/Q ratio (radial paths in the M-Q plane, [28, 29]), till the complete failure of the system. By a series of force-controlled pushover analyses, the bearing strength surface is ultimately determined.

Displacement controlled, also defined as "probe", analyses are also performed to track the bearing strength surface and especially to determine a suitable mathematical law for the direction of the plastic strain increments at failure. This test method, frequently adopted in several experimental (e.g. [30]) and numerical (e.g. [31]) studies consists of two steps: (a) in the first step a vertical displacement is applied to the caisson until a specific vertical load is reached (recall the parameter χ); (b) in the second step a constant displacement ratio probe (u/ϑ) is applied until

failure of the system. However, the values of u and ϑ for the displacement-based tests were not chosen randomly; instead, they correspond to the respective values calculated at the end of each load-based analysis.

In all the numerical experiments performed, the failure loads were determined at the points (on the Q-u or the M-ϑ curves), where the tangent stiffness equaled 1% of the initial. The range of the corresponding computed displacements at these failure loads was between 0.20 m - 0.35 m.

2.4. Results

The following sections provide the finite-element static pushover analyses results. Based on these results, analytical expressions are derived to represent the bearing strength surface, the ultimate capacities under pure loading (for certain cases) and the plastic flow rule.

2.4.1. The bearing strength surface

The bearing strength surface, also referred to as yield surface (e.g. [32]), or failure envelope (e.g. [33]), is a convenient way to describe all possible loading combinations that will cause bearing failure of the foundation [34]. From a macroelement perspective, the strength surface can be regarded as the yield function (f), marking the transition between elastic ($f < 0$) and plastic ($f = 0$) response of the system.

To fit the numerical results of this study, an ellipsoid of the following general form was considered:

$$f = \left(\frac{Q}{Q_u}\right)^{n_1} + \left(\frac{M}{M_u}\right)^{n_2} + n_3\left(\frac{Q}{Q_u}\right)\left(\frac{M}{M_u}\right) - 1 = 0 \quad (1)$$

prescribing the bearing strength surface in M-Q space at a particular vertical load level (χ). The coefficients n_1, n_2 and n_3 affect the shape and size of the surface and depend on the problem parameters, such as D/B, χ and μ. Their analytical extraction will be attempted in the sequel, for each case examined.

2.4.1.1. Cohesive soil and fully bonded interface

Bearing strength surfaces in M-Q space are shown in Fig. 4 for each D/B ratio and, for comparison, two vertical loading ratios, χ = 0 and χ = 0.4. The results are presented normalized with respect to the pure moment, M_u, and horizontal load, Q_u, capacity under each respective level of vertical load. Owing to symmetry properties, the surfaces are drawn only in the 1st and 4th quadrant. Though primarily calculated using load-based analyses, M-Q load paths derived from certain displacement-based analyses are also provided for juxtaposition of the two methods. It is evident that the load paths calculated by the "probe" tests track the load-based surfaces with striking agreement, providing thus strong support to the main assumption of this study, that the bearing strength surface (or yield surface) coincides with the plastic potential surface.

Regarding the shape and size of the normalized strength surface, it remains virtually unaffected by the magnitude of the applied vertical load. As embedment increases, however, the surface becomes more eccentric, as similarly observed for shallow embedded foundations [35].

Tracking around the strength surface, two distinct regions are identified. In the first quadrant, the horizontal force and overturning moment at the head of the caisson act in the same direction (or $MQ > 0$) mobilizing the same – passive – soil resisting mechanisms. Thus, their relationship is approximately linear. In the forth quadrant, however, (where $MQ < 0$) the overturning moment counterbalances the horizontal load and the system exhibits an enhanced capacity (here forth denoted as "over-strength") which increases with increasing embedment. Note, for instance, that the caissons sustain both maximum moment and horizontal load capacities, M_{max} and Q_{max}, in this area. Another noteworthy observation from the graphs is the non-perpendicular intersection of the surface with the load axes, indicative of the cross-coupling between the rotational and horizontal degrees of freedom. It should be useful at this point to facilitate the physical interpretation of the bearing strength surface, also corresponding to the yield locus (as will be shown in the sequel), by shedding light on the kinematic mechanisms accompanying failure at each point

along the locus; a first insight into the plastic flow rule, which will be detailed in the sequel. Fig. 5 illustrates the strength surfaces for D/B = 1 and D/B = 3 corresponding to two vertical loading ratios χ = 0.1 and χ = 0.8. Contours of plastic strain magnitude at failure (plotted on the deformed FE mesh) are also provided for certain points along the surfaces. These points are specifically selected with respect to either a limit value of a load component M or Q, or to the location of the rotation pole, z_p, along the z-axis (direction of w, in Fig. 3).

The failure modes can be distinguished as follows:

(***i***) a "*scoop*" mechanism, observed at pure moment capacity (point-*A*), (***ii***) a "*scoop-slide*" (or "*forward scoop*") mechanism, developed in the *A*-*C* region of the surface, resulting in a "*pendulum*" mechanism at point-*C*(z_p = D), (***iii***) a "*sliding*" mechanism, exhibited at maximum horizontal capacity (point-*A*, $z_p \rightarrow \infty$). (***iv***) Of particular interest is the convex transition between points *D* and *E*, where the caisson attains the maximum moment load: the failure mechanism becomes "*diffusive*" in nature, suggesting that the plastic strains appear diffused within the soil mass, rather than concentrated in a form of a distinct shear band, leading to (***v***) a "*pendulum*" mechanism at point-*E* (M_{max}, z_p = 0). In the remaining part of the strength surface, (***vi***) an oppositely directed "*scoop-slide*" mechanism is observed, commonly referred to as "*reverse-scoop*" mechanism.

The figures further reveal that:

(a) as embedment increases, the failure mechanisms are forced deeper into the soil mass. Worthy of note is that for deeply embedded caissons the plastic deformations at *D*-*E* ("overstrength" region) appear mainly diffused, whereas the contrary applies for the shallow embedded caissons, in which plasticity is concentrated at the base ("*sliding*" mechanism).

(b) As the vertical load (χ) increases, the symmetry in the failure mechanisms is lost and a clear accumulation of plastic deformations is observed towards the direction of the predominant loading.

A more illustrative exposition of the kinematic mechanisms mobilized at each limit state corresponding to the points *A*-to-*E* on the bearing strength surface is given in Fig. 6, in terms of incremental displacement vectors. A generic strength surface is used ad hoc and the respective vectors are plotted for embedment ratios D/B = 1, 3 and vertical load χ = 0.1. The location of the rotation pole (z_p), associated with each displacement mechanism, becomes now more evident. For the "*scoop*" mechanism mobilized under pure moment loading (point-*A*) z_p is located at approximately the geometric center, for shallow embedded foundations, moving towards the caisson's base as embedment increases. In contrast, maximum moment loading (M_{max}) results in a distinct "*pendulum*" mechanism (z_p at the top of the caissons) irrespective of the embedment. Worthy of note is that the latter corresponds to the failure mode observed in displacement-based tests with pure rotation (*u* constraint). The displacement vectors calculated under pure horizontal load (point-*B*) reveal the coupling between the horizontal and the rotational degrees of freedom. Moreover, the coupling becomes more pronounced with embedment, as more rotation and less horizontal movement accompanies failure. As the load path moves towards Q_{max}, however, the vectors reveal that failure is governed by "*pure sliding*", reflecting the mode observed in swipe tests under pure horizontal translation (ϑ constraint). Summarizing the above, as attested by the displacement vectors, maximum moment and maximum horizontal load capacities can be mobilized if horizontal translation and rotation, respectively, are constrained.

Based on Eq.1, the authors propose that the analytical expression for solid, square (in plan view) caissons in cohesive soil with fully bonded interface to fit the numerical data is a rotated ellipse with the following form:

$$f = \left(\frac{Q}{Q_u}\right)^2 + \left(\frac{M}{M_u}\right)^2 + n_3\left(\frac{Q}{Q_u}\right)\left(\frac{M}{M_u}\right) - 1 = 0 \quad (2)$$

where n_3 controls the expansion of the surface. The regression analysis resulted in the following expression for n_3:

$$n_3 = 1.84 - 0.21\left(\frac{D}{B}\right)^{-1.98} \tag{3}$$

To visualize the influence of n_3 in the shape of the strength surface, Fig. 7 illustrates the expansion of the surface with increasing D/B along with the corresponding graph. As an example, the case of χ = 0.5 (FS_v = 2) is presented. For the accurate extraction of this particular parameter, additional numerical analyses were performed to produce bearing strength surfaces for caissons with embedment ratios ranging from D/B = 0.5 to D/B = 4. Note that the shape of the normalized surface remains identical for embedment ratios D/B ≥ 2. In the analytical expression this behavior is reproduced with n_3 increasing until it reaches a plateau at n_3 = 1.8.

Analytical expressions to describe the ultimate capacities have also been fitted to the finite element results. As such, N_u, as a function of the embedment ratio, and Q_u, M_u with respect to the vertical load factor χ, are given by:

$$N_u = 9.64B^2 S_u\left(1+\frac{D}{B}\right)^{0.67} \tag{4}$$

$$Q_u = BDS_u\left(\frac{D}{B}\right)^{-2.15}\left(1+\frac{D}{B}\right)^{2.89}\left(1-\chi\right)^{0.17} \tag{5}$$

$$M_u = 0.46B^2 DS_u\left(\frac{D}{B}\right)^{-1.49}\left(1+\frac{D}{B}\right)^{3.39}\left(1-\chi\right)^{0.17} \tag{6}$$

Fig. 8 plots the numerical results along with the respective expressions.

Fig. 9 compares analytically with the numerically calculated strength surfaces in the dimensionless load space. For the sake of brevity, only results for moderately heavily (χ = 0.5) and lightly loaded (χ = 0.2) caissons are presented. The comparison manifests a rather reasonable quality of fit. Apropos, presenting the results in the dimensionless space facilitates the observation of the expansion of the strength surface as embedment increases and, furthermore, the decrease in the maximum

load-carrying capacity of the caissons with increasing vertical load. Note, however, that the eccentricity of the surfaces is maintained nonetheless.

2.4.1.2. Cohesive soil and nonlinear interface

The response of caisson foundations in cohesive soil considering a general interface is examined in Figs. 10-20. A first insight into the effect of interface nonlinearities on the combined capacity of the foundations is provided in Fig. 10: normalized bearing strength surfaces considering both fully-bonded and nonlinear interface are plotted alongside for all three D/B ratios and vertical load factor χ = 0.5. For the latter case, an interface friction coefficient of μ = 1 was used, representing limited slippage. The surfaces plotted with solid lines represent the ones calculated with the bonded interface while the dashed plots reflect the effect of gapping. The following are worthy of note:

- While in the 1st quadrant the surfaces are practically coincident, in the region where "overstrength" is exhibited (MQ< 0), the development of nonlinear phenomena (gapping, uplift) result in an increase in the eccentricity of the surface with increasing embedment, namely not only in the expansion (as observed in the fully-bonded interface conditions) but also in the rotation.

- For all three embedment ratios, an increase in the normalized maximum horizontal load-carrying capacity is observed when interface nonlinearities develop. However, for shallow embedded caissons the graph suggests that interface gapping reduces the maximum moment capacity. Although an explanation of these findings will be attempted in the sequel, along with the discussion on the respective failure mechanisms, it is evident that the interpretation of the response around the apex, where a rapid transition in the kinematic mechanisms occurs within a short range of loading combinations, is not a trivial task.

The manner in which vertical loading affects the combined capacity is illustrated in Fig. 11, where the strength surfaces for all three D/B ratios are given considering four vertical load factors, χ = 0.2, 0.5, 0.7 and 0.9. Interestingly, weather the surfaces

exhibit expansion or contraction as the vertical load increases is strongly dependent on the embedment depth: in shallow embedded foundations, the apex (maximum load-carrying capacity) increases with increasing χ until χ = 0.7 and decreases as χ approaches the ultimate capacity. In stark contrast, for D/B ≥ 2 the apex decreases with increasing χ, and this behaviour appears more prominent for D/B = 2. The reason for this difference in the response may be attributed to the contribution of the base of the caisson in the load resisting mechanisms developed at each case of D/B. More specifically, during the loading of shallow embedded caissons the base is fully mobilized and, as in the case of surface foundations (e.g. [36, 37]), the maximum M-Q capacity is observed with increasing vertical load up to a certain value (χ = 0.5 in surface footings, χ = 0.7 in our study), further increase of which leads to a decrease in the combined capacity. However, as embedment depth increases and the failure mechanisms are forced deeper within the soil mass, the contribution of the base becomes minimal and, hence, the intense initial soil yielding that develops around the caisson and at the interface as the vertical load increases, reduces the combined loading capacity. In the ensuing, the analysis of the kinematic mechanisms will serve in facilitating the interpretation of these observations.

Fig. 12 portrays strength surfaces for the three embedment ratios at χ = 0.5, considering two interface friction coefficients, μ = 0.1, 1, resembling a smooth and a rough interface, respectively. From the graphs it can be inferred that, with the exception of the shallow embedded D/B = 1 caisson, varying the roughness of the interface does not affect significantly the maximum load-carrying capacity of the caissons. The reason for the noteworthy increase in maximum capacity exhibited in the case of D/B = 1 when smooth interface is assumed lies once more in the participation of the base to the response; once the loading conditions mobilize the "*sliding*" mode (at Q_{max}), a smooth interface results in minimal shear stresses along the base, and thus the resistance is provided solely by the activated passive soil wedge, which in turn offers greater capacity than the well-formed shear band-type failure developed at the base when a rough interface is considered.

As promised, the kinematic mechanisms corresponding to various loading combinations, represented by the points $\mathcal{A}$-to-$\mathcal{E}$ on a generic strength surface, are shown in Fig. 13, by means of incremental displacement vectors at failure. At first, results at no vertical load (χ = 0) are given for all examined D/B cases, aiming to shed light on the effect of geometric nonlinearities on the M-Q capacity and the location of z_p. Not surprisingly, whereas under fully-bonded interface conditions the failure modes comprised of both passive and active soil wedges, passive-type failure dominates the response when detachment of the caisson from the soil is allowed. This is particularly evident in the shallow embedded caissons at maximum horizontal-load capacity, where the "*pure sliding*" mechanism is mobilized (point $\mathcal{D}$). As embedment increases, the detached area occupies only a portion of the embedded caisson, mainly near the surface. Noticeably, however, with the loss of contact between the caisson and the soil, a greater volume of soil mass is mobilized at failure than when no separation is allowed. This observation is further corroborated by the location of z_p, which for foundations with nonlinear interface it is found below the respective one when a bonded interface is considered. Fig. 14 graphically confirms this behaviour and, furthermore, illustrates the continuous transition of the failure mechanisms based on the loading combination, by plotting the depth of the rotation pole (normalized by the embedment D) with respect to the load ratio M/QD and the interface conditions.

In Fig. 15, contours of plastic strain magnitude at failure with superimposed the kinematic mechanism vectors plotted on the FE deformed mesh, highlight the effect of vertical load magnitude on the response. The comparison is presented for shallow and deeply embedded foundations (D/B = 1 and 3) under three vertical loading ratios (χ = 0, 0.2 and 0.5), at the points where the caissons attain the maximum horizontal and moment loads (points $\mathcal{C}$ and $\mathcal{D}$). For the caissons with D/B = 1, it now becomes clear that at Q_{max} as χ increases the failure mechanism appears diffused rather than concentrated at a sliding surface (case of χ = 0), which adds to the horizontal capacity of the system. At M_{max}, on the other hand, with increasing χ the

"coherence" of the pendulum mechanism is lost, z_p is diverted towards the upper-right corner of the caisson, and an intense plastic zone at the opposite corner is subsequently developed. This results in a slight decrease in the moment capacity, as shown from the contraction of the bearing strength surfaces with increasing χ, in Fig. 11. In contrast, interpreting the respective response for caissons with D/B = 3 is a more straightforward task; the less the magnitude of the vertical load, the more diffused the plastic strains appear within the soil, offering thus larger capacity in both moment and horizontal loading.

Given the numerical results on the bearing strength surface, the analytical derivation of the coefficients n_1, n_2 and n_3 (in Eq.1), controlling the shape and size of the surface, was performed on the epistemic presumption that, in the normalized load space, they relate only to the embedment ratio and remain unaffected by the vertical load, χ, and the friction coefficient, μ. Eq.1 was thus fitted to the mean value of the numerical data for all χ and two limit values for the friction coefficient (μ = 0.1 and 1) by means of a genetic algorithm-based optimization method. The procedure yielded the following expressions for the coefficients with respect to the embedment ratio:

$$n_1 = 2 - 0.25\left(\frac{D}{B}\right)^{-2.06} \tag{7}$$

$$n_2 = 2 + 0.1\left(\frac{D}{B}\right)^{-1.135} \tag{8}$$

$$n_3 = 1.891 - 0.386\left(\frac{D}{B}\right)^{-2.361} \tag{9}$$

As embedment increases, n_1 increases while n_2 decreases. However, for D/B ≥ 3 both parameters ultimately converge to n_1, $n_2 \rightarrow 2$; the value corresponding to the case of fully-bonded interface conditions. This comes in accord with the preceding observation that as D/B increases the separation of the caisson from the soil is restricted to a limited upper part of the foundation, and has thus no significant effect

on the response. Similarly, the coefficient n_3, which controls the expansion of the surface, converges to $n_3 \rightarrow 1.8$ as D/B ≥ 3.

Contrary to the presumption made for the normalized bearing strength surface, the effects of vertical load magnitude and interface friction coefficient cannot be neglected when the extraction of analytical expressions for the ultimate capacities in pure horizontal and moment loading is attempted. The following expressions are thus proposed:

$$Q_u = \alpha_Q BDS_u \left(\frac{D}{B}\right)^{\beta_Q} \left(1+\frac{D}{B}\right)^{\gamma_Q} \left[1+\varepsilon_Q \chi - \left(\varepsilon_Q+1\right)\chi^2\right]^{\zeta_Q} \tag{10}$$

for the ultimate capacity under pure horizontal load, where the coefficients were obtained from multivariate regression analysis of the finite element results, as:

$$\alpha_Q = 6.71\mu^{0.02851}\left(1+\mu\right)^{-1.551} \tag{11}$$

$$\beta_Q = 0.477\mu^2 - 2.29\mu + 1.013 \tag{12}$$

$$\gamma_Q = -0.564\mu^2 + 2.834\mu - 1.162 \tag{13}$$

$$\varepsilon_Q = 7.48 + 2.89\left(\frac{D}{B}\right)^{-3} \tag{14}$$

$$\zeta_Q = -0.298 + 0.496\left(\frac{D}{B}\right)^{-0.134} \tag{15}$$

and

$$M_u = \alpha_M B^2 DS_u \left(\frac{D}{B}\right)^{\beta_M} \left(1+\frac{D}{B}\right)^{\gamma_M} \left[1+\varepsilon_M \chi - \left(\varepsilon_M+1\right)\chi^2\right]^{\zeta_M} \tag{16}$$

for the ultimate capacity under pure moment loading, in which:

$$\alpha_M = 0.718\mu^{-0.361}\left(1+\mu\right)^{0.285} \tag{17}$$

$$\beta_M = -2.97 + 2.17\mu^{-0.235} \quad (18)$$

$$\gamma_M = 5.027 - 2.677\mu^{-0.23} \quad (19)$$

$$\varepsilon_M = 6.37 - 1.17\left(\frac{D}{B}\right)^{-1.04} \quad (20)$$

$$\zeta_M = 0.0365 + 0.163\left(\frac{D}{B}\right)^{-0.247} \quad (21)$$

Apparently, more elaborate expressions than the respective ones when considering a bonded interface were required in order to incorporate the effects of geometric nonlinearities. Regarding the extracted parameters, α, β and γ were found to vary with μ, while ε and ζ only with D/B. Figs. 16-17 present the ultimate uniaxial capacities in dimensionless forms, derived from the FE analysis and the fitted analytical curves. The comparison is presented with respect to χ and D/B, for a variety of interface friction coefficients. In stark contrast to the case of the fully-bonded interface, where Q_u and M_u were obtained as decreasing functions of χ, the respective ultimate load-carrying capacities of the caissons when detachment from the soil is allowed display an initial increase, until approximately χ = 0.5, followed by a decrease until bearing failure. As was anticipated after the analysis of the failure mechanisms, the ultimate horizontal load capacity of shallow embedded foundations is significantly affected by the interface friction, which is directly attributed to the participation of the base of the caisson in the response. For caissons with D/B ≥ 2, however, the curves appear closely banded irrespective of μ and, interestingly, D/B. In contrast, the graphs reveal a strong dependence of M_u on the embedment ratio. This behaviour can be justified considering that the "*scoop*" mechanism, dominating the response at M_u, mobilizes the entire length of the foundation (D), resulting thus in the noticeable increase in M_u as D/B increases.

The quality of fit of the analytical expression for the bearing strength surface (denoted as Eq.1) to the numerical data is validated in Figs. 18-19 in both normalized (Fig. 18) and dimensionless (Fig. 19) forms. The comparison is given for two

characteristic values of the vertical load ratio and a limit value for the interface friction coefficient (μ = 1).Finally, Fig. 20 plots the 3D representation of the strength surface according to Eqs.2, 7, 8, 9, for D/B = 1 and D/B = 3, considering μ = 1.

2.4.1.3. Frictional soil with nonlinear interface

The response of caisson foundations in frictional soil considering a Coulomb interface is examined in Figs. 21-31. Since the physics of the problem dictates that detachment of the caisson from the surrounding soil is not allowed, it is expected that the friction along the interface should play a significant role in the overall response. To begin with the results, Fig. 21 presents FEA computed bearing strength surfaces for all three D/B ratios at constant vertical load increments of χ = 0.2, 0.5, 0.7 and 0.9,considering initially a single interface friction coefficient of μ = 1, isolating thus its effect. The comparison is shown in dimensionless quantities, as introduced in Table 1. The graphs reveal once again that the strength surface maintains a negative eccentricity ("over-strength" attained at MQ< 0) and displays a noticeable expansion with increasing D/B.As anticipated, however, due to the nonlinear nature of the interface, the level of vertical loading affects the shape in a non-straightforward manner, especially in the shallow embedded foundations, where the base, along with the sides, is fully mobilized during the response. More specifically, an expansion of the apex is observed as the vertical load increases until χ = 0.5 ~ 0.7, followed by a contraction at higher χ levels up to bearing failure. Similar behaviour, though not as conspicuous, was observed in the case of cohesive soil with nonlinear interface.

The effect of interface conditions in the bearing capacity is examined in Fig. 22. Slices of normalized strength surfaces in M-Q space are given for all embedment ratios under two vertical load levels (χ = 0.3 and 0.5), while varying the interface friction coefficient (μ = 0.3, 0.5 and 1). As anticipated, although the shape and size of the surfaces are relatively independent of the friction coefficient (and, arguably, of χ) for embedment depths D ≥ 2B, interface conditions do affect noticeably the maximum horizontal load capacity of caissons with D/B = 1. Apparently, this behaviour is attributed to the shear resistance (relating to μ) that is allowed to develop along the foundation underside when the "*sliding*" mechanism, that governs the response at

Q_{max}, is mobilized. Interestingly, the strength surface exhibits an expansion of the apex as the coefficient of friction decreases. Bearing in mind that the results are presented normalized by their respective pure load capacities (Q_u), this –intuitively contradicting– response can be attributed to the following: under pure horizontal translation, the participation of the shear tractions, developed at the circumference of the caisson, to the lateral capacity is minimal compared to the ones offered by the base shear and, mainly, by the passive soil resistance. In contrast, when the "*scoop-slide*" mechanism is mobilized under Q_u, these circumferential shear stresses, the magnitude of which is directly proportional to μ, provide substantial moment resistance to the caisson rotation. Hence, even though $Q_{u,\,\mu=1} > Q_{u,\,\mu=0.3}$ (measured in absolute values, as shown for D/B = 1 in Fig. 22), the corresponding ratio is $\left.\frac{Q_{max}}{Q_u}\right|_{\mu=1} < \left.\frac{Q_{max}}{Q_u}\right|_{\mu=0.3}$.

The kinematic failure mechanisms of caissons in frictional soil are shown in Figs. 23-24 for D/B = 1 and D/B = 3, respectively, considering interface friction coefficient μ = 1. The results are now presented in terms of contours of resultant displacement at failure, unveiling in this way the location of the rotation pole. As before, the mechanistic behaviour is illustrated by a generic strength surface, at specific points of which (*A*-to-*E*) the snapshots from the last step of the FE analysis (at failure) under that particular M-Q loading combination are given. To examine the effect of not only geometric nonlinearities, but also material ones, results from two levels of vertical load are juxtaposed, namely from χ = 0.1 (lightly loaded caisson) and χ = 0.5 (moderately loaded caisson). Although slippage along the interface was the only admissible form of geometric nonlinearities, it can be observed that the failure modes, as those were identified in the previous sections, are retained. Notably, since detachment of the caisson from the surrounding soil was restrained, soil displacement mechanisms now also involve the formation of active wedges. This can be clearly visualized in the contours accompanying failure in the form of the "*scoop-sliding*" (points *B*-*C*) and the "*pure sliding*" mechanism (point *D*). The effect of

vertical loading, relating to the extent of the initial soil yielding surrounding the caisson, is manifested in the loss of symmetry of the kinematic mechanisms.

For the analytical extraction of the ultimate capacities in pure horizontal and moment loading, the following algebraic expressions were formulated to fit the numerical results:

$$\frac{Q_u}{Q_u^*} = \left(a_Q \chi^2 + \beta_Q \chi + 1\right)^{\delta_Q} \left(1 - \chi\right)^{\varepsilon_Q} \tag{22}$$

for the ultimate capacity under pure horizontal load, and:

$$\frac{M_u}{M_u^*} = \left(a_M \chi^2 + \beta_M \chi + 1\right)^{\delta_M} \left(1 - \chi\right)^{\varepsilon_M} \tag{23}$$

for the ultimate capacity under moment loading, where M_u^* and Q_u^* are the pure moment and horizontal load capacities, respectively, under zero vertical load (χ = 0).The coefficients a_Q, β_Q, δ_Q, ε_Q and a_M, β_M, δ_M, ε_M all relate to the interface friction μ and the embedment ratio D/B. Their values are presented in graphical form in Fig. 25. Figs. 26-27 depict the uniaxial capacities calculated from the FE analyses, and validate the fitted analytical expression for Q_u and M_u (Eqs. 22-23), respectively. Their variation is given with respect to the level of vertical loading, interface conditions and embedment ratio.

As similarly observed in the preceding section, under low-to-moderate levels of vertical load the uniaxial load-carrying capacities display an increase, which is reversed at higher levels of χ until bearing capacity failure ($\chi \geq 1$). Caissons with D/B = 1 expectedly show a strong dependence on the interface friction coefficient, due to the fact that their underside, and therefore the respective interface, is an integral part of the "*scoop*" and the "*scoop-slide*" failure mechanisms, mobilized at M_u and Q_u, respectively. It is interesting to note that the normalized lateral capacity curves (Q_u/Q_u*, M/M_u*) increase their concavity with decreasing aspect ratio (D/B), exhibiting a maximum value at $\chi \approx 0.5$ for D/B = 1, resembling the moment capacity of a vertically loaded shallow foundation free to uplift (e.g. [37-40]). As the aspect

ratio increases, the capacity curves reduce their concavity becoming more and more flat, shifting their maximum towards greater values of the inverse factor of safety χ. This decrease in concavity is attributed to the fact that the contribution of the base resistance to the overall lateral capacity of the caisson vanishes with increasing D/B, while the resulting increase of the side-walls resistance delays the mobilization of the base bearing capacity, moving the maximum to $\chi > 0.5$. Indeed, the local (base) inverse factor of safety (let us, for convenience, denote it as χ_b) reaches a value of 0.5 when the global one (χ) has far surpassed it.Furthermore, for D/B ≥ 2 the plots appear narrowly-banded, indicating a minor dependence on μ.

From the numerical results, the analytical extraction of the coefficients n_1, n_2 and n_3 of the generalized bearing strength surface (Eq.1) was once more attempted. In this case, however, closed-form expressions could not be developed, since all n_1, n_2 and n_3 relate to embedment ratio, vertical load level and interface friction coefficient in a highly nonlinear fashion. Hence, three separate artificial neural networks, one for each of the coefficients, were trained. The basic architecture of the multilayer neural network developed is shown in Fig. 28. The input data involve D/B, χ and μ, while the output is one of the parameters of Eq.1. The mathematical formulation of the neural network after the training is expressed as:

$$n_k = tanh\left[\sum_j^3 w2_j \, tanh\left(\sum_i^3 w1_{i,j}\, x_i + b1_j\right) + b2\right] \tag{24}$$

where $w1_{i,j}$ and $b1_j$ are the weights and biases of the hidden layer and $w2_j$ and $b2$ are the weights and biases of the output layer, given in Tables 2-4.

Table 2 Weights and the biases for parametern_1

Parameter n_1							
Hidden Layer					Output Layer		
$w1_{i,j}$				$b1_j$	$w2_j$		$b2$
	i=1	**i=2**	**i=3**				
j=1	5.844	0.060	-0.105	-0.064	**j=1**	1.917	-0.305
j=2	-0.710	0.142	-0.266	0.024	**j=2**	3.572	
j=3	0.358	-5.176	0.669	5.012	**j=3**	1.023	

Table 3 Weights and the biases for parameter n_2

Parameter n_2							
Hidden Layer					Output Layer		
$w1_{i,j}$				$b1_j$	$w2_j$		$b2$
	i=1	**i=2**	**i=3**				
j=1	2.053	5.570	9.210	2.998	**j=1**	-0.981	-0.179
j=2	43.883	15.482	50.120	10.219	**j=2**	0.248	
j=3	8.964	-29.112	-9.321	-13.381	**j=3**	-0.608	

Table 4 Weights and the biases for parameter n_3

Parameter n_3							
Hidden Layer					Output Layer		
$w1_{i,j}$				$b1_j$	$w2_j$		$b2$
	i=1	i=2	i=3				
j=1	-23.599	-5.272	0.572	-15.732	j=1	102.407	1.859
j=2	15.032	0.141	-1.515	4.299	j=2	102.431	
j=3	1.149	0.154	2.316	2.419	j=3	-1.912	

In Figs. 29-30, numerically calculated strength surfaces, for all three D/B ratios, are contrasted with the respective analytically derived ones (from Eq.1). In particular, Fig. 29 shows the comparison for vertical load ratios χ = 0.1, 0.5 and interface friction coefficient μ = 1. Fig. 30 presents the bearing strength surfaces for heavily loaded caissons (χ = 0.5 and 0.9) when μ = 0.3 (smooth interface). It should be noted that χ = 0.9 corresponds to a quite unfavorable loading state which is not commonly met during actual design. Evidently, the rather satisfactory quality of fit established in every case, validates once again the analytical approach adopted in the paper.

In Fig. 31, the bearing strength surface for square –in plan view– caisson foundations can be visualized in 3D, for embedment ratios D/B = 1, 3 and interface friction coefficient μ= 1.

2.4.2. On the plastic flow rule

In the preceding sections, a generalized bearing strength surface for caisson foundations was formulated and validated against an extensive 3D numerical study, considering various soil and interface conditions. Within the context of plasticity, this strength surface can be regarded as the yield surface of a force-resultant macroelement model that defines the boundary between elastic and plastic response. For the description of the resultant plastic displacements, an appropriate

flow rule should also be defined. The numerical evidence, drawn from the probe tests, suggests a flow rule of the associative type. In this section, however, this notion will be further examined.

2.4.2.1. M-Q load space

Based on the, already presented, analysis of the kinematic mechanisms, Fig. 32a illustrates schematically the evolution of the depth of the rotation pole during a random loading event. The diagram is drawn in a way so that the geometry of the response can be easily comprehensible, while the physical accuracy is maintained. The interpretation of the figure is further facilitated by the generic *Q*-*u* pushover curve plotted alongside.

Examining the response within a small-deformation framework, the depth to the rotation pole is by definition given by:

$$z_p = \frac{u}{\vartheta} \tag{25}$$

where u and ϑ are the absolute horizontal and rotational displacements, respectively. Considering that the elastic components of the deformation are only a very small fraction of the total ones, Eq. 25 can be rewritten as:

$$z_p = \frac{u}{\vartheta} \approx \frac{u_p}{\vartheta_p} \tag{26}$$

in which u_p and ϑ_p are the plastic components of the deformation. Neglecting second order effects (i.e. P-δ effects) leads to the following relation:

$$z_p = \frac{u}{\vartheta} \approx \frac{u_p}{\vartheta_p} \approx \frac{\delta u_p}{\delta \vartheta_p} \tag{27}$$

where δu_p and $\delta \vartheta_p$ are the incremental plastic horizontal translation and rotation, respectively. Therefore, from a macroelement perspective, the depth to rotation pole is approximately equal to the ratio of incremental plastic horizontal displacement and rotation at the head of the caisson, which in turns defines the

plastic flow rule. Equivalently, the depth to rotation pole is determined by the plastic potential function. Showing that this function is identical to the bearing strength surface, the normality condition is satisfied and the associative flow rule assumption is attested.

Note, however, that Eq. 27 is valid if and only if the position of the rotation pole remains constant ($\delta z_p = 0$) at post-failure loading conditions (when the load path intersects the bearing strength surface and attempts to move beyond it). To test the validity of this condition, Fig. 32b plots the evolution of numerically obtained z_p, corresponding to the representative points A-to-E of the strength surface, with respect to the horizontal displacement. The results, presented normalized with the embedment depth, are given herein for caissons with D/B = 1 and D/B = 3 in cohesive soil, considering both bonded and nonlinear interface conditions, while the level of vertical loading was taken $\chi = 0.2$. From the graphs, it can be deduced that indeed once the bearing strength load is reached, the position of the rotation pole remains constant.

To verify the possibility of an associated flow rule, the yield function (Eq. 1) is treated as the plastic potential function. The ratio of the plastic displacement increments is thus obtained by differentiating Eq. 1 with respect to Q and M, respectively, as:

$$\frac{\delta u_p}{\delta \vartheta_p} = \frac{\lambda \dfrac{\partial f}{\partial Q}}{\lambda \dfrac{\partial f}{\partial M}} = \frac{\dfrac{M n_3}{M_u Q_u} + \dfrac{n_1 \text{sign} Q \left(\dfrac{|Q|}{|Q_u|} \right)^{n_1 - 1}}{|Q_u|}}{\dfrac{Q n_3}{M_u Q_u} + \dfrac{n_2 \text{sign} M \left(\dfrac{|M|}{|M_u|} \right)^{n_2 - 1}}{|M_u|}} \tag{28}$$

where λ is the plastic loading parameter. Figs. 33-34 compare the numerical data with the predicted from Eq. 28, by plotting the depth of the rotation pole (normalized by the embedment D) with respect to the load ratio M/QD. In Fig. 33 the comparison is shown for caissons in cohesive soil, accounting for both bonded and nonlinear, under vertical load level $\chi = 0.2$. Fig. 34 presents the results for caissons in

frictional soil under vertical load χ = 0.3, considering interface friction μ = 0.5. A noteworthy observation regarding the variation of the analytical equation is the existence of negative values for z_p (the rotation pole develops above the caisson). This marks the area of response at the apex of the strength surface, and particularly where the transition of the kinematic mechanisms occurs between the "*sliding*" and the "*pendulum*" mechanism.

Strikingly, by assuming an associated flow rule for all cases presented, the analytical results reproduce the numerical experiments with remarkable agreement, implying that associativity could be regarded as an inherent property of the caisson's actual response rather than an oversimplification of it.

2.4.2.2. Q-N load space

As similarly performed for determining the flow rule in M-Q plane, the possibility of an associated flow rule in the Q-N (or M-N) plane can be tested assuming that the plastic displacement rate ratio $\delta u_p/\delta w_p$ is obtained by the ratio of the derivatives of Eq.1 with respect to Q (or M) and N, as:

$$\frac{\delta u_p}{\delta w_p} = \frac{\lambda \frac{\partial f}{\partial Q}}{\lambda \frac{\partial f}{\partial N}} \tag{29}$$

Two representative cases are presented: caissons with D/B = 1 founded in (a) cohesive soil with fully-bonded interface, and (b) frictional soil, with μ = 1. The latter case was considered of particular interest, due to the notable concavity exhibited in the variation of Q_u with χ (Fig. 26). The comparison between the numerical and analytical results is given in Fig. 35, in terms of $\delta u_p/\delta w_p$ as a function of χ. The striking agreement between the results provides once again strong evidence supporting an associated flow rule.

Contrary to the M-Q plane, in which the ratio of the plastic displacement increments equals the depth of the rotation pole, a physical and geometrical interpretation of the normality conditions in the Q-N load space could not be established.

2.5. Conclusions

The response of rigid caisson foundations, with D / B ≥ 1, in cohesive and frictional soils under combiner N-M-Q loading was investigated by an extensive series of 3-D finite element analyses. The analysis accounted for soil and interface nonlinearities, and examined parametrically the effect of the (a) embedment ratio D/B,(b) level of vertical loading χ and (c) caisson-soil interface friction coefficient μ, on the response. Emphasis was given to the physical and geometrical interpretation of the kinematic mechanisms that accompany failure and, in particular, the location of the rotation pole, z_p, under various loading combinations. Three-dimensional bearing strength surfaces are presented, either in normalized or in dimensionless form. The main conclusions of the study can be summarized as follows:

- For caissons in cohesive soil with a fully-bonded interface, the normalized strength surface exhibits expansion with increasing D/B, while remains practically unaffected by χ. The rate of expansion stops for D/B ≥ 1.8, which can be considered the boundary between shallow and deeply embedded foundations.

- For caissons in cohesive soil with nonlinear interface, both expansion and rotation of the surface is observed with increasing D/B, attributed to the soil-caisson detachment. The rotation of the surface diminishes as D/B → 3, denoting that the detachment has become limited to the upper part of the foundation and has thus a limited impact on the capacity. In contrast, it was shown that the level of vertical loading as well as the interface friction does not affect significantly the eccentricity of the normalized surface. However, the results suggest that χ and μ should be accounted for the extraction of the capacities under pure horizontal or moment loading.

- For caissons in frictional soil, where slippage along the interface is the only admissible form of geometric nonlinearity, there is a notable effect of χ and,

mainly, μ on the eccentricity of the strength surface, especially for the shallow caissons (D/B = 1).

- It was shown that the bearing strength surface can be viewed as a locus, on which certain types of failure are mobilized, with respect to the M/Q loading ratio. The effects of interface and soil nonlinearities due to vertical loading (expressed by the factor χ) are reflected in the loss of symmetry of the mechanisms and thus the slight change in the position of the rotation pole. Of particular interest is the evolution of the kinematic mechanisms around the apex of the surface, where within a very narrow load ratio region the depth of the rotation pole changes from to $z_p \rightarrow \infty$ to $z_p = 0$. At the apex, the mechanism governing the response of deeply embedded foundations (D/B ≥ 2) is not formed along continuous failure planes, but rather appears "*diffused*" within the soil mass.

- Interesting conclusions were also drawn for the ultimate uniaxial capacities, M_u and Q_u, with respect to soil and, especially, interface nonlinearities: while under fully-bonded interface these are found to be decreasing functions of χ, when interface nonlinearities develop (either in the form of gapping, in cohesive soil, or sliding, in frictional soil), an increase is initially observed for low to moderate levels of χ, followed then by a decrease until bearing failure. For all cases, closed-form expressions for M_u and Q_u were derived to fit the numerical results.

- All the aforementioned findings were employed to develop a generalized expression for the bearing strength surface in N-M-Q space, capable of capturing all aspects of the response. Most importantly, it was shown that, from a macroelement perspective, the plastic potential function is practically coincident to the bearing strength surface (the normality conditions are satisfied at any point on the failure surface) verifying the associated plastic flow rule assumption.

References

[1] Gerolymos N, Gazetas G (2006) Static and dynamic response of massive caisson foundations with soil and interface nonlinearities–validation and results. *Soil Dynamics and Earthquake Engineering* 26(5): 377–94.

[2] Gerolymos N, Gazetas G (2006) Winkler model for lateral response of rigid caisson foundations in linear soil. *Soil Dynamics and Earthquake Engineering* 26(5): 347–61.

[3] Gerolymos N, Gazetas G (2006) Development of Winkler model for static and dynamic response of caisson foundations with soil and interface nonlinearities. *Soil Dynamics and Earthquake Engineering* 26(5): 363–76.

[4] Davidson HL (1982) *Laterally loaded drilled pier research*. Research Report, Electric Power Research Institute, vol. 2. Pennsylvania: Gai Consultants, Inc.

[5] Saitoh M (2001) *Effective seismic motion of caisson and pile foundation*. RTRI Rep. 46.

[6] Gottardi G, Butterfield R (1993) On the bearing capacity of surface footings on sand under general planar load. *Soils and Foundations* 33(3): 68–79.

[7] Gourvenec S, Randolph MR (2003) Effect of strength nonhomogeneity on the shape and failure envelopes for combined loading of strip and circular foundations on clay. *Geotechnique* 53(6): 575–586, doi: 10.1680/geot.2003.53.6.575.

[8] Gourvenec S, Barnett S (2011) Undrained failure envelope for skirted foundations under general loading. *Géotechnique* 61(3): 263–270.

[9] Martin CM (1994) Physical and numerical modelling of offshore foundations under combined loads. DPhil. thesis, University of Oxford.

[10] Bransby MF, Randolph MF (1998) Combined loading of skirted foundations. *Geotechnique* 48(5): 637–655. doi: 10.1680/geot.1998.48.5.637.

[11] Bransby MF, Randolph MF (1999) The effect of embedment depth on the undrained response of skirted foundations to combined loading. *Soils Found* 39(4): 19–33.

[12] Gottardi G, Houlsby GT, Butterfield R (1999) Plastic response of circular footings on sand under general planar loading. *Geotechnique* 49(4): 453–469. doi: 10.1680/geot.1999.49.4.453.

[13] Taiebat HA, Carter JP (2002) Bearing capacity of strip and circular foundations on undrained clay subjected to eccentric loads. *Geotechnique* 52(1): 61–64. doi: 10.1680/geot.2002.52.1.61.

[14] Gourvenec S (2007) Failure envelopes for offshore shallow foundation under general loading. *Geotechnique* 57 (9): 715–727. doi: 10.1680/geot.2007.57.9.715.

[15] Hansen JB (1961) The ultimate resistance of rigid piles against transversal forces. Geoteknish Institute, Bulletin No. 12.

[16] Matlock H (1970) Correlations for design of laterally loaded piles in soft clay. Paper No. OTC 1204. In: Proceedings, Second Annual Offshore Technology Conference, Houston, Texas: 577–94.

[17] Randolph MF, Houlsby GT (1984) The limiting pressure on a circular pile loaded laterally in cohesive soil. *Geotechnique* 34: 613–23.

[18] Hossain MS, Randolph MF (2009) New mechanism-based design approach for spudcan foundations on single layer clay. *Journal of Geotechnical and Geoenvironmental Engineering* ASCE 135(9): 1264–1274.

[19] Hossain MS, Randolph MF (2009) Effect of strain rate and strain softening on the penetration resistance of spudcan foundations on clay. *Int J Geomechanics* ASCE; 9(3): 122–132.

[20] Bienen B, Gaudin C, Cassidy MJ, Rausch L, Purwana OA, Krisdani H (2012) Hybrid skirted foundation under combined loading. *Computers and Geotechnics* 45: 127–139.

[21] Zhang Y, Bienen B, Cassidy MJ, Gourvenec S (2012) Undrained bearing capacity of deeply buried flat circular footings under general loading. *Journal of Geotechnical and Geoenvironmental Engineering* ASCE 138(3): 385-397.

[22] ABAQUS User's manual (2009) Dassault Systèmes SimuliaCorp, Providence, RI, USA.

[23] Armstrong PJ, Frederick CO (1966) *A mathematical representation of the multiaxial Bauschinger effect*. Technical Report RD/B/N 731, Central Electricity Generating Board, Berkeley, UK [Reprint in: Armstrong PJ, Frederick CO (2007) A mathematical representation of the multiaxial Bauschinger effect. *Materials at High Temperatures* 24(1): 1–26].

[24] Zafeirakos A, Gerolymos N (2013) On the seismic response of *under*-designed caisson foundations. *Bulletin of Earthquake Engineering* 11(5): 1337-1372.

[25] Houlsby GT, Kelly RB, Huxtable J, Byrne BW (2005) Field trials of suction caissons in clay for offshore wind turbine foundations. *Geotechnique* 55(4): 287–296.

[26] Giannakos S, Gerolymos N, Gazetas G (2012) Cyclic lateral response of piles in dry sand: Finite element modeling and validation. *Computers and Geotechnics* 44: 116-131.

[27] Butterfield R, Houlsby GT, Gottardi G (1997) Standardized sign conventions and notation for generally loaded foundations. *Geotechnique* 47(5): 1051–1054.

[28] Cremer C, Pecker A, Davenne L (2001) Cyclic macro-elementfor soil-structure interaction: material and geometrical non-linearities. *International Journal for Numerical and Analytical Methods in Geomechanics* 25: 1257–1284.

[29] Gourvenec S (2004) Bearing capacity under combined loading - a study of the effect of shear strength heterogeneity. In: *Proceedings of the 9th Australian and New Zealand Conference on Geomechanics*, Auckland, New Zealand: 527-533.

[30] Martin CM, Houlsby GT (2000) Combined loading of spudcan foundations on clay: laboratory tests. *Geotechnique* 50(4): 325-338.

[31] Bransby MF, Randolph MF (1997) Shallow foundations subject to combined loadings. In: *Proc. 9th International Conference of the International Association for Computer Methods and Advances in Geomechanics*; Vol. 3: 1947-1952.

[32] Roscoe KH, Schofield AN (1956) The stability of short pier foundations in sand. *British Welding Journal:* 343–354.

[33] Butterfield R, Gottardi G (1994) A complete three-dimensional failure envelope for shallow footings on sand. *Geotechnique* 44(1): 181-184.

[34] Pender M. Seismic design and performance of surface foundations (2007) *Earthquake Geotechnical Engineering,* K.D. Pitilakis (ed.). Springer, pp. 217–243.

[35] Yun G, Bransby MF (2007) The horizontal-moment capacity of embedded foundations in undrained soil. *Canadian Geotechnical Journal* 44(4): 409-424.

[36] Taiebat HA, Carter JP (2000) Numerical Studies of the Bearing Capacity of Shallow Foundations on Cohesive Soil Subjected to Combined Loading. *Geotechnique* 50: 409−418.

[37] Panagiotidou A, Gazetas G, Gerolymos N (2012) Pushover and seismic response of foundations on stiff clay: analysis with P-D effects. *Earthquake Spectra* 28(4): 1589–618.

[38] Apostolou M, Gazetas G, Garini E (2007) Seismic response of slender rigid structures with foundation uplifting. *Soil Dynamics and Earthquake Engineering* 27: 642–654.

[39] Chatzigogos CT, Pecker A, Salencon J (2009) Macroelement modeling of shallow foundations.*Soil Dynamics and Earthquake Engineering* 29(6): 765–781.

[40] Gajan S, Kutter BL (2008) Capacity, settlement, and energy dissipation of shallow footings subjected to rocking. *Journal of Geotechnical Geoenvironmental Engineering* ASCE 134(8): 1129–1141.

Chapter 2

Figures

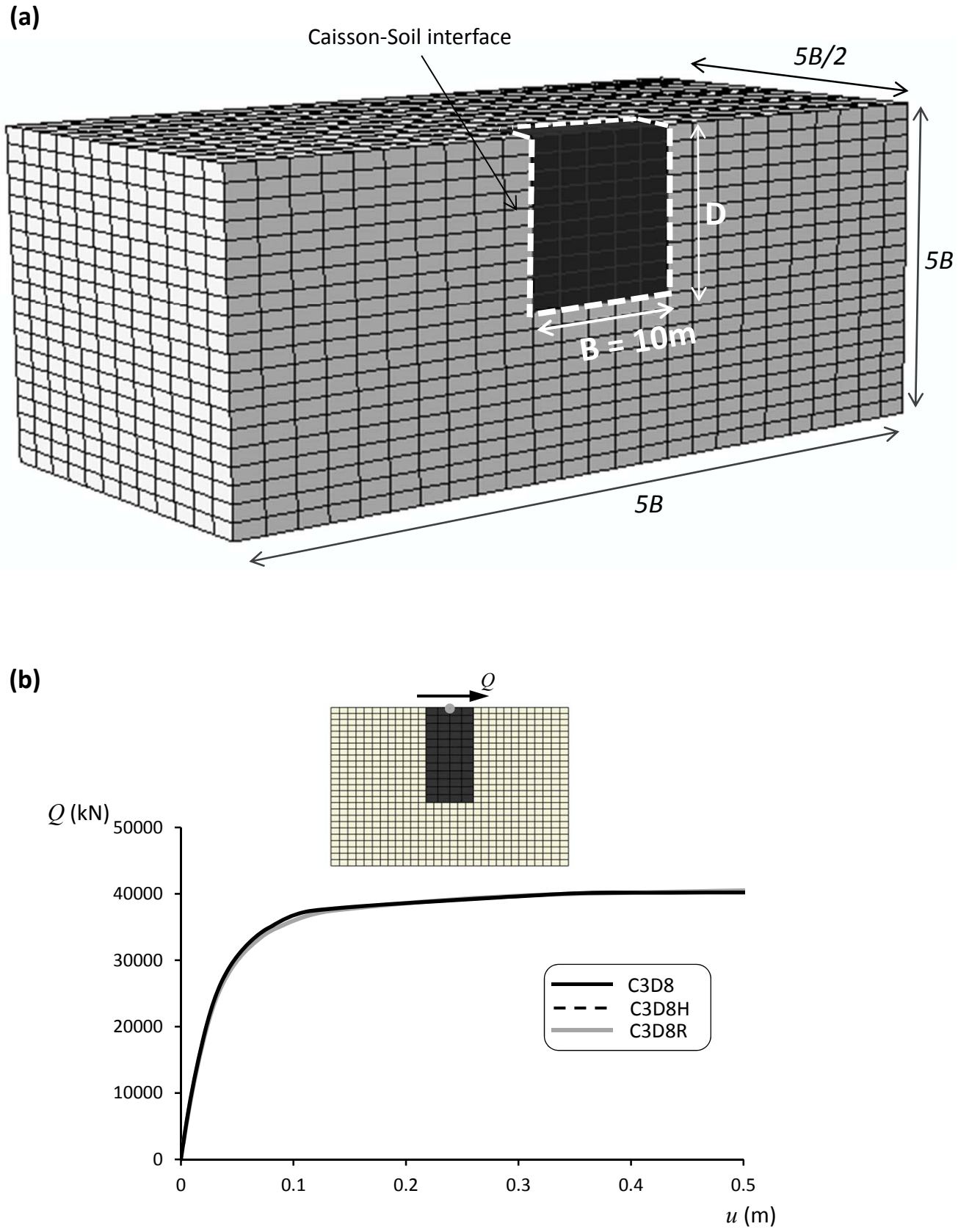

Fig. 2.1. (a) Typical finite element mesh for a caisson with D/B=1. (b) Results from sensitivity analysis with respect to the element type used for the numerical experiments. *Examined case*: caisson with D/B=2 in cohesive soil with nonlinear interface (considering μ = 1), under pure lateral loading Q.

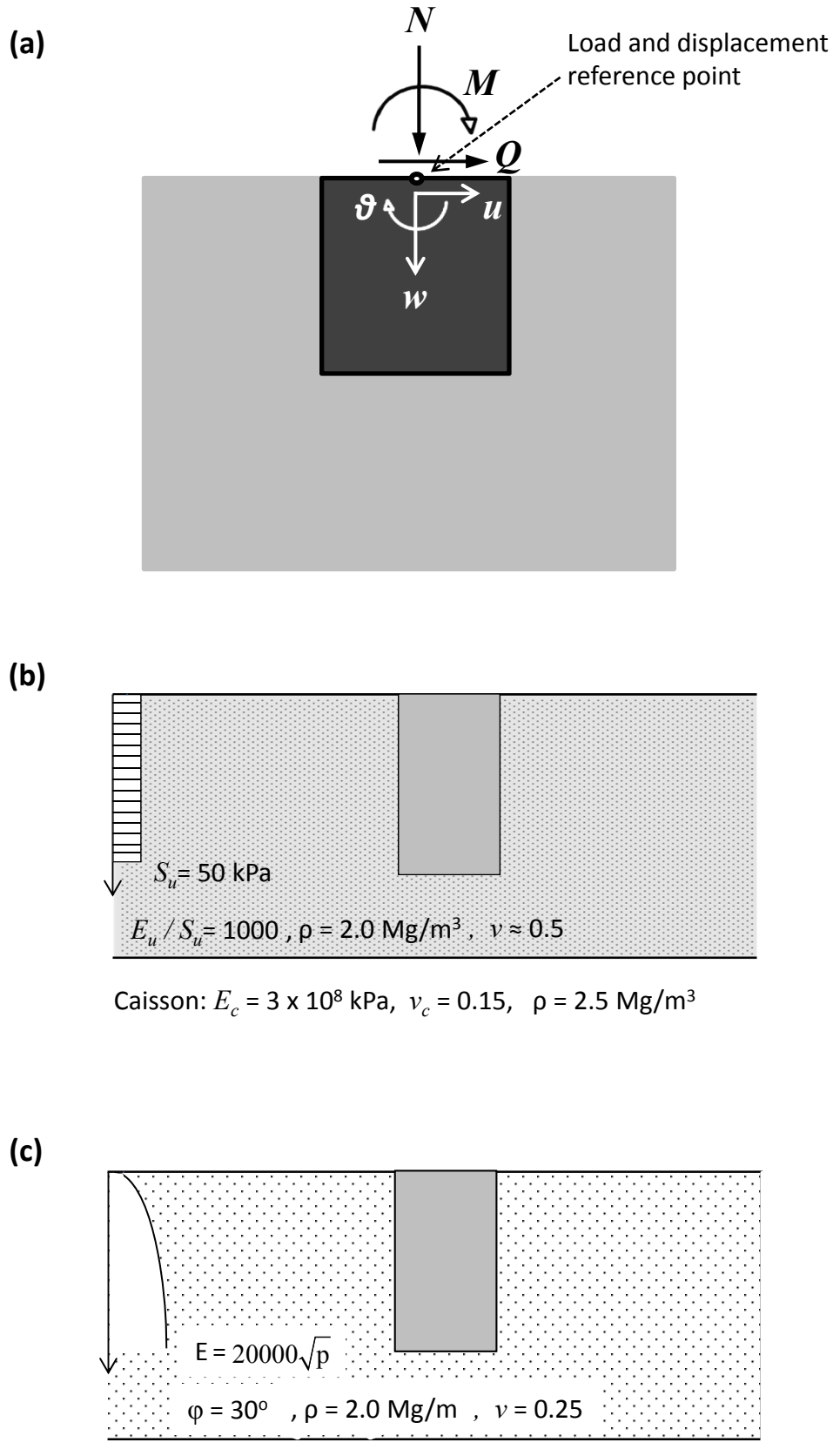

Fig. 2.2. (a) Sign conventions for loads and displacements, (b) the cohesive soil profile, (c) the frictional soil profile.

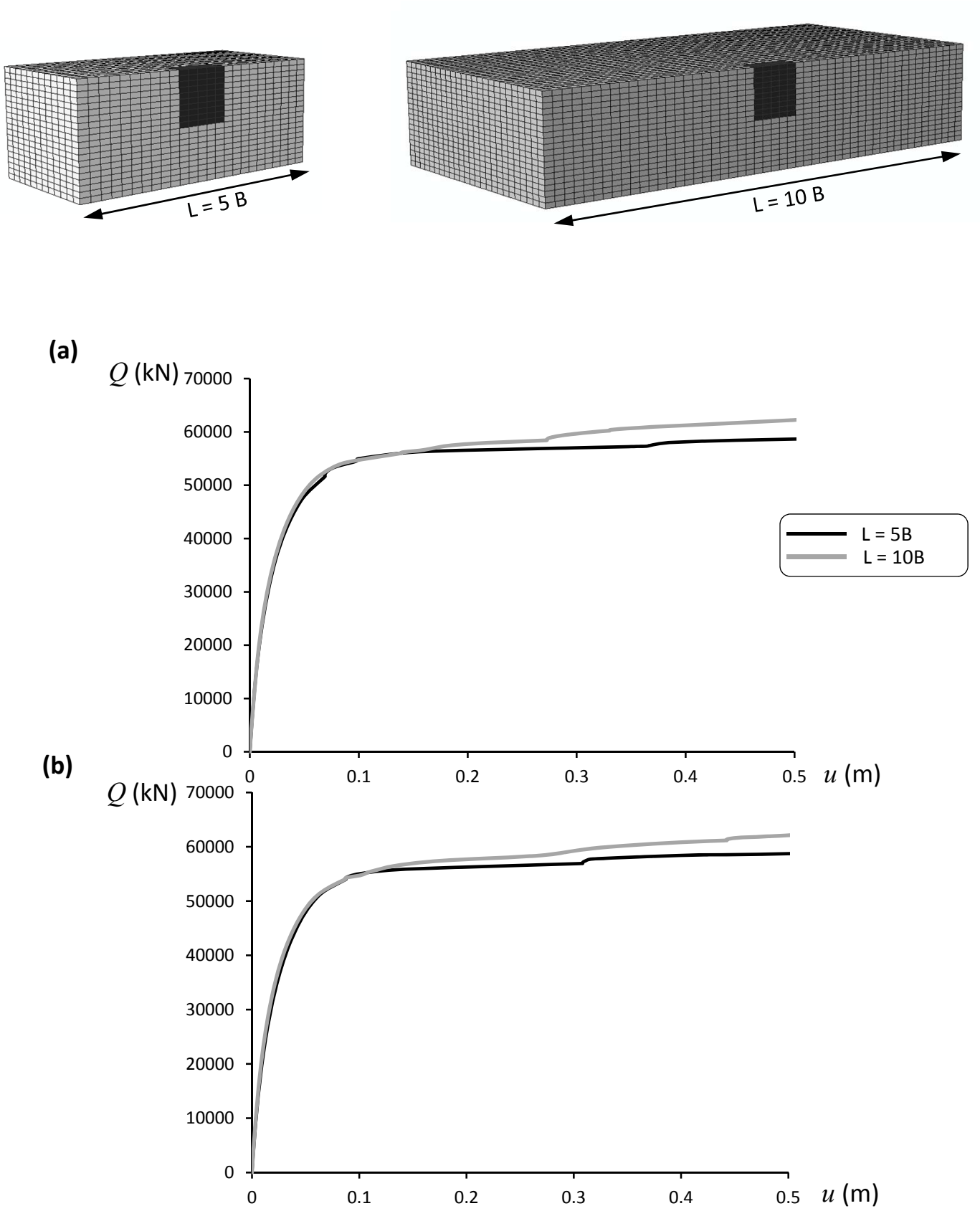

Fig. 2.3. Finite element model verification: caissons with D/B=1 in frictional soil, considering two finite element model sizes, L = 5 B and L = 10 B. Comparison in terms of static Q—u pushover curves, when (a) x = 0, μ = 1 , and (b) x = 0, μ = 0.5.

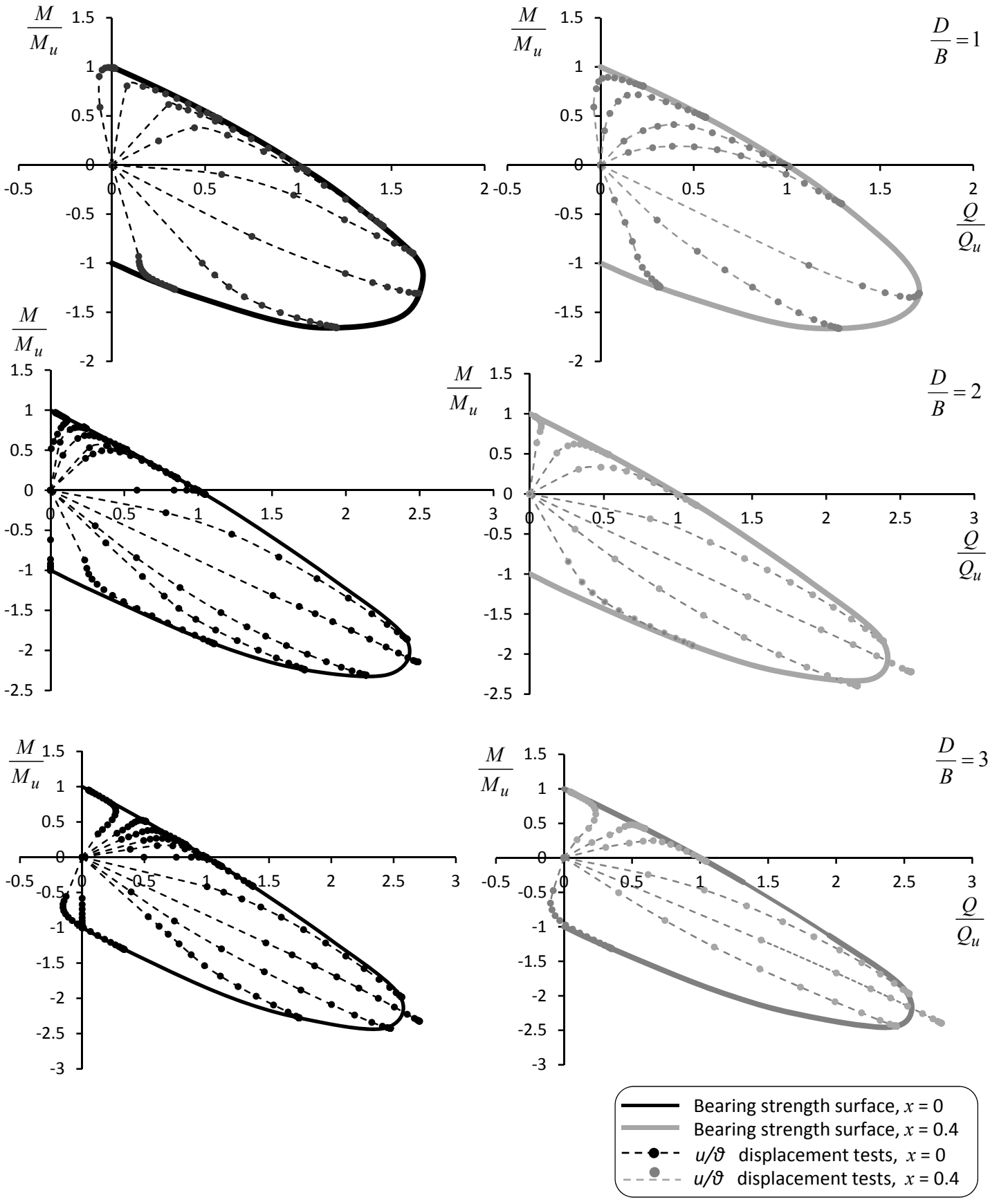

Fig. 2.4. Normalized bearing strength surfaces at χ = 0 and 0.4 calculated from FE analysis for (a) load-based (thick solid lines) and displacement-based tests (dashed lines).

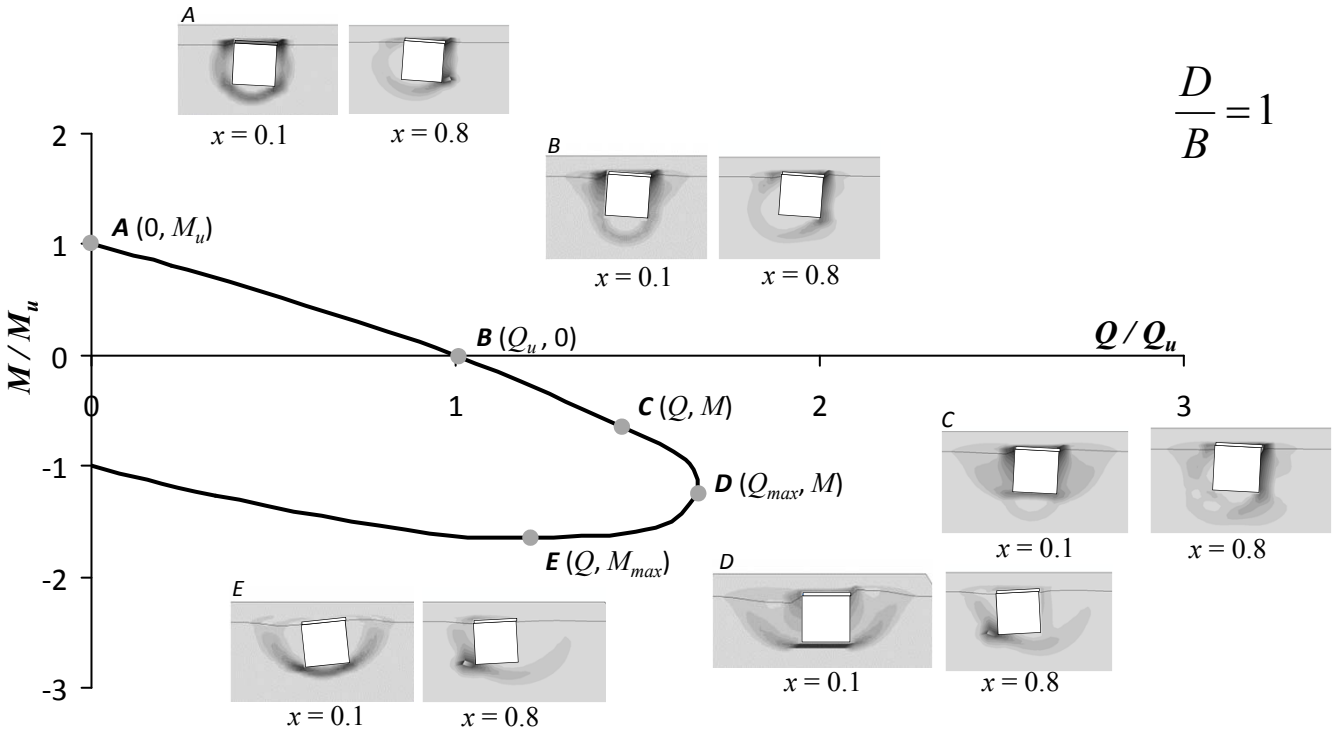

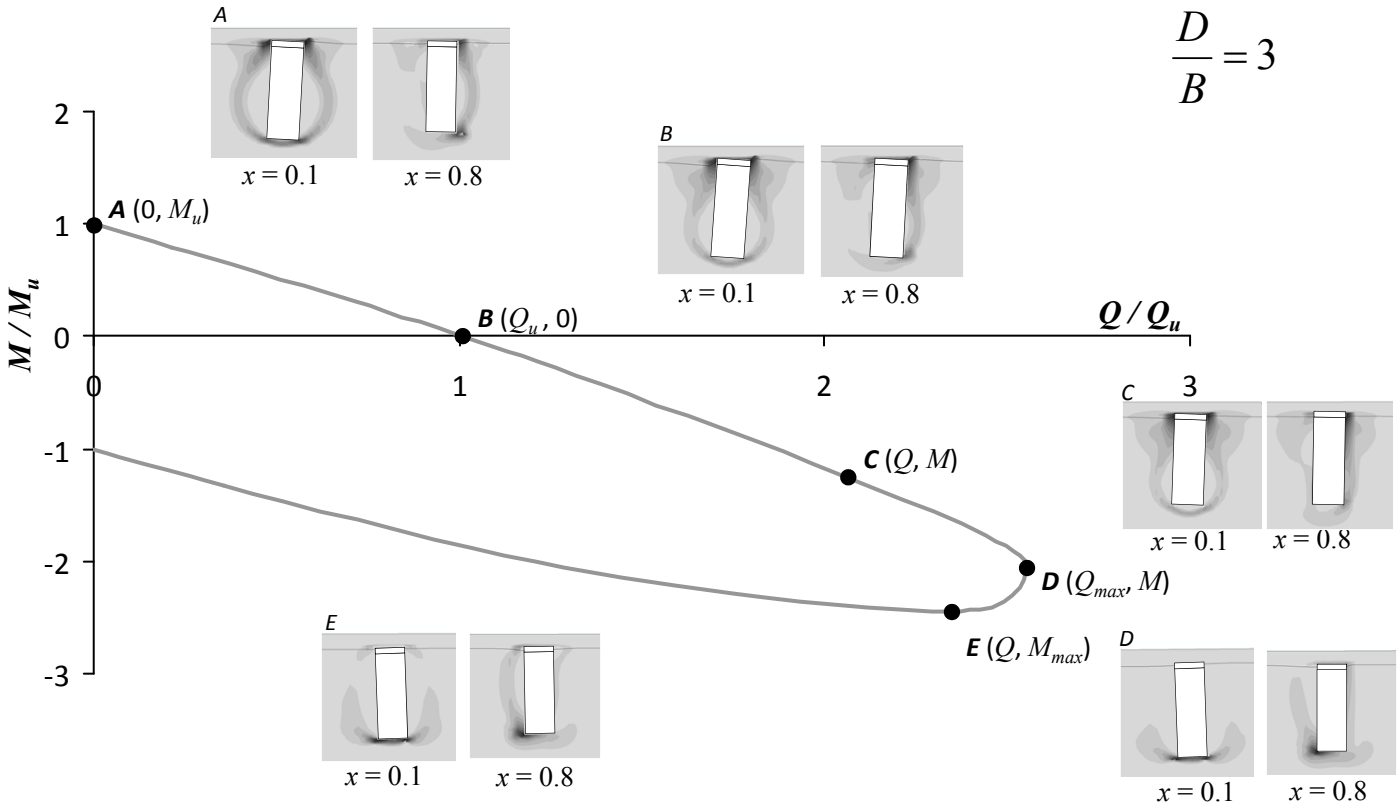

Fig. 2.5. Normalized bearing strength surfaces for D/B = 1 and 3 and for χ = 0.1 and 0.8. Snapshots of the computed (from FE analysis) plastic strain magnitude contours are also provided at characteristic points.

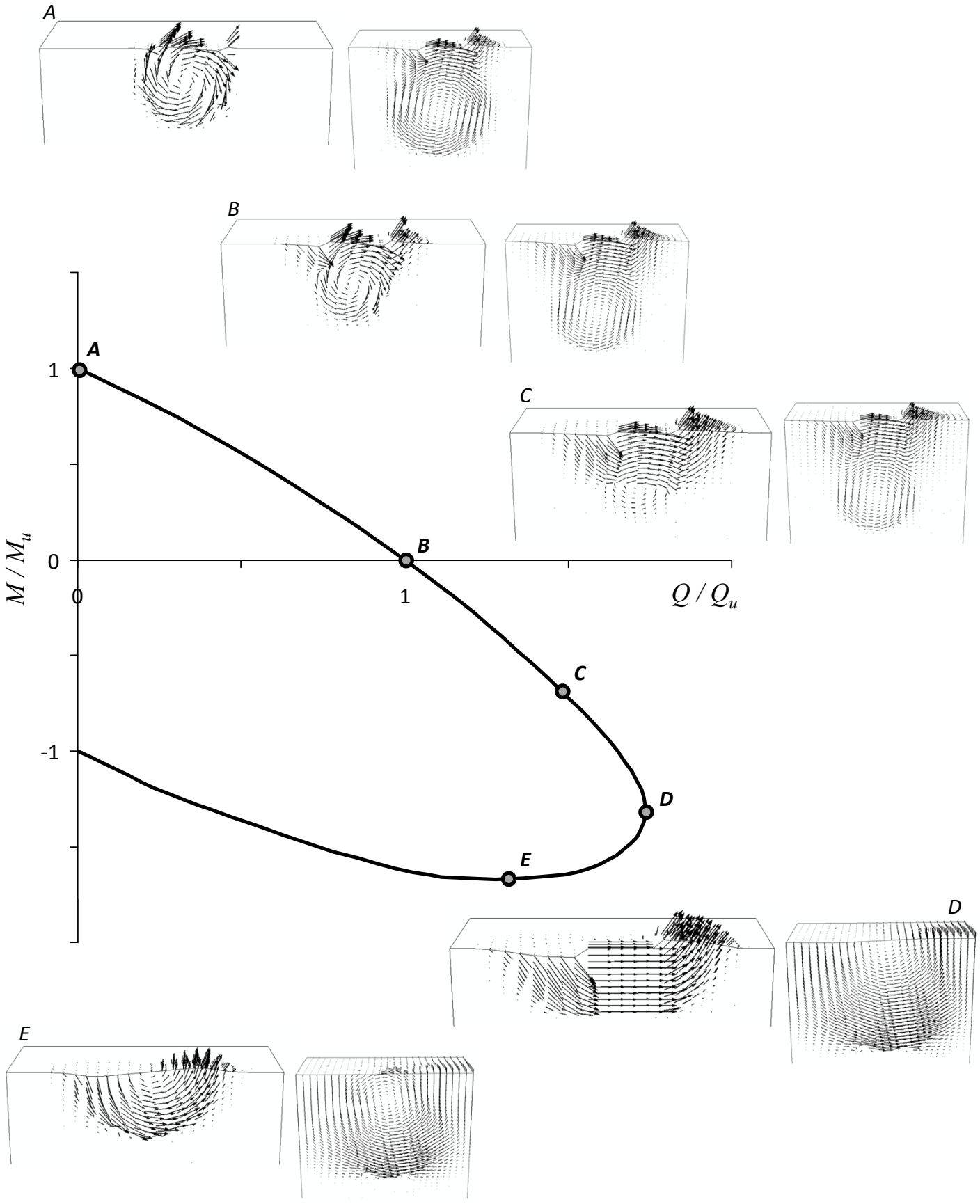

Fig. 2.6. Displacement vectors (plotted on the deformed FE mesh) for characteristic points of the bearing strength surface, at χ = 0.1 and for embedment ratios D/B = 1 and 3. Fully bonded interface conditions are considered.

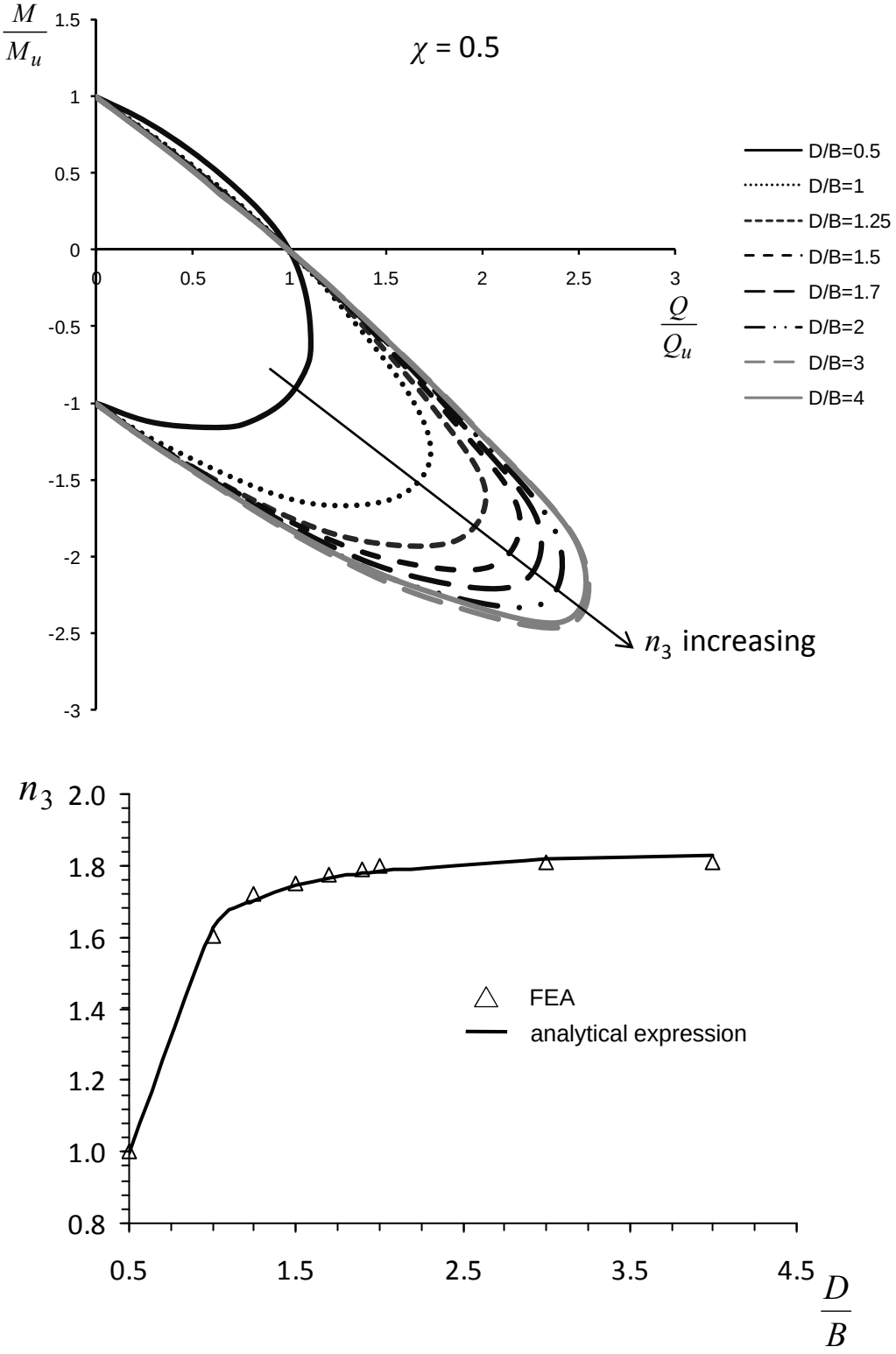

Fig. 2.7. Influence of the parameter n_3 on the shape of the strength surface at χ = 0.5. Comparison is given between numerical and analytical results with respect to D/B.

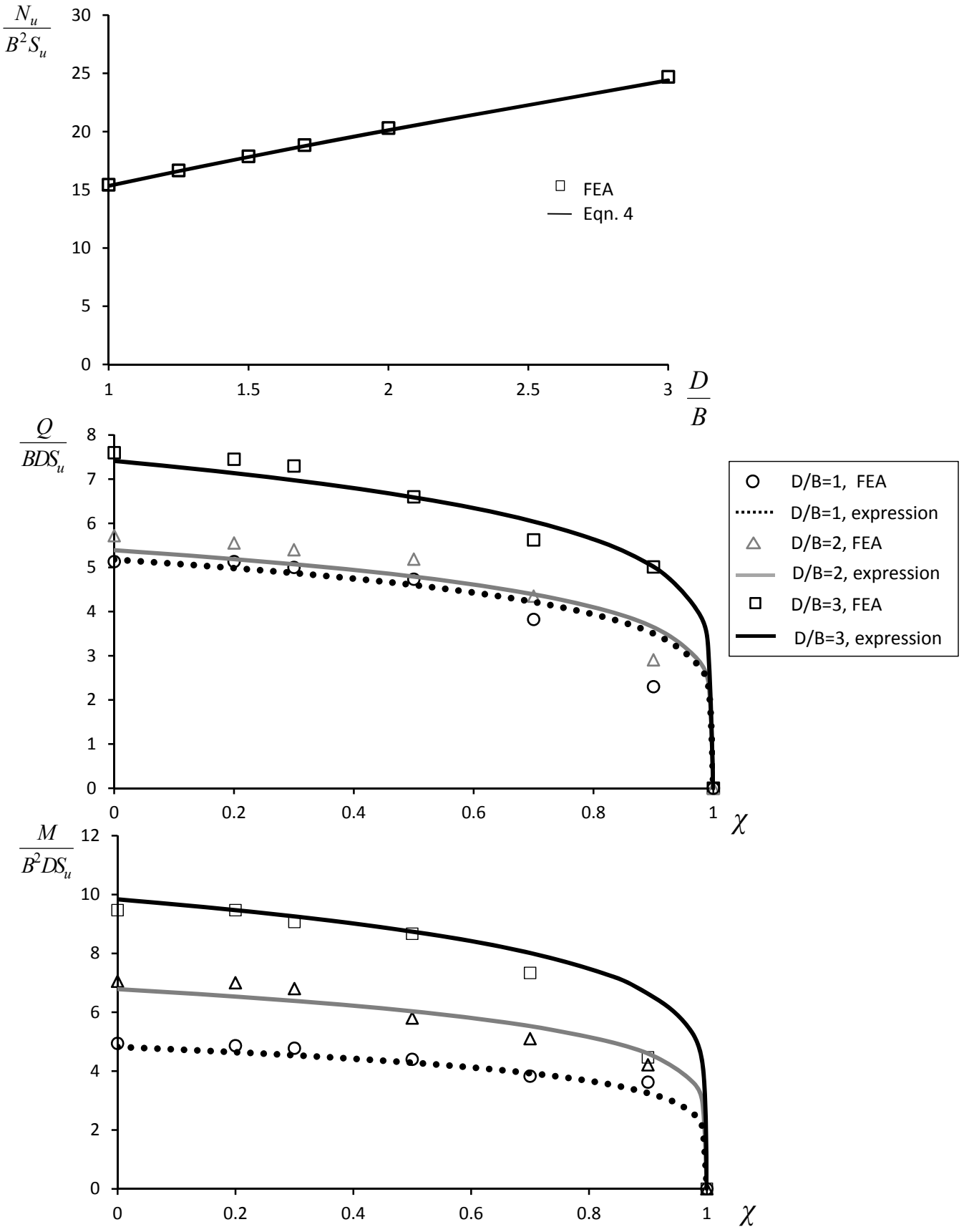

Fig. 2.8. Ultimate uniaxial capacities, N_u, Q_u and M_u, with respect to χ and D/B. Comparison is given between the FE results and predictions by the respective analytical expressions.

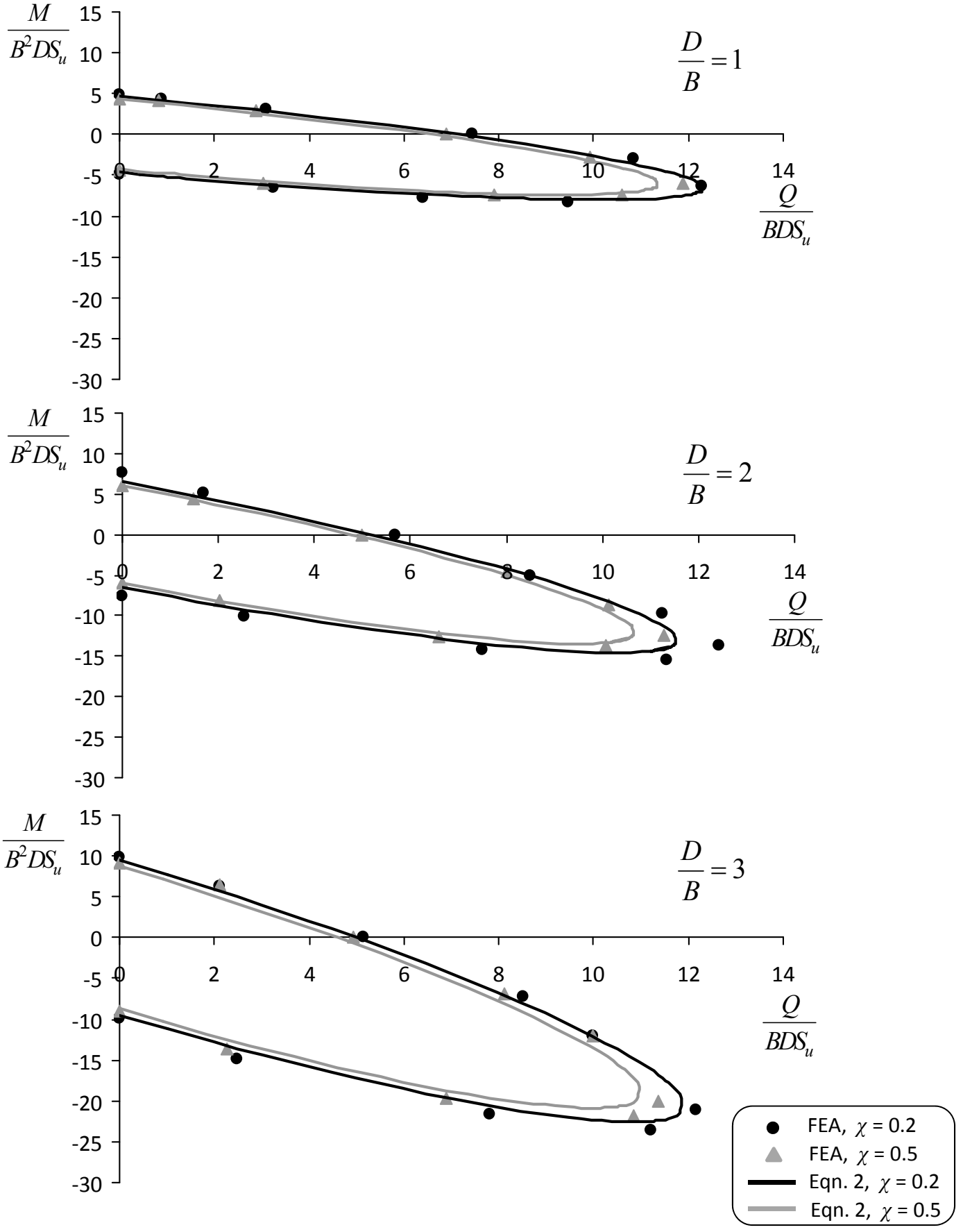

Fig. 2.9. Validation of the proposed analytical expression for the bearing strength surface in dimensionless quantities against FE results, for cohesive soil with fully-bonded interface conditions.

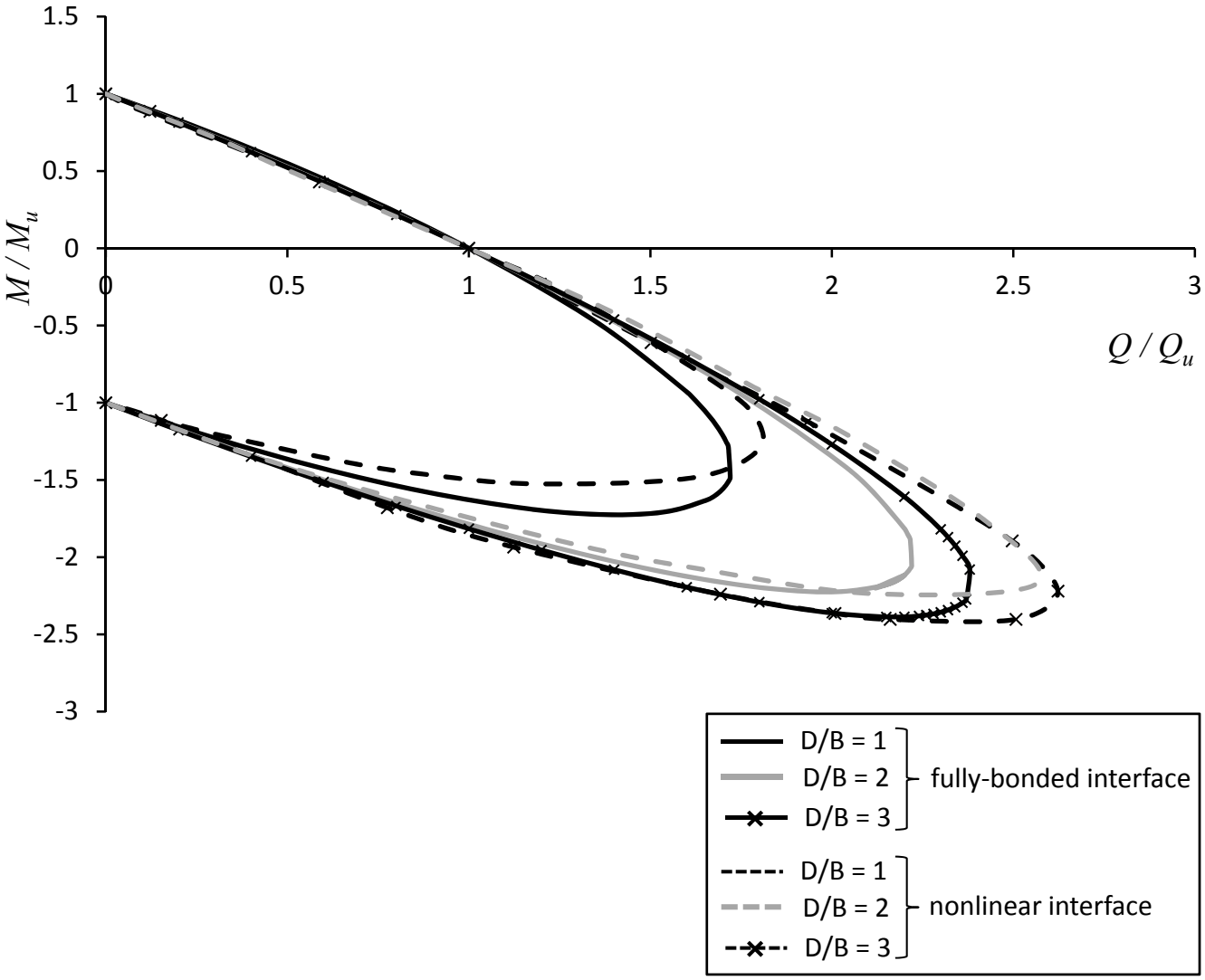

Fig. 2.10. Effect of interface nonlinearities on the bearing strength envelope in M-Q plane for D/B = 1,2, 3 at χ = 0.5. Comparison is given between fully bonded (solid lines) and nonlinear (dashed lines) interface conditions.

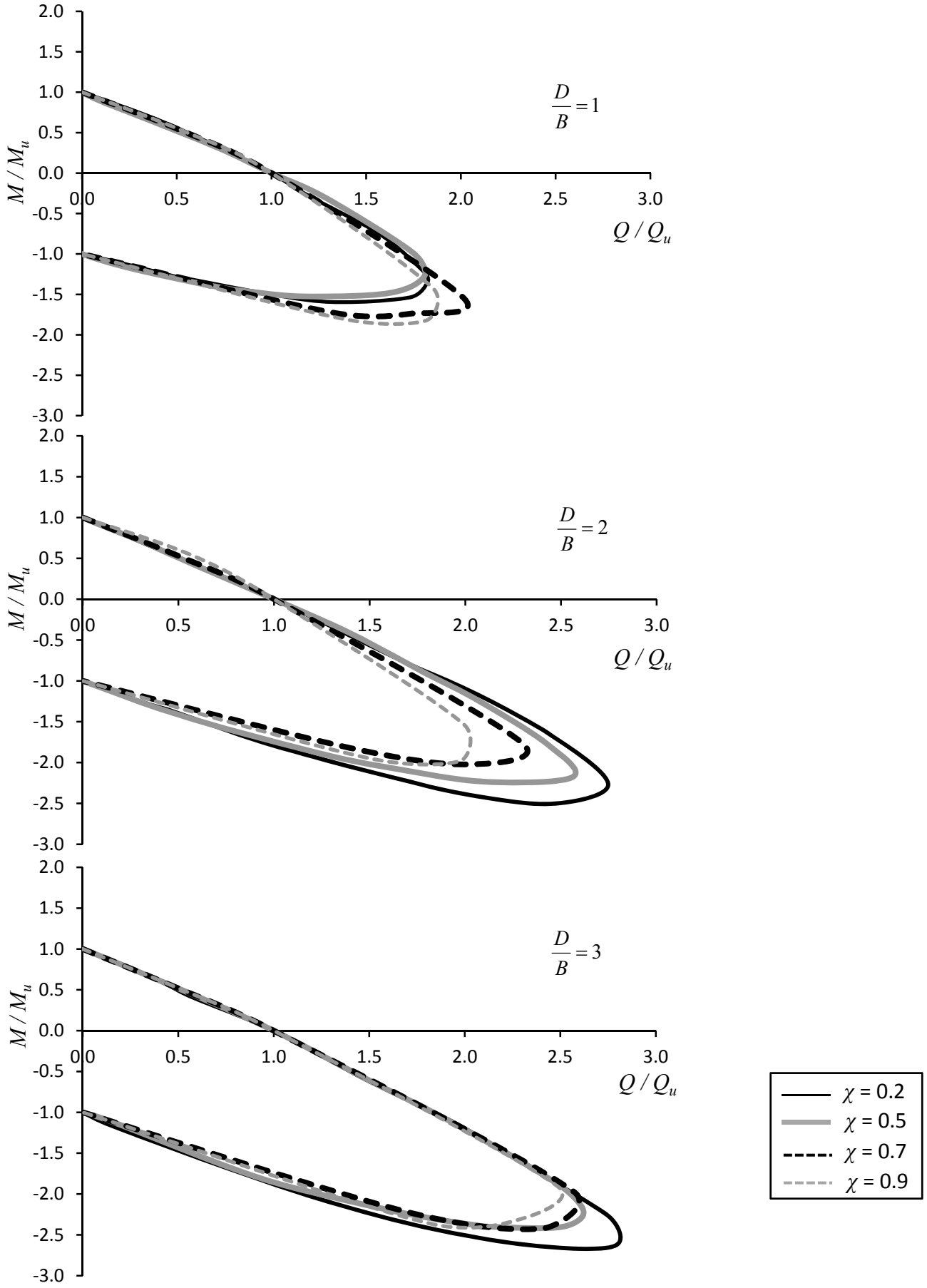

Fig. 2.11. Normalized bearing strength surfaces for caissons in cohesive soil with nonlinear interface: Effect of the level of vertical loading on the capacity.

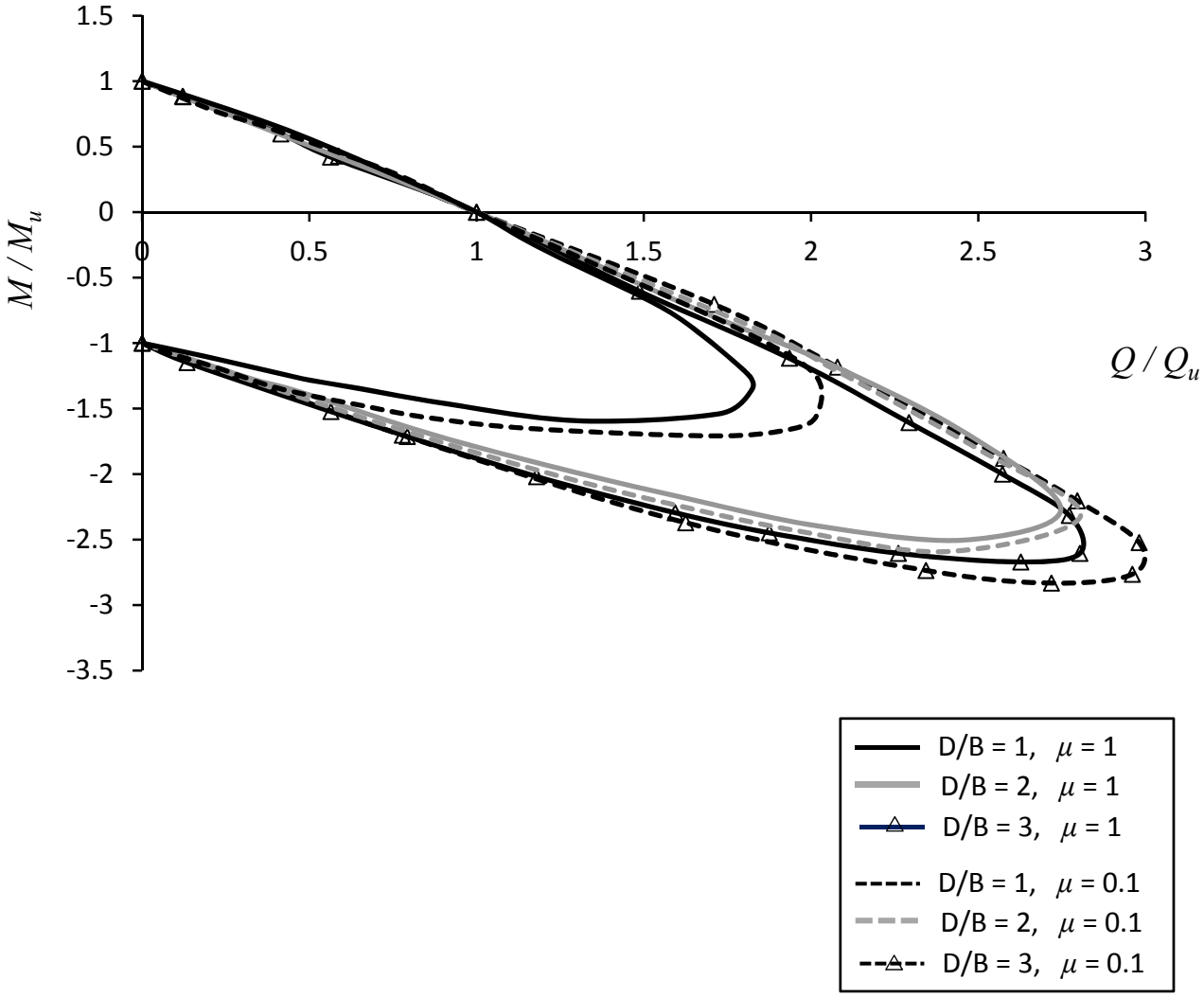

Fig. 2.12. Normalized bearing strength surfaces for caissons in cohesive soil with nonlinear interface at χ = 0.5: Effect of the interface friction coefficient on the capacity.

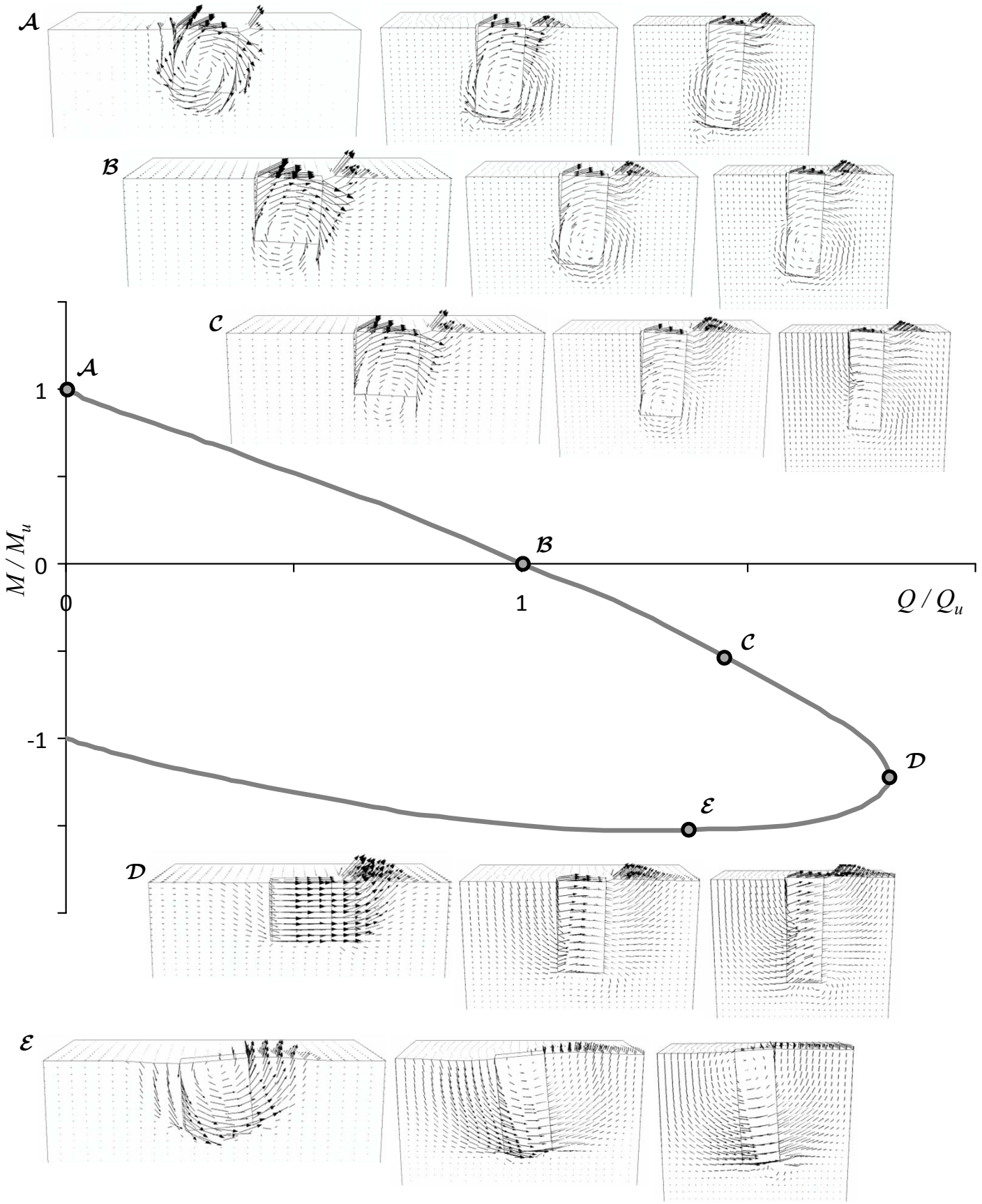

Fig. 2.13. Displacement vectors (plotted on the deformed FE mesh) for characteristic points of the bearing strength surface, at χ = 0 (zero vertical load) and for embedment ratios D/B = 1, 2 and 3. Nonlinear interface conditions are considered.

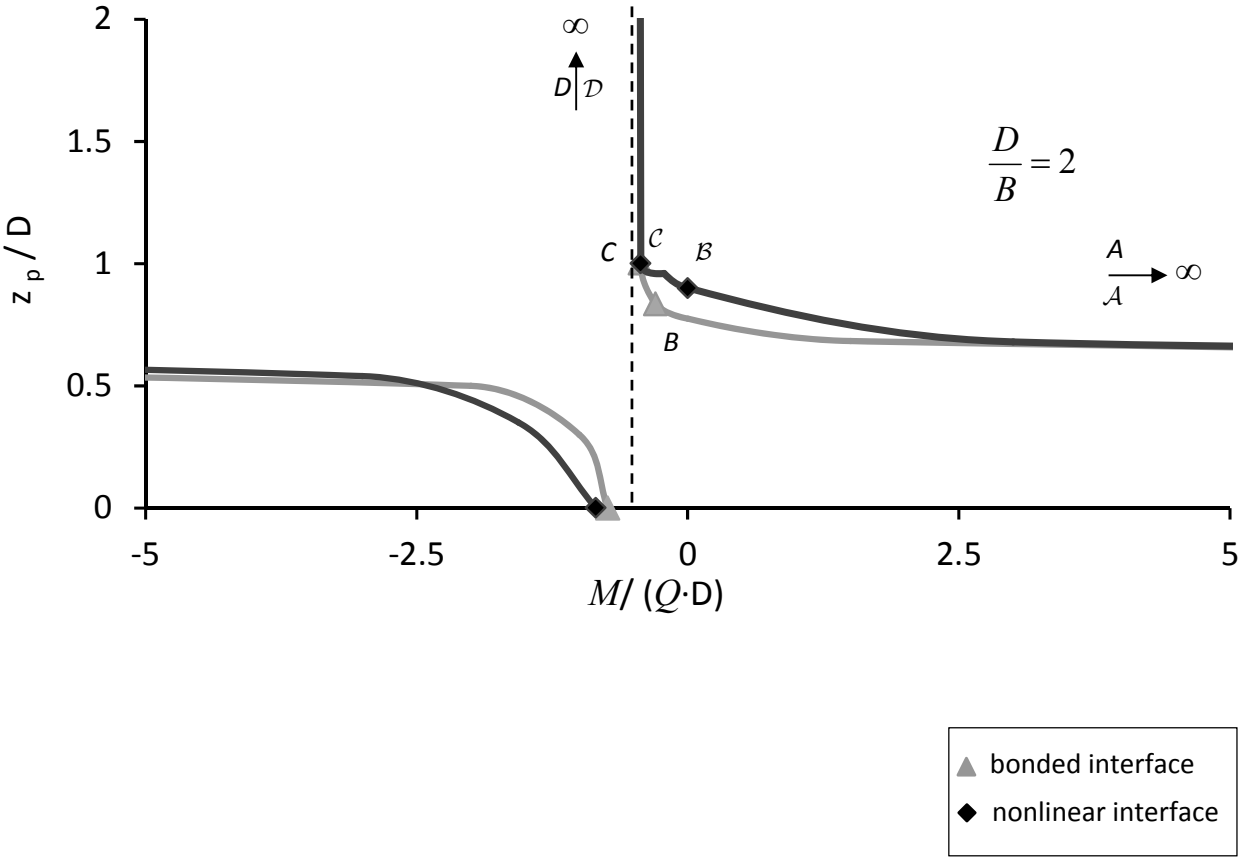

Fig. 2.14. Dimensionless diagram of the depth of rotation pole with respect to the loading ratio M/QD for caissons with D/B = 2 and χ = 0.2. Comparison is given between fully bonded and nonlinear interface conditions.

$\frac{D}{B}=1$

"*sliding*" – "*diffusive*" mechanism

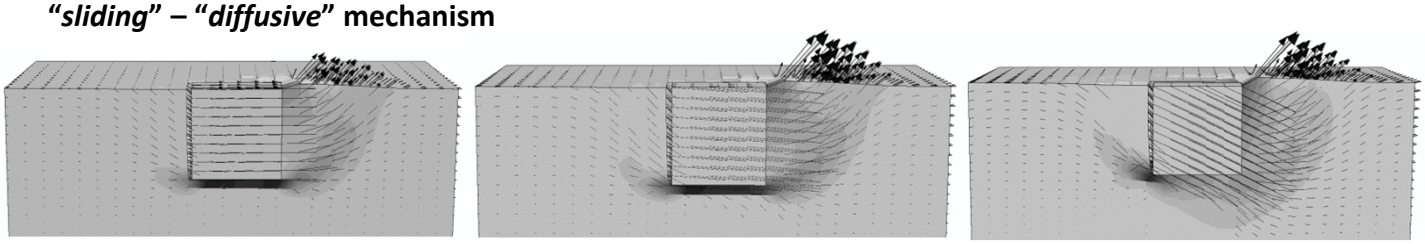

χ = 0 χ = 0.2 χ = 0.5

"*pendulum*" mechanism

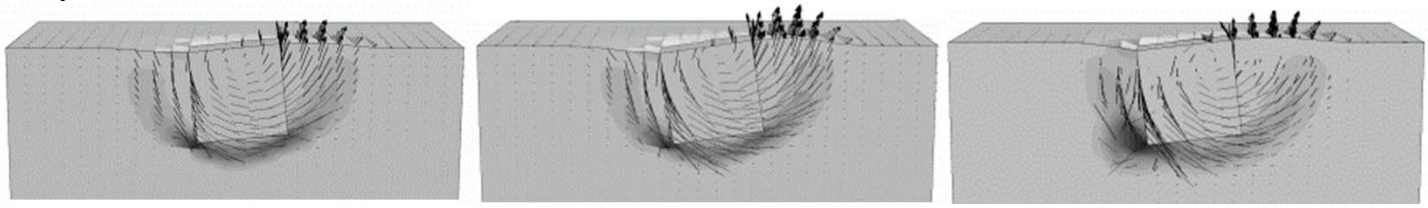

χ = 0 χ = 0.2 χ = 0.5

$\frac{D}{B}=3$

"*sliding*" – "*diffusive*" mechanism

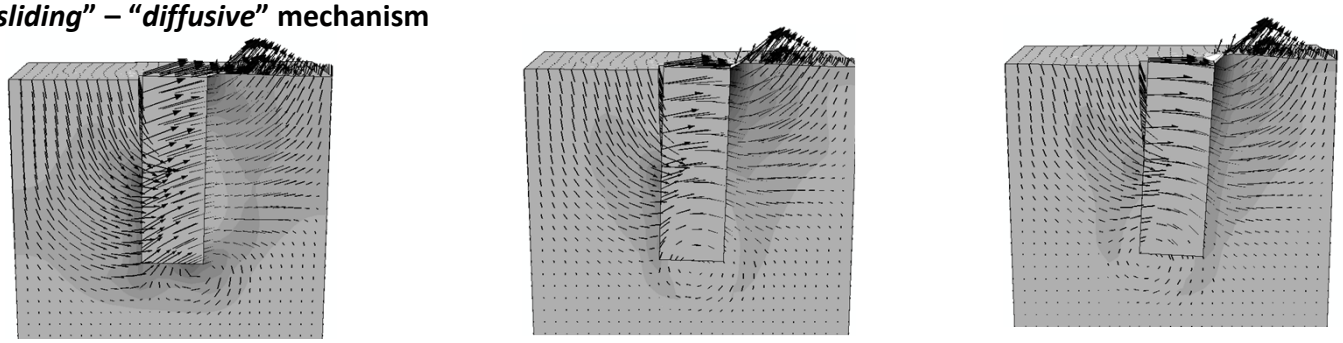

χ = 0 χ = 0.2 χ = 0.5

"*pendulum*" mechanism

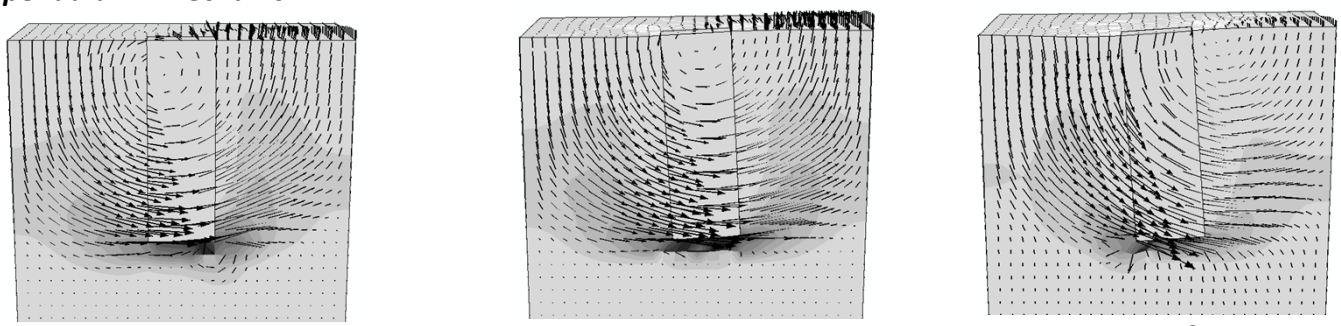

χ = 0 χ = 0.2 χ = 0.5

Fig. 2.15. Snapshots of plastic strain magnitude contours at failure with superimposed kinematic mechanism vectors: Effect of the vertical load level on the "*sliding*" and the "*pendulum*" failure mechanisms for D/B=1 and D/B=3.

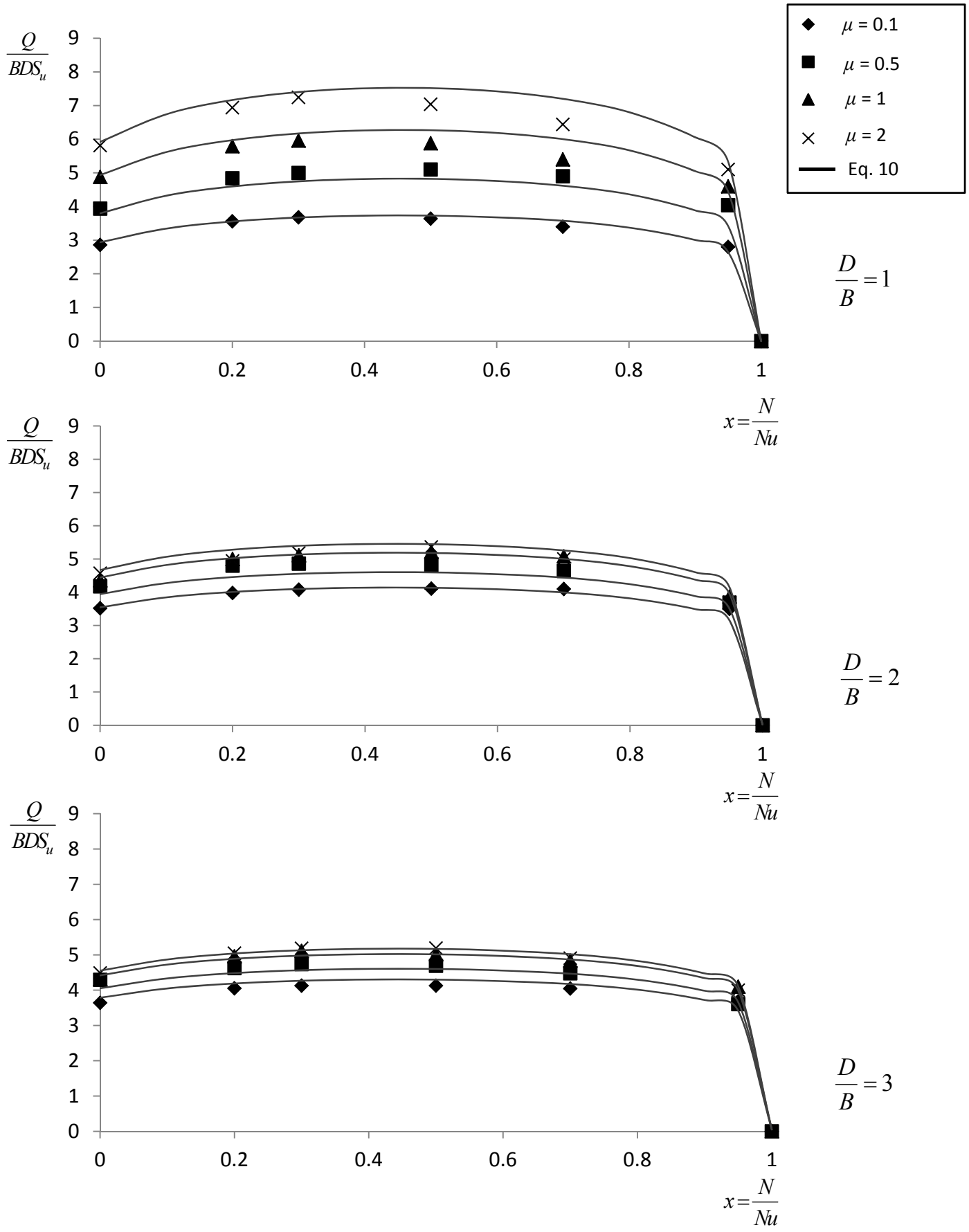

Fig. 2.16. Variation of the pure horizontal capacity, in dimensionless form, with respect to χ. Comparison is given between the finite element results and the analytical expression for selected values of the interface friction coefficient μ.

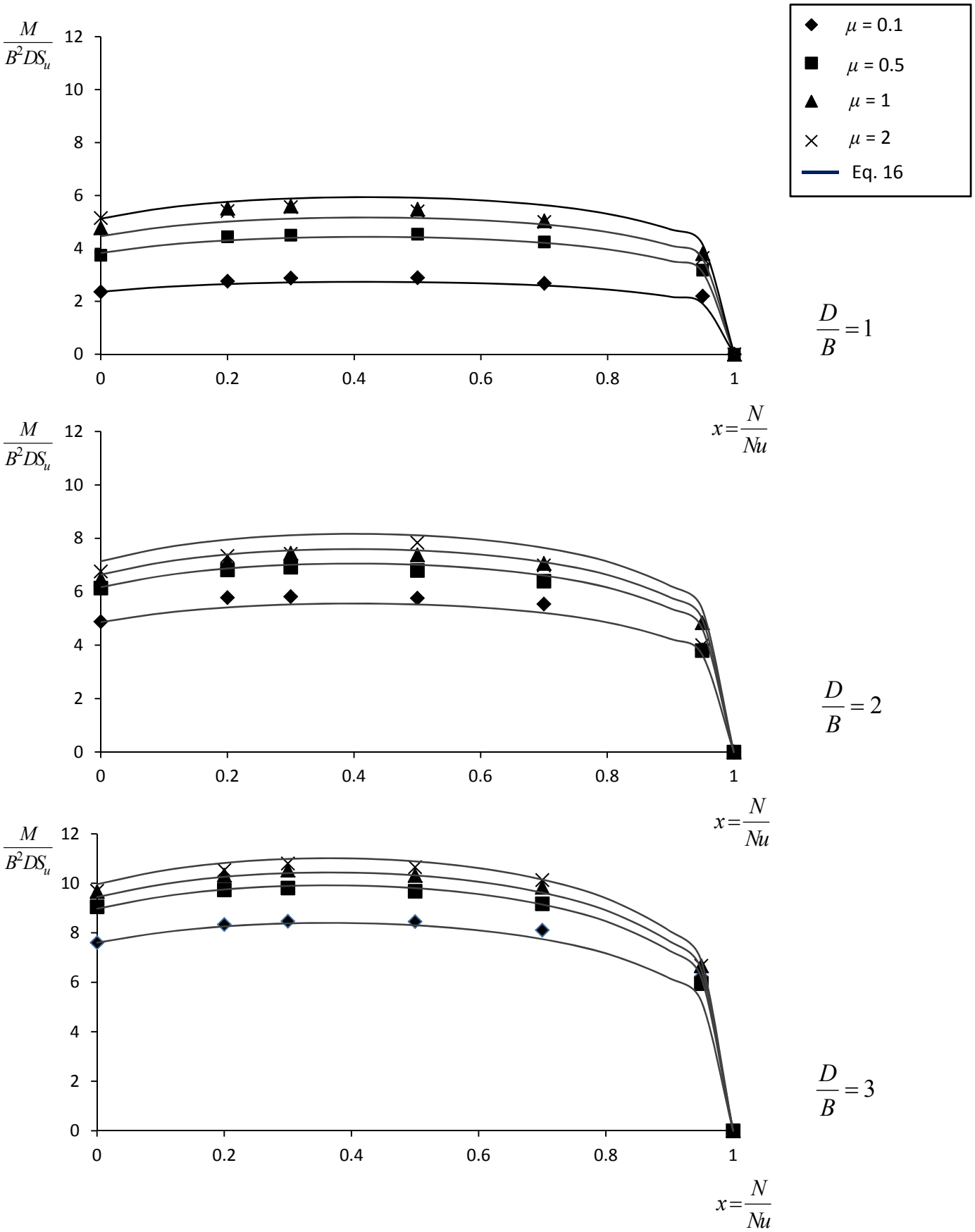

Fig. 2.17. Variation of the pure moment capacity, in dimensionless form, with respect to χ. Comparison is given between the finite element results and the analytical expression for selected values of the interface friction coefficient μ.

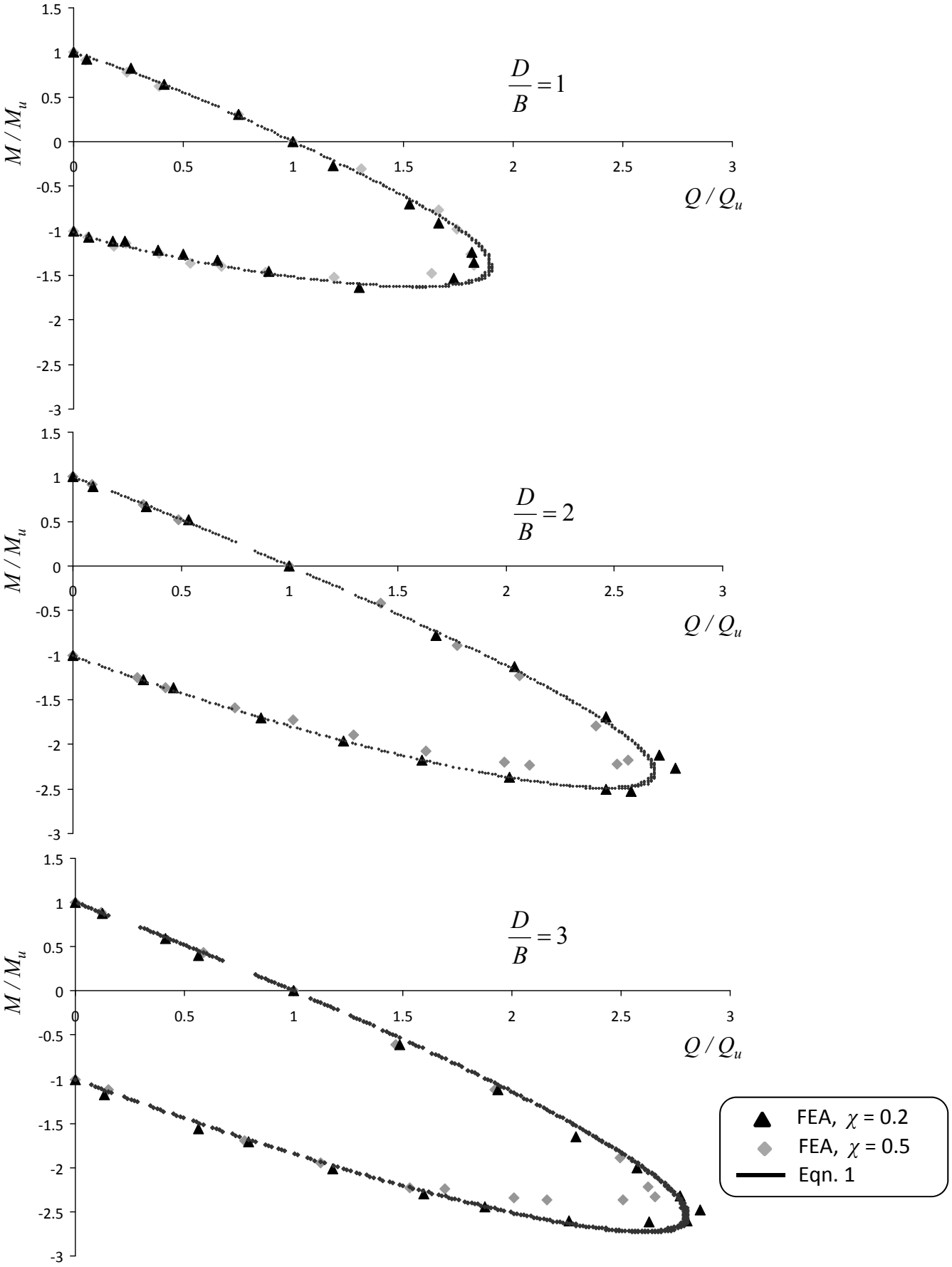

Fig. 2.18. Validation of the proposed analytical expression for the bearing strength surface in normalized quantities. Comparison is given between numerical and analytical results for χ = 0.2 and 0.5 and for D/B = 1,2 and 3.

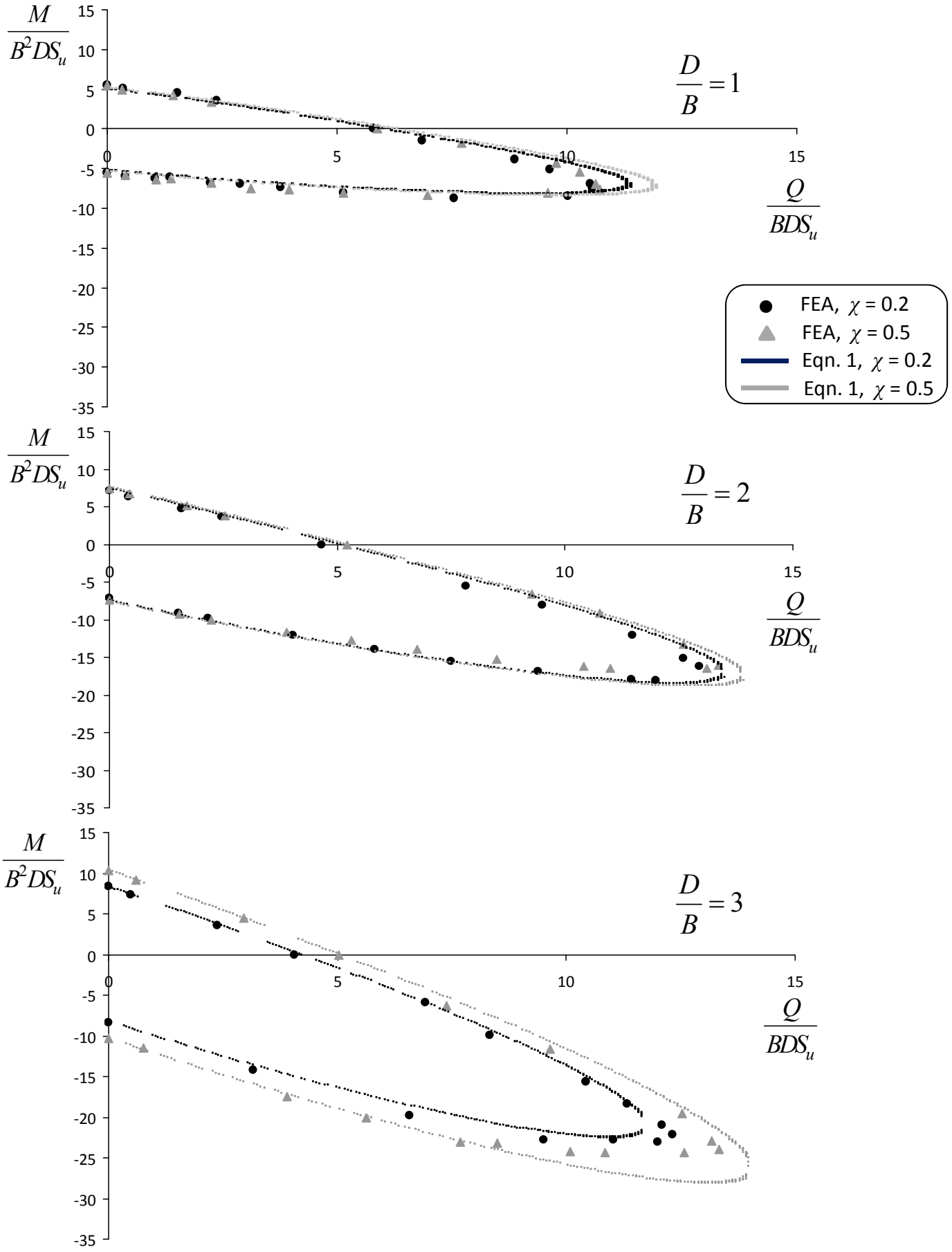

Fig. 2.19. Validation of the proposed analytical expression for the bearing strength surface in dimensionless quantities. Comparison is given between numerical and analytical results for χ = 0.2 and 0.5 and for D/B = 1,2 and 3.

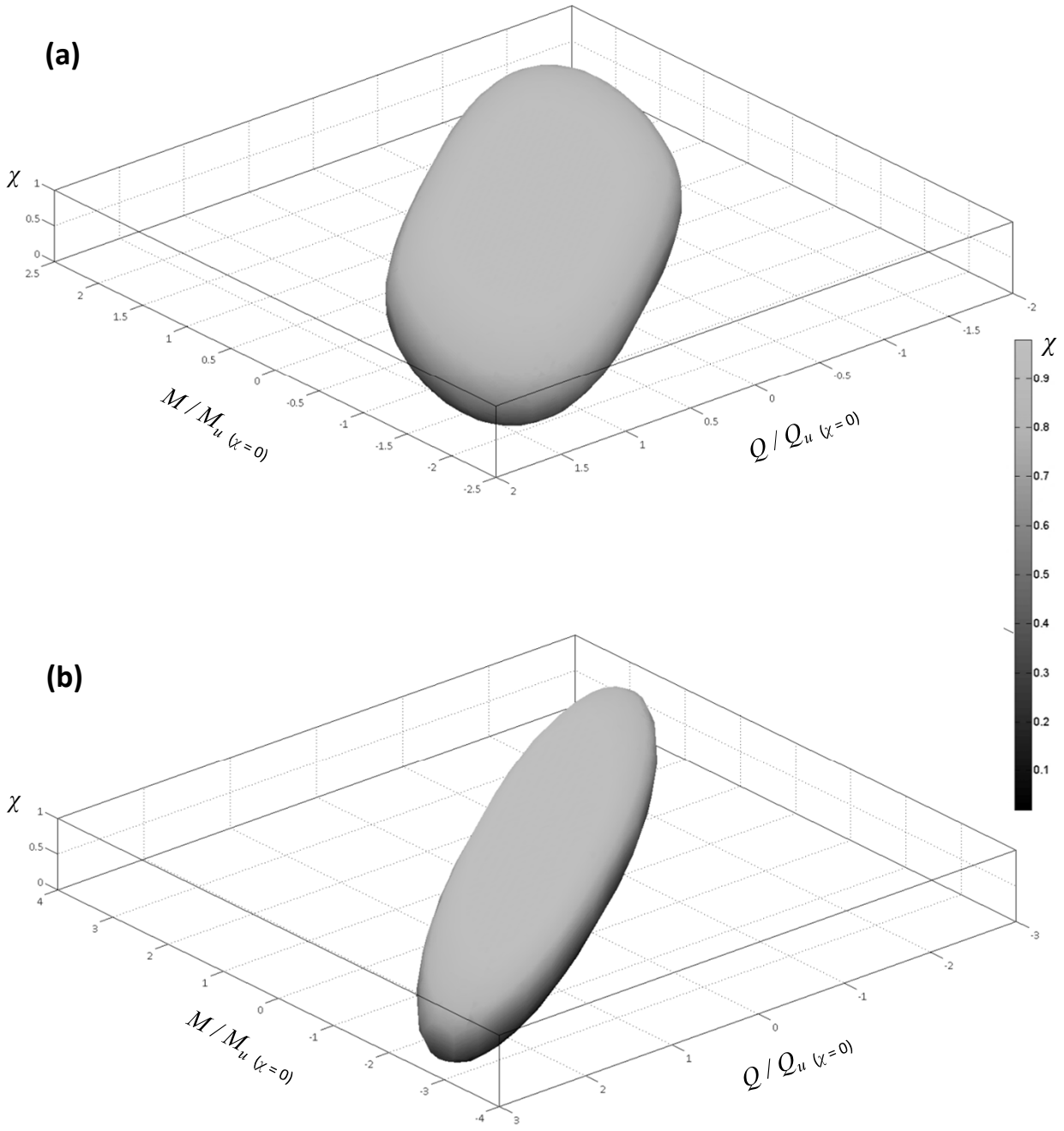

Fig. 2.20. 3-D representation of the bearing strength surface in Q-M-N space for caissons in cohesive soil with nonlinear interface conditions (interface friction coefficient μ = 1). The results are normalized by the respective pure (at χ = 0) lateral capacities $M_u{}^*$ and $Q_u{}^*$, for (a) D/B = 1 and (b) D/B = 3.

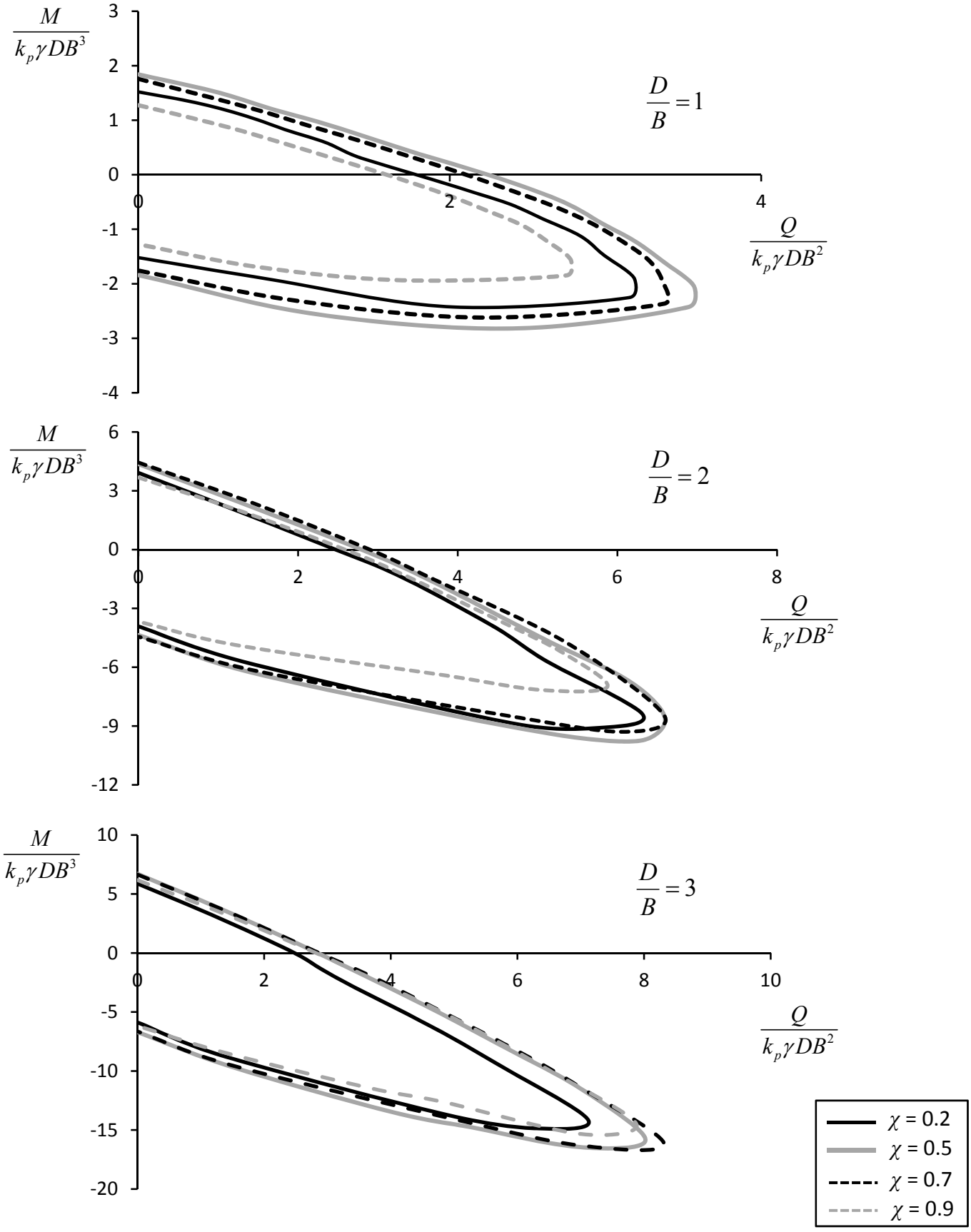

Fig. 2.21. Bearing strength surfaces, in dimensionless form, for caissons in frictional soil: Effect of the level of vertical loading on the capacity.

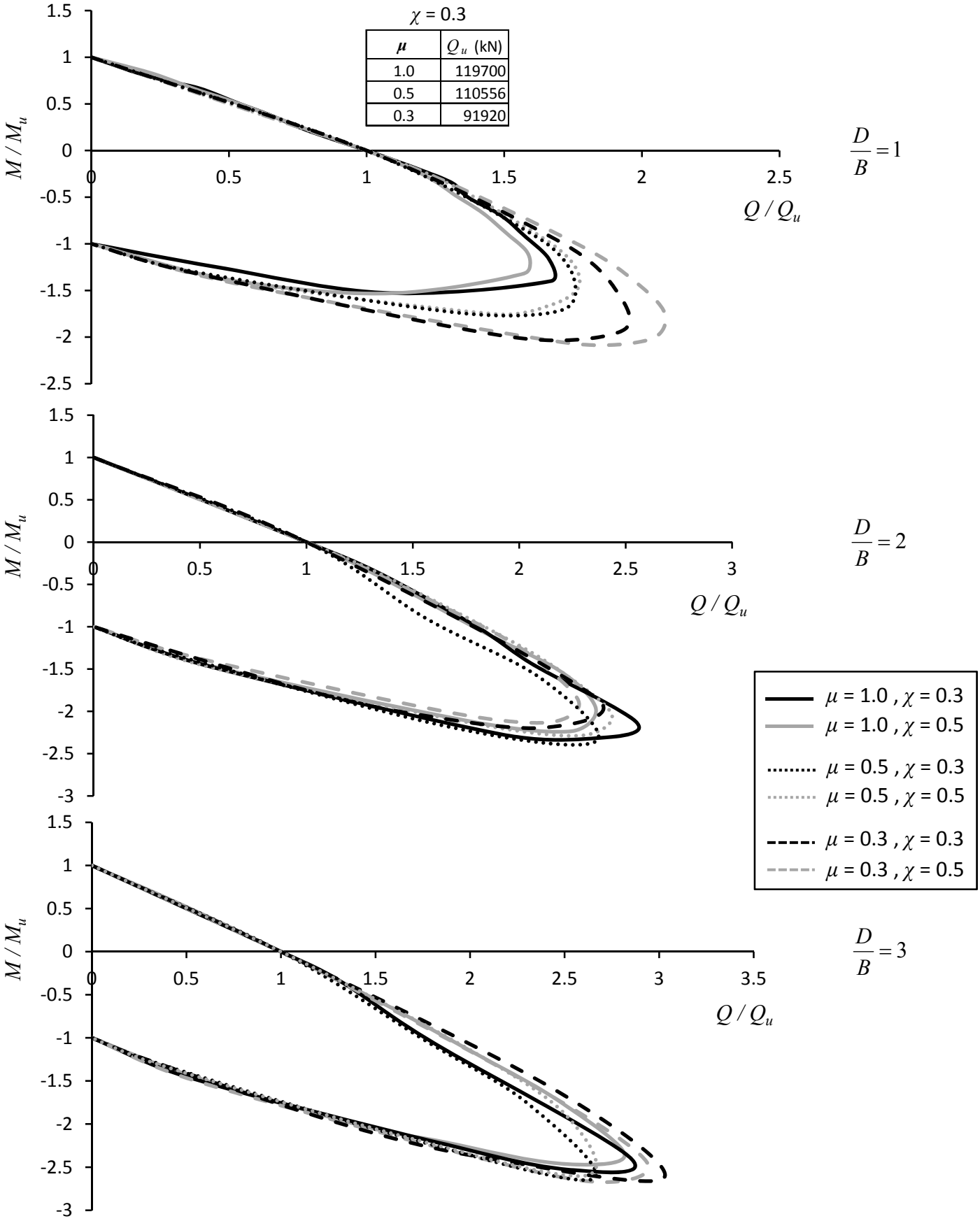

Fig. 2.22. Normalized bearing strength surfaces for caissons in frictional soil: Effect of the interface conditions on the capacity.

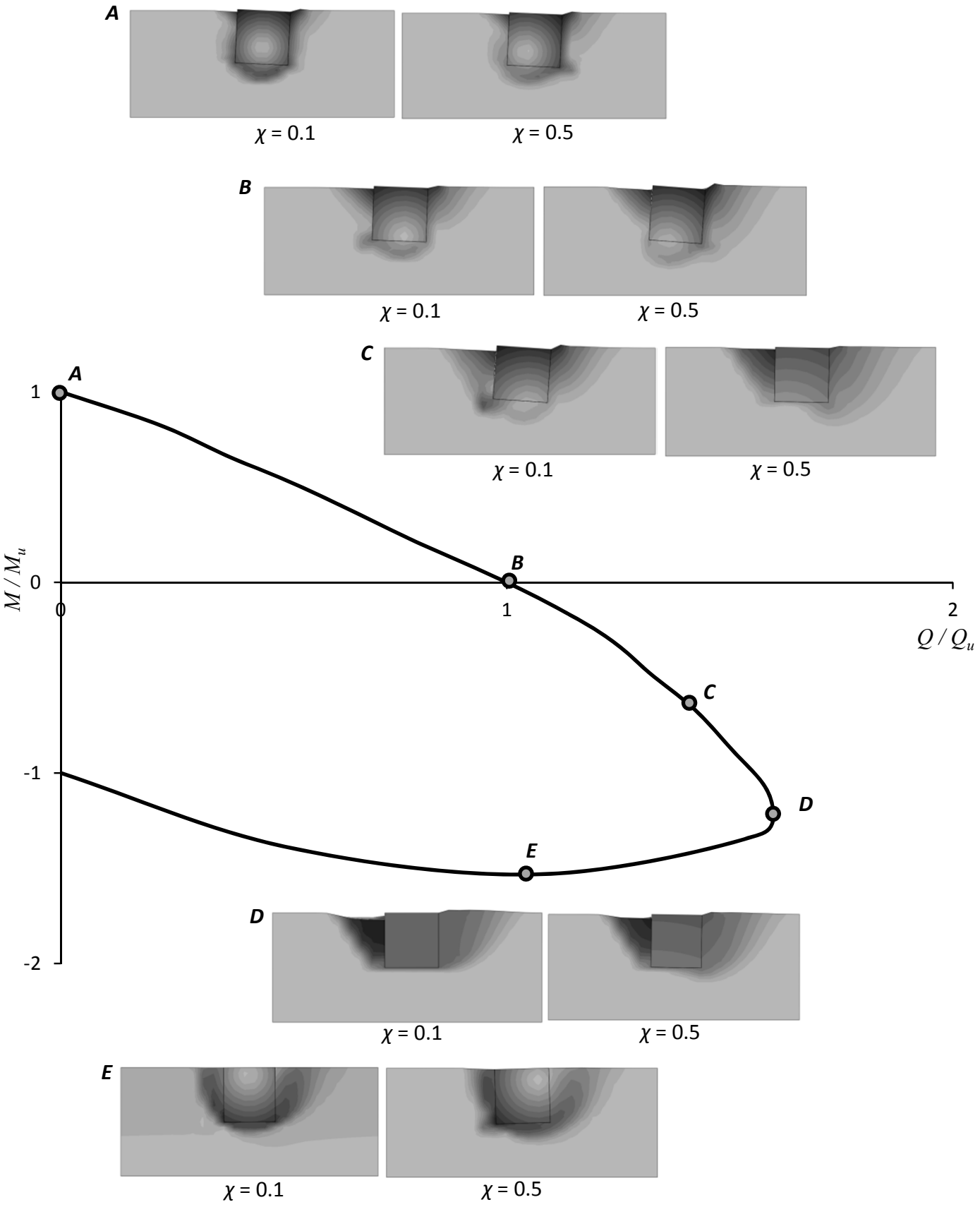

Fig. 2.23. Displacement contours (plotted on the deformed FE mesh) for characteristic points on the bearing strength surface, for D/B = 1 and for χ = 0.1 and 0.5 (frictional soil).

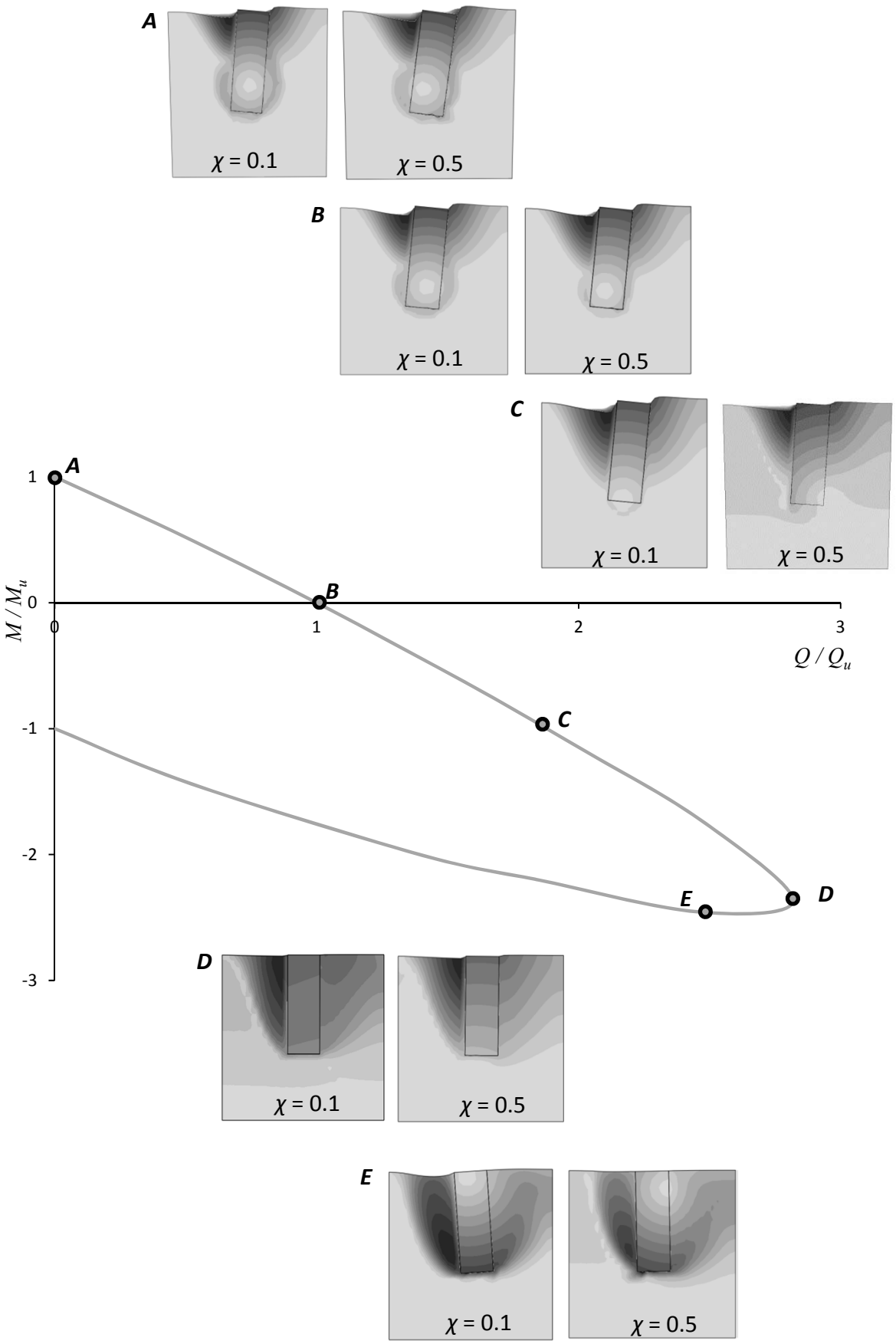

Fig. 2.24. Displacement contours (plotted on the deformed FE mesh) for characteristic points on the bearing strength surface, for D/B = 3 and for χ = 0.1 and 0.5 (frictional soil).

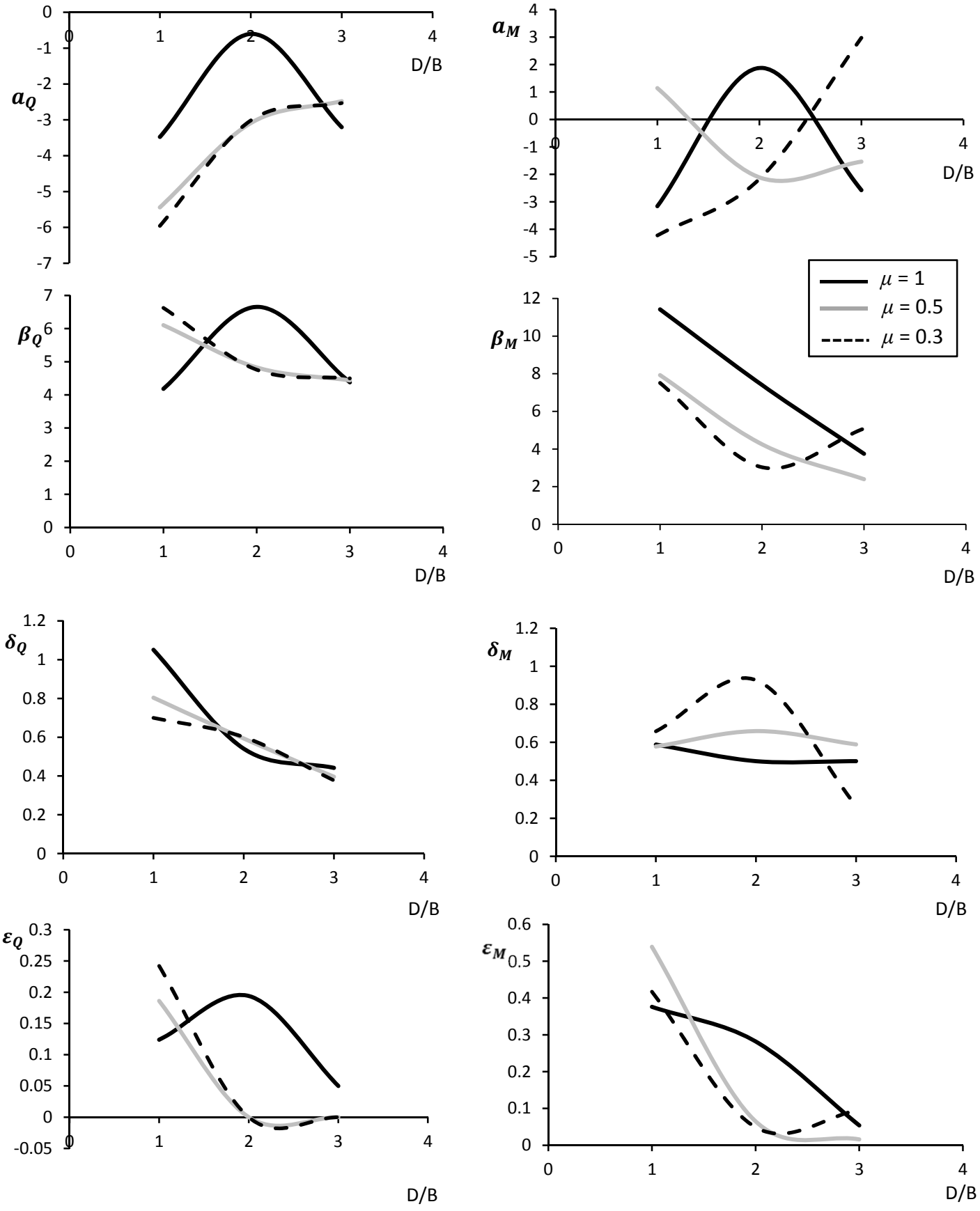

Fig. 2.25. Variation of the coefficients controlling the pure horizontal and moment load capacities, with respect to D/B and μ, as derived from the FE analysis.

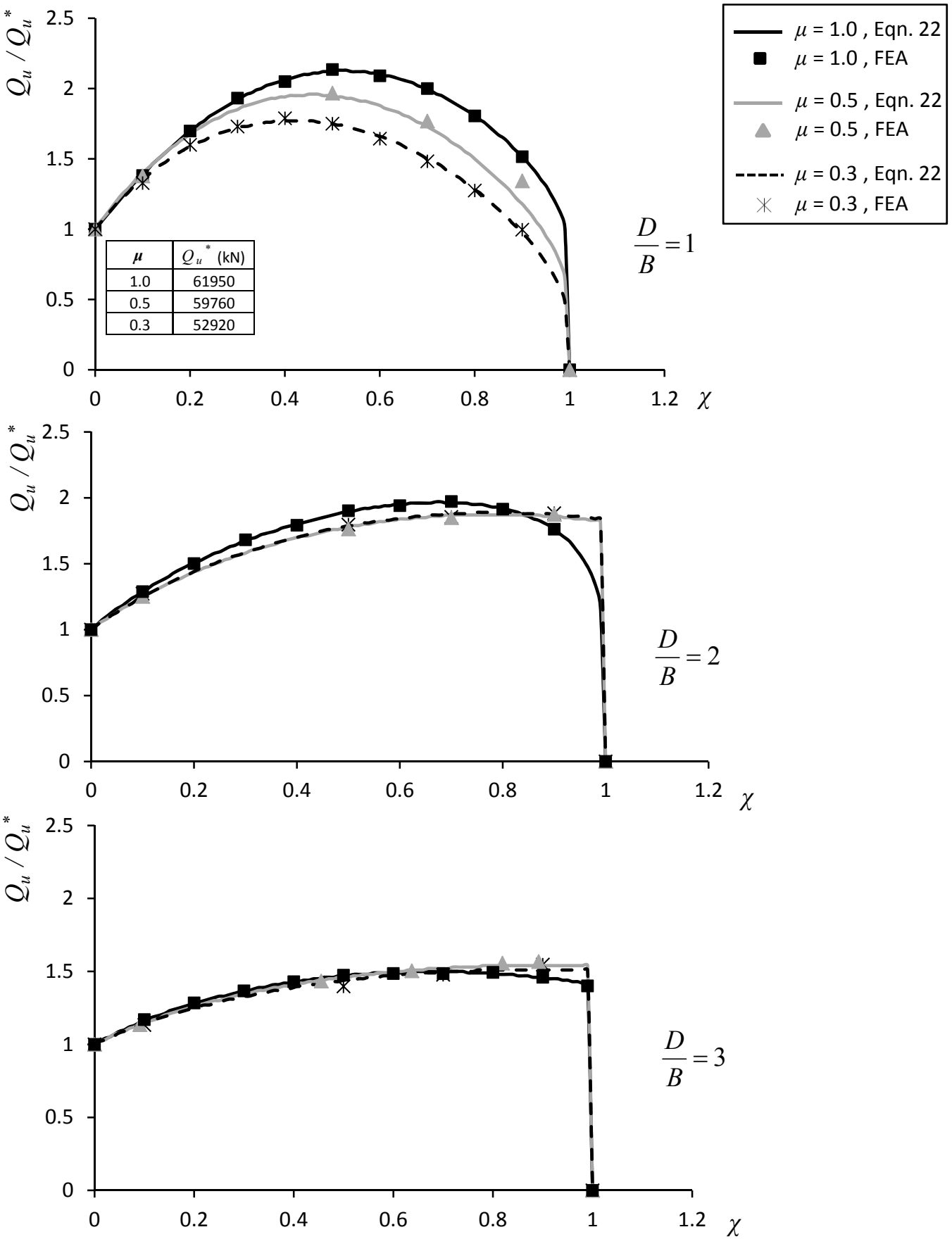

Fig. 2.26. Variation of the pure horizontal load capacity, normalized with the respective one at zero vertical load (Q_u^*), with respect to χ. Comparison is given between the FEA results and the analytical expression for selected values of the interface friction coefficient μ and for D/B = 1,2 and 3.

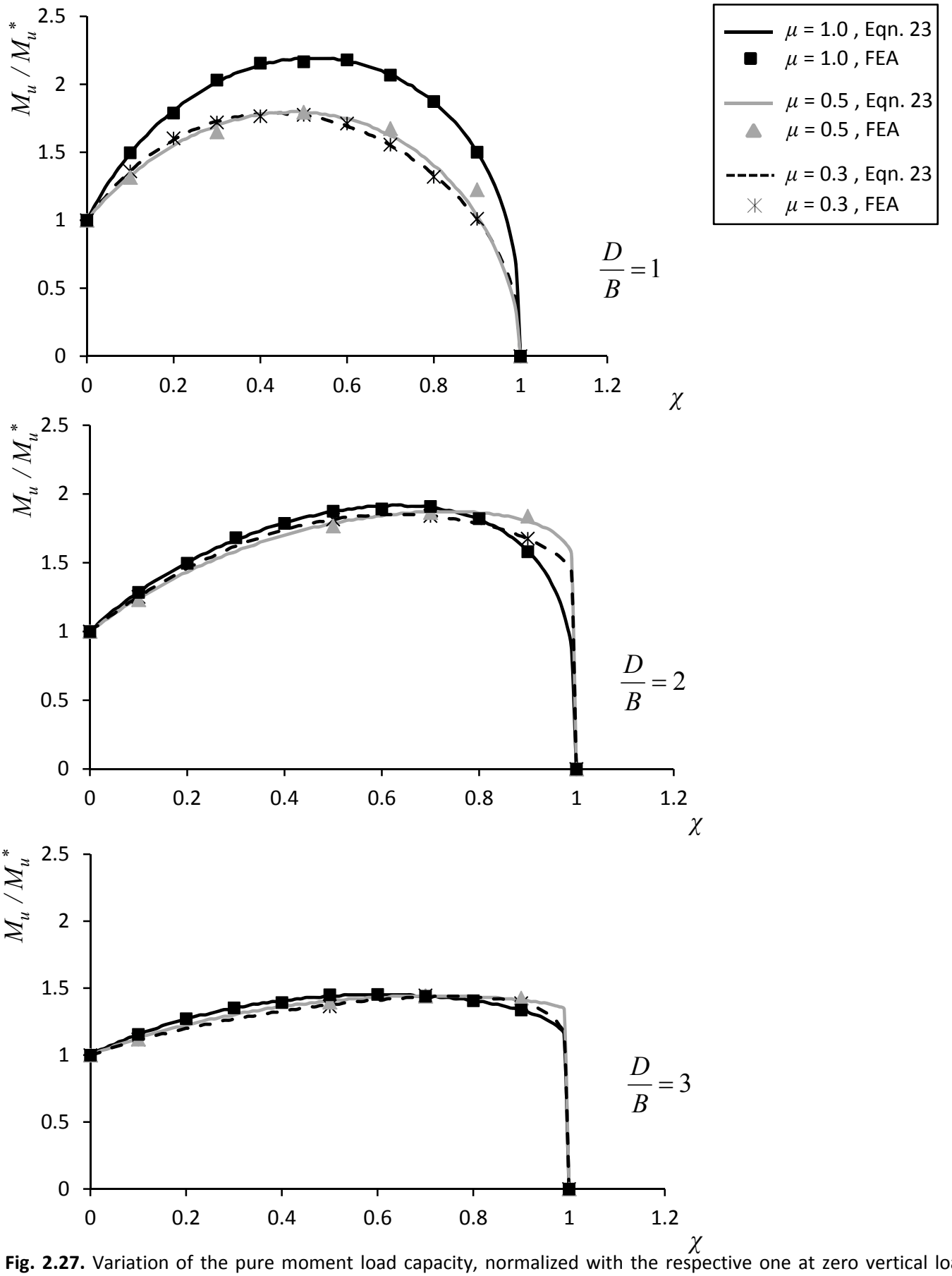

Fig. 2.27. Variation of the pure moment load capacity, normalized with the respective one at zero vertical load (M_u^*), with respect to χ. Comparison is given between the FEA results and the analytical expression for selected values of the interface friction coefficient μ and for D/B = 1,2 and 3.

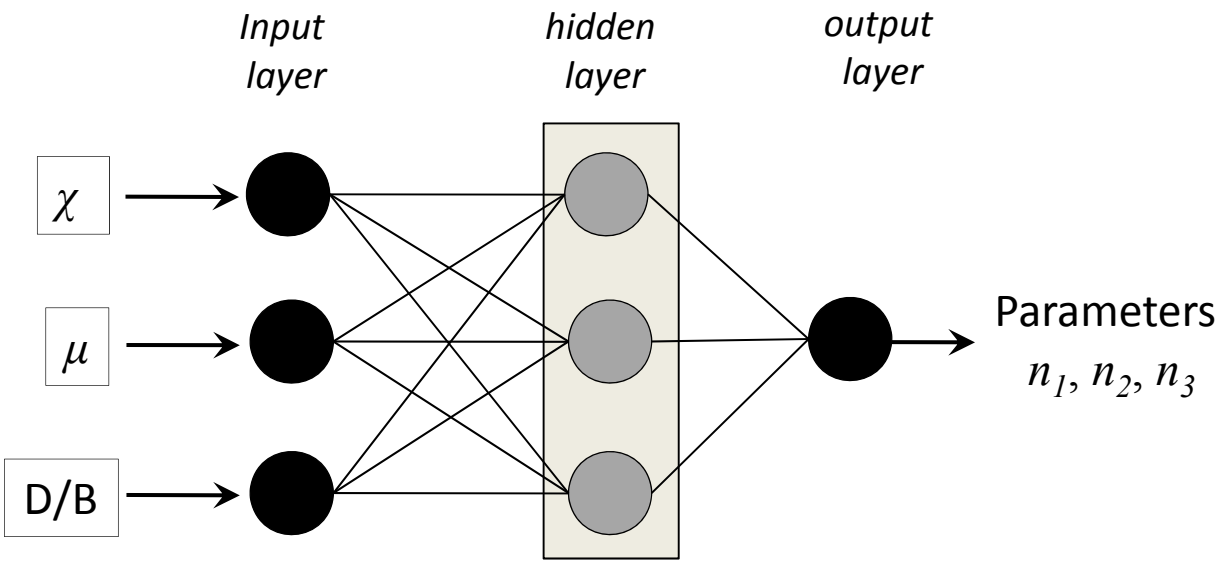

Fig. 2.28. Schematic illustration of the neural network's architecture for establishing a relation between parameters n_1, n_2, n_3 and the three input parameters: (i) the applied vertical load χ, (ii) the interface friction coefficient μ, and (iii) the embedment ratio D/B.

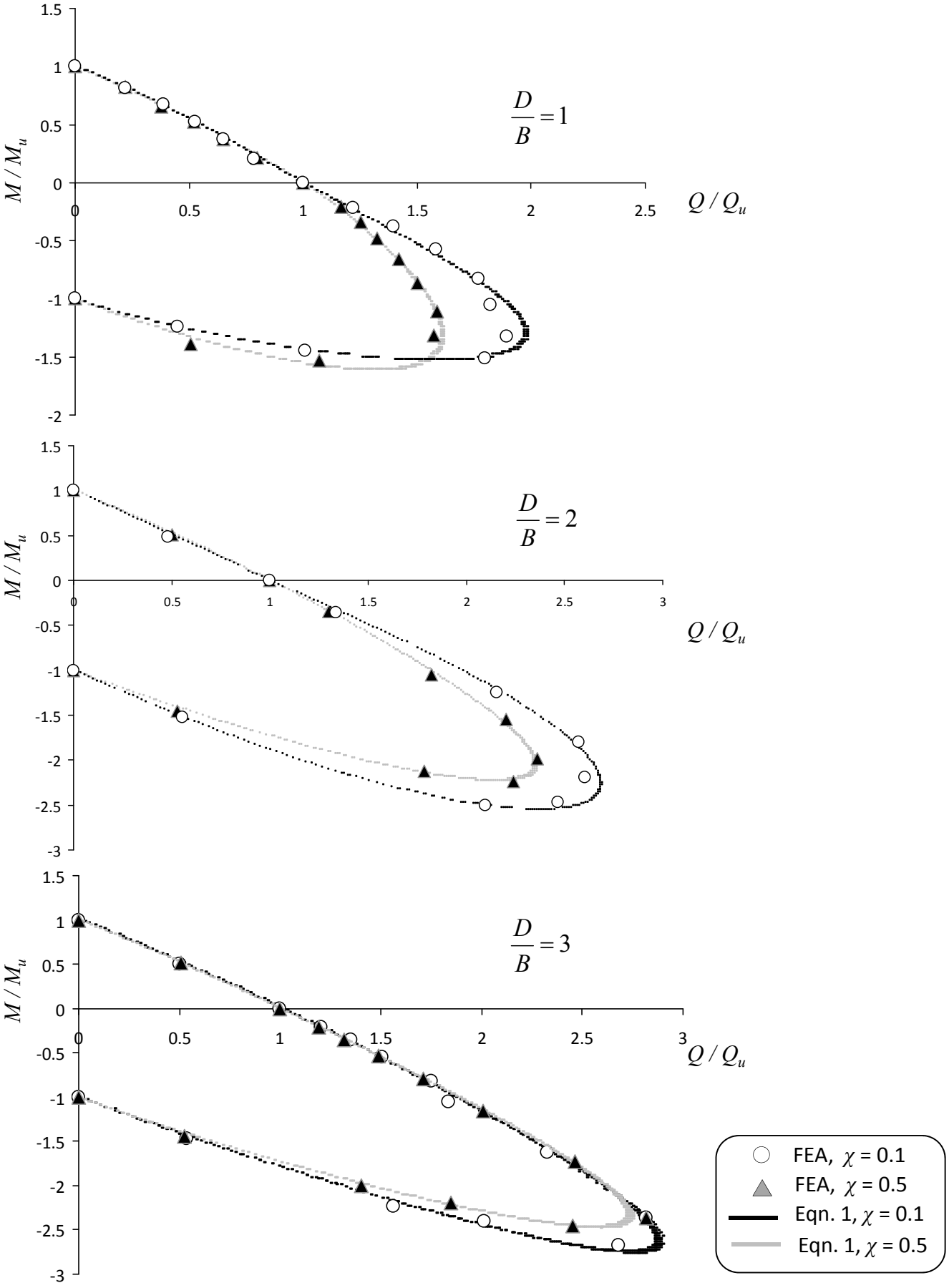

Fig. 2.29. Validation of the proposed analytical expression for the bearing strength surface in normalized quantities. Comparison is given between numerical and analytical results for χ = 0.1 and 0.5, D/B = 1,2 and 3 and μ = 1.

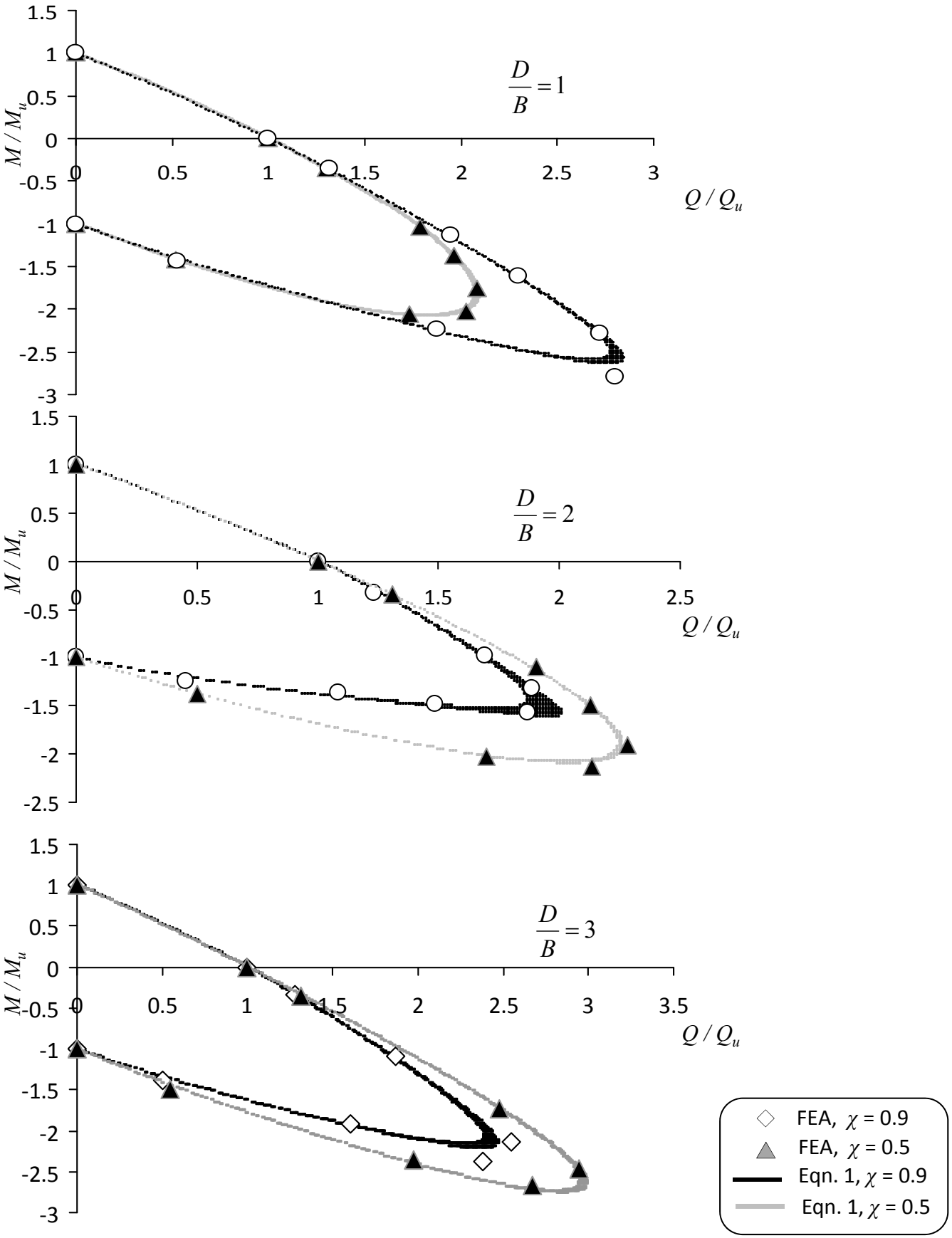

Fig. 2.30. Validation of the proposed analytical expression for the bearing strength surface in normalized quantities. Comparison is given between numerical and analytical results for χ = 0.5 and 0.9, D/B = 1,2 and 3 and μ = 0.3.

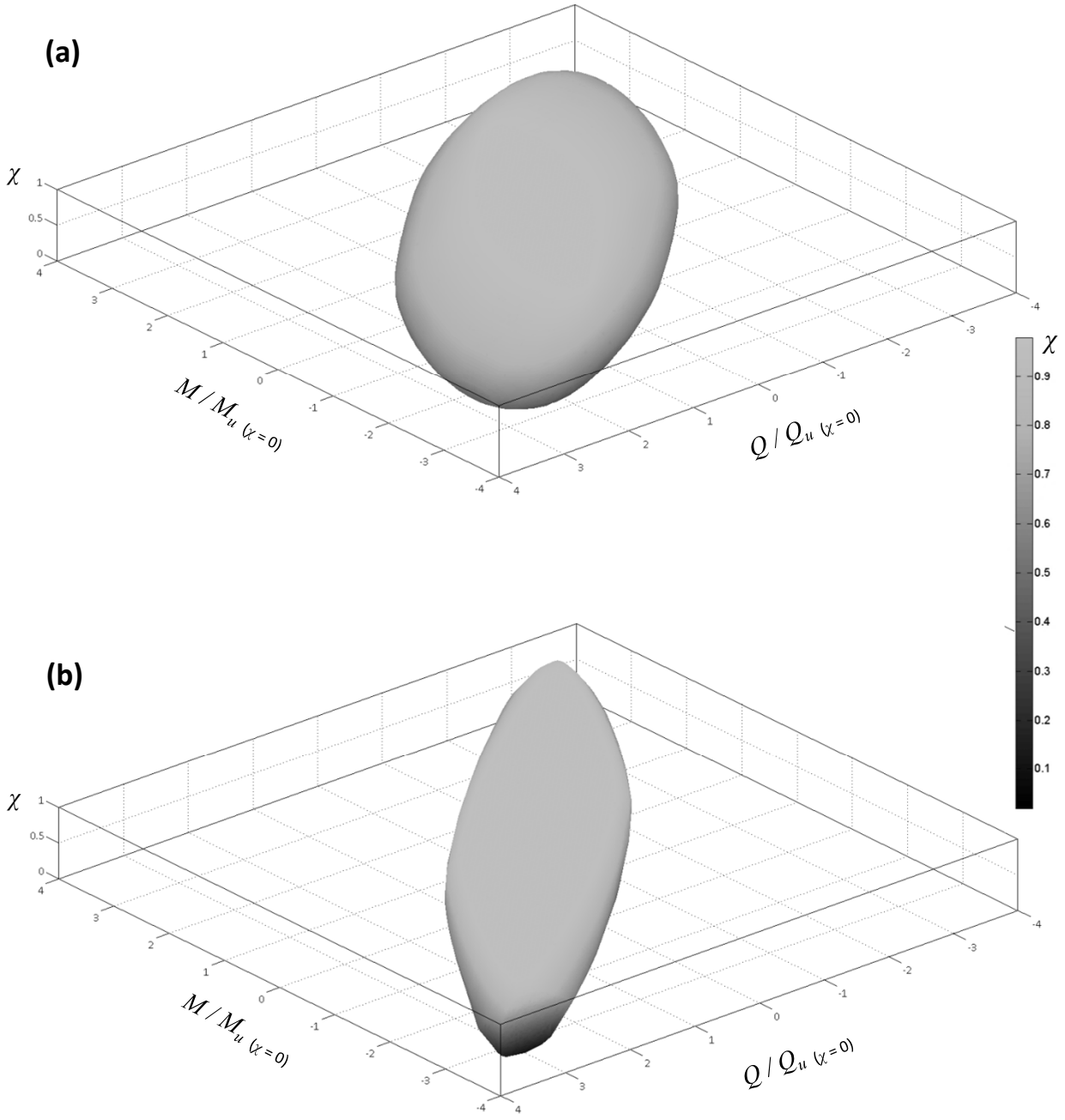

Fig. 2.31 3-D representation of the bearing strength surface in Q-M-N space for caissons in frictional soil for interface friction coefficient μ= 1. The results are normalized by the respective pure (at χ = 0) lateral capacities $M_u{}^*$ and $Q_u{}^*$, for (a) D/B = 1 and (b) D/B = 3.

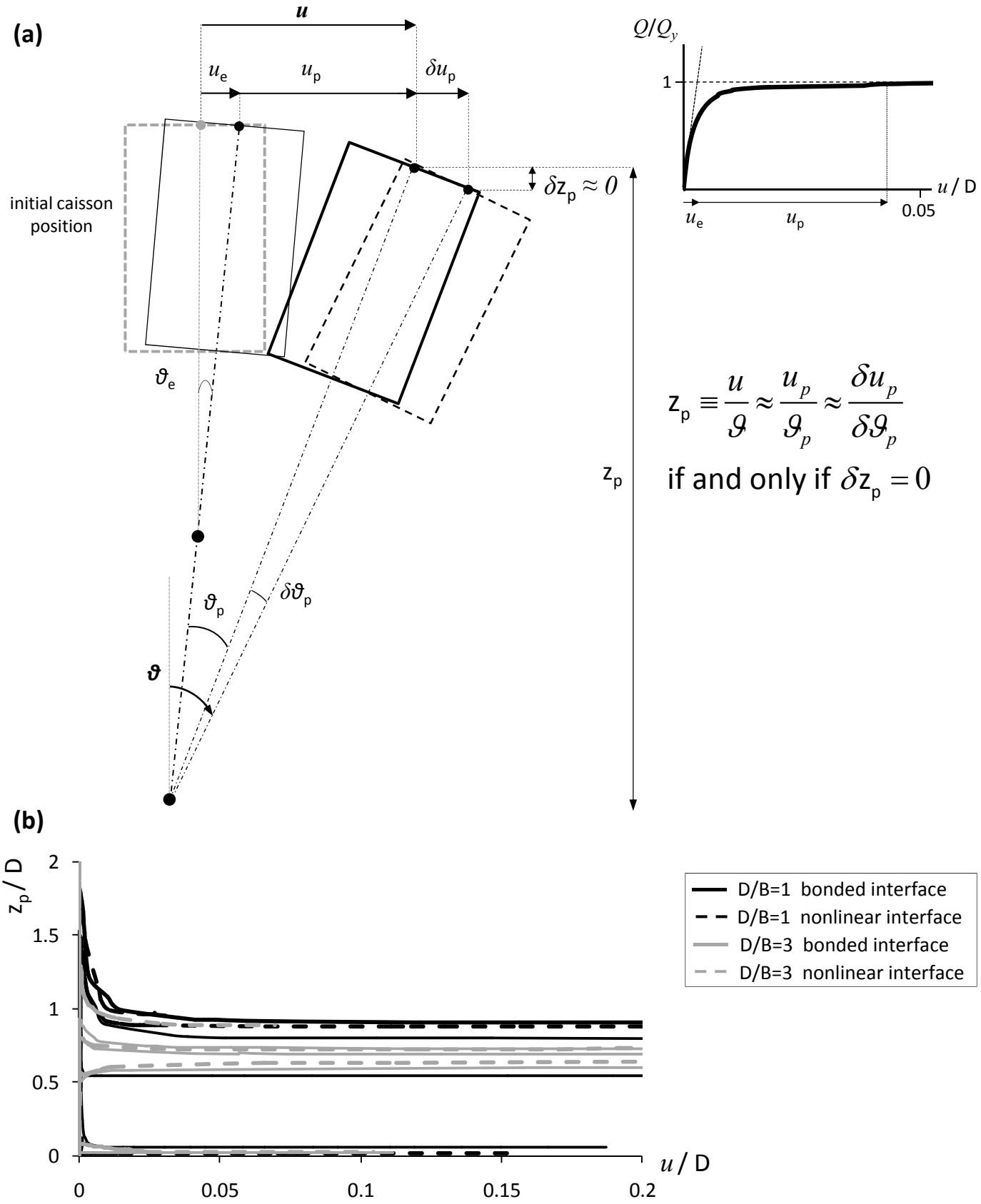

Fig. 2.32 (a) Schematic diagram of the evolution of the depth to rotation pole (z_p) for combined M-Q-N loading. The generic pushover curve at the top-right corner facilitates the interpretation. (b) Variation of the depth to rotation pole z_p (corresponding to the characteristic points of Fig. 6 and Fig. 13) with respect to the horizontal displacement, both normalized with the embedment depth. Results are presented for caissons with D/B =1 and 3 in cohesive soil . Comparison is given between bonded and nonlinear interface (with μ =1) at χ =0.2.

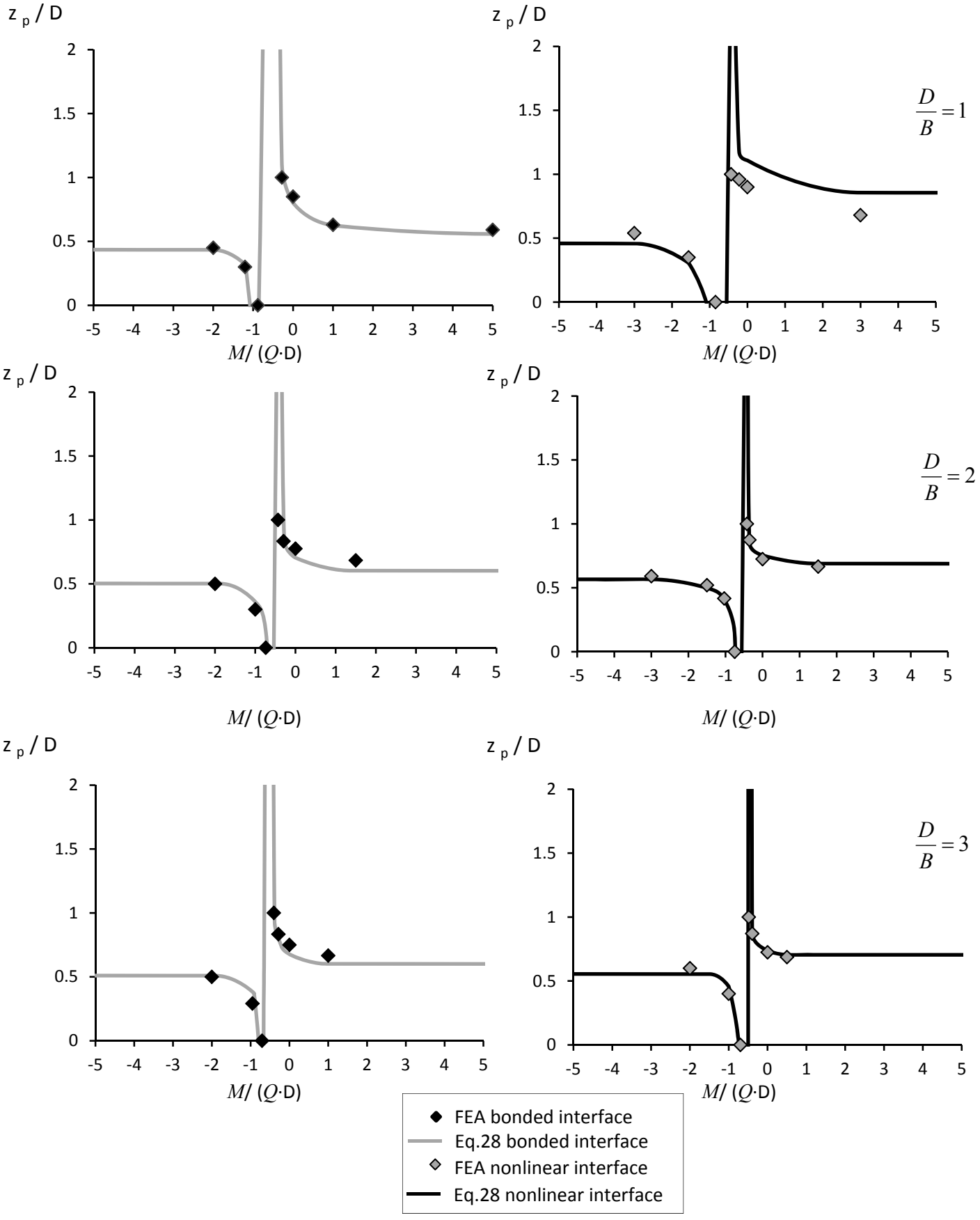

Fig. 2.33. Dimensionless diagrams of the evolution of the depth to rotation pole z_p versus the applied load ratio M/QD, according to Eq. 28 (associated plastic flow rule assumption). Comparison is given with the FE results. *Cases examined*: cohesive soil, D/B=1-3, bonded and nonlinear interface (with μ =1) and χ =0.2.

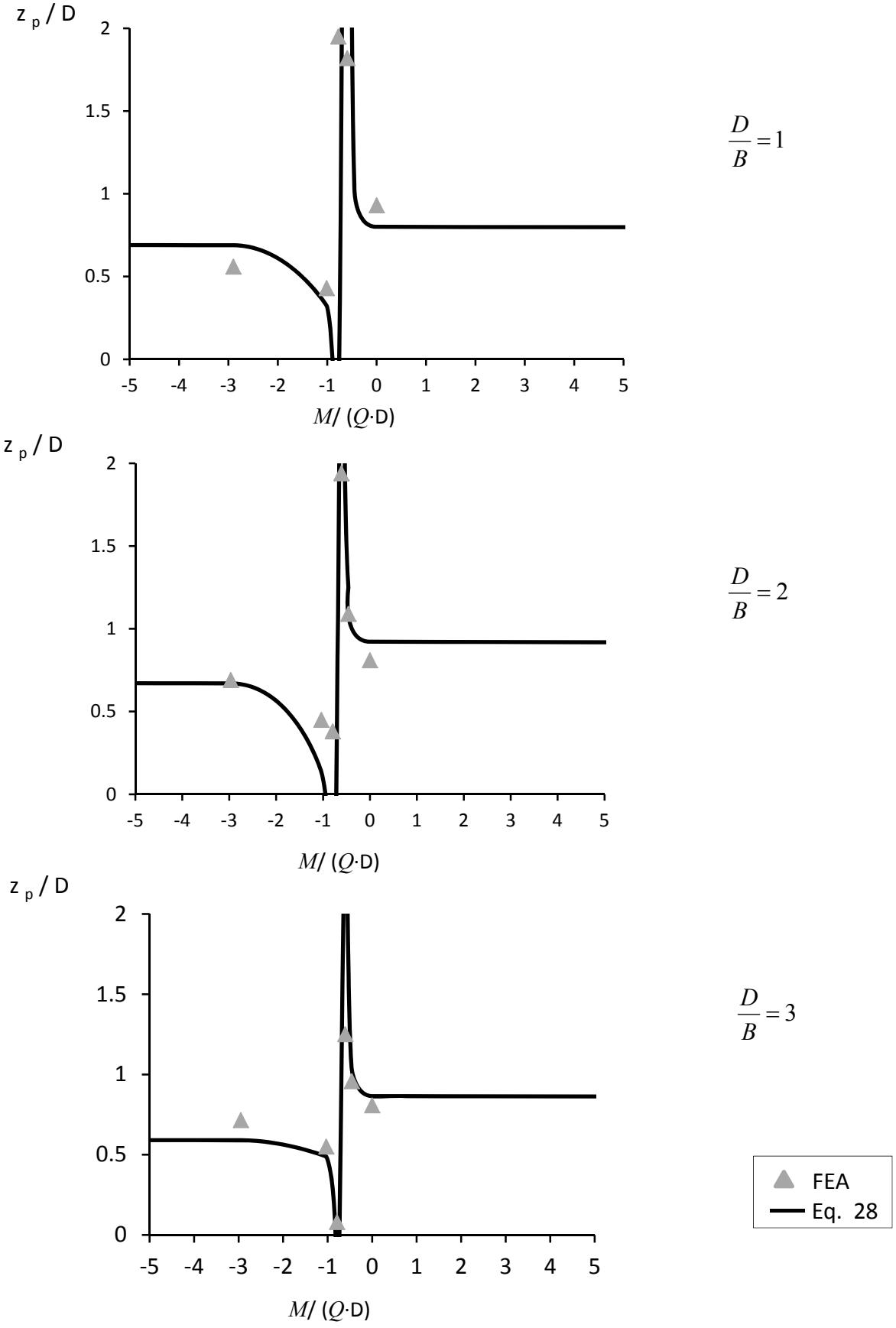

Fig. 2.34. Dimensionless diagrams of the evolution of the depth to rotation pole z_p versus the applied load ratio M/QD, according to Eq. 28 (associated plastic flow rule assumption). Comparison is given with the FE results. *Cases examined*: frictional soil, D/B=1-3, interface friction coefficient μ =0.5 and χ =0.3.

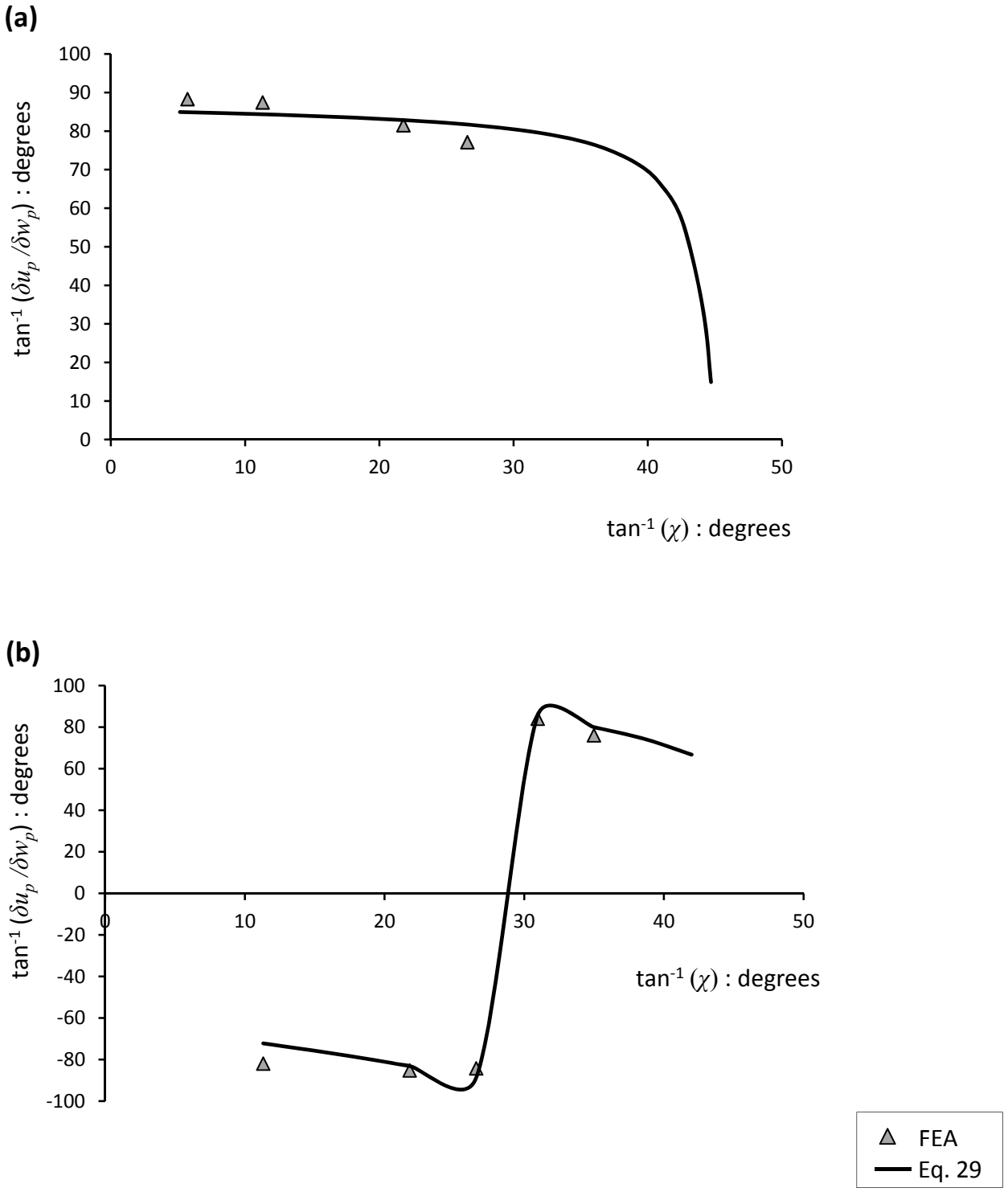

Fig. 2.35. Diagrams of the evolution of the horizontal to vertical plastic displacement increments ratio versus the inverse of the safety factor, assuming associated plastic flow rule (Eq. 29). Comparison is given with the FE results. *Cases examined*: (a) cohesive soil with D/B=1 and fully bonded interface, (b) frictional soil with D/B=1 and interface friction coefficient μ = 1.

Towards a preliminary seismic capacity design of caisson foundations supporting bridge piers

ABSTRACT

The present work investigates, by means of finite element analysis in 3D, the nonlinear response under lateral monotonic and slow-cyclic loading of caisson foundations supporting bridge piers in cohesive soils. The study is performed with respect to the combined moment (M)-horizontal load (Q) on the foundation, and involves similar rigid cubic caissons carrying a column-mass superstructure of varying height (H) and pier-to-deck joint rigidity. The latter is simulated by a rotational spring at the deck level with parametrically varying stiffness, relating to the rigidity of the connection. The lateral load is imposed at the deck level, and the resulting M-Q load path on the caisson is mapped within the bounds of the respective failure envelope. The analysis revealed that due to pier-to-deck joint stiffness and the nonlinear coupling between the rotational and translational degrees of freedom at the foundation, triggering the "*negative effective height*" effect, the loading at the caisson follows a nonlinear path. Most interestingly, the load-path displays certain characteristics, such as a particular "overstrength" in bearing capacity that can be mobilized by the foundation, irrespective of the stiffness properties and constraints

at the superstructure system. Regarding the response under cyclic loading, the M-Q loops are shown to be well enveloped by the monotonic "backbone" curve for all examined cases. Finally, from the numerical results, a closed-form expression for the load-path is formulated, and a methodology to be used towards the preliminary seismic design for caisson foundations is proposed.

3.1. Introduction

The design of critical civil engineering structures (e.g. bridges, offshore platforms) requires the thorough understanding of the mechanics, from the material level to the complex interaction between structural, foundation and soil elements. Admittedly, the contemporary advancements in material science and technology have facilitated the feasibility of major projects. However, the cost-effective design of structures exposed to extreme environmental loading, either of climatic (e.g. wind, waves) or of tectonic (e.g. in earthquake prone areas) origin, requires the role of the nonlinear *soil–foundation–structure interaction* (*SFSI*) on the final performance to be explicitly considered. Thus, for the realistic estimation of maximum and residual displacements of foundation-superstructure systems, which in essence constitutes the core of performance-based design philosophy, all sources of nonlinearities should be taken into account; namely nonlinearities developed above and below ground level. In fact, there is a growing awareness among the geotechnical and structural engineering communities towards incorporating the effects of soil compliance into advanced static and dynamic response analysis techniques. Perhaps surprisingly, the field of performance based design of deep embedded foundations has received little attention (e.g. 1-5).

For caisson foundations, which have been widely used as supports and anchors for major structures (especially bridges) in soft soils, the necessity for considering inelastic foundation response stemmed from recent strong earthquake events (e.g. Kobe 1995), where it was evidenced that their massive dimensions do not guarantee elastic response.

According to the conventionally employed analysis methodologies, the foundation is substituted with a set of linear, or even nonlinear, springs attached at the base of the superstructure. Yet, these springs are usually uncoupled, resulting in most cases in an erroneous foundation response, as will be shown in the sequel. Nowadays, the improvement in computational efficiency would suggest the three-dimensional (3-D) finite elements (FE) as the obvious method for solving complex nonlinear SFSI problems. Still, the success of the FE method lies in a complete geotechnical site investigation and a rigorous constitutive modeling, restricting thus its use in common practice.

To date, the analysis methods that attract increasing attention from geotechnical and structural engineers are based on the strain-hardening plasticity theory. These propose a single *macroelement*, a term first used in geomechanics by Nova and Montrasio [6], to describe the macroscopic soil-foundation response to applied forces and moments. Placed at the base of the superstructure, the macroelement reproduces the nonlinear interaction phenomena of material (soil yielding) and geometric (slippage and gapping at soil-foundation interface) nature. It, essentially, consists of a generalized inelastic stiffness matrix, in which the translational and the rotational degrees of freedom are fully coupled. The behavior of the foundation is thus described in an elegant and comprehensive manner [7]. One of the main components of a macroelement is the representation of the ultimate limit states under combined vertical-horizontal and moment (N-Q-M) loading are by a failure envelope (or bearing strength surface). Analytical expressions for the failure criterion of deeply buried foundations have been proposed by Cassidy *et al.* [8] (skirted caissons in clay), Zhang *et al.* [9] (deeply buried footings in clay), and by the authors ([3], rigid caissons with D/B ≥ 1 in cohesive soil).

3.1.1. Motivation

The motivation of the present study is unveiled by means of an illustrative example. Fig. 1 depicts a bridge pier founded on a caisson foundation. The superstructure (pier, deck) is modeled as a single degree of freedom (SDOF) oscillator. For the design of the foundation, two of the aforementioned methodologies will be (qualitatively)

employed and compared: (i) a set of uncoupled nonlinear springs, and (ii) a rigorous FE model, schematically represented by the coupled elasto-plastic stiffness matrix at the base of the pier. The comparison of the response under lateral loading, which in this case is transferred at the foundation level as a pair of shear force (Q) - overturning moment ($M = QH$), is shown on an indicative bearing strength surface of the caisson, plotted in normalized form with respect to the pure horizontal (Q_u) and moment (M_u) capacities of the foundation (e.g. 10-11).The oblique shape of the strength surface owes to the coupling between the translational and the rotational degrees of freedom. The graph reveals that modeling the foundation with uncoupled springs results in a non-admissible state, outside of the strength surface. Note that in this example the path corresponds to a rotational spring failure (M_u) prior to the respective horizontal one ($Q < Q_u$). In contrast, the "actual" load path tracks the failure envelope with accuracy.

At this point it is noted that when the superstructure is modeled as a SDOF, the load path will always be tracked in the first quadrant (where $MQ > 0$). The shape of the failure envelope, however, reveals that admissible load states lie also in the fourth quadrant ($MQ < 0$), in which, more importantly, the loading combinations result in a bearing capacity of the foundation exceeding Q_u or M_u ("*overstrength*"). We therefore extended the investigation into the nonlinear *SFSI* of systems that mobilize the increased capacity of the foundation.

A caisson foundation supporting a bridge pier is again considered, as shown in Fig. 2. This time, however, a more realistic assumption is adopted. More specifically, it is anticipated that the deck applies certain kinematic constraints on the soil-foundation-pier system, owing to its rotational stiffness. An appropriate way to model these constraints is by attaching a rotational spring at the deck level. When the system is subjected to lateral loading (Q) applied at the deck, the deck, and more specifically the deck-pier joint, will develop a moment reaction to the loading, proportional to its stiffness K_R. Consequently, the moment loading on the foundation may differ significantly from the case where a SDOF is considered ($M = QH$). The graph shows the indicative load paths derived from the prior used

methodologies. The discrepancy in the response is now obvious: although both methodologies are capable of capturing a nonlinear response of the foundation, the assumption of uncoupled springs leads again in a non-admissible state within the first quadrant. In marked contrast, the "real" load path, as calculated form the rigorous FE solution, manifests that the nonlinear coupling between the translational and the rotational degrees of freedom at the foundation mobilize the "overstrength" of the caisson; the load path now terminates near the apex of the failure envelope. The observed response is attributed to the "negative effective height "effect, the meaning of which will be discussed in the following section.

3.1.2. The meaning of "negative effective height"

The response of a bridge-pier subjected to a pseudo-statically imposed seismic horizontal force Q_t at the deck level is analyzed herein. The bridge-pier system comprises a single-column bent of height H, supported by a caisson. Five idealized versions of the actual system are considered with respect to the top (pier-bridge-deck support connection) and bottom (foundation compliance) boundary conditions:

1. A top free to rotate column (appropriate for modeling the lateral response of relatively long-spanned bridges, or when the bridge columns and beams are connected through a hinge) fixed at its base (e.g. foundation in rock).
2. A top free to rotate column on a compliant foundation, represented by a set of coupled linear springs associated with the swaying K_H, rocking K_M and cross-swaying-rocking K_{HM} , K_{MH} motion of the caisson.
3. A beam column fixed at its base, the motion of which is hampered at its top against rotation via a rotational spring K_R representing the pier-to-deck connection rigidity.
4. Similar to model 3 with the difference of a compliant base represented by a set of uncoupled linear swaying K_H and rocking K_M springs.
5. Similar to model 4, but with consideration of a fully-coupled linear stiffness matrix for the foundation compliance.

The goal of the analysis is to calculate the effective height of the bridge-pier-foundation system, determined as the ratio of the overturning moment M_b to the horizontal force Q_b transmitted to the head of the caisson. The response of the bridge-pier, namely the (absolute) displacement and rotation of the pier top (deck) and bottom (caisson head), can be computed from:

$$\begin{Bmatrix} 0 \\ 0 \\ Q_t \\ 0 \end{Bmatrix} = \begin{bmatrix} [K_{bb}] + [K_f] & [K_{bs}] \\ [K_{sb}] & [K_{ss}] + [K_d] \end{bmatrix} \begin{Bmatrix} U_b \\ \theta_b \\ U_s \\ \theta_s \end{Bmatrix} \tag{1}$$

where $[K_{ss}]$, $[K_{sb}]$, $[K_{bs}]$ and $[K_{bb}]$ are the four stiffness sub-matrices corresponding to the superstructure (s) and its base (b). $[K_f]$ and $[K_d]$ are the foundation stiffness matrix and the stiffness matrix representing the pier-to-deck connection rigidity:

$$[K_{bb}] = \frac{EI_c}{H}\begin{bmatrix} \frac{12}{H^2} & \frac{6}{H} \\ \frac{6}{H} & 4 \end{bmatrix}, \qquad [K_{ss}] = \frac{EI_c}{H}\begin{bmatrix} \frac{12}{H^2} & -\frac{6}{H} \\ -\frac{6}{H} & 4 \end{bmatrix}$$

$$[K_{bs}] = \frac{EI_c}{H}\begin{bmatrix} -\frac{12}{H^2} & -\frac{6}{H} \\ -\frac{6}{H} & 2 \end{bmatrix}, \qquad [K_{sb}] = [K_{bs}]^{\mathrm{T}} \tag{2}$$

$$[K_d] = \begin{bmatrix} 0 & 0 \\ 0 & K_R \end{bmatrix}, \qquad [K_f] = \begin{bmatrix} K_H & K_{HM} \\ K_{MH} & K_M \end{bmatrix} \tag{3}$$

The boundary conditions are as follows:

- Model 1: $U_b = \vartheta_b = 0$, $[K_d] = [K_f] = [0]$
- Model 2: $[K_d] = [0]$ ($Q_b = -K_H U_b - K_{HM} \vartheta_b$, $M_b = -K_{MH} U_b - K_M \vartheta_b$)
- Model 3: $U_b = \vartheta_b = 0$, $[K_f] = [0]$
- Model 4: $K_{HM} = K_{HM} = 0$ ($Q_b = -K_H U_b$, $M_b = - K_M \vartheta_b$)
- Model 5: ($Q_b = -K_H U_b - K_{HM} \vartheta_b$, $M_b = -K_{MH} U_b - K_M \vartheta_b$)

After some algebra, the following expressions for the effective height H_{eff} ($= M_b / Q_b$) are obtained:

Models 1 & 2

$$H_{eff} = H \tag{4}$$

Model 3

$$H_{eff} = \frac{H}{2} \frac{2EI_c + K_R H}{EI_c + K_R H} \tag{5}$$

Model 4

$$H_{eff} = \frac{H}{2} \frac{K_M \left(2EI_c + K_R H\right)}{K_R EI_c + K_M EI_c + K_R K_M H} \tag{6}$$

Model 5

$$H_{eff} = \frac{2EI_c K_R K_{HM} - 2EI_c K_{HM}^2 H - K_R K_{HM}^2 H^2 + K_R K_H K_M H^2 + 2EI_c K_H K_M H}{2\left(EI_c K_R K_H - K_R K_{HM}^2 H - EI_c K_{HM}^2 + EI_c K_H K_M + K_R K_H K_M H\right)} \tag{7}$$

In an attempt to demonstrate the physical meaning of the negative effective height, Eqs.4-7 are applied to an actual case study involving a major highway bridge on caisson foundations in soft rock.

The bridge deck was constructed by the cantilever method and is rigidly connected to the piers. The bridge has a total length of 200 m and a central span of 90 m. The tallest of the two supporting piers is about 30 m high with a rectangular hollow cross-section of 5 m x 7.3 m x 0.75 m. The bending rigidity of the pier is EI_c ≈ 1.8 x 10^9 kN m^2 and the stiffness of the rotational spring (accounting for the rotational rigidity of the deck at the connection with the pier) is estimated to K_R ≈ 0.2 x 10^9 kNm/rad, resulting in a K_{ratio} = 0.9 (the definition of K_{ratio} is given in the next section). The foundations are squared reinforced concrete caissons of *B* (width) = *D* (depth of embedment) = 10 m and the shear modulus of rock at very small deformations is

estimated to G_0 = 1 GPa. Assuming homogeneous elastic soil conditions, the stiffness matrix of the foundation with respect to the top of the caisson can be computed by the following expressions [12, 13]:

$$K_H \approx 9.4 G_0 B, \quad K_M \approx 10.8 G_0 B^3, \quad K_{HM} = K_{MH} \approx -6.3 G_0 B^2 \tag{8}$$

Numerical substitution of EI_c, H, K_R and G_0 into Eqs.4-8 results to the plots of Fig. 3, which shows the normalized (with respect to the geometric height H) effective height ratio as a function of the shear modulus ratio G_s / G_0. G_s is an equivalent secant shear modulus accounting for the decrease in foundation stiffnesses due to soil and interface nonlinearities, in an equivalent-linear approximation of the actual non-linear response of the caisson. The following observations are worthy of note:

- The effective height for models 1 and 2 is equal to the geometric height H, irrespective of the caisson compliance.
- The normalized effective height for model 3 is calculated to H_{eff} ≈ 0.62 H implying a nearly inflexible rotational stiffness of the deck. An infinitely rigid deck would result in an effective height ratio of 0.5 (fixed-end beam boundary conditions), while in the case of a very flexible joint (e.g. support on elastomeric bearings) the effective height ratio would be equal to 1 (cantilever beam boundary conditions).
- When the rotational rigidity of the pier-to-deck connection and the foundation compliance are both considered (models 4 and 5), the response at very small deformations (G_s / G_0 ≈ 1--quasi elastic response) is similar to that for fixed-base conditions (model 3) irrespective of the coupling of the foundation degrees of freedom (coupled or uncoupled springs). There is a gradual deviation of the predictions by the two models, however, with increasing soil nonlinearity. Indeed, as the G_s / G_0 ratio decreases, the effective height tends to zero for model 4 while exhibits negative values for model 5 (fully-coupled foundation stiffness matrix) when G_s / G_0 becomes smaller than 0.3 %. The negative values for H_{eff} imply that the overturning

moment and shear force at the head of the caisson are counteractive (of the opposite sign). The conditions in the response that should be satisfied for a bridge pier to exhibit the negative effective height effect, are: (1) negative cross-swaying-rocking stiffnesses (an inherent property of the embedded and deep foundations), and (2) extensive soil yielding and bearing capacity mobilization.

The latter observation will serve as the basis in developing a methodology for the preliminary seismic design of caisson foundations supporting bridge piers. It will be shown in the sequel that a "negative effective height" response could be manifested even for very small values of K_R (e.g. response of a long-spanned bridge in the transverse direction) at the cost, however, of larger displacements.

3.1.3. Scope of work

The above analysis demonstrated that the simplistic approaches, usually employed in practice, and refer to (a) the separation between structural and geotechnical design, and (b) the modeling of foundation elements, cannot reproduce many essential features of the actual foundation behaviour. It is to this end that the present paper is directed. By means of a series of numerical analyses in 3-D, the response of caisson foundations supporting a pier-to-deck system is investigated, with due consideration to nonlinearities developed below (soil, caisson-soil interface) and above ground (pier, deck-pier joint). From the analysis, a closed-form expression for the “actual” monotonic load path, in M-Q space, is developed. It is furthermore shown that the monotonic curve envelopes the load paths derived from slow-cyclic loading with striking precision. Finally, a methodology for the preliminary seismic response evaluation, in capacity terms, of caisson foundations supporting bridge piers is proposed.

3.2. Problem definition and method of analysis

3.2.1. Problem definition

The studied problem is portrayed in Fig. 4. It involves a bridge pier-to-deck system supported by a cubic caisson of side h = 10 m in a 20 m thick 2-layer cohesive soil stratum. The caisson is modeled as a rigid body, with loads and displacements relating to a single load reference point (LRP), as shown in Fig. 2. The sign convention obeys a right-handed axes and clockwise positive convention, as proposed by Butterfield *et al* [14]. Three different pier heights, to represent three different loading conditions with respect to moment loading on the foundation, are used; namely H = 6 m, 17 m and 55 m. The mass of the deck, *m*, is given the value of 2.700 Mg, corresponding to a static factor of safety of $\mathrm{FS}_V = 5$ [4]. The kinematic constraints imposed by the pier-to-deck joint are simulated by a rotational spring attached at the mass level, while the respective axial stiffness was neglected. Although, admittedly, an idealized case, it is considered adequate for representing the deck connection (in the longitudinal direction) to the abutments with elastomeric joints.

3.2.2. Finite element modeling

The problem is analyzed with use of the commercially available finite element code ABAQUS. Both caisson and soil are modeled with 3D 8-noded brick elements, assuming elastic behavior for the former and elasto-plastic for the latter. Fig. 4 shows a half caisson cut through one of the orthogonal planes of symmetry. The size of the finite element mesh is 5B x 5B x 5B carefully weighing the effect of boundaries on the caisson's response and the computational time [4]. Zero-displacement boundary conditions prevent the out of-plane deformation at the vertical sides of the model, while the base is fixed in all three coordinate directions. The caisson is connected to the soil with special contact surfaces, allowing for realistic simulation of the possible detachment and sliding at the soil–caisson interfaces. The mesh for the soil–caisson consists of 12.500 elements. To improve the computational cost without jeopardizing the accuracy of the analysis, the surface-to-surface contact

interaction was modeled by exponential (''softened'') pressure–overclosure relationship through the direct constraint enforcement method that makes use of Lagrange multipliers. For more details on the contact interaction algorithm, the reader may refer to ABAQUS manual [15]. The caisson material is modeled as isotropic linear elastic, with a unit weight of γ = 25 kN/m^3, a Young's modulus of E_c = 3 x 10^8 kPa and a Poisson's ratio of v_c = 0.15.

The pier columns are modeled with 3-D Timoshenko beam elements, with elasticity modulus E_c = 3 x 10^8 kPa and v_c = 0.15. The geometric properties of the piers, namely the cross-sectional areas (A: m^2) and moments of inertia (I: m^4), are given in Table 1. To investigate the effect of per-to deck stiffness on the response of the foundation, the stiffness of the rotational spring, K_R, was appropriately modified so that the stiffness ratio $K_{ratio} = \dfrac{K_R}{\left(\dfrac{4E_cI}{H}\right)}$, where ($4EI_c/H$) is the flexural stiffness of the column, yields the following values: K_{ratio} = 0.1, 0.25, 0.5, 1.0, for every case examined. Moreover, the case of K_{ratio} = 0 (inactive rotational spring) is also provided, for reference.

At the first stage of the analysis, the pier column and the deck (rotational spring) are considered to respond in a linear elastic fashion. The insight into the effect of structural nonlinearity will be given in the ensuing sections.

Table 1. **Geometric properties of the pier columns**

H : m	A : m^2	I : m^4
6	13.85	3.98
17	22.90	15.27
55	40.72	41.74

3.2.3. Constitutive model

Soil behavior is described by an elasto-plastic constitutive model [16], which is a reformulation of that originally developed by Armstrong and Frederick [17]. The model is available in the material library of ABAQUS. It uses the Von Mises failure criterion along with a nonlinear combined kinematic—isotropic hardening law and an associated plastic flow rule.

The clayey soils are saturated responding in undrained fashion with shear strength S_u = 65 kPa at the upper 6 m, S_u = 130 kPa at the lower 14 m and a constant stiffness to strength ratio E_u / S_u = 1.500. The unit weight of the soil materials is taken γ = 20 kN/m^3. To approximate the constant volume response under undrained conditions, a Poisson's ratio of $\nu \approx 0.5$ (= 0.49 to avoid numerical instabilities) was assumed.

The authors in [4] validated the constitutive model employed herein for the nonlinear response of embedded and caisson foundations against field tests of suction caissons in clay [18]. From the validation process, provided for reasons of completeness in Fig. 5, it was deduced that the model is capable of capturing the response observed in the field trials with satisfactory agreement, in both small and large amplitude lateral loading, including the development of caisson-soil interface nonlinearities (gapping).

3.2.4. Method of analysis

At first, a series of finite element (FE) static pushover-type of analyses are carried out to derive the bearing strength surface of the caisson–soil system in M-Q space [3, 19, 20]. Firstly, the soil undergoes geostatic loading and then a part of the soil is replaced by the foundation, on which a vertical load is applied till the specified value of the factor of safety (FS_V = 5) is reached. Afterwards, the vertical load is kept constant and a combination of horizontal force Q and overturning moment M is applied at the head of the caisson until failure. By a series of force-controlled analyses the strength surface is ultimately determined. The surface is presented normalized with respect to the pure moment capacity M_u (with no horizontal loading) and the pure horizontal capacity Q_u (no moment loading) of the foundation.

The analysis yielded the following values for the pure capacities: Q_u = 44 MN, and M_u = 430 MNm. The whole soil-foundation-superstructure system is then subjected to lateral loading at the deck level, monotonically increasing until system failure. The analysis terminates either due to bearing capacity failure of the foundation or due to failure of the superstructure, as will be shown in the sequel. Throughout the analysis, the load path on the foundation is being constantly tracked in M-Q space.

3.3. Results

3.3.1. Monotonic loading: effect of column height and deck stiffness

Figures 6-8 portray the computed load paths at the foundation level with respect to the rotational stiffness ratio (K_{ratio}), for each of the pier heights examined. This section deals with elastic response of the superstructure (pier column and deck). To facilitate the interpretation of the results, the response is also presented in terms of the evolution of the horizontal loading Q (normalized with Q_u) with respect to the horizontal displacement at the foundation level ($u_{caisson}$) and at the deck (u_{deck}). Noticeably, the presence of the rotational spring, in conjunction with the nonlinear response of the foundation, has a distinct effect on the shape of the load paths. Considering moment equilibrium at the pier base (caisson top, the following condition is obtained:

$$M = QH - M_R \tag{9}$$

By dividing each term of the equation with Q, Eq. 1 becomes

$$\frac{M}{Q} = H - \frac{M_R}{Q} \tag{10}$$

Eq.10 thus reveals that the load path in the M-Q space is a function of the pier height (H) and a term (M_R/Q) that depends on both the stiffness of the rotational spring (K_R) as well as the nonlinear stiffness of the foundation. In the case of K_R = 0, Eq.10 yields the height of a cantilever beam, bearing no dependence on the stiffness of the foundation. It thus becomes evident that the mapping of the nonlinear *SFSI* effects (nonlinear load path) in the M-Q space is "triggered" by the rotational rigidity at the deck.

Given that the moment sustained by the deck increases constantly (in proportion to its stiffness, K_R) during the lateral loading, the following can be inferred from the graphs:

- The nonlinear load path on the foundation exhibits an initial increase until a maximum value in the $MQ > 0$ region, after which the path is directed towards the "overstrength" (the moment loading decreases and re-develops in opposite sign, $MQ < 0$). As anticipated, the maximum "positive" moment increases with increasing pier height (higher lever arm), but decreases with increasing K_{ratio} (the stiffer the deck, the more moment loading it sustains).

- The slope of the tangent to the $M/M_u - Q/Q_u$ curve at the origin ("elastic" region) does not correspond to the pier height, H, but to the initial effective height of the pier column ($H_{eff,\,0}$). This, in turn, can be calculated, for each examined case, by the methodology presented in the previous section.

  Quite strikingly, the load paths appear to terminate at a specific area on the failure envelope, irrespective of the stiffness ratio and the pier height. In terms of kinematic mechanisms that accompany failure, that area corresponds to mobilization of an "*inverted pendulum*" mechanism [20], as can be visualized by the contours of plastic strain magnitude (herein corresponding to K_{ratio} = 0.25), shown at the top of each figure. As will be thoroughly discussed in the sequel, in order to facilitate the analytical approach to the problem, we assume that failure occurs at a single point on the failure envelope, with the approximate coordinates $\left\{\frac{\pi}{2}\left(\frac{Q}{Q_u}\right), -\frac{2}{3}\left(\frac{M}{M_u}\right)\right\}$.

Yet, as revealed from the evolution of the horizontal displacement $u_{caisson}$ with respect to the lateral loading Q, each load path tracks the failure envelope at a different point. The shorter piers carrying a rotationally stiff deck ($K_{ratio} \rightarrow 1$) exhibit a quasi elasto-plastic Q-u response. This is congruent with the respective load paths, which can be tracked within the failure envelope (elastic response) until the bearing capacity load is reached. Note, however, that (a) as the deck becomes more

rotationally flexible (K_{ratio} → 0.10), and (b) as the pier height increases (large initial moment loading on the foundation), the loading paths reach the failure envelope at an earlier point, and then follow it asymptotically until the termination point. In the respective Q-u graphs, this behaviour is manifested from the quasi tri-linear shape of the plots; the first yielding point corresponds to the point where the load path first reaches the failure envelope.

The discrepancy in the loading paths with respect to the pier height is further demonstrated by the snapshots of plastic strain magnitude at failure; even though eventually all load paths mobilize an "*inverted pendulum*" failure mechanism, the taller pier (H = 55 m) exerted overall greater moment loading on the foundation, as compared to the respective one exerted from the shorter (H = 6 m) pier. As a result, a "*scoop*" mechanism is formed underneath the caisson in the former case, in contrast with the intense shearing, observed at the base of the caissons supporting the shorter piers.

Regarding the horizontal displacements at the deck level, they follow closely the respective ones computed at the top of the caisson, when short piers carrying rotationally stiffer decks are considered. However, it is evident that with an increase in the pier height and a decrease in the deck's rotational stiffness, the deck displacements exceed the respective caisson ones even by a factor of 2.

3.3.2. Accounting for structural nonlinearity

At this section, the numerical investigation is directed towards the effect of the nonlinear response of the superstructure on the load path at the foundation level. The presentation of the methodology and the results precedes a graphical illustration (Fig. 9a) that serves to elucidate the contribution of each of the load-carrying mechanisms within the foundation-superstructure system. Yet, the emphasis is again given to the response of the foundation.

The caisson and the pier base are subjected to moment loading that is represented by the load path. The moment that develops at the pier- deck joint (M_R), however, is given by the vertical distance between the load path and the (extended) line

corresponding to the respective (for that specific pier height) cantilever beam (K_R = 0). It should be noted that Fig. 9a portrays and ideal case, in which the pier and the deck respond elastically, and they are therefore capable of carrying substantial loading.

A more realistic, though simplified, nonlinear response is now introduced for the superstructure, by means of a bi-linear moment-rotation law for the deck and a bi-linear moment-curvature law for the pier, as shown in Fig. 9b. The analysis aims at gaining insight into the effects of the interplay between the nonlinearities, developed above and below ground level, on the load path at the foundation. Hence, the values of the bi-linear laws are deliberately pre-defined, so that structural failure precedes bearing capacity failure of the foundation.

To begin with, we consider a nonlinear rotational spring attached to the top of an elastic pier column. Three characteristic cases are examined, the properties of which, along with the predefined values of the bilinear moment-rotation model for the spring, are given in Table 2.

Table 2. **Predefined bilinear moment-rotation values for the rotational spring**

H : m	M_R : MNm	K_{ratio}	θ_1 : rad	θ_2 : rad
6	198	0.25	0.00264	1
17	276	0.40	0.002307	1
55	1070	1.0	0.003568	1

The results are shown in Fig. 10. For reference, each characteristic response is accompanied with the respective ones considering (a) cantilever beam (K_R = 0), and (b) a linear rotational spring. Moreover, the evolution of the normalized moment loading on the foundation (solid black line) and on the deck (solid grey line) with respect to the caisson rotation, are given alongside. For clarity reasons, the negative (in sign) moment developed at the rotational spring is plotted in absolute values.

The computed response can be interpreted as follows: as long as the spring is loaded within its elastic regime, the loading on the foundation follows the respective nonlinear path (dashed line). However, when the moment capacity of the spring (M_R) is reached, denoting the formation of a plastic hinge, the spring cannot sustain any further increase in moment loading. The additional moment is now imposed onto the foundation as positive (in sign) loading, and the system exhibits the response of a caisson carrying a cantilever beam; the load path is tracked parallel to the respective one of a cantilever with height H, and continues until bearing capacity failure of the foundation occurs.

However, caution should be exercised during the design of such systems, since spring failure corresponds to a pier-to-deck joint failure. Hence, appropriate provisions should be adopted, mainly to accommodate for large displacements at the deck level.

The response is now examined accounting for nonlinearity in both structural, elements, namely the pier and the deck. Two characteristic cases are considered: a pier height of H = 55 m, kinematically restrained at the deck level by a rotational spring that yields a stiffness ratio of (a) K_{ratio} = 0.40, and (b) K_{ratio} = 1.0. The values for the bi-linear models (as schematically shown in Fig. 9b) are given in Table 3. It is noted at this point, that given that the determination of shear strength and especially of shear deformation characteristics of (e.g. reinforced concrete) structures are still controversial issues [21], the interplay between shear and flexure in the inelastic regime is not taken into account, and the controlled mode of failure of the piers is assumed to be flexure-dominated.

Table 3. **Predefined bilinear moment-curvature and moment-rotation values for the pier column and rotational spring, respectively**

H : m	M_P : MNm	κ_1 : rad/m	κ_2 : rad/m	M_R : MNm	K_{ratio}	θ_1 : rad	θ_2 : rad
55	215	0.0000544	0.0000550	107	0.40	0.00089	1
55	195	0.0000493	0.0000510	85	1.0	0.000283	1

The results, provided in Fig. 11, highlight that contrary to the "ductile" progressive failure of the superstructure-foundation system observed following the yielding of the deck, column yielding leads in an abrupt system failure. This "brittle-type" system response is further illustrated from the graphs of the normalized moment loading at the pier base (solid black line) and on the deck (solid grey line) with respect to the caisson rotation, which are plotted alongside the load paths.

In summary of the above, Fig. 12 schematically represents the nonlinear SFSI effects, and identifies the possible failure modes of the system; point A signifies pier column failure; point B corresponds to yielding at the pier-to-deck joint, followed by a ductile foundation response; point C indicates bearing capacity failure of the foundation.

3.3.3. Analytical description of the load path

Based on the analysis presented in the preceding sections, an analytical representation of the load path in M-Q space is attempted. Hence, a generalized expression of the following form is considered:

$$\frac{M}{M_u} = \gamma \left[(1+\alpha) \left(1 - e^{-\beta \frac{Q}{Q_u}} \right) - \alpha \frac{Q}{Q_u} \right] \tag{11}$$

where the coefficients α, β and γ control the shape of the load path, and depend on: the properties of the pier (H, I), the rotational stiffness of the spring (K_R), and the pure uniaxial capacities of the foundation (Q_u, M_u), which incorporate the effects of soil conditions and foundation's geometry. The determination of the three unknown coefficients requires the consideration of appropriate conditions. These conditions were identified from Fig 13a, where the collection of the load paths for all examined cases is plotted, and detailed in Fig 13b. More specifically:

1. Point $\boldsymbol{C}$, is the point on the failure envelope of caisson foundations with D/B = 1 with approximate coordinates $\left\{ \frac{\pi}{2}\left(\frac{Q}{Q_u} \right), -\frac{2}{3}\left(\frac{M}{M_u} \right) \right\}$, on which the load paths terminate. Substituting the coordinates into Eq. 11, gives the equation for the first condition:

$$-\frac{2}{3}=\gamma\left[\left(1+\alpha\right)\left(1-e^{-\beta\frac{\pi}{2}}\right)-\alpha\frac{\pi}{2}\right] \tag{12}$$

2. Point ***A***, that corresponds to the slope of the tangent to the load path at the initial stages of loading. The tangent represents the load path when considering a cantilever beam of initial effective height $H_{eff,\,0}$. Given that $M=H_{eff,0}Q$, the equation of the tangent in the normalized M/M_u–Q/Q_u space can be rewritten as:

$$\frac{M}{M_u}=\left(H_{eff,0}\frac{Q_u}{M_u}\right)\frac{Q}{Q_u} \tag{13}$$

where $H_{eff,0}\dfrac{Q_u}{M_u}$ is the respective slope. By differentiating Eq.11 with respect to Q/Q_u, one obtains:

$$\frac{\partial\left(\dfrac{M}{M_u}\right)}{\partial\left(\dfrac{Q}{Q_u}\right)}=\gamma\left[\left(1+\alpha\right)\left(1+\beta e^{-\beta\frac{Q}{Q_u}}\right)-\alpha\right] \tag{14}$$

At the region of initial lateral loading, where $Q/Q_u \rightarrow 0$, the slope of the tangent can be substituted into Eq.14, resulting in the following condition:

$$H_{eff,0}\frac{Q_u}{M_u}=\gamma\left[\left(1+\alpha\right)\left(1+\beta\right)-\alpha\right] \tag{15}$$

3. Point ***B***, which marks the maximum positive (in sign) value of M/M_u, with coordinates $\left\{\dfrac{Q_r}{Q_u},\dfrac{M_r}{M_u}\right\}$. Furthermore, point ***B*** is also the point of intersection between (a) the nonlinear load path, and (b) the (dashed) line that connects the point where the linear load path of the respective cantilever (K_R = 0) meets the failure envelope $\left\{\dfrac{Q_f}{Q_u},\dfrac{M_f}{M_u}\right\}$, and the abscissa at $\left\{0.5\left(\dfrac{Q}{Q_u}\right),0\right\}$. Hence, and after some algebra that is detailed in the Appendix, the following expression for the third condition is derived:

$$\frac{1}{\beta} ln\left(\frac{\beta(1+\alpha)}{\alpha}\right)\left(\frac{-2HQ_u}{HQ_u - M_u} - \alpha\gamma\right) - \left(\gamma + \alpha\gamma\right)\left(\frac{\alpha}{\beta(1+\alpha)} + 1\right) = \frac{HQ_u}{HQ_u - M_u} \quad (16)$$

Eqs.12, 15, 16 constitute the system of nonlinear algebraic equations, the solution of which yields the parameters α, β and γ, and thus the equation for the load path. It is important to note that the generalized form of the load path (Eqs.11), as well as the resulting equation system, can be applied as a general design scheme for caisson foundations supporting bridge piers in cohesive soils.

The numerical (solid lines) and the analytically derived (dashed lines) results regarding the load path are plotted in Fig.14, for all cases examined in this paper. As evident from the graphs, the results from the proposed methodology fit the finite element results rather satisfactorily.

3.3.4. Response under cyclic loading: characteristic results

The investigation of the response of the caisson-superstructure systems under cyclic loading serves as a preliminary evaluation of the possible effects of seismic loading. Slow cyclic results are thus shown for four representative cases: pier height H = 6 m and 17 m, with pier- deck rotational stiffness ratio K_{ratio} = 0.10 and 0.40. Since the emphasis is given on the response of the foundation, the pier-to-deck systems were modeled as linear elastic. The lateral load imposed at the deck level increased gradually until the bearing capacity of the foundation-superstructure systems was almost reached; however, collapse was prevented. The loops in M-Q space, together with the corresponding settlement-rotation (w-ϑ) loops, are shown in Figs. 15-16.

It is rather interesting to observe the remarkable agreement with which the monotonic path envelopes the cyclic loops, in all examined cases. The following are worthy of note:

- When shorter piers and decks imposing increased rotationally rigidity are considered, the M-Q loops at the foundation follow a smooth path. However, for taller piers carrying more rotationally flexible decks, thus resulting in greater moment loading on the foundation, the loops are wider, more

irregular, and the residual settlements are substantial. Yet, small residual rotations were observed at the end of the loading for all examined systems; a clear indication of the restoring role of the significant dimensions and weight of the caisson.

- Admittedly, the M-Q loops are not a typical representation of the response under cyclic loading, such as the M-ϑ hysteresis loops. Nevertheless, from the loops, the development of phenomena associated with strong inelastic response of the foundation (e.g. gapping) can also be identified. More specifically, their pinched shape denotes that the plastic deformations, which develop in the resisting part of the soil during the loading at one direction, form an irrecoverable gap, as the direction of loading changes. Consequently, when re-loading occurs, the passive-type soil resistance can only be mobilized after the closing of the gap. In the case of caissons supporting SDOF cantilever beams, the result is an overall reduction in the capacity of the foundation, in-between the large loading amplitudes. Yet, the presence of the rotational spring at the deck level offers "overstrength" to the system, by redistributing the moment loading between the deck and the foundation. Perhaps expectedly, clear evidence for the detachment of the caisson from the surrounding soil is manifested only during the strongly nonlinear response of the foundation supporting the tall H = 17 m pier with K_{ratio} = 0.10, in which the loops exhibit flattened shape at certain parts.

3.4. Practical aspects and implications for design

The results of the study highlighted important aspects of the lateral response of caisson foundations supporting bridge pier-to-deck systems, when the complex interplay between nonlinearities developed below and above ground level are accounted for. It was shown that in the case of a deck imposing constraints in rotation at the top of a pier, the combined base shear-moment loading that is transferred at the foundation follows a nonlinear path in M-Q space. Most

importantly, it was found that when the superstructure is given sufficient strength, the caisson foundation exhibits a particular "overstrength" in both moment and horizontal load capacities, irrespective of the stiffness properties of the pier-to-deck system. Given that actual design involves finite strength of the structural elements, this finding has serious implications for the cost-effective seismic design of caisson foundations. The objective of this section is therefore to present a methodology which incorporates the findings of this study, so that it can be utilized as a preliminary seismic capacity design of caisson foundations.

The methodology, which is presented by means of a flowchart in Fig. 17, is developed for the typical scenario met in practice, where the task is to design a caisson foundation for a given pier-to-deck superstructure and a specific seismic design load. To facilitate the understanding, Fig 9a should be studied alongside. Taking into account that according to the modern bridge code requirements [22, 23]: (a) the moment capacity of the pier base is greater or equal (e.g. in steel columns) than the respective capacity of the top of the pier, and (b) pier-to-deck failure should be avoided, and any development of plastic hinge is directed to the top of the pier, it becomes obvious that the critical component in the superstore system is the top of the pier. However, as clearly shown in Fig 9a, the pier top is subjected to substantial moment loading, M_R, as compared to the pier base, M. Regarding the caisson foundation, an optimum design in terms of cost-effectiveness would take advantage of the "overstrength" that can be mobilized, in order to reduce the caisson's dimensions, and thus its cost. The foundation is therefore designed so that its "overstrength" corresponds to the bearing capacity under:

(i) A horizontal load $Q = S_a mg$, where S_a is the design spectral acceleration.

(ii) A moment load M load that is determined by the moment capacity at the pier top (from structural properties). For caissons with D/B = 1, simple geometry based on Fig 9a yields:

$$M = \left(H \frac{Q_u}{M_u} + \frac{2}{3} \right) M_u \ .$$

From (i) and (ii) the pure capacities (Q_u, M_u) are calculated, and hence the dimensions of the caisson can be determined.

At this point, the particularly significant condition regarding the static safety factor ($FS_V \geq 2$) should be checked. If the condition is satisfied, the preliminary design ends. If, on the other hand, the condition is not met, the dimensions of the foundation should increase accordingly. Yet, an increase in the dimensions results in an increase in Q_u and M_u, respectively. In terms of the normalized failure envelope, this can be visualized by the ordinate, M_R, moving towards the left ($Q < \frac{\pi}{2} Q_u$). In this case, however, the loading state could even reach the first quadrant ($Q < Q_u$), where it is possible that the moment loading at the pier base is greater than that at its top ($M > M_R$). Thus, the respective capacity should also be checked against M. In order to estimate the exact moment load that is transferred at the pier base, the failure envelope and the nonlinear load path must be drawn. The former can be based on already published works (e.g. [3]), while the latter on Eq.11, given the properties of the foundation-superstructure system.

In summary of the above, a capacity-based approach is proposed, involving a trial-and-error optimization procedure. Consideration of the expected performance of the foundation (e.g. developed displacements) belongs to a later design stage (performance-based design).

3.5. Conclusions

The aim of the present study was to qualitatively and quantitatively express the nonlinear *SFSI* effects in the case of rigid caisson foundations supporting bridge piers subjected to lateral loading. A series of finite element analysis in 3D was therefore employed to assess the performance, with respect to the combined M-Q loading at the foundation, of similar rigid cubic caissons carrying a column-mass superstructure. The pier height (H) and the pier-to-deck joint rigidity (K_R) varied parametrically, with the latter being modeled by a rotational spring at the deck level. The stiffness of the

spring was taken as a ratio of the flexural stiffness of the pier. In total, three pier heights, H = 6 m, 17 m and 55 m, and four stiffness ratios (K_{ratio} = 0.1, 0.25, 0.5, 1.0), ranging from flexible to rigid, were considered. The foundation-superstructure systems were then subjected to lateral monotonic and slow-cyclic loading at the deck level.

Throughout the loading, the resulting M-Q load paths at the caisson were constantly monitored and plotted on the normalized of M/M_u-Q/Q_u space, along with the failure envelope of the foundation. To evaluate the effects of the interplay between foundation and structural nonlinearities on the load path, the latter was also introduced, by means of bi-linear moment-rotation and moment-curvature laws for the spring and the pier, respectively.

The main conclusions of the study can be summarized as follows:

- It was highlighted that contrary to conventional design, in which uncoupled springs are used to model the foundation elements, accurate prediction of the foundation response can be achieved only if the nonlinear coupling between the horizontal and the rotational degrees of freedom is accounted for.

- Due to the pier-to-deck joint stiffness and the nonlinear coupling between the rotational and translational degrees of freedom at the foundation, that trigger the "*negative effective height*" effect, the loading at the caisson follows a nonlinear path in M-Q space. This load-path was found to display certain characteristics, such as a particular "overstrength" in bearing capacity that can be mobilized by the foundation, irrespective of the stiffness properties and constraints at the superstructure system. From the analysis results, a closed-form expression for the load path was formulated and validated in all examined cases.

- The load paths under slow-cyclic pushover loading track the respective monotonic path with striking agreement, justifying thus the use of the latter as a "backbone" curve for seismic analysis.

Based on the results, the paper developed and proposed a methodology to be used towards the preliminary seismic capacity design of caisson foundations, accounting for nonlinearities at the foundation and the pier-to-deck superstructure system.

3.6. APPENDIX

Determination of the condition regarding point *B* in Fig 12b

At point ***B***, the load path exhibits a maximum value and the slope of the tangent equals zero. Therefore, Eq.14 yields:

$$0 = \gamma \left[(1+\alpha) \left(1 + \beta e^{-\beta \frac{Q_r}{Q_u}} \right) - \alpha \right] \quad \text{(i)}$$

from which the following Q_r/Q_u coordinates are obtained:

$$\frac{Q_r}{Q_u} = \frac{ln\,\beta + ln(1+\alpha) - ln\,\alpha}{\beta} \quad \text{(ii)}$$

To extract the equation of the straight line that intersects with the nonlinear load path at its maximum, $\left\{ \frac{Q_r}{Q_u}, \frac{M_r}{M_u} \right\}$, the coordinates $\left\{ \frac{Q_f}{Q_u}, \frac{M_f}{M_u} \right\}$ should first be determined. These are the coordinates of the intersection between the failure envelope and the load path of the respective cantilever (K_R = 0), which is given by Eq.13. Regarding the expression for the failure envelope at the first quadrant (MQ > 0), it can be approximated by a straight line with the form:

$$\frac{M}{M_u} = 1 - \frac{Q}{Q_u} \quad \text{(iii)}$$

From the system of Eq.13 and Eq.(iii), the following coordinates for their intersection are derived:

$$\frac{Q_f}{Q_u} = \frac{M_u}{M_u + HQ_u} \tag{iv}$$

$$\frac{M_f}{M_u} = \frac{HQ_u}{M_u + HQ_u} \tag{v}$$

Hence, the expression for the (dashed) line, that intersects the nonlinear load path at point ***B***, is obtained, as:

$$\frac{M}{M_u} = \frac{-2HQ_u}{HQ_u - M_u}\left(\frac{Q}{Q_u}\right) + \frac{HQ_u}{M_u + HQ_u} \tag{vi}$$

Since point ***B***, with coordinates $\left\{\frac{Q_r}{Q_u}, \frac{M_r}{M_u}\right\}$, marks the intersection of the lines expressed by Eq.11 and Eq.(vi), the solution of the respective system yields:

$$\frac{Q_r}{Q_u}\left(\frac{-2HQ_u}{HQ_u - M_u} - \alpha\gamma\right) + e^{-\beta\frac{Q_r}{Q_u}}\left(-\gamma - \alpha\gamma\right) = \gamma + \alpha\gamma + \frac{HQ_u}{HQ_u - M_u} \tag{vii}$$

Substituting Eq.(ii) into Eq.(vii), yields Eq.16.

References

[1] Hutchinson TC, Chai YH, Boulanger RW, Idriss IM. Inelastic Seismic Response of Extended Pile-Shaft-Supported Bridge Structures. EERI *Earthquake Spectra* 2004; 20(4): 1057-1080.

[2] Silva PF, Manzari MT. Nonlinear Pushover Analysis of Bridge Columns Supported on Full-Moment Connection CISS Piles on Clays. EERI *Earthquake Spectra* 2008; 24(3): 751-774.

[3] Gerolymos N, Zafeirakos A, Souliotis C. Insight to Failure Mechanisms of Caisson Foundations Under Combined Loading: a Macro-Element Approach. In: *Proceedings of the 2nd International Conference on Performance-Based Design in Earthquake Geotechnical Engineering*, 28-30 May 2012, Taormina, Italy. Paper No: 11.10.

[4] Zafeirakos A, Gerolymos N. On the seismic response of *under*-designed caisson foundations. *Bulletin of Earthquake Engineering* 2013; 11(5): 1337–72.

[5] Zafeirakos A, Gerolymos N, Drosos V. Incremental dynamic analysis of caisson-pier interaction. *Soil Dynamics and Earthquake Engineering* 2013; 48: 71–88.

[6] Nova R, Montrasio L. Settlements of shallow foundations on sand. *Géotechnique* 1991; 41(2): 243–256.

[7] Randolph MF, Gourvenec S. *Offshore Geotechnical Engineering*. Spon Press/ Taylor & Francis 2011. ISBN: 978-0-415-47744-4.

[8] Cassidy MJ, Randolph MF, Byrne BW.A plasticity model describing caisson behaviour in clay. *Applied Ocean Research* 2006; 28: 345–358.

[9] Zhang Y, Bienen B, Cassidy MJ, Gourvenec S. Undrained bearing capacity of deeply buried flat circular footings under general loading. *Journal of Geotechnical and Geoenvironmental Engineering*, ASCE, 2012; 138(3): 385-397.

[10] Gourvenec S, Randolph MF. Effect of strength non homogeneity on the shape of failure envelopes for combined loading of strip and circular foundations on clay. *Géotechnique* 2003; 53(6): 575–586.

[11] Bransby MF, Yun GJ. The undrained capacity of skirted strip foundations under combined loading. *Géotechnique* 2009; 59(2): 115–125.

[12] Gazetas G. Formulas and charts for impedances of surface and embedded foundations. *Journal of Geotechnical Engineering*, ASCE, 1991 ; 117(9);1363−1381.

[13] Gerolymos N, Gazetas G. Winkler model for lateral response of rigid caisson foundations in linear soil. *Soil Dynamics and Earthquake Engineering* 2006; 26(5): 347-361.

[14] Butterfield R, Houlsby GT, Gottardi G. Standardized sign conventions and notation for generally loaded foundations. *Géotechnique* 1997; 47(5): 1051–1054.

[15] ABAQUS, Inc. ABAQUS Analysis User's Manual, Version 6.10, Providence, RI, USA, 2010.

[16] Gerolymos N, Gazetas G. Static and dynamic response of massive caisson foundations with soil and interface nonlinearities–validation and results. Soil Dynamics and Earthquake Engineering 2006; 26(5): 377–94.

[17] Armstrong PJ, Frederick CO. A mathematical representation of the multiaxial Bauschinger effect. Technical Report RD/B/N 731, Central Electricity Generating Board, Berkeley, UK, 1966 [Reprint in: Armstrong PJ, Frederick CO. A mathematical representation of the multiaxial Bauschinger effect. *Materials at High Temperatures* 2007; 24(1): 1–26].

[18] Houlsby GT, Kelly RB, Huxtable J, Byrne BW. Field trials of suction caissons in clay for offshore wind turbine foundations. *Géotechnique* 2005; 55(4): 287–296.

[19] Gourvenec S. Bearing capacity under combined loading - a study of the effect of shear strength heterogeneity. In: *Proceedings of the 9th Australian and New Zealand Conference on Geomechanics*, Auckland, New Zealand, 2004, pp. 527-533.

[20] Karapiperis K, Gerolymos N. Combined loading of caisson foundations in cohesive soil: Finite element versus Winkler modeling. *Computers and Geotechnics* 2014; 56: 100–120.

[21] Mergos PE, Kappos AJ. Seismic damage analysis including inelastic shear–flexure interaction. *Bulletin of Earthquake Engineering* 2010; 8:27–46.

[22] California Transportation Agency. *Seismic design criteria*. Ver.3.1, 2004 ,Caltrans, California

[23] European Committee for Standardization. *Eurocode 8: design of structures for earthquake resistance – part 2: bridges*. CEN, 2005, Brussels.

Chapter 3

Figures

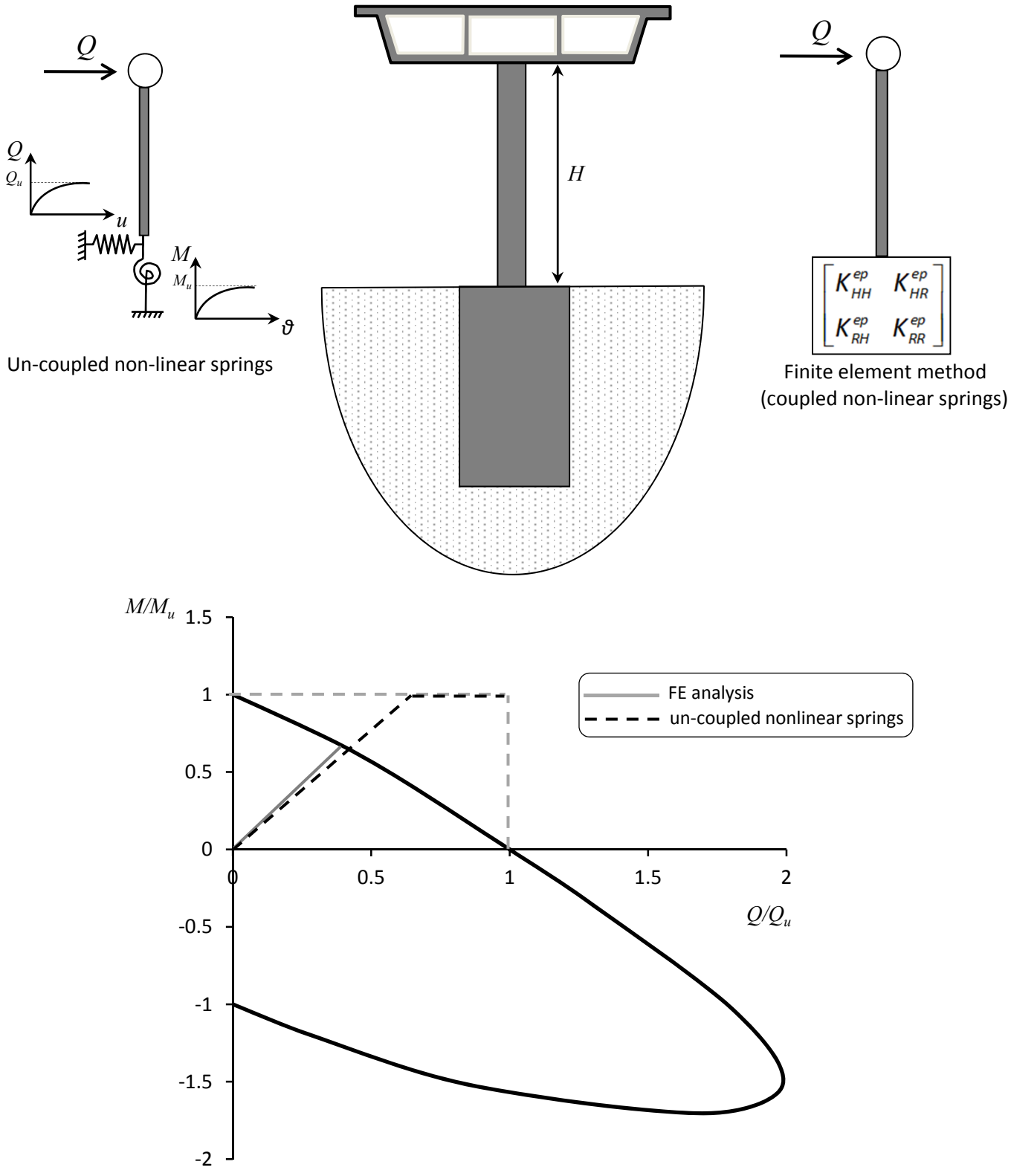

Fig. 3.1 Motivation of the study: a caisson foundation supporting a bridge pier-deck subjected to lateral loading. The pier is simulated as a SDOF oscillator. Indicative results are plotted for the load path at the caisson, when the foundation is modeled: (i) by un-coupled nonlinear springs, and (ii) by the rigorous finite element method.

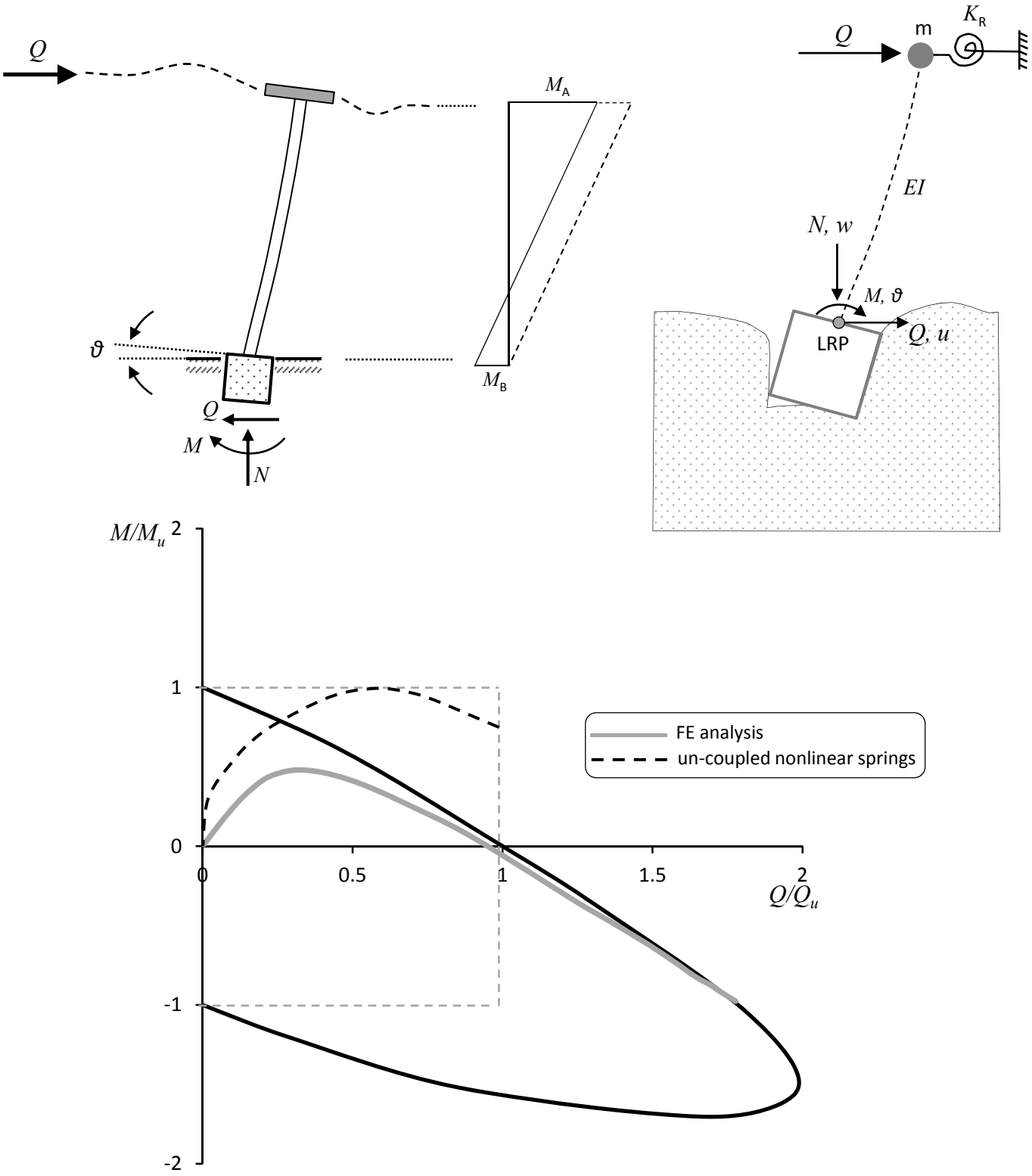

Fig. 3.2 Motivation of the study : a caisson foundation supporting a bridge pier-deck subjected to lateral loading. The deck now applies kinematic constraints at the pier-deck joint, simulated by a rotational spring. Indicative results are plotted for the load path at the caisson, when the foundation is modeled: (i) by un-coupled nonlinear springs, and (ii) by the rigorous finite element method.

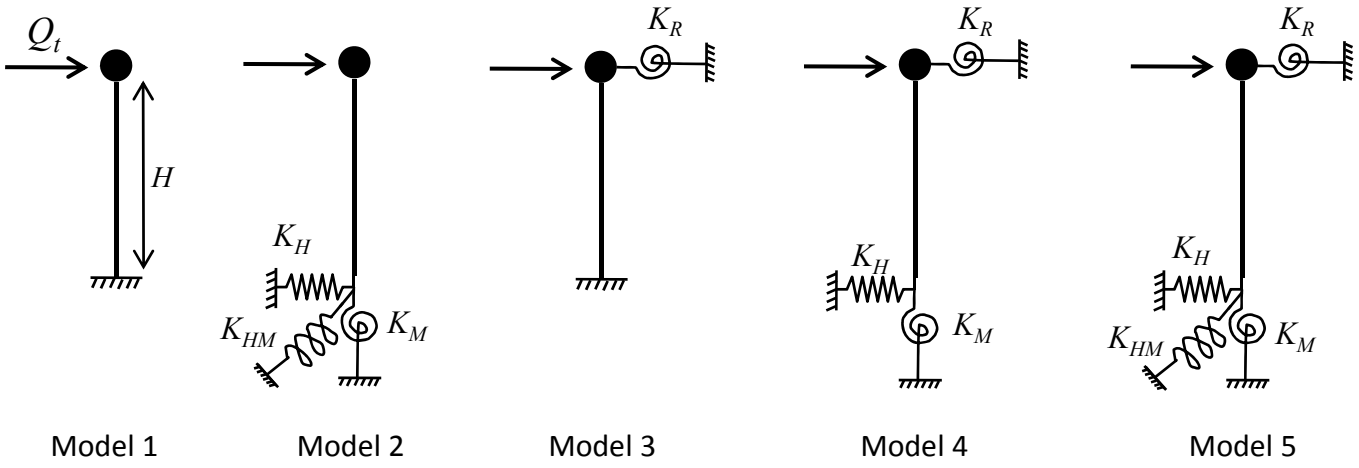

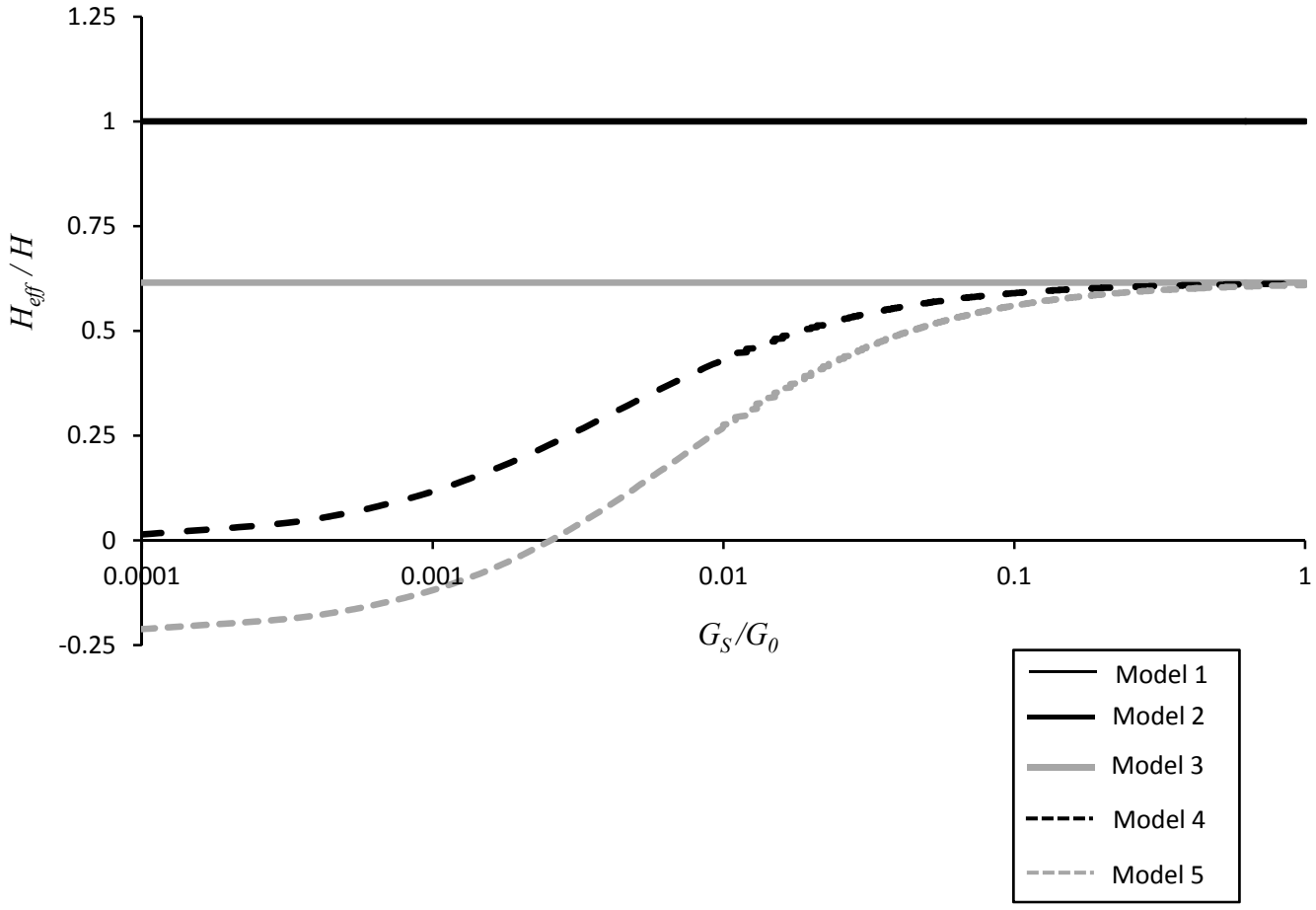

Fig. 3.3 Effective height H_{eff}, normalized by the geometric height H, of various idealized bridge pier-foundation systems subjected to lateral loading, as a function of soil compliance.

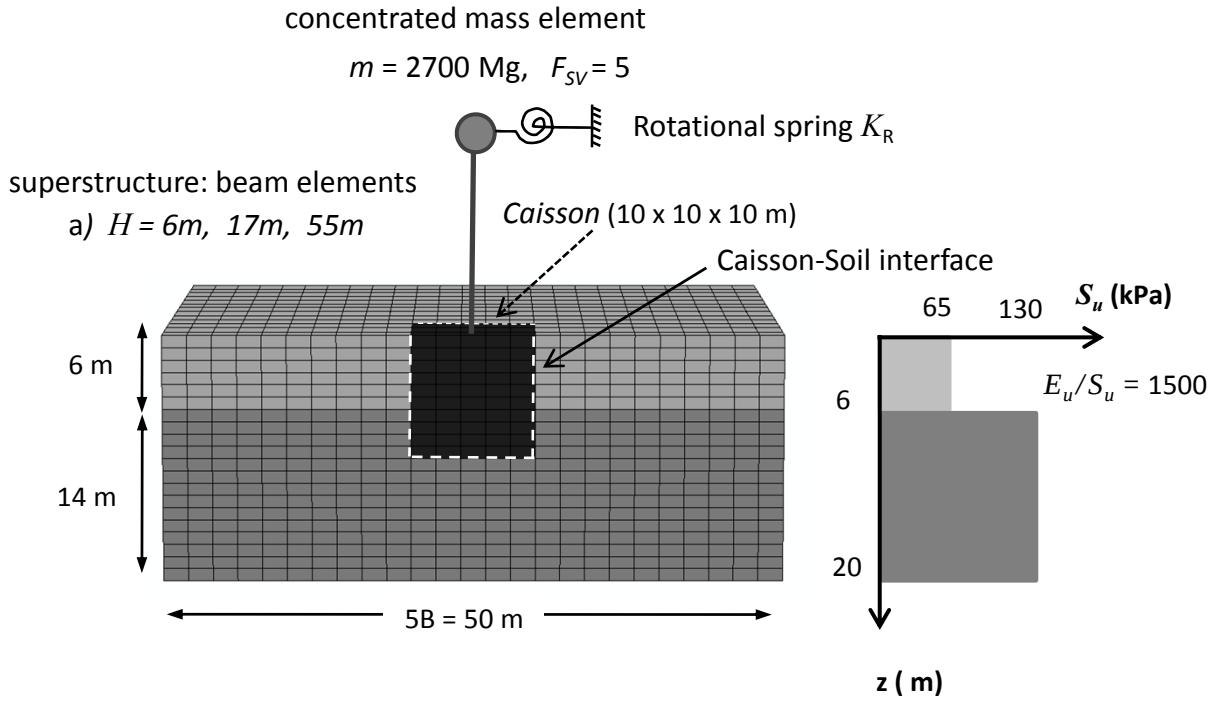

Fig. 3.4 Overview of the 3D finite element model with the parameters used in the analysis.

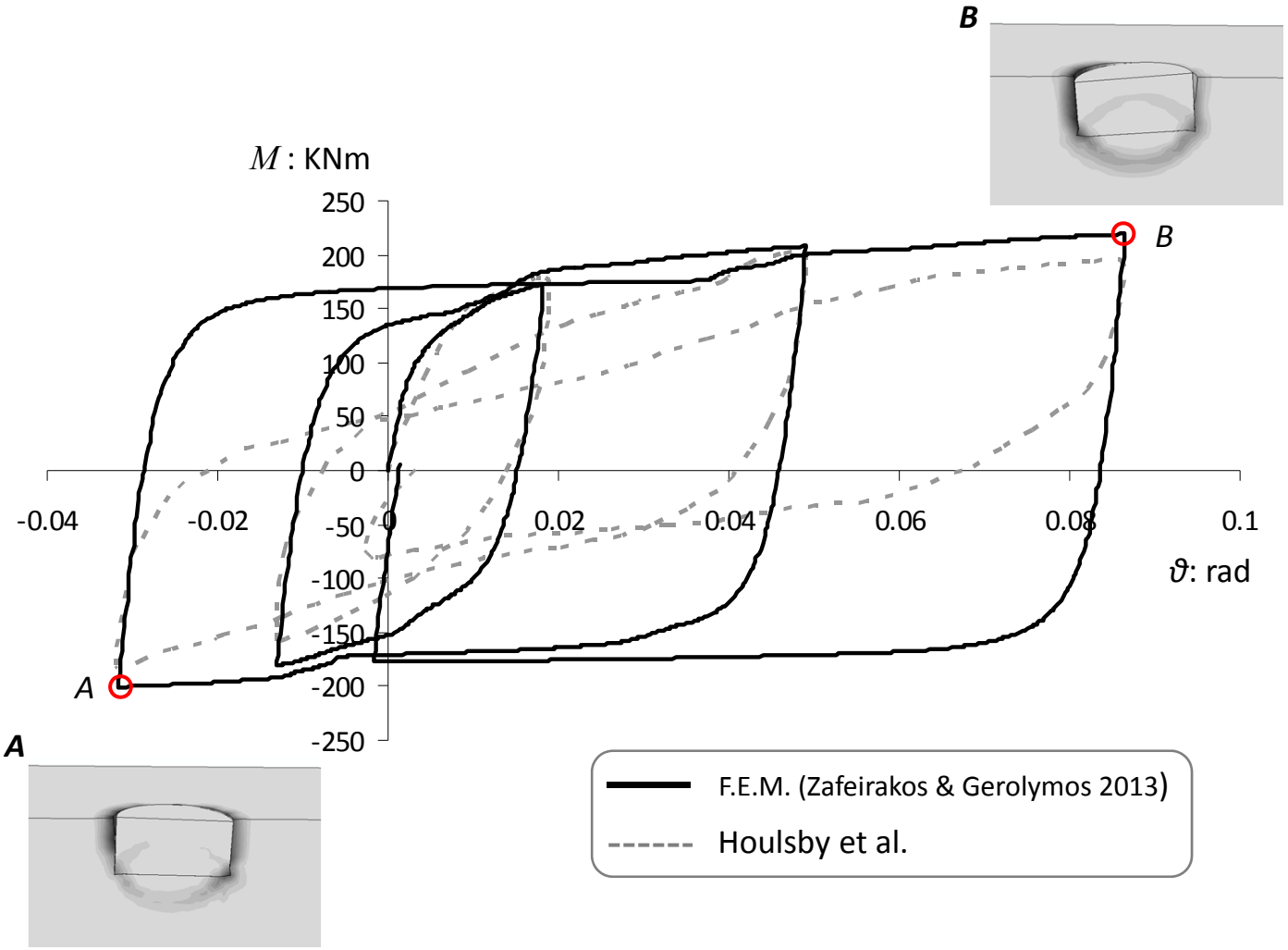

Fig. 3.5 Constitutive model validation in terms of **a** M-ϑ, along with snapshots from the FE analysis at points *A* and *B* (after Zafeirakos and Gerolymos, 2013).

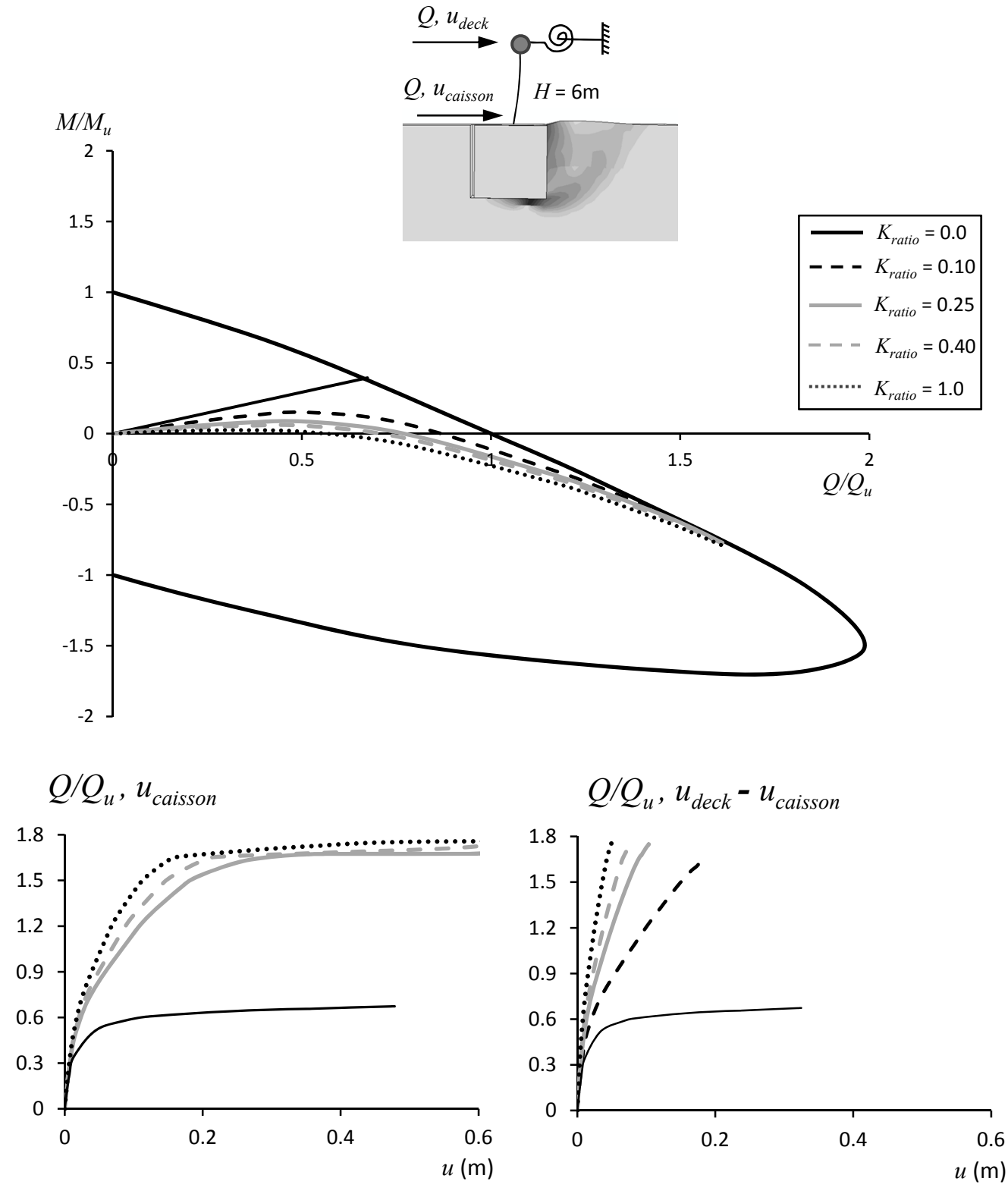

Fig. 3.6 FE analysis results for a caisson foundation supporting a bridge pier with H = 55m, subjected to parametrically varying constraints in rotation (K_{ratio}) imposed at the deck level.

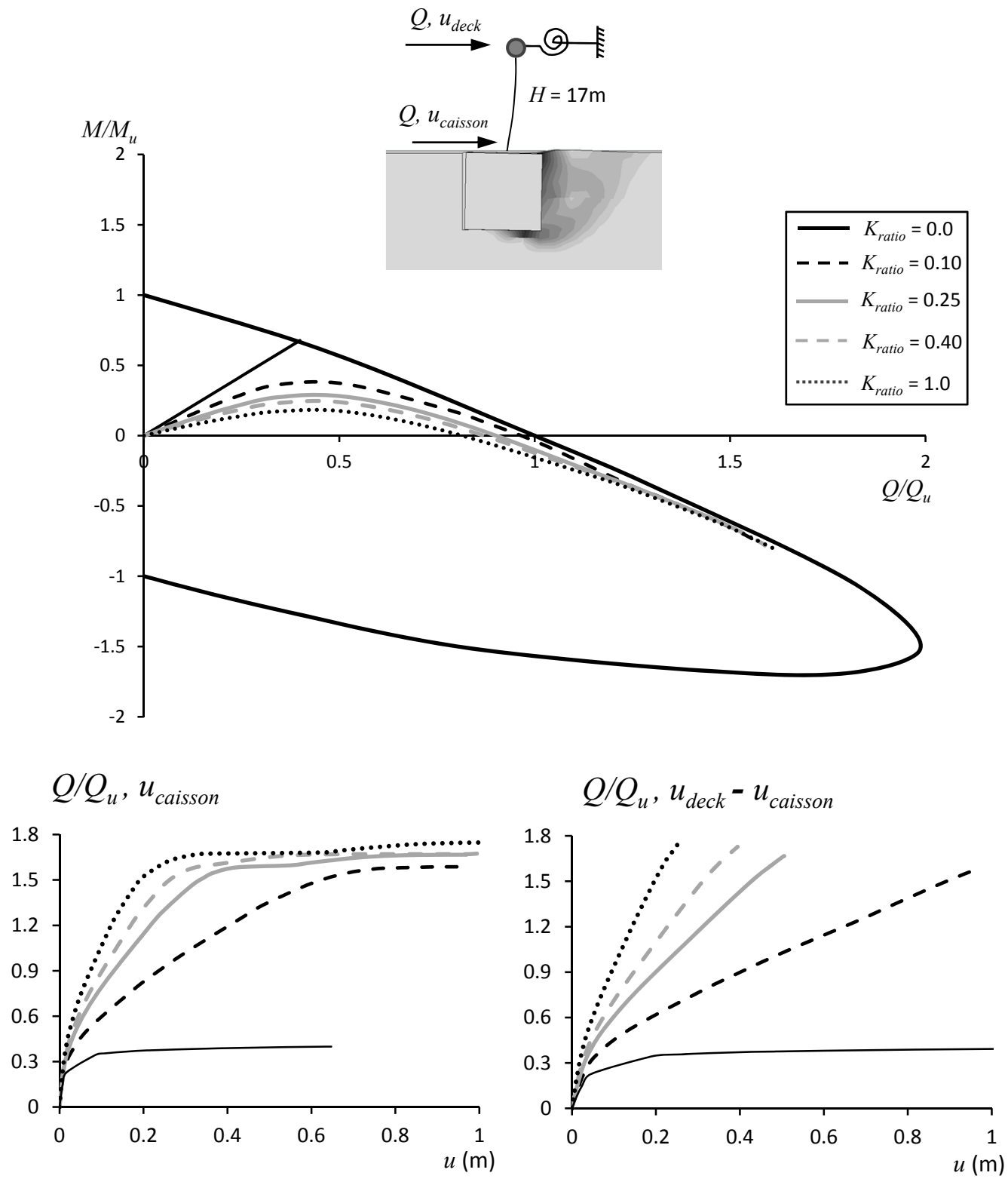

Fig. 3.7 FE analysis results for a caisson foundation supporting a bridge pier with H = 55m, subjected to parametrically varying constraints in rotation (K_{ratio}) imposed at the deck level.

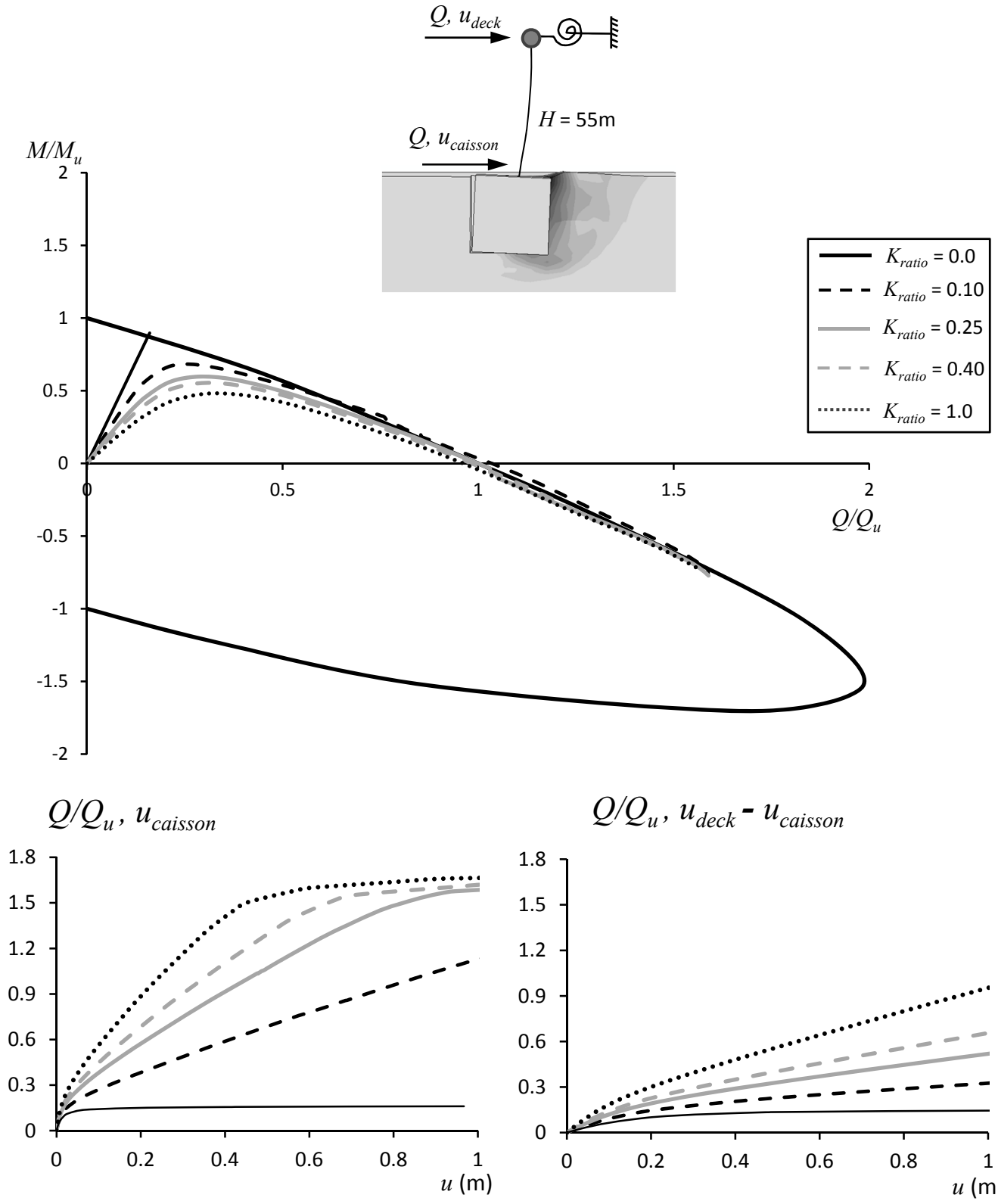

Fig. 3.8 FE analysis results for a caisson foundation supporting a bridge pier with H = 55m, subjected to parametrically varying constraints in rotation (K_{ratio}) imposed at the deck level.

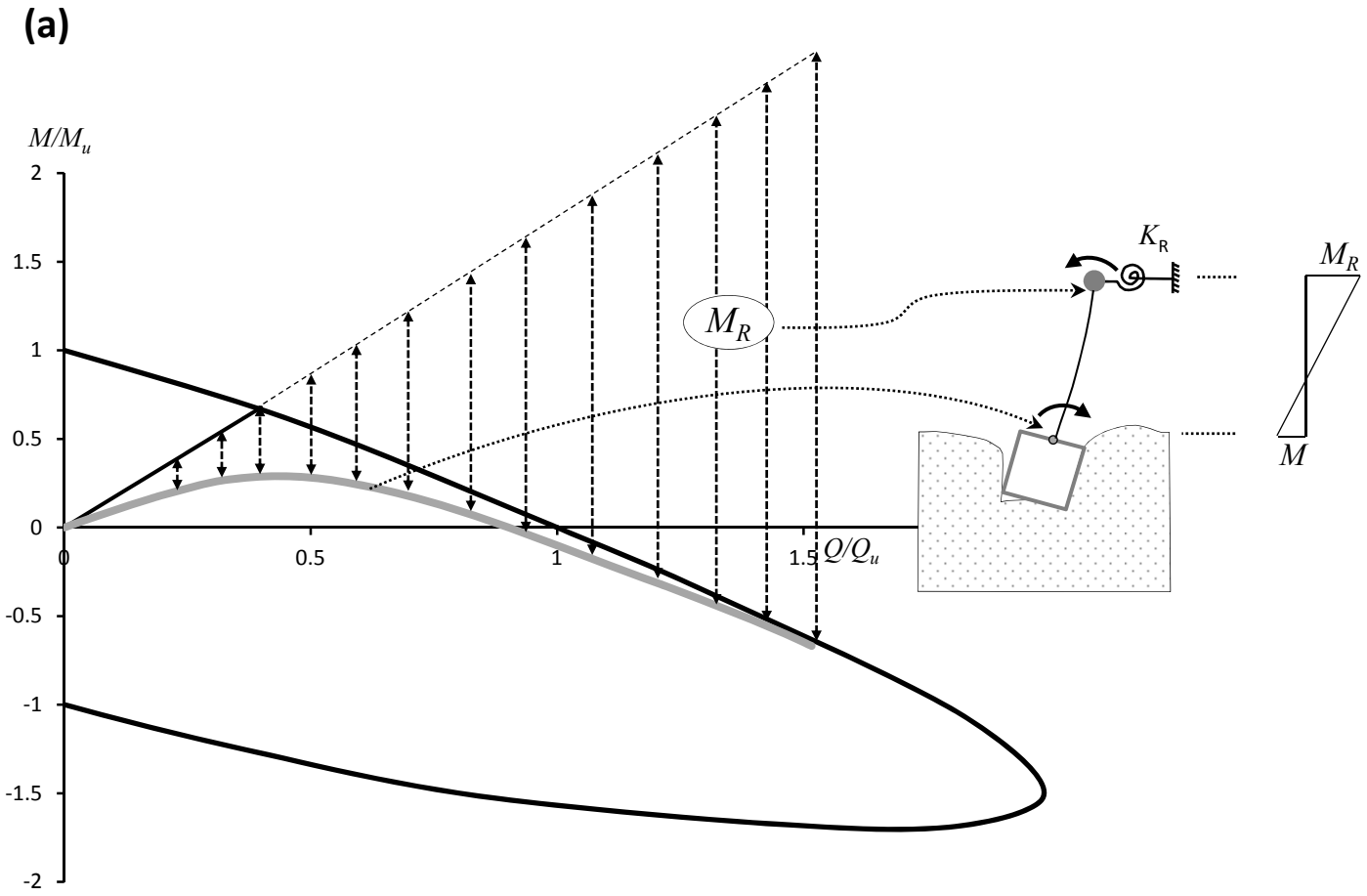

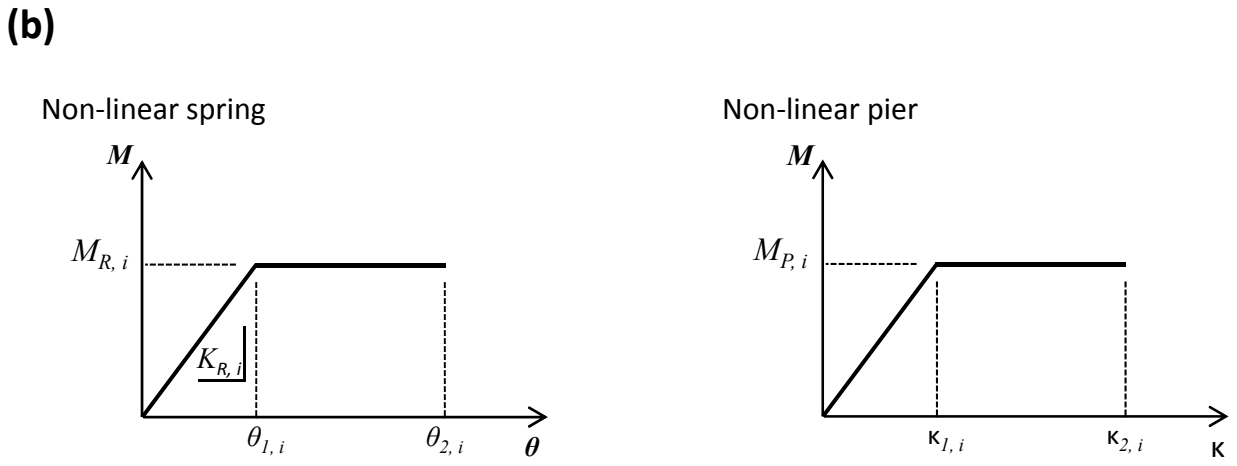

Fig. 3.9 Schematic representations of : (a) the moment sustained by the pier-deck joint, M_R. (b) the bi-linear moment-rotation and moment-curvature laws used to model the spring and the pier, respectively.

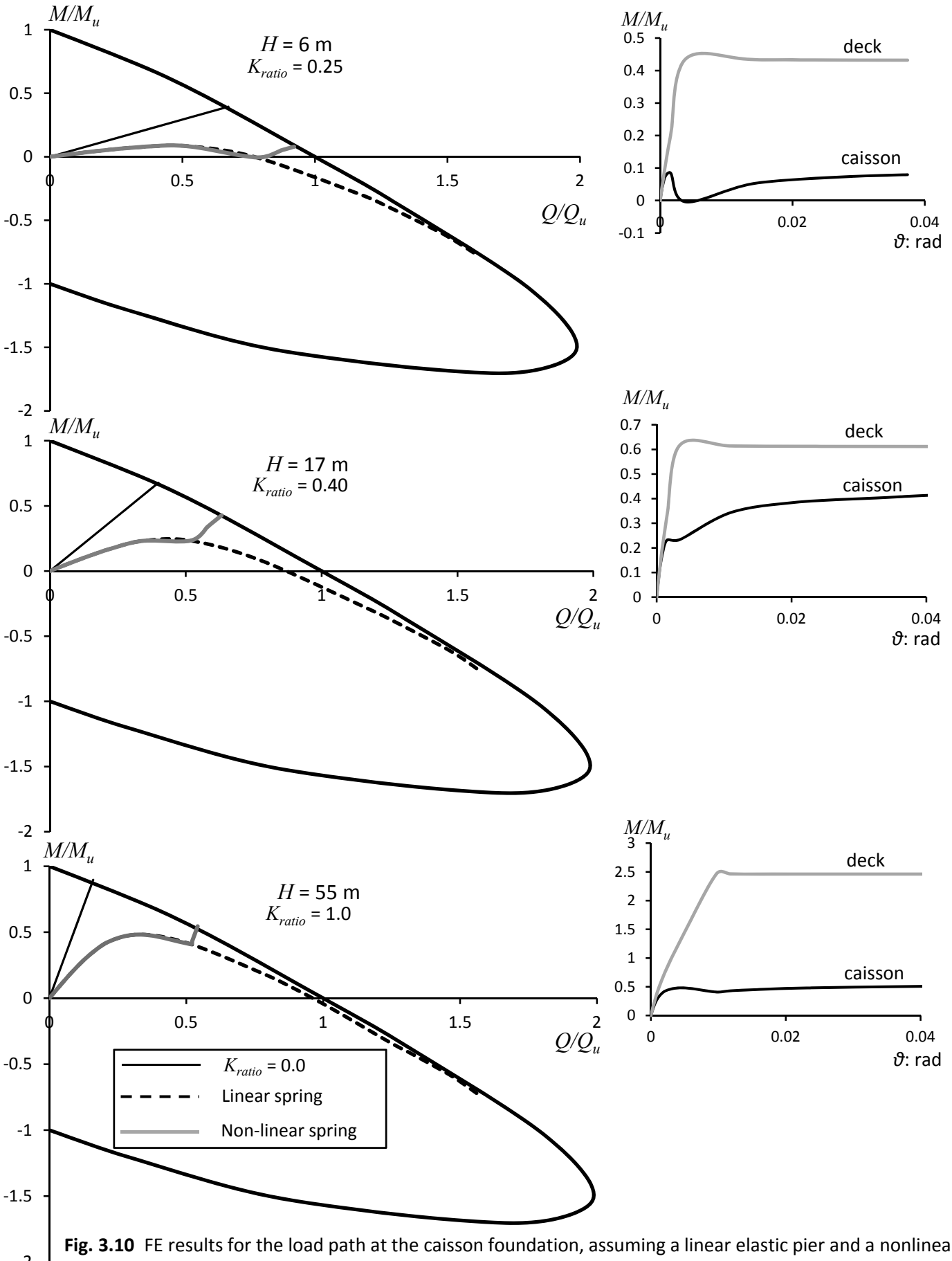

Fig. 3.10 FE results for the load path at the caisson foundation, assuming a linear elastic pier and a nonlinear spring. The corresponding evolution of the moment sustained by the caisson (solid black line) and at the deck (solid grey line) with respect to the caisson's rotation are plotted alongside.

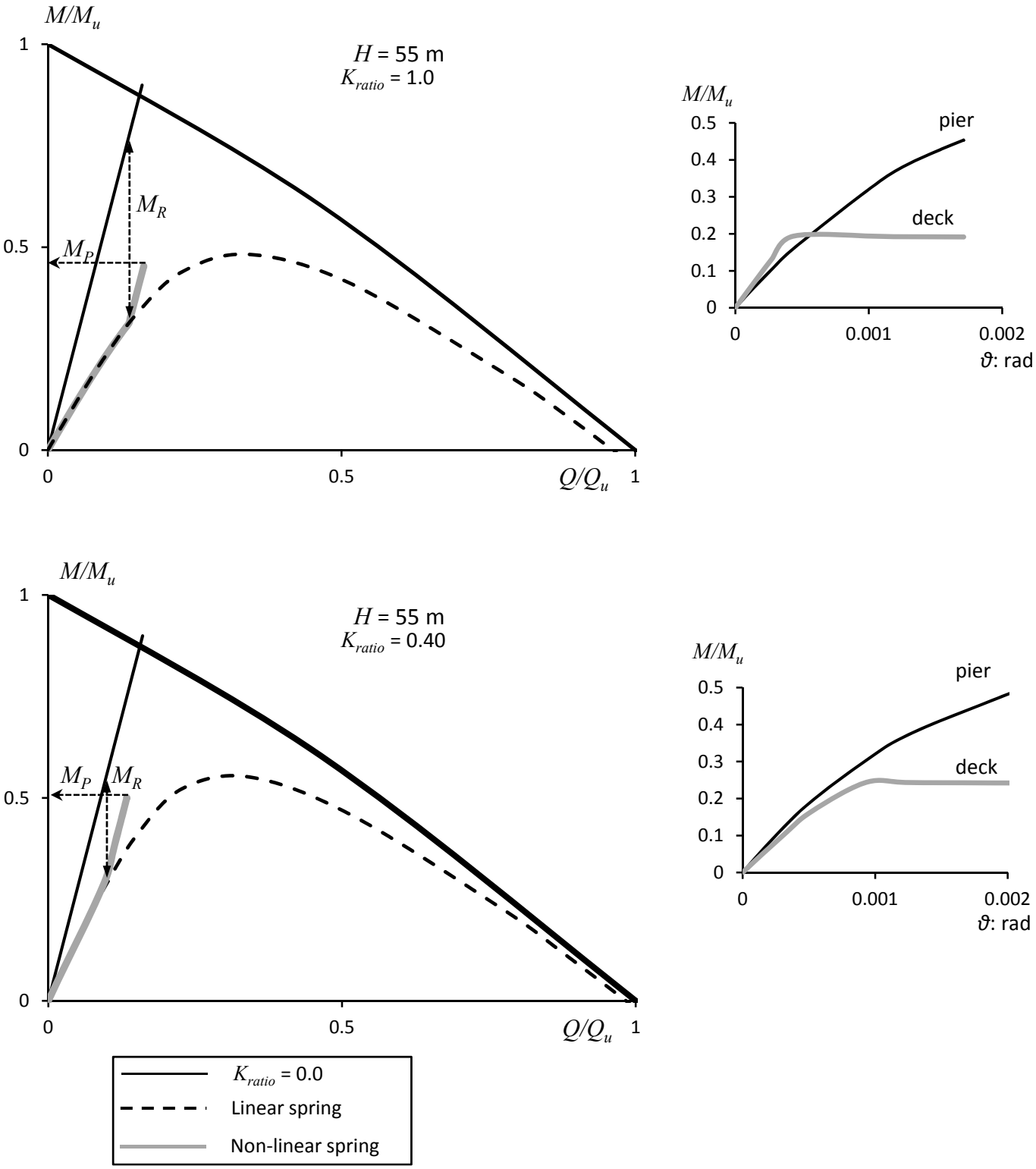

Fig. 3.11 FE results for the load path at the caisson foundation, assuming nonlinear response of both the pier and the pier-deck joint. The corresponding evolution of the moment sustained by the caisson (solid black line) and at the deck (solid grey line) with respect to the caisson's rotation are plotted alongside.

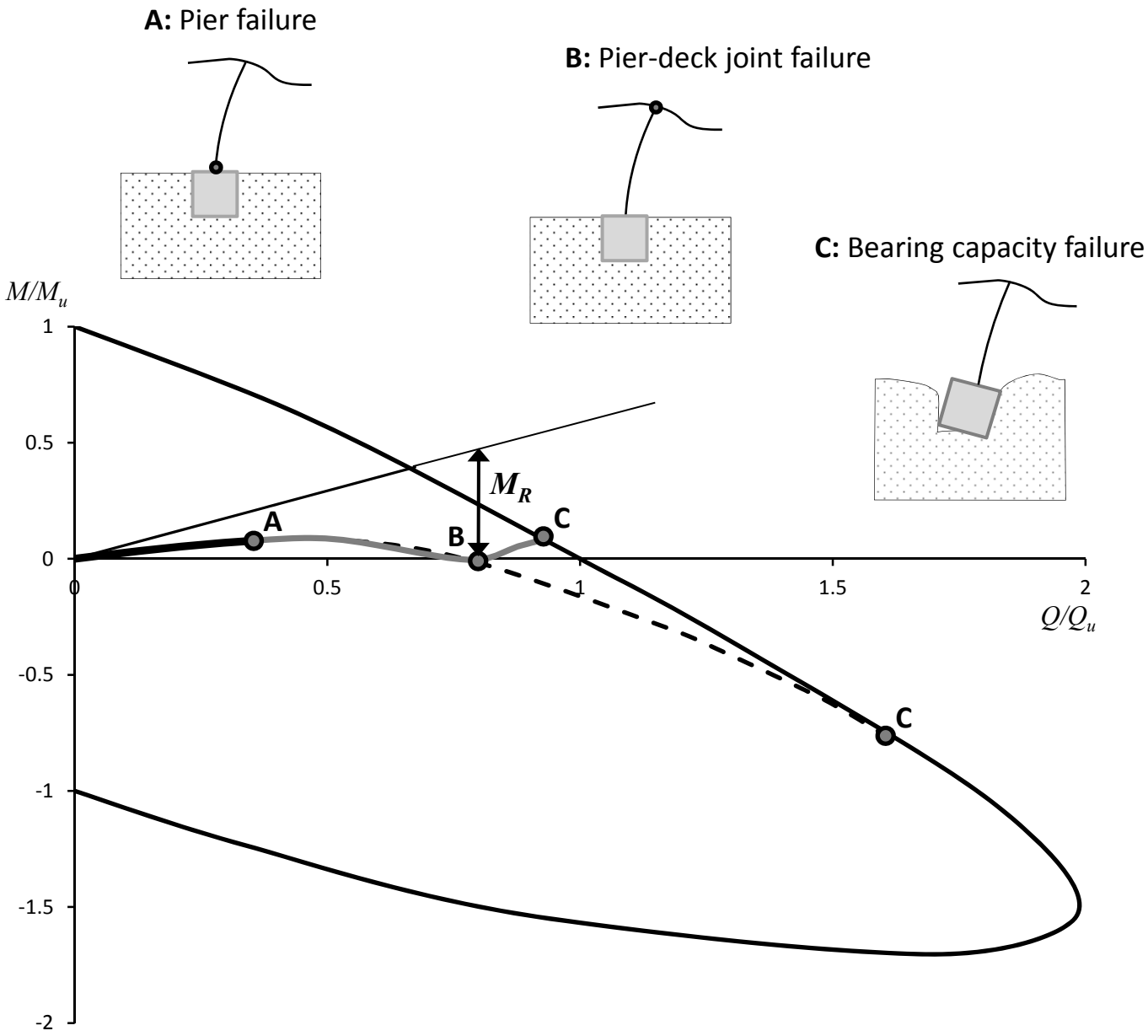

Fig. 3.12 Schematic illustration of the possible failure modes of a caisson foundation-pier-deck system, accounting for nonlinearities above and below ground level.

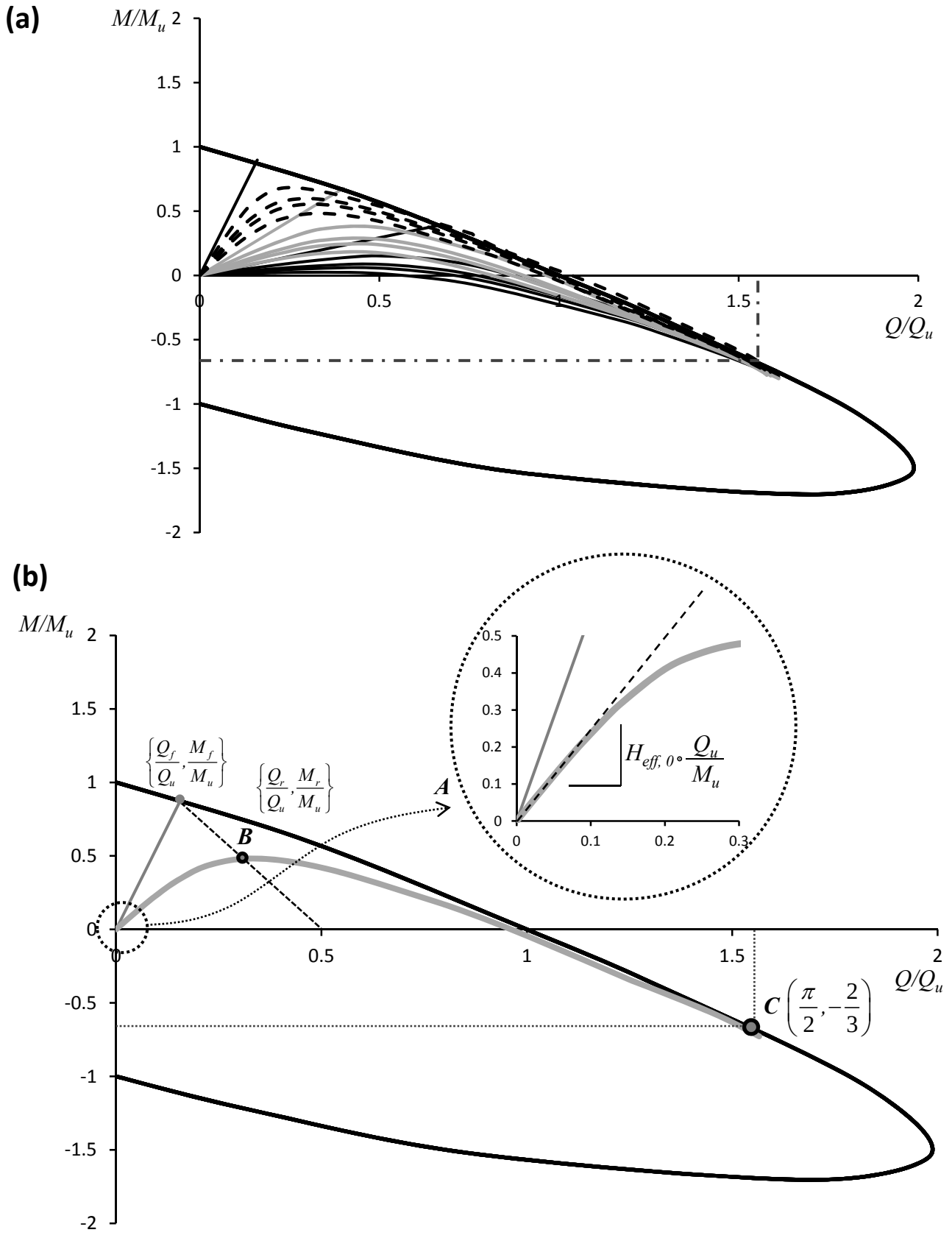

Fig. 3.13 (a) Collection of the numerically calculated load paths examined in this study. (b) Graphical representation of the three conditions applied for the extraction of a closed-form expression for the load path. The particular coordinates at point ***C*** belong to the failure envelope of caisson foundations with D/B = 1.

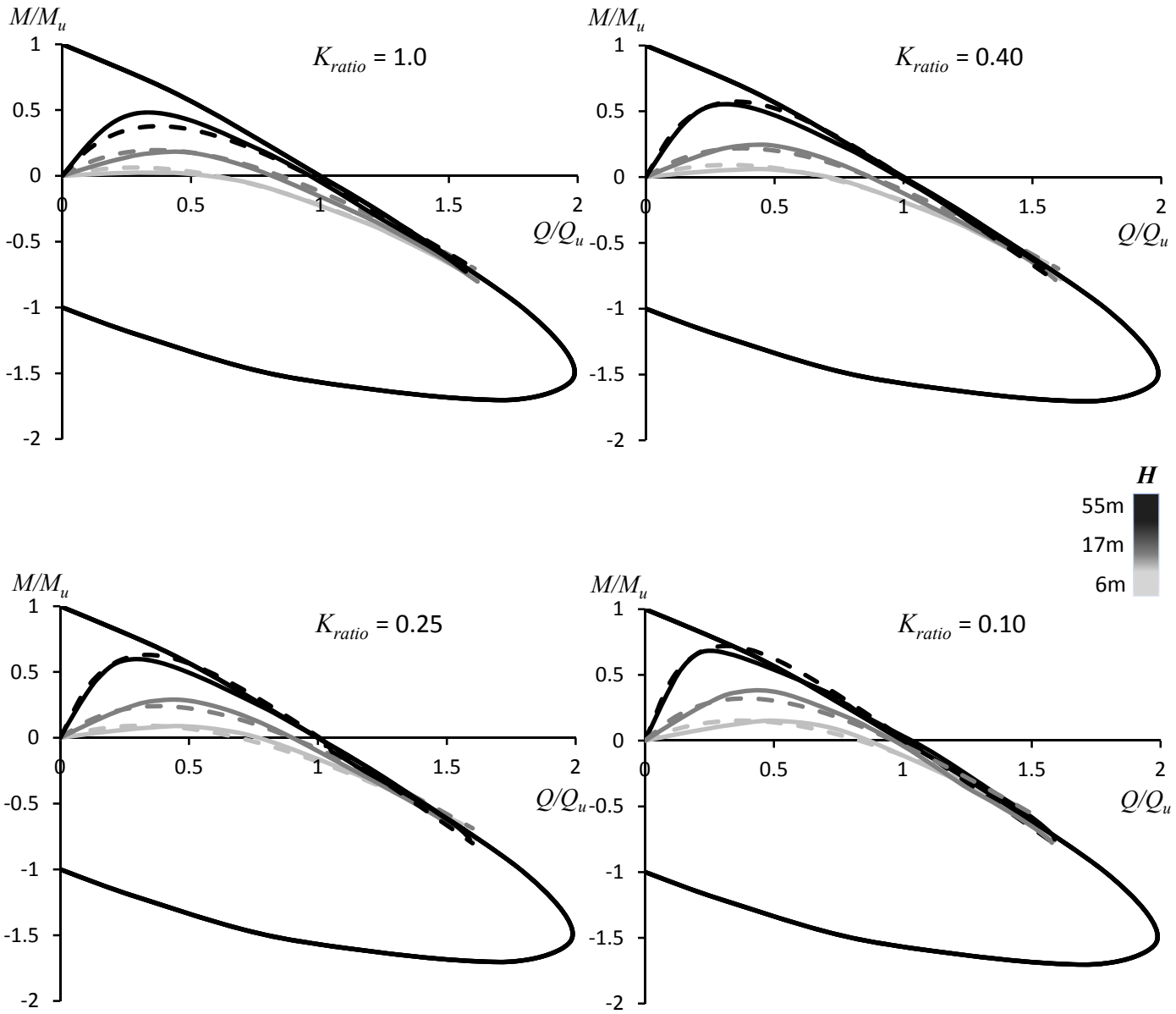

Fig. 3.14 Comparison between numerical (solid lines) and analytical (dashed lines) results for the nonlinear path at the foundation in M-Q space.

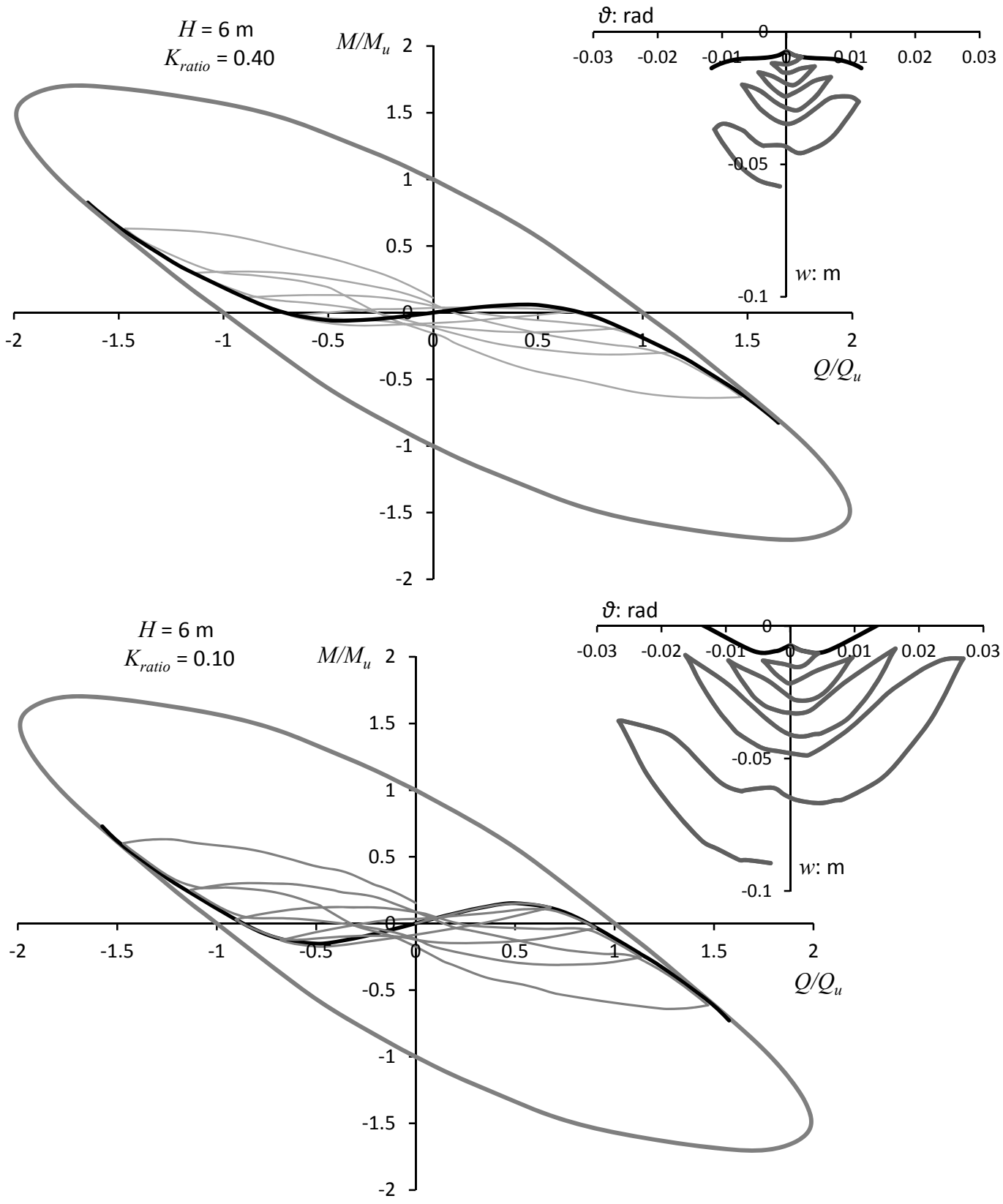

Fig. 3.15 Slow cyclic loops in M-Q space and corresponding w-ϑ loops , for caissons supporting a pier with H = 6m and pier-deck joint stiffness ratios K_{ratio} = 0.10 and 040.

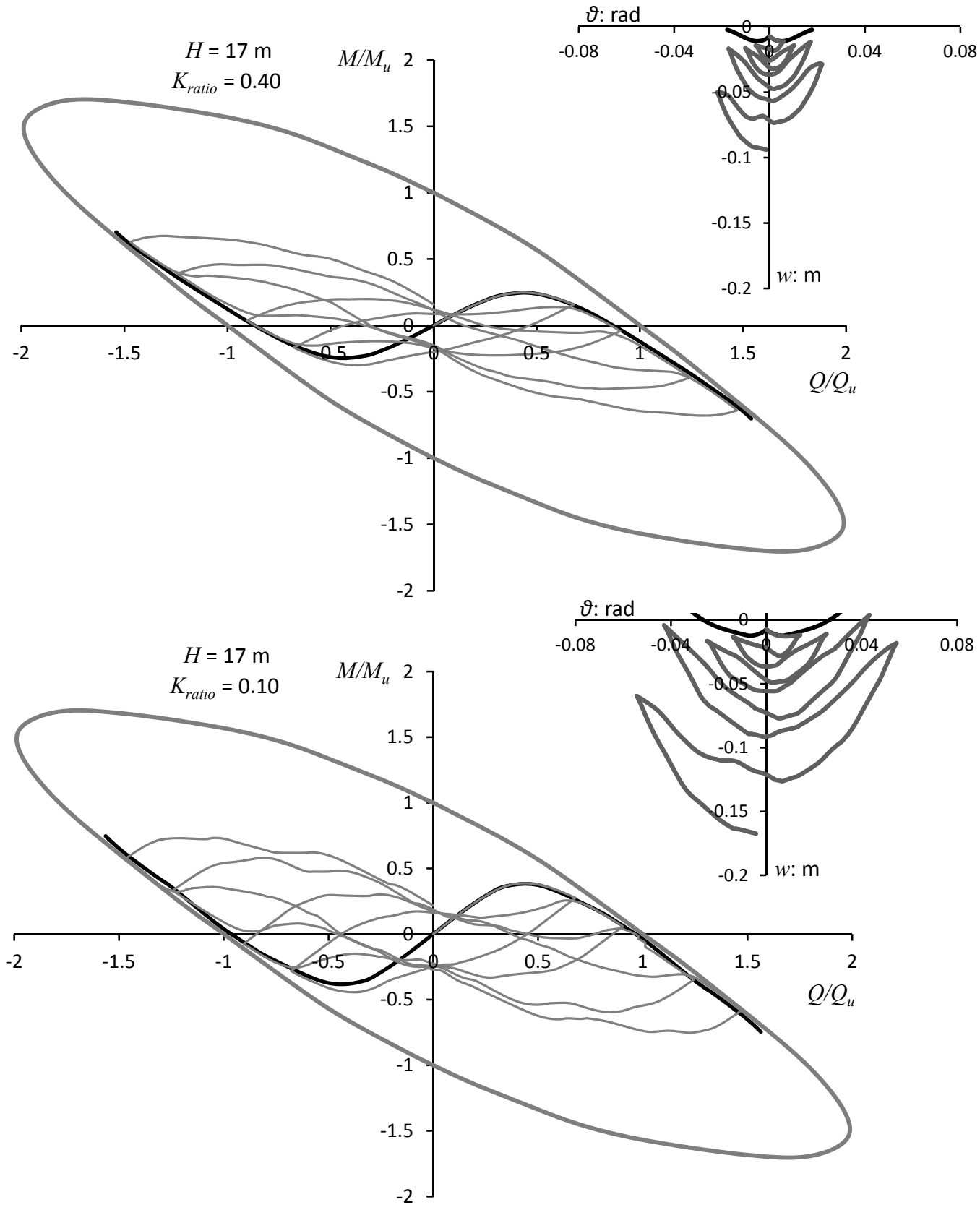

Fig. 3.16 Slow cyclic loops in M-Q space and corresponding w-ϑ loops , for caissons supporting a pier with H = 17m and pier-deck joint stiffness ratios K_{ratio} = 0.10 and 040.

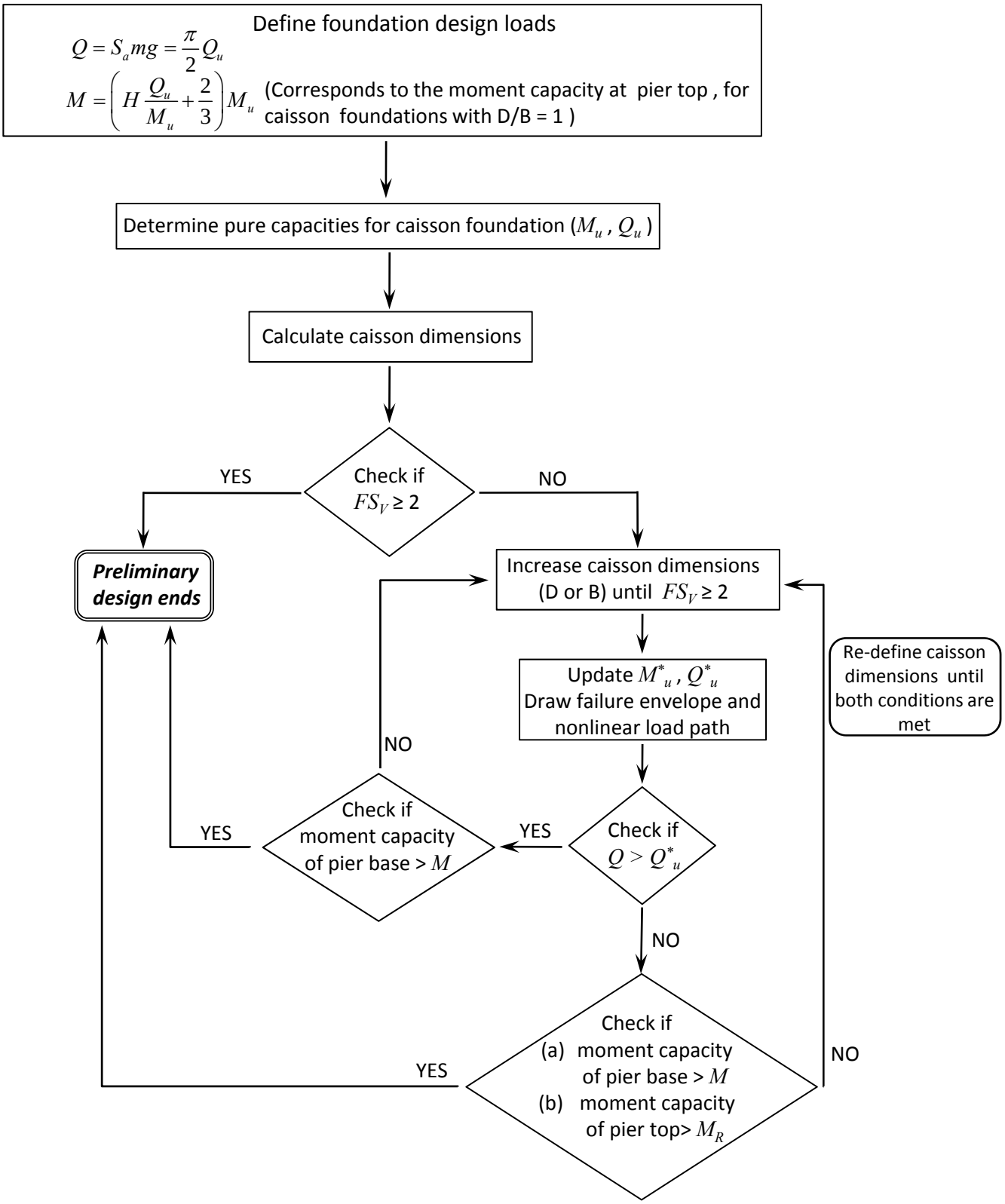

Fig. 3.17 Flow chart of the proposed methodology for the preliminary seismic design of caisson foundations.

On the seismic response of under-designed caisson foundations

A B S T R A C T

The seismic behaviour of caisson foundations supporting typical bridge piers is analysed with 3D finite elements, with due consideration to soil and interface nonlinearities. Single-degree-of freedom (SDOF) oscillators of varying mass and height, simulating heavily and lightly loaded bridge piers, founded on similar caissons are studied. Four different combinations of the static (FS_V) and seismic (FS_E) factors of safety are examined: (*a*) a lightly loaded ($FS_V = 5$) seismically *under*-designed ($FS_E < 1$) caisson, (*b*)) a lightly loaded seismically *over*-designed ($FS_E > 1$) caisson, (*c*) a heavily loaded ($FS_V = 2.5$) seismically *under*-designed ($FS_E < 1$) caisson and (*d*) a heavily loaded seismically *over*-designed caisson. The analysis is performed with use of seismic records appropriately modified so that the effective response periods (due to soil-structure-interaction effects) of the studied systems correspond to the same spectral acceleration, thus allowing their inelastic seismic performance to be compared on a fair basis. Key performance measures of the systems are then contrasted, such as: accelerations, displacements, rotations and settlements. It is shown that the performance of the lightly loaded seismically *under*-designed caisson is advantageous: not only does it reduce significantly the seismic load to the superstructure, but it also produces minimal residual displacements of the foundation. For heavily loaded

foundations, however (FS_V = 2.5), the performance of the two systems (*over* and *under* designed) is similar.

4.1. Introduction

Caisson foundations deeply embedded in soft soil have been widely used to support major structures, especially bridges. Despite their large dimensions, however, caissons have also been proven vulnerable to strong seismic shaking, as was revealed from recent earthquake events (e.g. Kobe 1995).

Interestingly, although a number of methods of varying degrees of accuracy, efficiency and sophistication have been developed for the lateral and seismic response of deep foundations, only few of them are actually *devoted* to caissons. Among the most noteworthy studies, Davidson et al. (1982) developed a four-spring Winkler model for rigid caissons, and calibrated it with 3D finite element analysis, and static load tests. Also of related interest is the work of Mylonakis (2001) who introduced the Vlasov-Leontiev 'Winkler-with-shear-layer' idealization to model: (a) the dynamic soil reaction against caissons, (b) the dynamic impedance of the caisson, and (c) the dynamic interaction between two neighboring caissons. He derived explicit closed-form solutions for a flexible large-diameter cylindrical shaft embedded in a homogeneous soil resting on a rigid base, for various boundary conditions. In a series of papers, Gerolymos and Gazetas (2006a, b, c) proposed a multi spring model for the static, cyclic, and dynamic response of massive caisson foundations embedded in nonlinear layered or inhomogeneous soil and loaded at the top. Their model was validated against results from load tests and 3D finite element analysis. In the most recent study, Tsigginos et al. (2008) provided an analytical method, using translational and rotational distributed Winkler springs and dashpots to simulate the soil-caisson interaction, to study the seismic response of a bridge pier supported on a rigid caisson foundation embedded in a deep soil stratum. Their model was found to compare well with results from finite element (FE) analysis and other available solutions.

The seismic design of bridges is based on a presumed ductile response of the superstructure, while dictating elastic response for the foundation elements and the surrounding soil. This essentially-elastic response of the foundation is usually ensured by introducing appropriate "overstrength" factors plus factors of safety larger than 1 against each "failure" mode, as in static design, so that plastic hinging occurs in the pier rather than the foundation. Following the suggested and commonly used capacity design regulations, the regions of expected inelastic deformation are then carefully detailed to provide adequate structural ductility, without transforming the structure into a mechanism.

The concept of "allowing" foundation elements to yield is still relatively new in earthquake engineering practice. Development of nonlinearities below ground surface is forbidden in existing regulations, codes and specifications. For the case of deep embedded and caisson foundations, this indicates that nonlinearities of material (soil yielding) and geometric nature, involving separation (gapping) between the caisson shaft and the soil, slippage at the soil–caisson shaft interface and base uplifting, are prohibited. Such a restriction may, at first, appear reasonable, due to the fact that the inspection and rehabilitation of foundation damage after a strong earthquake is not a trivial task. This concept, however, may result in economically unfeasible designs, especially in areas where strong earthquake events are anticipated and soil nonlinearity is unavoidable unless *over*-designed foundations are used. Moreover, neglecting the aforementioned phenomena prohibits the exploitation of strongly non-linear energy dissipating mechanisms in defense of the superstructure.

Even though, surprisingly, little research has been conducted in the field of performance–based design of deep embedded foundations (e.g. Hutchinson et al. 2004, Silva and Manzari 2008, Gerolymos et al. 2009, Zafeirakos et al 2013), extensive studies have been presented for the case of shallow foundations, suggesting that soil–foundation plastic yielding under seismic excitation is not only unavoidable, but may even be beneficial (Paolucci 1997; Pecker 1998, 2003; Martin and Lam 2000; FEMA 356 2000; Kutter et al. 2003; Faccioli et al. 2001; Gazetas et al. 2007; Gajan et al. 2005, 2008; Mergos and Kawashima 2005; Apostolou and Gazetas 2005;

Paolucci et al. 2007; Kawashima et al. 2007; Gajan and Kutter 2008; Chatzigogos et al. 2009; Anastasopoulos et al. 2010).

In this respect, this paper presents a comparative numerical study of the seismic performance of caisson foundations under four different loading conditions, with respect to vertical (FS_V) and moment (FS_E) loading. The comparison is performed between single degree of freedom (SDOF) oscillators, simulating bridge piers, founded on similar caissons, while varying the mass of the bridge deck and the pier height. Since the paper focuses on the nonlinearities developed below ground level, the superstructures are considered elastic. The complex interplay between the induced soil and structural nonlinearities during the seismic response of caisson foundations supporting nonlinear structures, was investigated by the authors in a recent publication (Zafeirakos et al 2013).

The following configurations are analysed and compared: (*a)* the first consists of a 1.5 m and a 12 m pier, corresponding to a seismically *over*-designed and a seismically *under*-designed caisson, respectively, resulting from a "heavy" deck (safety factor for static loading FS_V = 2.5), and (*b*) the second comprises a 10 m and a 26 m pier, for a seismically *over* and an *under*-designed caisson respectively, resulting from a "light" deck (safety factor for static loading FS_V = 5). Fig. 1 schematically illustrates the expected response of a seismically *over*-designed as opposed to a seismically *under*-designed caisson foundation.

For the nonlinear dynamic analysis of the systems, three artificial acceleration time histories are imposed at the base. The artificial seismic excitations are appropriately calibrated in a way that the spectral acceleration of a SDOF oscillator placed at the surface remains constant for a wide range of frequencies, practically unaffected by the dynamic characteristics of the soil-structure system (e.g. effective fundamental period). The analysis methodology will be explained thoroughly in the sequel.

Evidently, it is shown that in the seismically *under*-designed caissons, the unavoidable development of plasticity below ground surface restricted the loading transmitted onto the superstructure, but without avoiding an increase of earthquake-induced foundation settlements

and rotations. Overall, however, soil failure mechanisms offer substantial ductility capacity to the caisson-superstructure system.

It should be noted at this point that the results presented herein can be seen as a first demonstration of the potential advantages of seismically *under*-designing a caisson foundation. To become applicable in practice, further analytical and careful experimental verification is required.

4.2. Problem definition and analysis methodology

4.2.1. Problem definition

The studied problem is portrayed in Fig. 2: A bridge pier is founded through a rigid cubic caisson of side h = 10 m in a 20 m thick 2-layer cohesive soil stratum. The clayey soils are saturated responding in undrained fashion with shear strength S_u = 65 kPa at the upper 6 m, S_u = 130 kPa at the lower 14 m and constant stiffness to strength ratio E/S_u = 1500. The mass of the deck, *m*, is given parametrically the values of 5400 and 2700 Mg, corresponding to a static factor of safety FS_V = 2.5 ("heavy" superstructure) and FS_V = 5 ("light" superstructure) respectively. For each case of FS_V, two different column heights, corresponding to a seismic safety factor (a) FS_E > 1.0, and (b) FS_E < 1.0, are calculated. In total, a set of four structural configurations are analysed. The design spectral acceleration is chosen Sa = 0.6 g. The material properties of the soil profile and the pier columns are summarized in **Table 1.**

Table 1. Material parameters used in the analyses

material	Young's Modulus: MPa	Mass density : kg/m3	Poisson's ratio	Shear strength: kPa
Clay	97.5	2.0	0.45	65
Stiff clay	195	2.0	0.45	130
Concrete piers	30.000	2.5	0.15	*(elastic)*

The column heights associated with the seismic factor of safety are calculated according to the following procedure:

- A series of finite element (FE) static pushover-type of analyses are carried out to derive the bearing strength surfaces of the caisson−soil system in moment (M)−horizontal load (Q) space. Two envelopes are produced, depicted in Fig. 3, one for each case of vertical load applied from the mass weight. The results are normalized with respect to the pure moment capacity M_u (with no horizontal loading) and the pure horizontal capacity Q_u (no moment loading) of the caisson−soil system. To verify the aforementioned entities, Fig. 4 presents the Q-u and M-ϑ curves, along with the contours of plastic strain magnitude at failure, corresponding to the pure horizontal and moment capacities, respectively.
- In the next step, given the deck mass (m = 5400 Mg, for FS_V = 2.5 and m = 2700 Mg, for FS_V = 5.0) and the design spectral acceleration, 0.6 g, the respective vertical (mg) and pseudo-static shear force, $Q = m \cdot Sa$, is applied at the head of the caisson (pier base). Then, the caisson is subjected to a monotonically increasing overturning moment until failure. Since $M = Q \cdot H$, the interaction between M and Q may also be interpreted as the lever arm height above the pier base (H) that leads to failure for a given Q. This state corresponds to a safety factor for seismic loading FS_E = 1.0.
- Finally, a shorter pier (H = 1.5 m for FS_V = 2.5 and H = 10 m for a FS_V = 5.0) is designed assuming a FS_E = 1.3 (greater than 1.0) rendering the respective caissons as seismically *over*-designed, and a taller pier (H = 12 m for FS_V = 2.5 and H = 26 m for a FS_V = 5.0) resulting from a FS_E = 0.7 (lower than 1.0 − seismically *under*-designed caissons). In fact, as it will be shown below, the seismically *under*-designed foundation will not allow the design seismic action to develop. Hence, FS_E does not really have a physical meaning in this case; it is just an *apparent* temporary factor of safety.

The geometric properties of the piers are calculated so they correspond to elastic (fixed-base) vibration period T_{str} = 0.6 sec, for all cases, which is deliberately larger than the first natural period (T_{soil} = 0.41 sec) of the soil profile used in the analysis. The reason for this assumption will

be detailed in the sequel. The resultant cross-sectional areas (A: m^2) and moment of inertias (I: m^4) for the examined cases are given in **Table 2**.

Table 2. geometric properties of the pier columns

FS_V	H : m	A : m^2	I : m^4
5.0	26	26.97	57.88
5.0	10	6.42	3.28
2.5	12	11.95	11.35
2.5	1.5	0.53	0.02

4.2.2. Finite element model

The problem is analysed with the finite element code ABAQUS. The analysis is conducted taking account for material (in the soil) and geometric (interface) nonlinearities. Both caisson and soil are modeled with 3-D elements, elastic for the former and nonlinear for the latter. The mass-and-column superstructures are modeled as single degree of freedom oscillators.

As the focus of the paper is on the role of soil and interface nonlinearities, the behaviour of the bridge piers was deliberately assumed elastic. The caisson is connected to the soil with special contact surfaces, allowing for realistic simulation of possible detachment and sliding at the soil-caisson interfaces. The surface-to-surface contact interaction was modeled by exponential ("softened") pressure-overclosure relationship through the direct constraint enforcement method that makes use of Lagrange multipliers. For more details on the contact interaction algorithm the reader may refer to ABAQUS manual [ABAQUS, 2009].

For the total stress analysis under undrained conditions, soil behavior is described through an elasto-plastic constitutive model with kinematic hardening, available in the material library of ABAQUS. The calibration of the model parameters is based on a methodology proposed by Gerolymos and Gazetas (2006c). A detailed description of the model is given in the following sections. To avoid spurious oscillations at very small deformations (nearly elastic response), mass and stiffness proportional Rayleigh damping is also introduced into the model, accounting for an equivalent hysteretic damping between the eigenfrequency of the soil deposit and the

dominant frequency of the earthquake ground motion, equal to 2%. The seismic loading is applied at the base of the soil profile.

4.2.3. Model verification

The purpose of verifying our finite element model is to gain confidence in the proposed methodology by ensuring that the model does what it is intended to do. In this context, two very important aspects of our model are verified: the location and the type of the lateral boundaries, in both static and dynamic loading conditions. We therefore performed sensitivity analysis with respect to the total width x length, *L x L*, of the FE discretized field, while verifying the validity of a lateral boundary condition, where kinematic constraints are imposed to the edges of the model (multiple point constraint, ABAQUS 2009), allowing it to move as the free field in the direction of the seismic motion (Gerolymos et al. 2008). This condition has been found to be representative of the boundaries imposed in the *laminar boxes*, which are used in shaking table and dynamic centrifuge experiments. Two L x L configurations are considered in this study, namely 5B x 5B and 10B x 10B. The mesh for the soil-caisson consists of 12500 elements in the former (5Bx5B) and 52020 elements in the latter (10Bx10B) case.

4.2.3.1. Static loading

Static pushover analyses were performed for all four structural configurations, for both model sizes. For such analysis, horizontal displacement is applied on the mass of the superstructure. The results from the tests, given in the form of horizontal force (P) - horizontal displacement (*u*) at the mass level and presented in Fig. 5, are hardly distinguishable and thus confirm (already known from the literature) that the lateral boundaries can be placed fairly close to the foundation (just outside the “pressure bulb”) and they can be of any “elementary” type (from “free” to “fixed”).

4.2.3.2. Dynamic loading

The location and type of the lateral boundaries is a significant issue in dynamic modelling. Under transient loading waves emanating from the caisson–soil interface cannot propagate to infinity unless special transmitting boundaries are placed at suitably large distances. "Elementary" boundaries may cause spurious reflections, thereby contaminating the wave field around the caisson. The boundary conditions employed in this study, however, placed at an "*adequate*" distance from the foundation might suffice. The reason lies in an important effect, often overlooked in seismic foundation engineering; that is the existence of a *cutoff* period for the radiation damping, equal to the first natural period of the soil profile, above which spurious reflections at the boundaries are limited as a result of a *destructive interference* and, hence, there is no radiation damping (Veletsos & Wei 1971, Luco & Westman 1971, Kausel 1974, Gazetas 1987, Wolf & Song 2002). In an attempt to take advantage of this effect and given that the first natural period of the soil profile is T_{soil} = 0.41 sec, the piers were deliberately modelled with a fixed fundamental period larger than that of the soil (T_{str} = 0.6 sec). During the dynamic analysis the effective period of the superstructures is expected to increase due to the nonlinear soil-structure interaction effects, thus further reducing the amount of the radiated energy. In the absence of a *cutoff* frequency for the radiation damping, then the boundaries should be placed at far distances from the loaded caisson, increasing prohibitively the computational cost (Panagiotidou et al. 2012).

To verify the ability of our model to accurately reproduce the aforementioned phenomena, we extended the parametric study including the following:

(i) *Transient dynamic excitation*

Dynamic analysis was performed assuming linear elastic soil and pier. Fully bonded conditions between soil and caisson were considered. The superstructure height and mass were arbitrarily chosen H = 10m and m = 2700 Mgr, respectively, while the geometric properties were modified to correspond to a structure with fixed-base period (a) T_{str} = 0.6 sec, larger than the T_{soil} = 0.41

sec, and (b) T_{str} = 0.2 sec, smaller than T_{soil} (note that the criterion applies for the effective T_{SSI} ; a condition which, in this case, is met). The Rinaldi (1994) record was used as seismic excitation at the base of the soil profile. Material and stiffness proportional Rayleigh damping is taken equal to 2% between the eigenfrequency of the soil deposit and the dominant frequency of the seismic motion. Two model sizes were considered, 5B x 5B and 10B x 10B, to examine the effect of the distance of the lateral boundaries. Fig 6 shows the analysis results. As anticipated, for the case of $T_{SSI} > T_{soil}$ the distance of the lateral boundaries has minimal effect on the response, in terms of both acceleration time-histories and response spectra at the mass level, highlighting the "absence" of *trapped* seismic energy within the borders of the model. In stark contrast, the respective response differs considerably when assuming a "stiffer" superstructure than the soil profile ($T_{SSI} < T_{soil}$), denoting noticeable boundary effects.

(ii) *Harmonic excitation*

For the direct comparison with available theoretical solutions concerning the radiation damping (Gazetas, 1991), the model, considering homogenous soil conditions, was subjected to harmonic dynamic loading. In this case, however, instead of a superstructure, a harmonic displacement loading was applied at the top of the caisson. The amplitude of the loading was u_0 = 0.001 m. Two vibration periods were used, (a) T = 1.25 sec > T_{soil} (= 0.42 sec), and (b) T = 0.13 sec < T_{soil} . Elastic soil conditions were assumed, bearing the material properties of the stiff clay. Again, two model sizes were investigated (5Bx5B and 10Bx10B). The comparison, presented in Fig 7, is performed in terms of the equivalent dashpot coefficient, C, calculated from the horizontal force (Q) - horizontal displacement (u) loops, as (Gazetas, 1991):

$$C = \frac{\Delta W}{\pi \omega u_0^{\,2}} \tag{1}$$

where ΔW is the viscous energy consumed during a cycle of motion, and ω the vibration frequency. The theoretical value for the dashpot coefficient, C, was estimated using the method of Gazetas (1991), as C = 270 MN·s·m^{-1}. The results once again reveal the validity of our approach. The response under short period excitation (b, in Fig 7) clearly demonstrates the

influence of the location of the lateral boundaries on the response and, moreover, the presence of a great amount of undamped wave energy into the domain of the model, even though slightly smaller than the theoretically estimated value. Therefore, in this case, special transmitting boundaries should have been placed at the lateral boundaries to absorb this radiation energy. In stark contrast, the respective response under the long-period excitation (a, in Fig 7) is almost linear and hardly distinguishable between the two model sizes. Most significantly, however, the radiated seismic energy is negligible; yet another evidence for the existence of the *cutoff* frequency.

Taking into consideration the above model verification and in order to reduce the computational cost in the nonlinear dynamic analyses performed in this study, we adopted the L=5 B distance in all studied cases.

4.2.4. Soil constitutive modelling

Soil behavior is described through a constitutive model which is a reformulation of that originally developed by Armstrong & Frederick (1966). It belongs to the general category of single surface plasticity models, and it is available in the material library of ABAQUS (2009). According to their theory, the evolution of stresses is described by the relation:

$$\sigma = \sigma_0 + \alpha \tag{2}$$

where σ_0 is the value of stress at zero plastic strain, assumed to remain constant. The parameter α is the "back-stress", which defines the kinematic evolution of the yield surface in the stress space. Integration of the back-stress evolution law over a half cycle of unidirectional load (e.g. tension or compression) yields the following expression:

$$\alpha = \frac{C}{\gamma}\left[1 - \exp\left(-\gamma \varepsilon^{pl}\right)\right] \tag{3}$$

in which, *C* and *γ* are hardening parameters that define the maximum transition of the yield surface, and the rate of transition, respectively, and ε^{pl} is the plastic strain. Differentiating α with respect to ε^{pl} and taking the limit at zero, one obtains for parameter *C* (Gerolymos and Gazetas 2006):

$$\left.\frac{\partial \alpha}{\partial \varepsilon^{pl}}\right|_{\varepsilon^{pl}\to 0} = C = E \tag{4}$$

where *E* is the modulus of elasticity.

The evolution of the kinematic and the isotropic hardening components of the hardening rule is illustrated in Fig. 8a and 8b for unidirectional and multiaxial loading, respectively. The evolution law for the kinematic hardening component implies that the backstress is contained within a cylinder of radius:

$$\sqrt{\frac{2}{3}}\,\alpha^{s} = \sqrt{\frac{2}{3}}\,\frac{C}{\gamma} \tag{5}$$

where α_s is the magnitude of α at saturation. Since the yield surface remains bounded, this implies that any stress point must lie within a cylinder of radius $\sqrt{(2/3)}\,\sigma_y$. At large plastic strains, any stress point is contained within a cylinder of radius $\sqrt{(2/3)}\,(\alpha_s + \sigma_s)$ where σ_s is the equivalent stress defining the size of the yield surface at large plastic strain.

The maximum yield stress (at saturation) is:

$$\sigma_y = \frac{C}{\gamma} + \sigma_0 \tag{6}$$

According to the Von Mises yield criterion this ultimate stress is:

$$\sigma_y = \sqrt{3}\, S_u \tag{7}$$

From Eqs. 4, 6 and 7 we have (Gerolymos and Gazetas 2006):

$$\gamma = \frac{E}{\sqrt{3}\, S_u - \sigma_0} \tag{8}$$

To avoid numerical instability, the stress at zero plastic strain, σ_0 , should be expressed as a small fraction of the uniaxial strength σ_y (usually of the order of 1/5 to 1/20).

Substituting Eqs. 3, 4, and 8 into Eq. 2, and setting $\varepsilon^{pl} = \gamma^{pl} / \sqrt{3}$, the authors derived the following analytical expression for the shear modulus reduction ratio:

$$\frac{G}{G_0} = \begin{cases} 1\,, & \gamma < \gamma_y \\ \dfrac{1}{(\gamma - \gamma_y)\sqrt{3}\, G_0} \left(\sqrt{3}\, S_u - \sigma_0\right)\left(1 - e^{\frac{-3G_0}{\sqrt{3}\, S_u - \sigma_0} \cdot \frac{(\gamma - \gamma_y)}{\sqrt{3}}}\right) & otherwise \end{cases} \tag{9}$$

in which

$$\gamma_y = \frac{\sigma_0}{\sqrt{3}\, G_0} \tag{10}$$

is the shear strain at incipient yielding, G_0 is the maximum shear modulus related to the elasticity modulus according to $E \approx 3G_0$. Accordingly, the equivalent damping ratio ξ is calculated as follows:

$$\xi = \begin{cases} 0\,, & \gamma < \gamma_y \\ \dfrac{2}{\pi}\left(\dfrac{1+e^{\frac{-3G_0(\gamma-\gamma_y)}{\sqrt{3}S_u-\sigma_0}}}{1-e^{\frac{-3G_0(\gamma-\gamma_y)}{\sqrt{3}S_u-\sigma_0}}} - \dfrac{2(\sqrt{3}S_u-\sigma_0)}{3G_0(\gamma-\gamma_y)} \right) & otherwise \end{cases} \quad (11)$$

Based on Eqs. 9 and 11, the model parameters are calibrated to fit published $G-\gamma$ and $\xi-\gamma$ curves of the literature. Fig. 8c and 8d illustrate the validation of the kinematic hardening model (through simple shear finite element analysis) against published published $G-\gamma$ and $\xi-\gamma$ curves by Ishibashi and Zhang (1993). As anticipated, given that the Masing criterion is adopted for loading-unloading, the model overestimates the hysteretic damping for large shear strain amplitudes ($\gamma > 10^{-2}$). It should be observed, however, that with the addition of 2% Rayleigh damping to the hysteretic damping the two curves in Fig. 8c practically coincide for small too moderate shear stain amplitudes ($\gamma < 0.003$).

4.2.5. Validation of constitutive model

The constitutive model used in this study has already been applied in the analysis of caisson foundations in clayey deposits by Gerolymos and Gazetas (2006). Furthermore, Anastasopoulos et al (2011) validated the model for the case of shallow footings on clay against centrifuge tests under cyclic loading. However, the model has not yet been validated for the nonlinear response of embedded and caisson foundations. Therefore, the authors believe that prior to embarking to sophisticated dynamic analyses, the ability of our model to reliably reproduce complex soil-structure interaction phenomena associated with embedded foundations has to be validated. To the authors' knowledge, the published experimental work that best relates to our study is the "*field trials of suction caissons in clay for offshore wind turbine foundations*", by Houlsby et al (2005). Having been conducted in field conditions, the results from the tests are unaffected from any unavoidable scale effects present in small-scale experiments. Moreover, the loading amplitude ranged from very small (nearly elastic response) to very large (near soil failure),

where caisson-soil interface sliding and gapping was observed; precisely the behaviour our model aspires to simulate.

Since the purpose of this paper is to examine the response at very large soil deformations (with the subsequent mobilization of interface nonlinearities), the large amplitude ***Jack_3.0_1*** cyclic test was considered the most appropriate to be used for our validation process. Fig 9 displays the schematic of the field test along with the undrained shear strength profile, as provided specifically for the Bothkennar test site by Nash et al (1992) and considered in the work of Houlsby et al (2005). For details on the experimental setup, soil conditions and tests sequence, the reader may refer to Houlsby et al (2005). The constitutive model parameters, detailed in the previous section, were calibrated using the given soil profile.

The FE-computed bearing capacity under undrained conditions was Nult = 743 kN, strikingly comparable to the bearing-capacity Nult = 746 kN that was analytically estimated by Houlsby et al (2005). The results of numerical simulations are compared with the experimental ones in Fig 10, in terms of (a) moment-rotation response, and (b) secant stiffness values as a function of the amplitude of rotation. Moreover, to illustrate the failure mechanisms developed during the response of suction caissons under large amplitude moment loading, snapshots depicting contours of plastic strain magnitude are also presented in Fig 10a for (*A*) the end of second unloading, and (*B*) the end of the third loading.

In Fig 10a, the agreement between numerical and experimental results is satisfactory, especially for the first loading-unloading cycles. After that, although good matching is observed in terms of peak rotation, the experimental results demonstrate a considerable rotational stiffness degradation, especially in the large amplitude cycles, that could not be adequately described by the numerical model. The reasons for this difference lie in the following:

(a) The Masing criterion for loading-unloading, adopted in our model.

(b) The field test conditions. More specifically, the authors of the experiment commented on this behaviour in a following publication, by Kelly et al (2006). Through comparison between laboratory experiments aiming to reproduce their field tests, they stated that this marked

stiffness degradation is due to softening of the Bothkennar clay over time, given that the tests were conducted with considerable time-lag. Thus, it is safe to assume that the initial assumption of undrained condition is not entirely valid, since partial drainage (and subsequent softening) is very probable to have occurred.

Worthy of note is the evidence of interface gapping, as observed from the characteristic shape of the cycles, in both the experimental and our numerical results; After an initially stiff unloading, a very flexible response is observed (denoting the 'gap'), followed by a slight stiffening as the gap (created by the previous half cycle) is closed.

Finally, the model reliably reproduces the experimental secant stiffnesses as a function of moment amplitude, as shown in Fig 10b.

Overall, throughout the validation process our model has shown to yield quite reasonable results. The discrepancies between the experimental and the numerical results can be attributed to the approximate nature of the model and some experimental details, which are either not known or impossible to capture.

Thus, the constitutive model parameters for the 2-layer clayey soil profile used in the dynamic analysis were derived accordingly. The respective values are presented in **Table 3.**

Table 3. Soil constitutive model parameters used in the dynamic analysis

	σ_0	C	γ
Clay	11.26	97500	962.25
Stiff clay	22.52	195000	962.25

4.3. Analysis methodology

The seismic performance of all four examined systems is investigated through nonlinear time-history analysis. It should be highlighted that in most published earthquake response analyses the examined systems are subjected to a variety of seismic motions to capture the interplay between the exciting dynamic characteristics (e.g. dominant periods, frequency content, PGAs, sequence of pulses) and the vibrational characteristics (natural, T_{str}, and effective fundamental

period, T_{SSI}) of the structures; a process that comes with a significant computational cost. A technique, however, that is used in practice to address this issue is to modify the frequency content and phasing of the real records to match a target spectrum. In this respect, this paper follows a methodology in which the systems are subjected to appropriately calibrated seismic motions, so that their effective fundamental periods, T_{SSI}, fall within a plateau of constant spectral acceleration, thus eliminating the aforementioned interactions. A similar procedure has been adopted by Abrahamson (1992), Bazzurro and Luco (2006) and Hancock at al. (2006). Having, in this way, removed any bias of the response mechanisms on the dynamic properties, we may focus on the main question posed in this study, whether mobilization of soil nonlinearities is beneficial or detrimental, and compare the response on a "*fair*" basis. Carballo and Cornell (2000) suggested that the use of spectrum-matched records is not only legitimate, but also useful, because it limits the number of nonlinear dynamic analysis runs compared to the use of real records without compromising the estimation accuracy.

The procedure, schematically illustrated in Fig. 11, consists of the following steps:

1) Three real accelerograms (Fig. 11a, also denoted as "natural" records) are selected as seismic excitations for all examined systems. In this paper the ones recorded at *Sakarya*, 1999 Turkey earthquake, *Rinaldi*, 1994 Northridge earthquake, and *JMA*, 1995 Kobe earthquake are used, covering a wide range of forward-rupture directivity effects, large number of significant cycles, and/or flingstep effects.

2) Within a heuristic optimization procedure (trial and error technique), also presented through a detailed flowchart in Fig. 12, the "natural" records are modified until their response spectra match an artificial *target response spectrum* (Fig. 11b), which, in our case, resembles a typical code design spectrum, having a plateau in 0.6 g for a wide range of periods (0.2 to 1.6 sec; it will be shown that the effective periods T_{SSI} of both *over*- and *under*-designed systems fall into this specific range).

3) Upon matching, the new records (Fig. 11c) are deconvoluted to the base of the profile, resulting in the *modified* records used in the nonlinear dynamic analyses (Fig. 11d).

The three selected "natural" records, the *modified* (input) motions and the corresponding elastic response spectra are presented in Fig. 13. The advantages of the aforementioned procedure are: (a) the *modified* record retain the near-fault characteristics (e.g. forward-directivity or fling-step pulses) of its "natural" counterpart and (b) the phase angles of the natural record are not affected by the process.

4.4. Analysis Results and Discussion

The performance of the four systems is compared in Figs. 14–24, in terms of acceleration and displacement time–histories at the deck mass, "*floor*" response spectra, moment–rotation and settlement–rotation loops at the head of the caisson.

To facilitate the understanding and explanation of results, it should be fruitful to give a brief description of the mobilized impedance mechanisms that govern the response of the studied systems. That is :

(a) Soil inelasticity and bearing capacity failure that generate hysteretic damping. It will be shown that that this type of impedance mechanism dominates the response of *over*-designed foundations.

(b) Radiation damping due to the outward---originated from the caisson---spreading waves (only marginal in our case due to the existence of a *cutoff* period).

(c) Geometric nonlinearities: uplift and sliding at the caisson-soil interfaces, that lead to a threshold value (*cutoff*) for the maximum transmitted seismic forces. It will be shown that this type of impedance mechanism is the most influential one to the response of the *under*-designed foundations.

The acceleration time–histories calculated at the deck are presented in Fig. 14. Keeping into consideration that all systems were a priori designed to exhibit spectral acceleration smaller than 0.6 g, the following observations are drawn:

- In the case of FS_V = 5.0 ("light" superstructure) the accelerations developed at the structure founded on the *under*-designed caisson (FS_E = 0.7) is significantly smaller, reaching a maximum of a = 0.4 g, compared to the one founded on the *over*-designed caisson, where almost the maximum seismic action is developed. That is : a = 0.6 g for the system subjected to the modified Sakarya record and a = 0.55 g for the ones under JMA and Rinaldi records. This small discrepancy is attributed to the severe nature of the two records, bearing forward directivity effects, which cause intense soil and geometric nonlinearities, further reducing the transmitted accelerations to the deck.

- It is rather interesting to observe that in the case of FS_V = 2.5 ("heavy" superstructure) there is no notable difference in the response of the superstructures founded on either the *over*-designed or the *under*-designed foundations, especially in the first cycles. A possible explanation is that the intense initial soil plastification imposed by the heavy superstructure "consumes" most of the available soil capacity, leaving, in the *under*-designed cases, a relatively low excess potential for acceleration *cutoff* by the dynamically induced geometric nonlinearities (uplift of the base, detachment and sliding of the side walls from the soil) that would additionally attenuate the transmitting seismic forces.

Fig. 14 depicts the natural vibration periods due to soil–structure–interaction effects, T_{SSI}, derived from the response acceleration time histories after the input motion has subsided. These parameters are needed for the evaluation of our methodology. It can be observed that T_{SSI} in all occasions fall well within the range of the target spectrum plateau, Sa = 0.6 g for T : 0.2−1.6 sec (Fig. 11); a main prerequisite for the validity of our methodology is thus met.

The strong contribution of geometric nonlinearities in de-amplifying the seismic motion is more evident in Fig. 15, where the comparison of the "*floor*" spectral accelerations at the mass of the superstructure (i.e., the spectral accelerations of the computed motion of the superstructure mass) is unveiled. The following observations are worthy of note:

- As expected, the "flexible" response of the *under*-designed foundation results in reduced spectral accelerations at the deck and increased effective vibration periods.

- In the *over*-designed foundations, the "heavy" and "light" structures exhibit similar spectral accelerations. It is thus evident in this case that both the hysteretic impedance mechanism, due to soil inelasticity experienced by the "heavy" structure, and the interface nonlinearities (expected for the lightly loaded caissons), have a marginal to moderate effect on the response.

- In the *under*-designed caissons, substantial interface nonlinearities develop in the case of the lightly loaded case. These uplift and sliding capacities of the caisson set a threshold value for the transmitted seismic force, thus acting as a seismic isolation for the superstructure. The aforementioned behaviour has only a moderate effect in the case of the heavily loaded foundation, where the larger area of the caisson walls in contact with the soil mobilizes additional soil resistance which increases the seismic load capacity of the superstructure, thus leading to slightly larger "*floor*" spectral accelerations. The magnitude of spectral maxima decrease for each case of FS_V serves to elucidate the effect of the main impedance mechanisms: for FS_V = 5.0 the reduction reaches 58% (*Rinaldi* excitation), whereas for FS_V = 2.5 it reaches 50% (*JMA* excitation).

In brief, the contribution of each one of the two damping mechanisms in the reduction of the spectral accelerations for all the examined cases may be summarized in **Table 4**:

Table 4

systems	hysteretic damping	geometric nonlinearities	reduction in "*floor*" spectral accelerations
$FS_V = 5.0$, $FS_E = 0.7$	*moderate*	*substantial*	*high*
$FS_V = 2.5$, $FS_E = 0.7$	*substantial*	*moderate*	*moderate*
$FS_V = 5.0$, $FS_E = 1.3$	*marginal*	*marginal*	*minor*
$FS_V = 2.5$, $FS_E = 1.3$	*marginal to moderate*	*marginal*	*small*

Note that the secondary peaks in the spectra at larger periods, mainly present at the *under*-designed foundations, may be attributed to the subharmonic motions produced during the earthquake by the continuous impact between the caisson and the soil due to the intense interface separation and gapping.

The time histories of deck horizontal displacement, i.e. the *drift*, for all cases of static and seismic safety factors and exciting motions are compared in Figs. 16 and 17. As graphically illustrated in the adjacent sketch notation, the *drift* has two components (see also Priestley et al. 1996): (i) the "*rigid drift*" $U_{rigid} = \vartheta H$, i.e. the displacement due to motion of the caisson as a rigid body, and (ii) the "*flexural drift*", i.e. the structural displacement due to flexural distortion of the pier column. Both U_{rigid} and U_{flex} are presented normalized with the respective maximum total displacement, U_{total_max}, the values of which are also given in the graphs. This way, the contribution of pier flexural distortion and caisson rotation to the final result of interest (i.e. the total drift) can be inferred. For reasons of reciprocality, the two figures should be observed alongside. As might have been expected, in the *over*-designed foundations the drift is mainly due to pier distortion U_{flex}, leading to a subsequent increase in structural distress. Exactly the opposite is observed in the *under*-designed foundations: the *drift* is mainly due to foundation rotation U_{rigid}, causing less seismic loading on the pier but increased dynamic and residual displacements due to soil yielding. As for the latter ($U_{residual}$), worthy of note is the relative severity of the forward directivity pulses (*Rinaldi* and *JMA* records) on the response of the lightly loaded seismically *under*-designed caisson; under *Rinaldi* excitation, the $U_{residual} \approx 13$ cm

(compared to ≈ 2.5 cm computed for the *over*-designed alternative). Yet, given that the pier height is 26 m, this results in a quite tolerable drift ratio of 0.5%. Under *JMA* excitation, $U_{residual}$ ≈ 2.5 cm (compared to ≈ 1.0 cm for the *over*-designed), again resulting in a drift ratio of only 0.09%. Rather interestingly, the deck maintains almost no $U_{residual}$ when subjected to the fling-step pulse of the *Sakarya* record.

In summary of the above, choosing to design a caisson foundation allowing for plasticity below ground could substantially reduce the cost but might also demand appropriate structural provisions to accommodate for increased seismic displacements.

The moment–rotation (M–ϑ) curves at caisson head for FS_V = 2.5 and FS_V = 5.0 are portrayed in Figs. 18 and 19 respectively. The additional aggravating moment induced by the mass (mgϑh : P-δ effects) was considered in the calculations. Respecting their design principles, the response of the *over*-designed foundations remains practically elastic, while the response of the respective *under*-designed caissons is strongly inelastic. Since the pier columns behave elastically, this difference in the response manifests qualitatively the effect of each one of the nonlinear damping mechanisms acting below ground surface; that is the material nonlinearities (in the *over*-designed foundations) and the interface nonlinearities (in the *under*-designed foundations). Note the highly irregular shape of the loops in Fig. 19 which reflects the successive detachments/re-attachments of the lightly loaded seismically *under*-designed caisson from the surrounding soil. Another noteworthy observation from the M–ϑ loops of both heavily and lightly loaded foundations is that that they do not exhibit significant strength degradation, indicating minor P-δ effects.

Fig. 20 compares the settlement–rotation (w–ϑ) response of the seismically *over*- and *under*-designed caissons, for FS_V = 2.5. Being governed by the soil yielding around and below the caisson induced by the heavy structure, the response is surprisingly comparable; the loops are quite similar in terms of both dynamic settlements and rotations. As expected, however, the *under*-designed foundations reach a slightly more unfavorable residual state.

In the lightly loaded foundations, presented in Fig. 21, the *over*-designed caissons experience practically elastic settlements w ≈ 3 cm. In marked contrast, in the *under*-designed caissons the

dynamic settlements are larger but quite tolerable: $w \approx 5$ cm. It is noteworthy, herein, that the latter experience larger residual tilting when subjected to the strong directivity pulses of *JMA* and *Rinaldi* records (as already attested by the residual deck drift), while the maximum settlement is attained during the fling type pulse of *Sakarya* record.

Perhaps the most important observation from the above is that despite the soil and interface nonlinearities, not only the structures do not collapse, but the permanent settlements and rotations are rather limited, providing further evidence that mobilization of failure mechanisms below ground may act as a "*safety valve*" for the superstructure.

Fig 22 further elucidates the aforementioned observations by plotting the ratio

$$\lambda = \lambda(t) = \frac{\alpha(t)}{A} \tag{12}$$

(Panagiotidou et al. 2012) of the effective contact area, $\alpha = \alpha(t)$, divided by the (total) area A of the respective caisson side (note that the discontinuous form of the λ(t) plots is an undesirable but unavoidable consequence of the discretization of the contact surface). For reasons of brevity, results from only the two "extreme", though representative, systems are given, namely the *under*-designed lightly loaded and the over-designed heavily loaded caisson, under the *modified* JMA record. The interpretation of these curves is straightforward. Note in particular that the FS_v = 2.5 system attains full base contact and almost full side contact [λ(t) > 0.8] for most of the duration of the seismic motion. In contrast, the *under*-designed caisson experiences immediate intense interface gapping at the sides and moderate at the bottom. The remarkably similar residual gapping attained by the systems is attributed to different mechanisms, already detailed in the prequel: in the former case, the loss of the side-contact is due to the gapping, whereas in the latter, it is mainly attributed to the large dynamic settlements.

In Fig 22 shear stress–strain loops calculated at a designated point on the caisson-soil interface near the surface are also given for the two extreme cases examined. The response of the *under*-designed caisson clearly demonstrates the intense shearing that is exerted into the soil by the interface gapping during dynamic loading.

It is interesting to observe that in neither case the ultimate shear stress exceeds the undrained shear strength (S_u = 65 kPa). This implies that material hardening due to cyclic loading is not reproduced by the utilized constitutive model at this case.

Figs. 23 and 24 compare the response in terms of plastic shear strain contours at the end of the shaking. It is now evident that the extended soil yielding dominates the response of the heavily loaded caissons (Figs. 23a), since the contribution of the interface separation, in the *under*-designed (FS_E = 0.7) alternatives, is minimal. In stark contrast, the *over*-designed lightly loaded caissons (Fig. 24a) experience very little inelastic action in the soil, concentrated mainly at the top and bottom of the caisson, whereas the respective *under*-designed foundations suffer a passive–type soil failure in front and back of the caisson accompanied by gap formation and sliding in the sides and base (deformation scale factor = 20). Note again the distribution of the plastic zone around the caissons subjected to directivity pulses (*JMA* and *Rinaldi* records) resulting in permanent, though acceptable, tilting of the foundation.

4.5. Summary and Conclusions

The seismic performance of caisson foundations supporting bridge piers was investigated parametrically through a series of 3D finite element nonlinear dynamic analyses. The emphasis was given on the role of soil and caisson-soil interface nonlinearities. Prior to embarking on the parametric investigation, the finite element model was verified in static and dynamic loading conditions and the soil constitutive model was validated against available related experimental data.

Similar caissons supporting elastic SDOF structures were examined. The mass and height of the superstructure was varied to correspond to heavily and lightly loaded, seismically *over*- ($FS_E > 1$) and *under*-designed ($FS_E < 1$) caisson. A series of modified seismic records was used as base excitation. It was found out that seismically *under*-designing a caisson foundation generally leads to :

- Reduction in superstructure response and spectral accelerations.
- Significant reduction in flexural deformations (structural demand).
- Increased dynamic settlements and rotations but minimal residual displacements and tilting.

It was observed that the response of heavily loaded caissons is determined by excessive material (soil) inelasticity, whereas intense caisson–soil interface separation and gapping prevails in the response of lightly loaded foundations. Furthermore, the mobilization of caisson-soil interface nonlinearities provides a threshold for the transmitted seismic forces to the superstructure. Finally, it may be inferred that the seismically *under*-designed foundations combined with a high static safety factor are more advantageous compared to the seismically *over*-designed heavily loaded caissons, in both static and dynamic terms, providing a low-cost solution with high seismic isolation potential.

References

ABAQUS, Inc. (2009), *ABAQUS user's manual*, Providence, R.I.

Abrahamson NA (1992) Non-stationary spectral matching. *Seismological Research Letters*, 63 (1), 30-30.

Anastasopoulos I, Gazetas G, Loli M, Apostolou M, Gerolymos N (2010) Soil failure can be used for seismic protection of structures. *Bulletin of Earthquake Engineering* 8(2): 309-326.

Anastasopoulos I, Gelagoti F, Kourkoulis R, Gazetas G (2011) Simplified Constitutive model for Simulation of Cyclic Response of Shallow Foundations: Validation against Laboratory Tests. *Journal of Geotechnical and Geoenvironmental Engineering*, ASCE, 137 (12): 1154-1168.

Apostolou M, Gazetas G (2005) Rocking of foundations under strong shaking: mobilisation of bearing capacity and displacement demands. *1st Greece–Japan Workshop, Seismic Design, Observation, Retrofit*, Athens, 11–12 October, pp 131–140.

Armstrong PJ, Frederick CO (1966) *A mathematical representation of the multiaxial Bauschinger effect*. Technical Report RD/B/N 731, Central Electricity Generating Board, Berkeley, UK. Reprint in: Armstrong PJ, Frederick CO (2007) A mathematical representation of the multiaxial Bauschinger effect. *Materials at High Temperatures*, 24 (1): 1-26.

Bazzurro P, Luco N (2006) Do scaled and spectrum-matched near-source records produce biased nonlinear structural responses*? 8th US National Conference on Earthquake Engineering* (15): 8811-8820, San Francisco, CA.

Carballo JE, Cornell CA (2000) *Probabilistic seismic demand analysis: Spectrum matching and design.* Research Report No. RMS-41; Department of Civil and Environmental Engineering, Reliability of Marine Structures Program, Stanford University, CA.

Chatzigogos CT, Pecker A, Salencon J (2009) Macroelement modeling of shallow foundations. *Soil Dynamics and Earthquake Engineering* 29(6):765–781.

Davidson HL (1982) *Laterally loaded drilled pier research*. Research Report EL-2197, EPRI.

Faccioli E, Paolucci R, Vivero G (2001) Investigation of seismic soil-footing interaction by large scale cyclic tests and analytical models. *4th Int. Conf. Recent Advances in Geotechnical Earthquake Engineering and Soil Dynamics*, March 26-31, San Diego, California.

FEMA 356 (2000) *Prestandard and commentary for the seismic rehabilitation of buildings*. Federal Emergency Management Agency, Washington DC.

Gajan S, Phalen JD, Kutter BL, Hutchinson TC, Martin G (2005) Centrifuge modeling of load-deformation behavior of rocking shallow foundations. *Soil Dynamics and Earthquake Engineering* 25(7–10):773–783.

Gajan S, Hutchinson TC, Kutter BL, Raychowdhury P, Ugalde JA, Stewart JP (2008) *Numerical models for the analysis and performance-based design of shallow foundations subjected to seismic loading*. Research Report to Pacific Earthquake Engineering Research Center (PEER), Univ. of California, Berkeley, California.

Gajan S, Kutter BL (2008) Capacity, settlement, and energy dissipation of shallow footings subjected to rocking. *Journal of Geotechnical and Geoenvironmental Engineering*, ASCE 134(8): 1129–1141.

Gazetas G (1991) Formulas and charts for impedances of surface and embedded foundations. *Journal of Geotechnical Engineering*, ASCE, 117 (9): pp 1363-1381.

Gazetas G, Anastasopoulos I, Apostolou M (2007) Shallow and deep foundations under fault rupture or strong seismic shaking. *Earthquake Geotechnical Engineering*, K.D. Pitilakis (ed), Chapter 9, pp 185-215, Springer.

Gerolymos N, Drosos V, Gazetas G (2009) Seismic response of single-column bent on pile: evidence of beneficial role of pile and soil inelasticity. *Bulletin of Earthquake Engineering* 7(2): 547–573 Special Issue: Earthquake Protection of Bridges.

Gerolymos N, Gazetas G (2006a) Winkler model for lateral response of rigid caisson foundations in linear soil. *Soil Dynamics and Earthquake Engineering* 26(5): 347-361.

Gerolymos N, Gazetas G (2006b) Development of Winkler model for static and dynamic response of caisson foundations with soil and interface nonlinearities. *Soil Dynamics and Earthquake Engineering* 26 (5): 363-376.

Gerolymos N, Gazetas G (2006c) Static and dynamic response of massive caisson foundations with soil and interface nonlinearities - Validation and results. *Soil Dynamics and Earthquake Engineering* 26(5): 377-394.

Gerolymos N, Giannakou A, Anastasopoulos I, Gazetas G (2008) Evidence of beneficial role of inclined piles: observations and numerical results. *Bulletin of Earthquake Engineering* 6(4):705–722. Special Issue: *Integrated approach to fault rupture- and soil-foundation interaction*.

Hancock J, Watson-Lamprey J, Abrahamson NA, Bommer JJ , Markatis A, McCoy E, Mendis R (2006) An improved method of matching response spectra of recorded earthquake ground motion using wavelets. *Journal of Earthquake Engineering* (10) Special Issue (1): 67-89.

Houlsby GT, Kelly RB, Huxtable J, Byrne BW (2005) Field trials of suction caissons in clay for offshore wind turbine foundations. *Geotechnique* 55(4): 287-296.

Hutchinson TC, Chai YH, Boulanger RW, Idriss IM (2004) Inelastic Seismic Response of Extended Pile-Shaft-Supported Bridge Structures. EERI *Earthquake Spectra* 20(4): 1057-1080.

Ishibashi I, Zhang X (1993) Unified dynamic shear moduli and damping ratios of sand and clay. *Soils and Foundations* 33(1): 12−191.

Kausel E (1974) Forced vibrations of circular foundations on layered media. *Research Report R74-11*, MIT.

Kawashima K, Nagai T, Sakellaraki D (2007) Rocking seismic isolation of bridges supported by spread foundations. *2nd Japan–Greece workshop on seismic design, observation, and retrofit of foundations*, Tokyo, Japan, April 3–4, pp 254–265.

Kelly RB, Houlsby GT, Byrne BW (2006) A comparison of field and laboratory tests of caisson foundations in sand and clay. *Geotechnique* 56(9): 617-626.

Kutter BL, Martin G, Hutchinson TC, Harden C, Gajan S, Phalen JD (2003) Status report on study of modeling of nonlinear cyclic load-deformation behavior of shallow foundations. *PEER workshop*, University of California, Davis.

Luco JE, Westman RA (1971) Dynamic response of circular footings. *Journal of the Engineering Mechanics Division*, ASCE, 97, No5: 1381–1395.

Martin GR, Lam IP (2000) Earthquake resistant design of foundations: retrofit of existing foundations. *Geoeng 2000*, International Conference on Geological and Geotechnical Engineering, Melbourne, Australia.

Mergos PE, Kawashima K (2005) Rocking isolation of a typical bridge pier on spread foundation. *Journal of Earthquake Eng*ineering 9(sup2): 395–414.

Nash DFT, Powell JJM, Lloyd IM (1992) Initial investigations of the soft clay test site at Bothkennar. *Geotechnique* 42(2): 163-181.

Panagiotidou AI, Gazetas G, Gerolymos N (2012) Pushover and Seismic Response of Foundations on Stiff Clay: Analysis with P-Delta Effects. EERI *Earthquake Spectra* 28(4): 1589-1618.

Paolucci R (1997) Simplified evaluation of earthquake induced permanent displacement of shallow foundations. *Journal of Earthquake Engineering* 1(3): 563–579.

Paolucci R, Shirato M, Yilmaz MT (2007) Seismic behavior of shallow foundations: shaking table experiments vs numerical modeling. *Earthquake Engineering and Structural Dynamics* 37(4): 577–595.

Pecker A (1998) Capacity design principles for shallow foundations in seismic areas. *Proc. 11th european conference on earthquake engineering*, A.A. Balkema Publishing, Amsterdam.

Pecker A (2003) Aseismic foundation design process, lessons learned from two major projects: the Vasco de Gama and the Rion Antirion bridges. *ACI international conference on seismic bridge design and retrofit*, University of California at San Diego, La Jolla, USA.

Priestley MJN, Seible F, Calvi GM (1996) *Seismic design and retrofit of bridges*. Wiley, New York

Silva, P. F., and Manzari, M. T. (2008) Nonlinear Pushover Analysis of Bridge Columns Supported on Full-Moment Connection CISS Piles on Clays. EERI *Earthquake Spectra* 24(3): 751-774.

Tsigginos C, Gerolymos N, Assimaki D, Gazetas G (2008) Seismic response of bridge pier on rigid caisson foundation in soil stratum. *Earthquake Engineering & Engineering Vibration* 7(1): 33-44.

Vetetsos AS, Wei YT (1971) Lateral and rocking vibration of footings. *Journal of the Soil Mechanics and Foundations Division*, ASCE, 97: 1227–1248.

Wolf JP, Song C (2002) Some cornerstones of dynamic soil–structure interaction. *Engineering Structures* 24: 13–28.

Zafeirakos A, Gerolymos N, Drosos V (2013) Incremental dynamic analysis of caisson-pier interaction. *Soil Dynamics and Earthquake Engineering* 48: 71-88.

Chapter 4

Figures

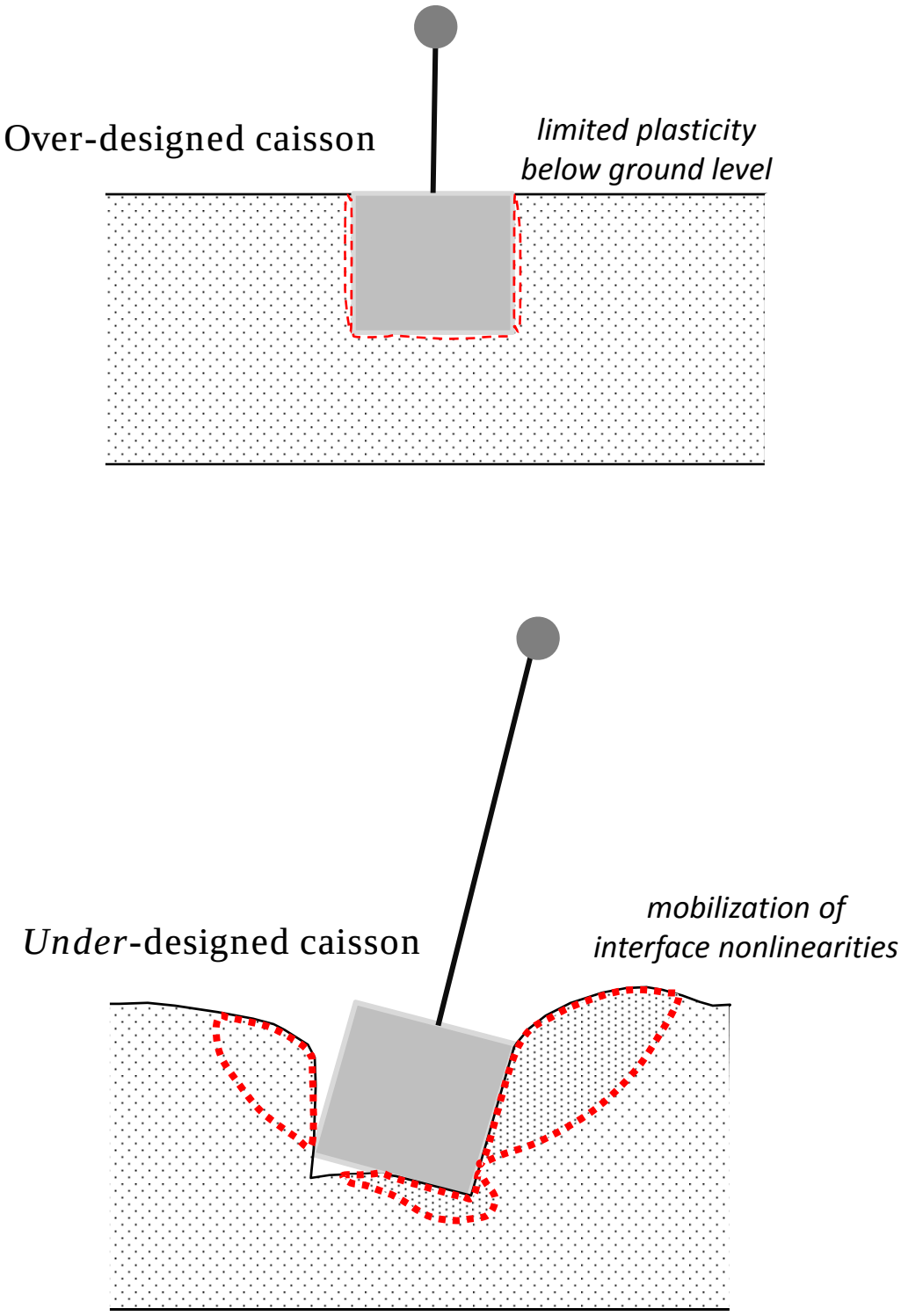

Fig. 4.1 Schematic illustration of a seismically over-designed caisson (limited plasticity below ground level) and a seismically *under*-designed caisson (development of soil-caisson interface nonlinearities).

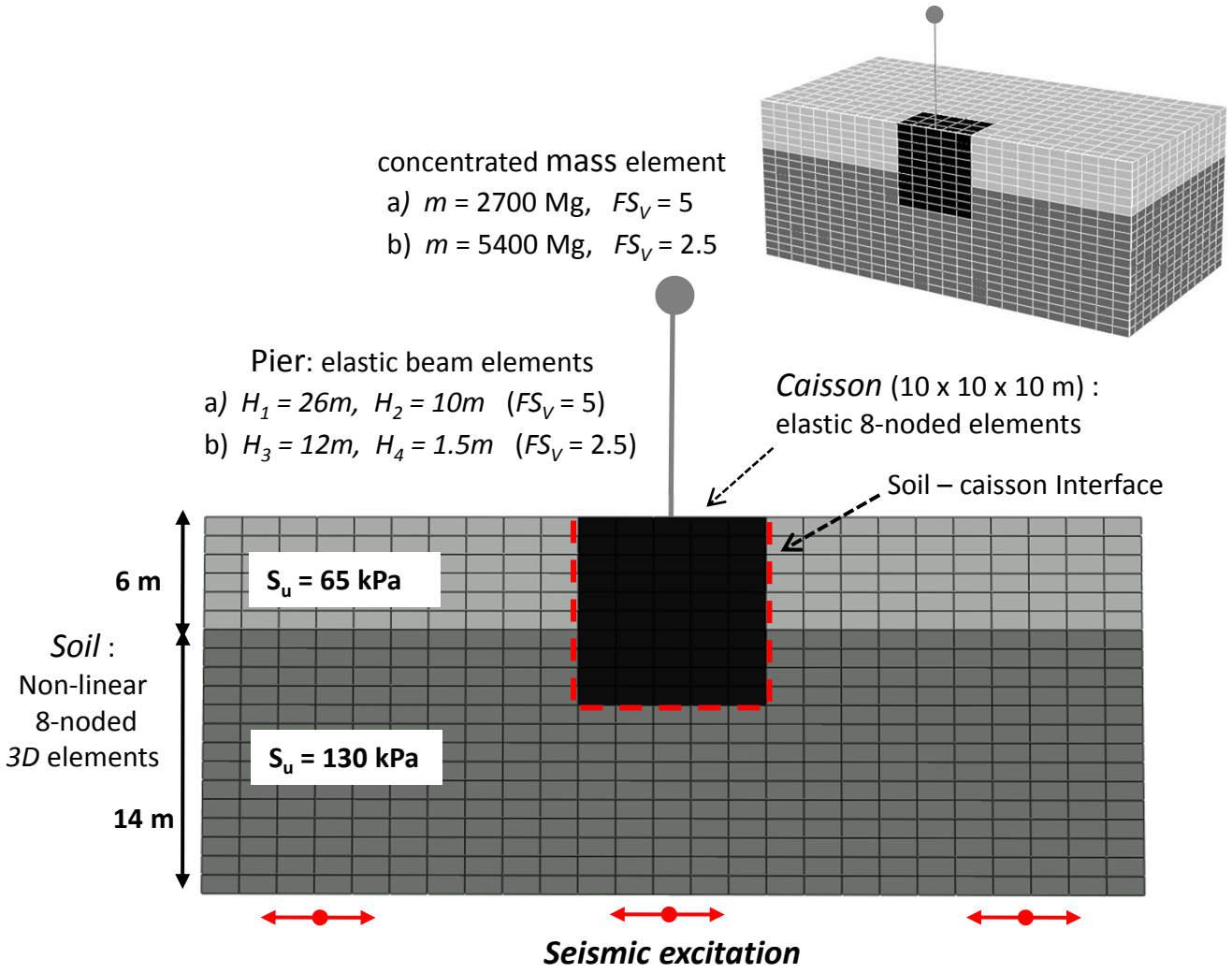

Fig. 4.2 Overview of the 3D finite element model used in the analyses

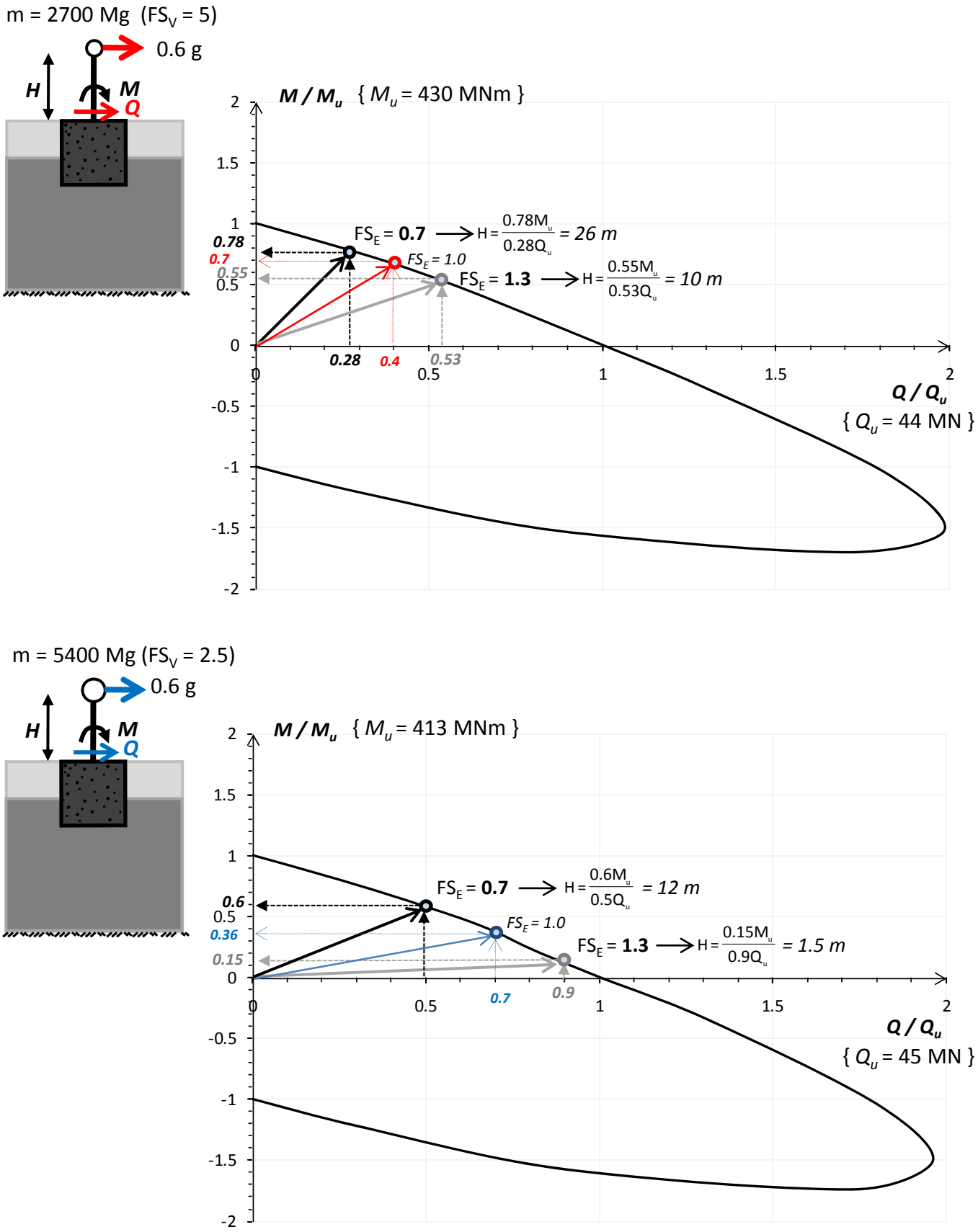

Fig. 4.3. Normalized M-Q bearing strength surfaces for **FS_V=5** and **FS_V=2.5 :** Calculation of the column heights for the *over*-designed (FS_E= 1.3) and *under*-designed (FS_E= 0.7) foundations.

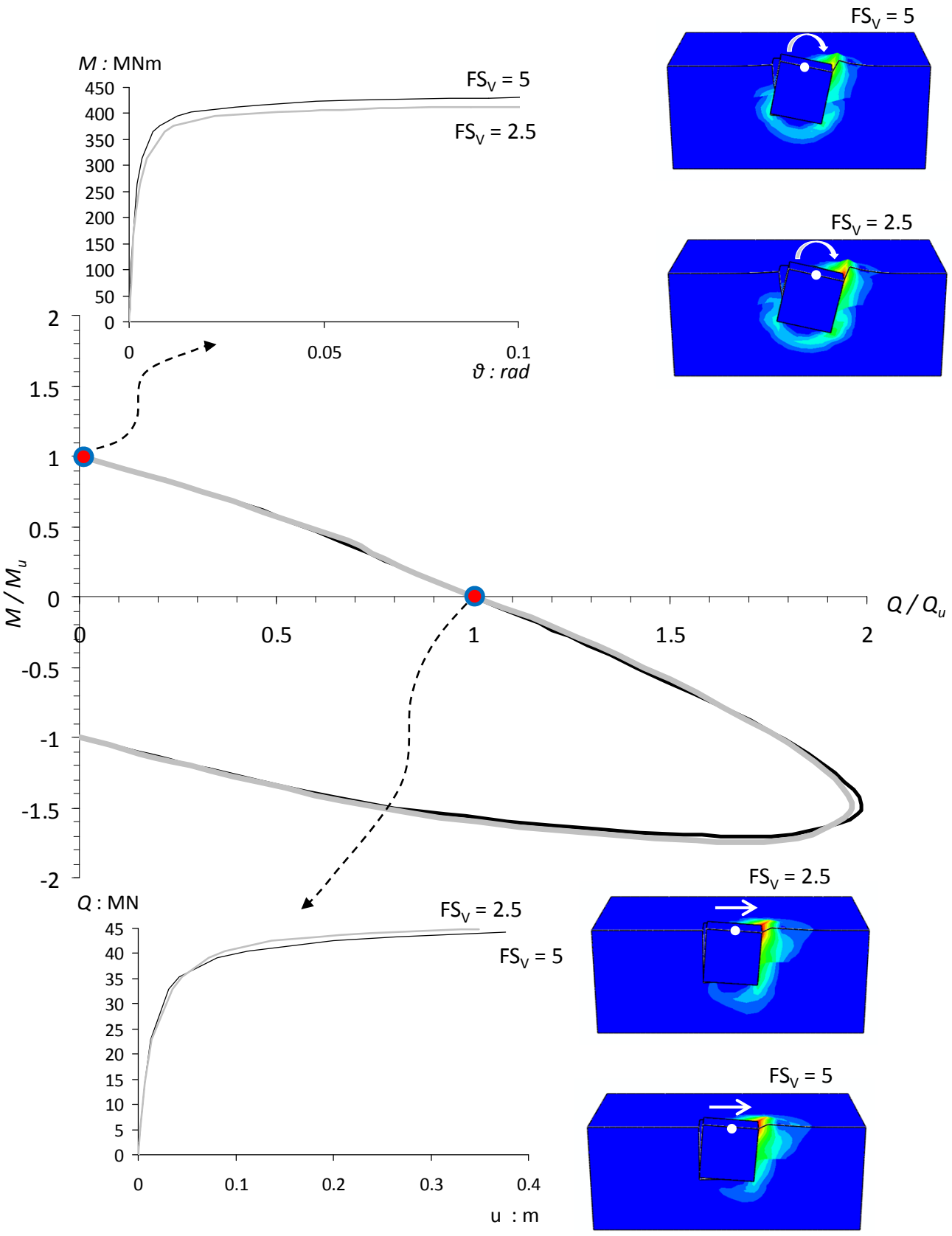

Fig. 4.4. Normalized bearing strength surfaces and the Q-u and M-ϑ curves corresponding to monotonic loading at the top of the caisson along with the respective contours of plastic strain magnitude at failure, for FS_V**=5** and FS_V=2.5.

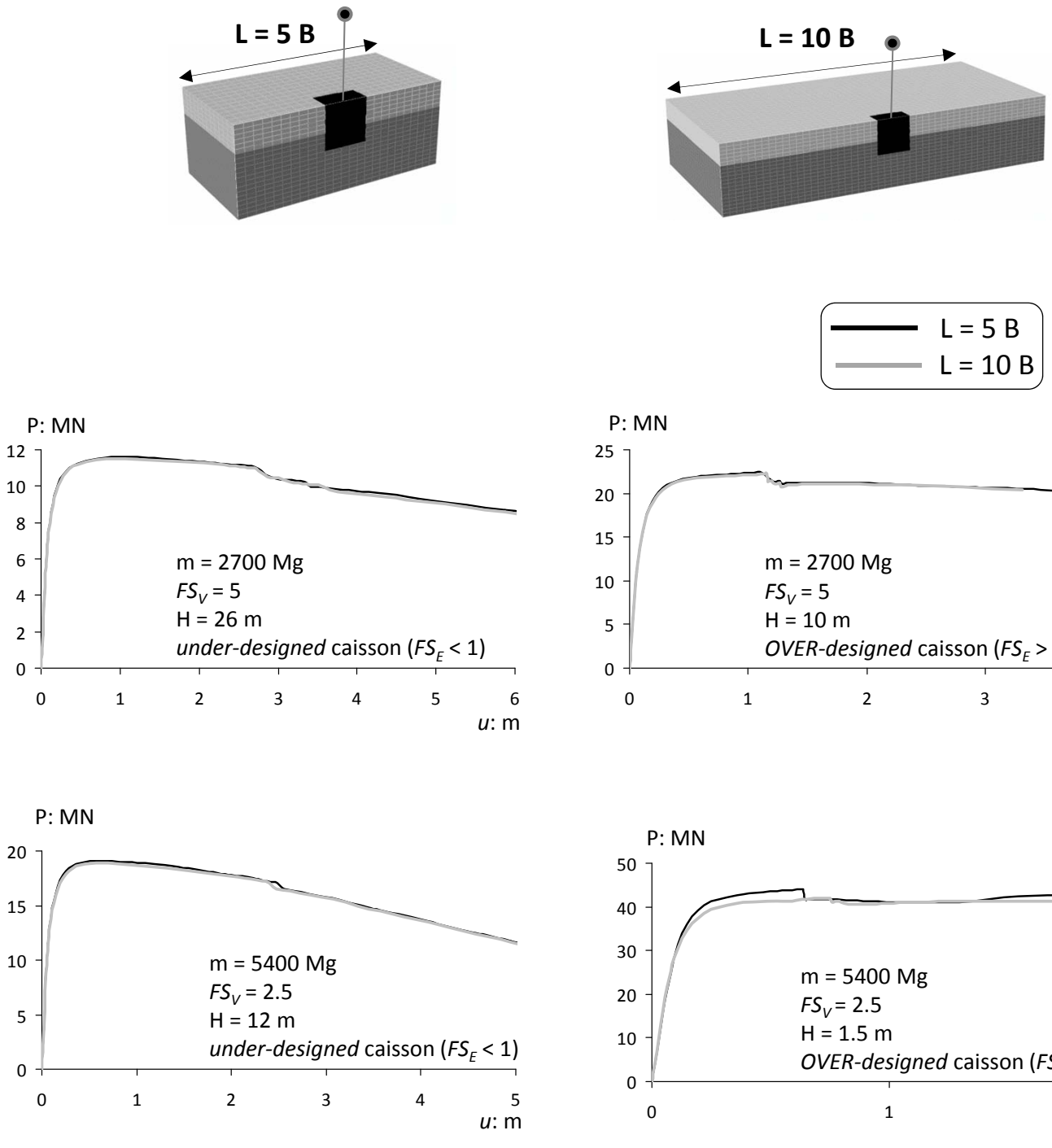

Fig. 4.5 Model verification: static pushover P (horizontal force at mass level) — *u* (horizontal displacement) curves for the four configurations, considering two finite element model sizes, L=5B and L=10B.

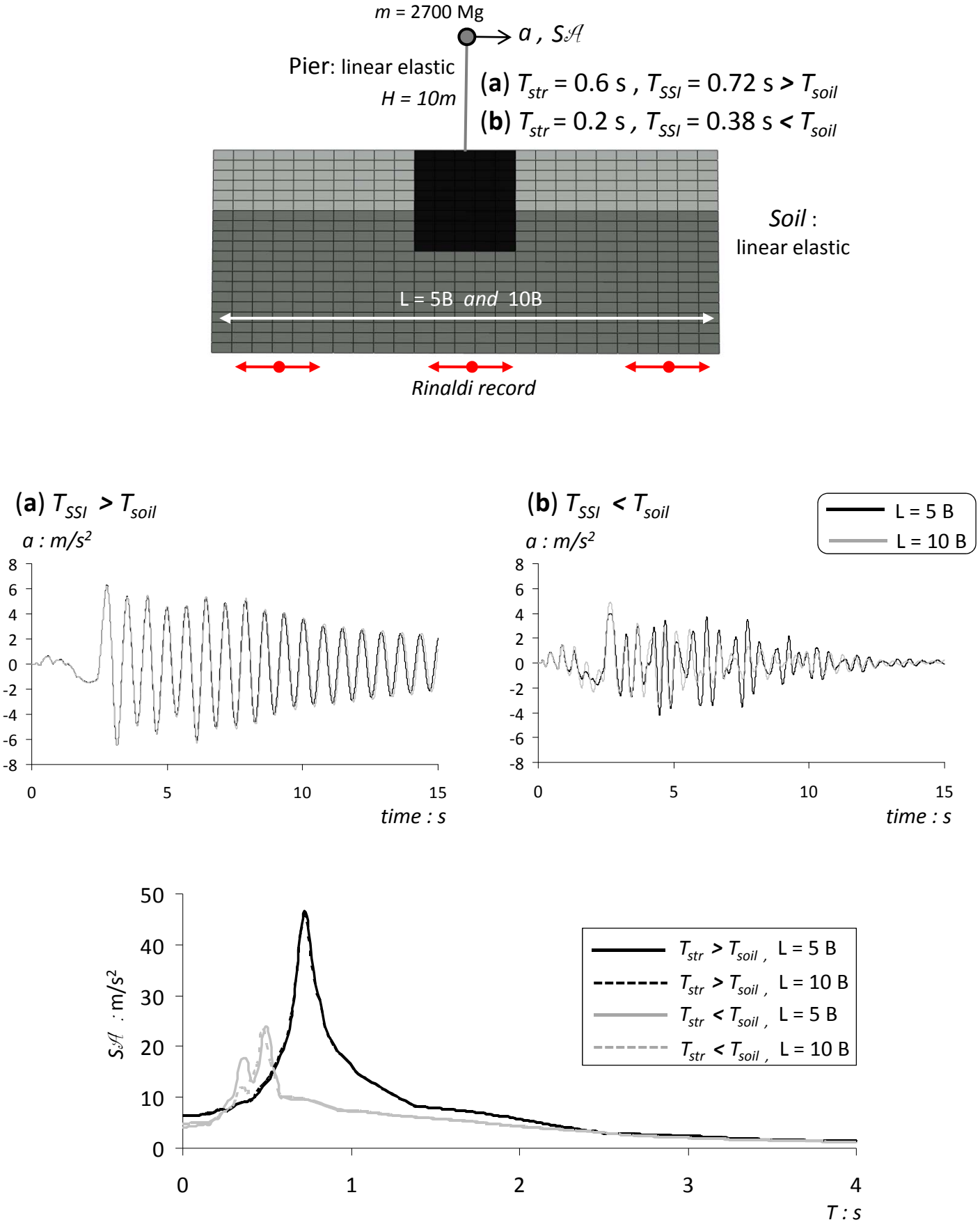

Fig. 4.6 Model verification: proof of the existence of a *cutoff* period for radiation damping. *Floor* acceleration time-histories and corresponding response spectra. The response for two *effective* structural periods and two model sizes (L=5B and L=10B) is analysed.

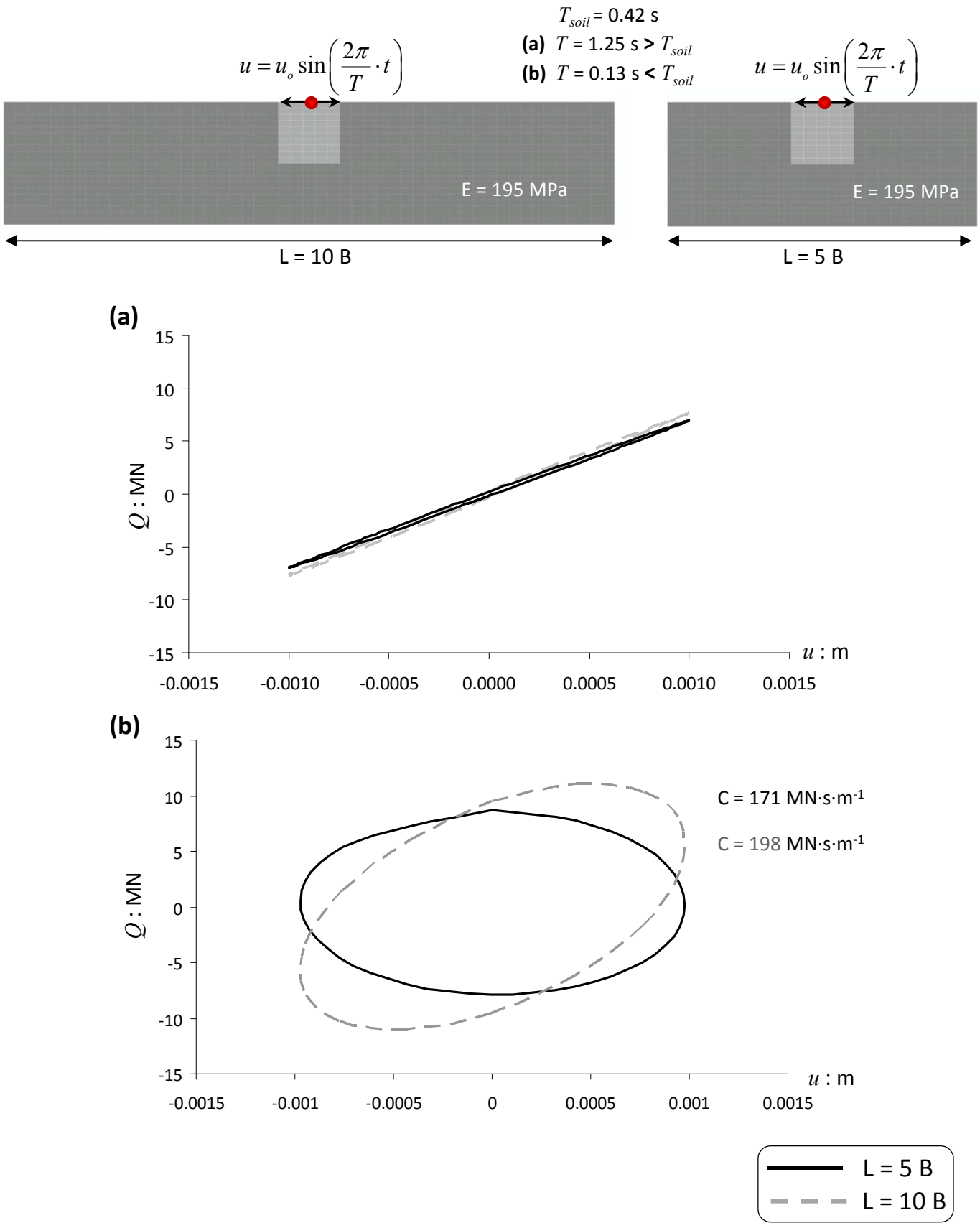

Fig. 4.7 Model verification: proof of the existence of a *cutoff* period for radiation damping. Elastic dynamic analysis of homogeneous stiff clay profile. Harmonic excitation at the top of the caisson. The response for two vibration periods ($T < T_{soil}$, $T > T_{soil}$) and two model sizes (L=5B and L=10B) is analysed.

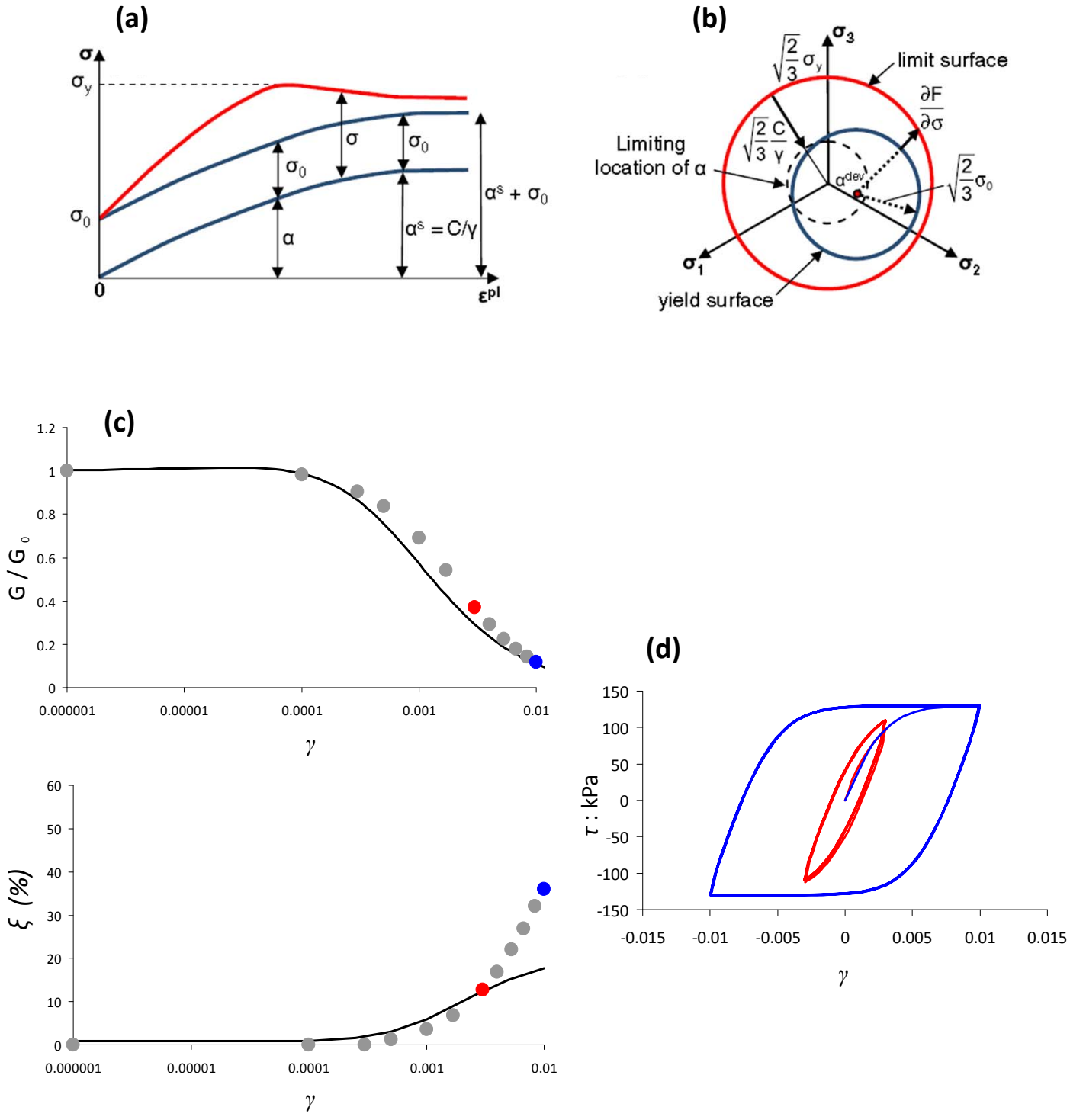

Fig. 4.8 **(a)** Simplified one-dimensional representation of the hardening. **(b)** Three-dimensional representation of the hardening in the nonlinear isotropic/kinematic model (Armstrong and Frederick 1966). **(c)** Calibration of kinematic hardening model for soil (stiff clay, Su =130 kPa, G_0 = 500 Su) against published *G*–*γ* and *ξ*–*γ* (PI = 30, σ_v = 200 kPa) curves (Ishibashi and Zhang 1993). **(d)** Shear stress−strain loops corresponding to the designated points in (**c**).

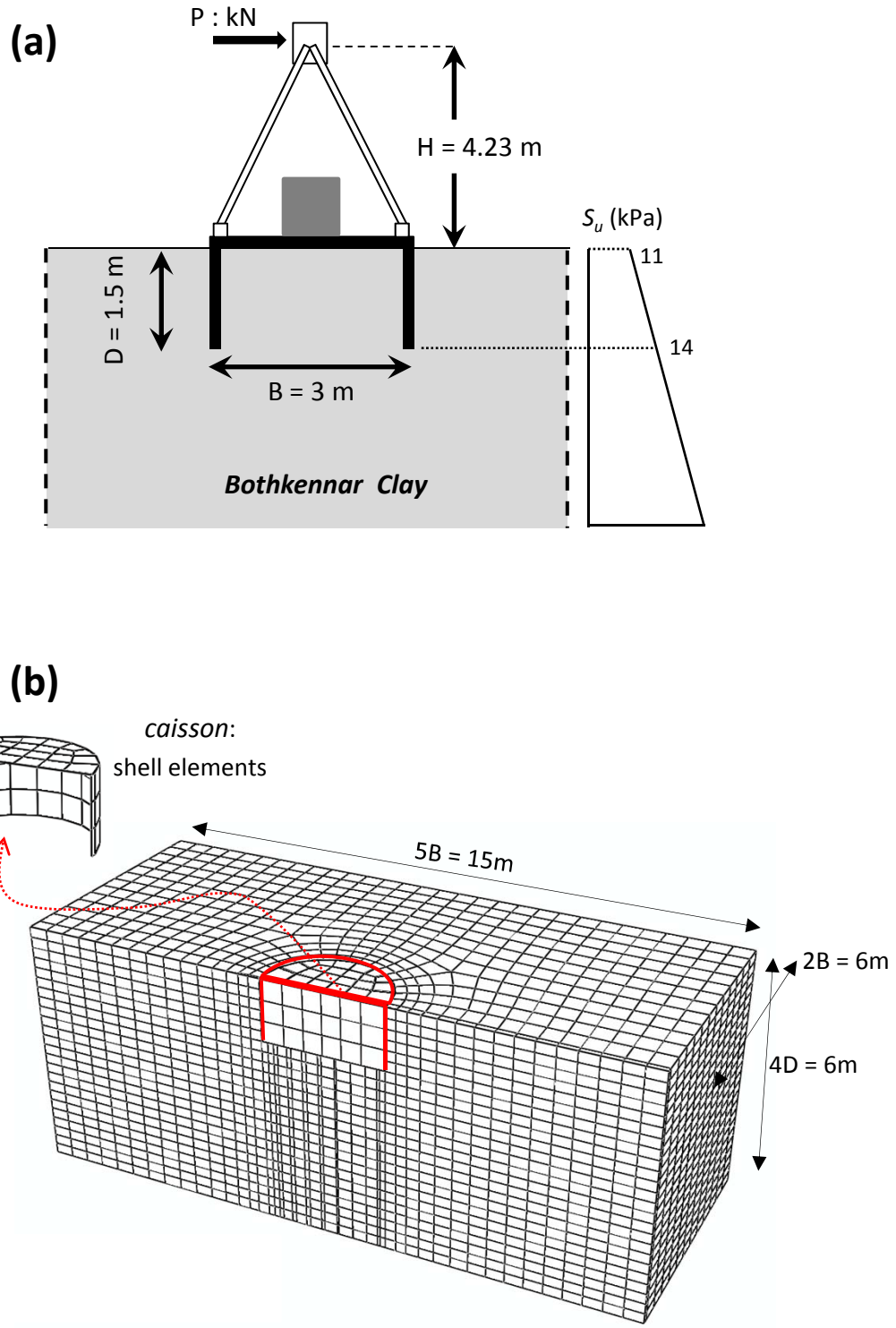

Fig. 4.9 **(a)** Schematic of the field test for the 3.0 m suction caisson conducted at the Bothkennar test site (modified after Houlsby et al. 2005). Test: Jack_3.0_1, very large amplitude cyclic lateral push. **(b)** 3D finite-element half-model utilized in the validation procedure against the field test.

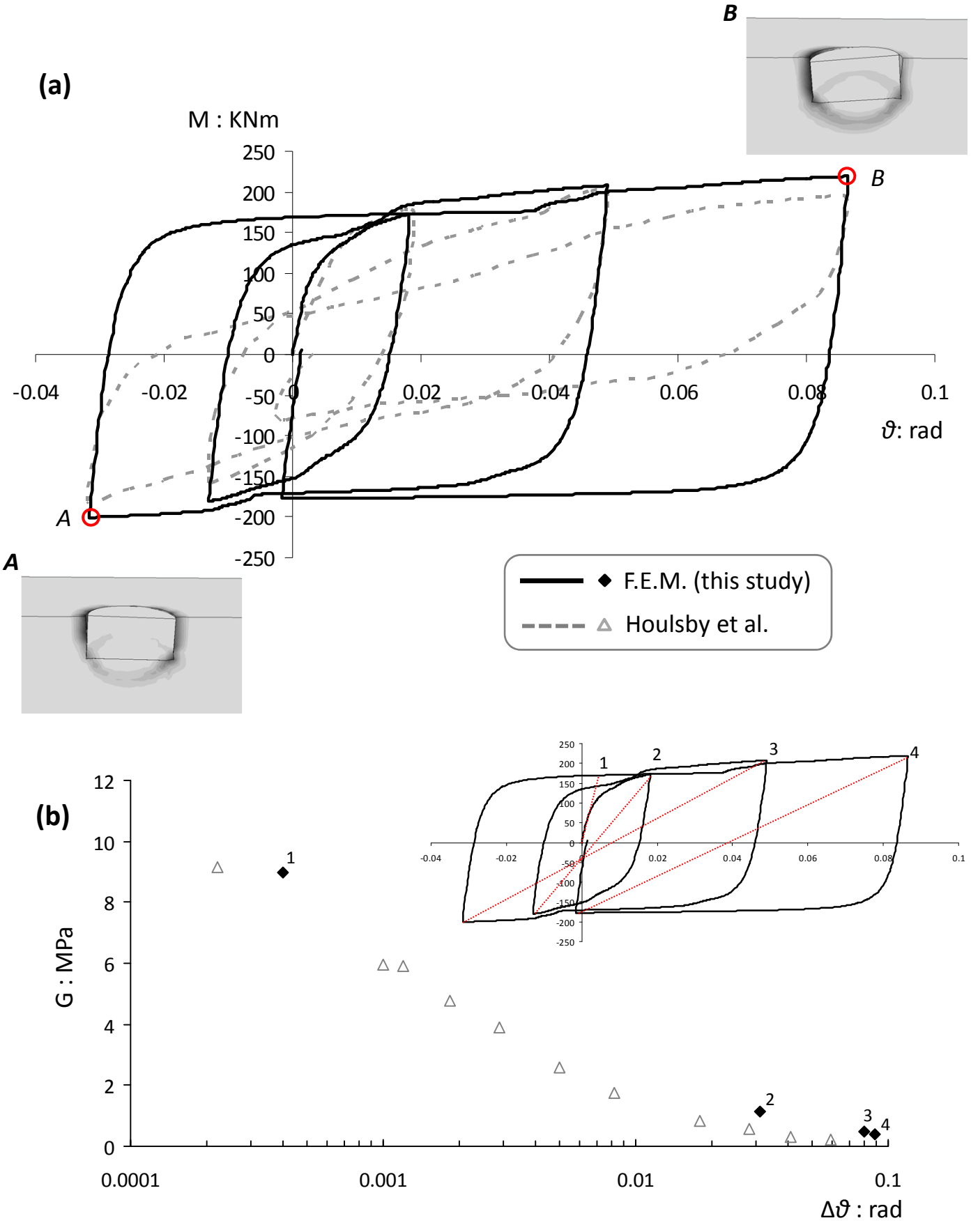

Fig. 4.10 Constitutive model validation in terms of **(a)** M-ϑ, along with snapshots from the FE analysis at points *A* and *B*, and **(b)** computed secant stiffness modulus as a function of the amplitude of rotation.

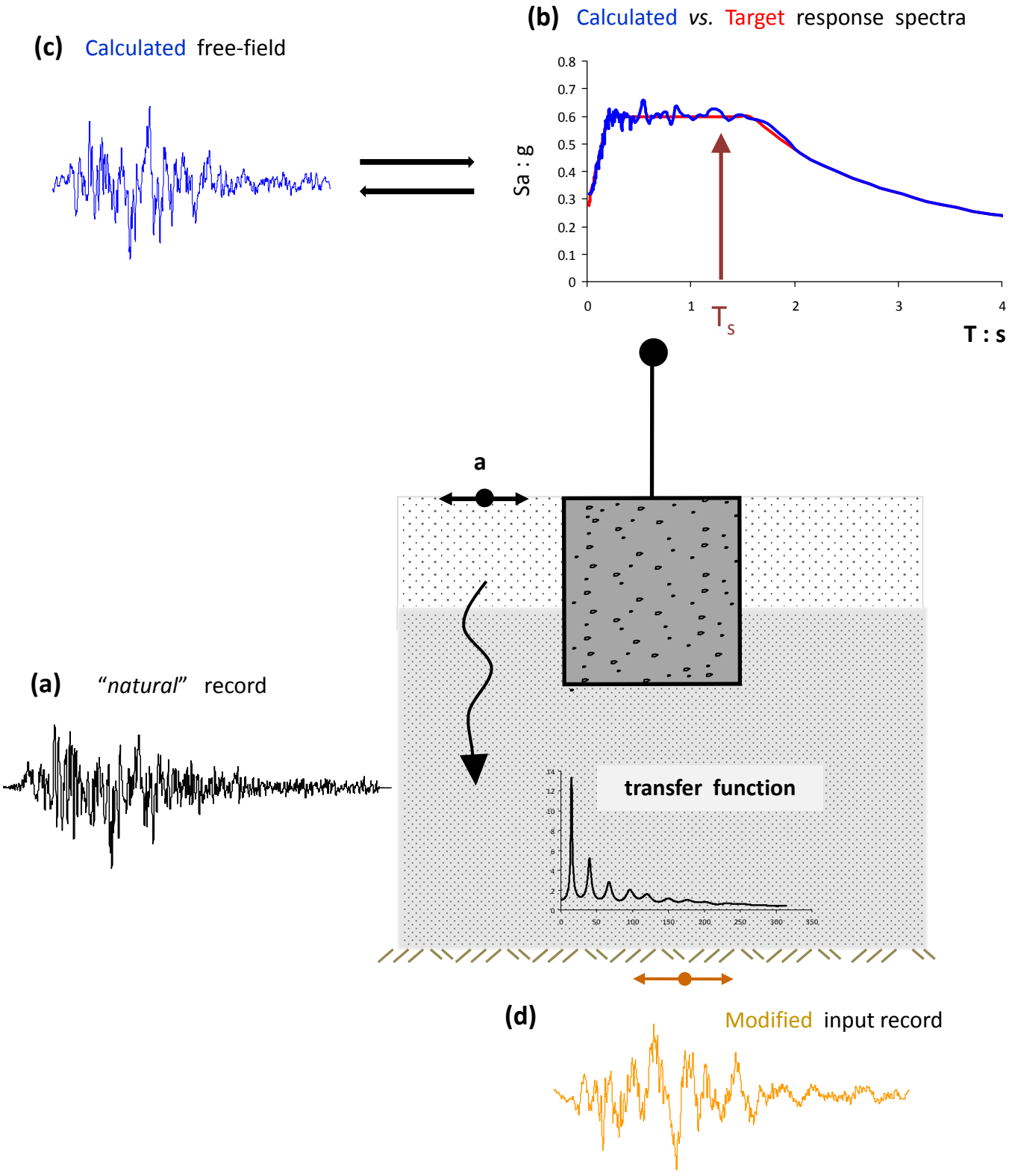

Fig. 4.11 Schematic illustration of the methodology for calculating the artificial accelerograms (spectral matching) used in the dynamic analysis: the "*natural*" record used as base excitation is **modified** through a trial-and error procedure so that the response spectrum matches a "**target"** spectrum.

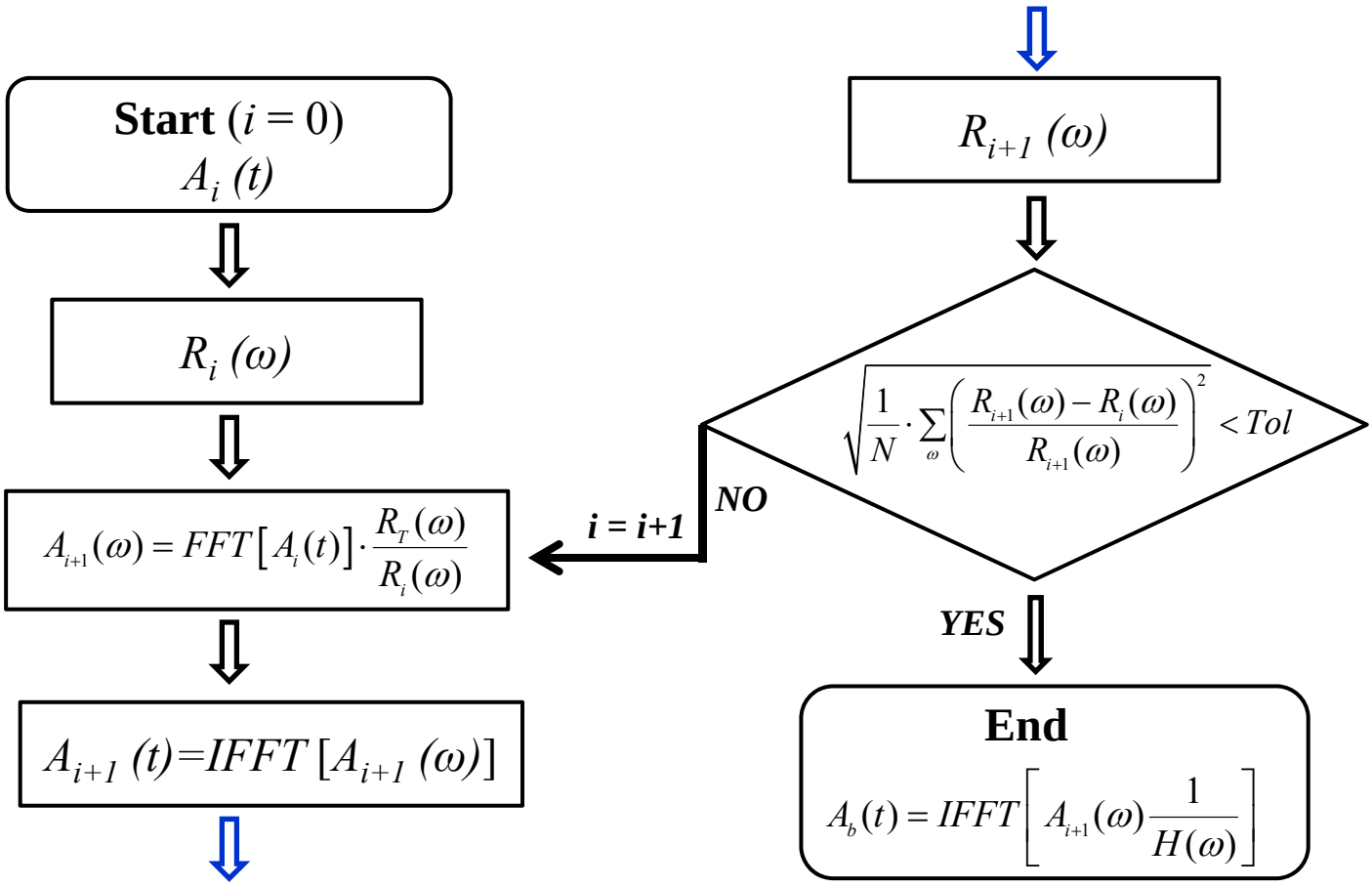

Notation

i = Total number of iterations

$Tol = 10^{-2}$

$A_0\ (t)$ = Natural acceleration time history

$R_i\ (\omega)$ = Response spectrum of the A_i time history (frequency domain)

$R_T\ (\omega)$ = *Target* response spectrum (frequency domain)

FFT = Fast Fourier Transform

$A_i\ (t)$ = Modified acceleration time history at the i^{th} iteration

$IFFT$ = *Inverse* Fast Fourier Transform

$H\ (\omega)$ = Transfer function of the 2-layer soil medium

$A_b\ (t)$ = ***Input*** acceleration time history (for the 3-D finite element analyses)

Fig. 4.12 Flowchart of the methodology for calculating the artificial accelerograms used in the dynamic analysis

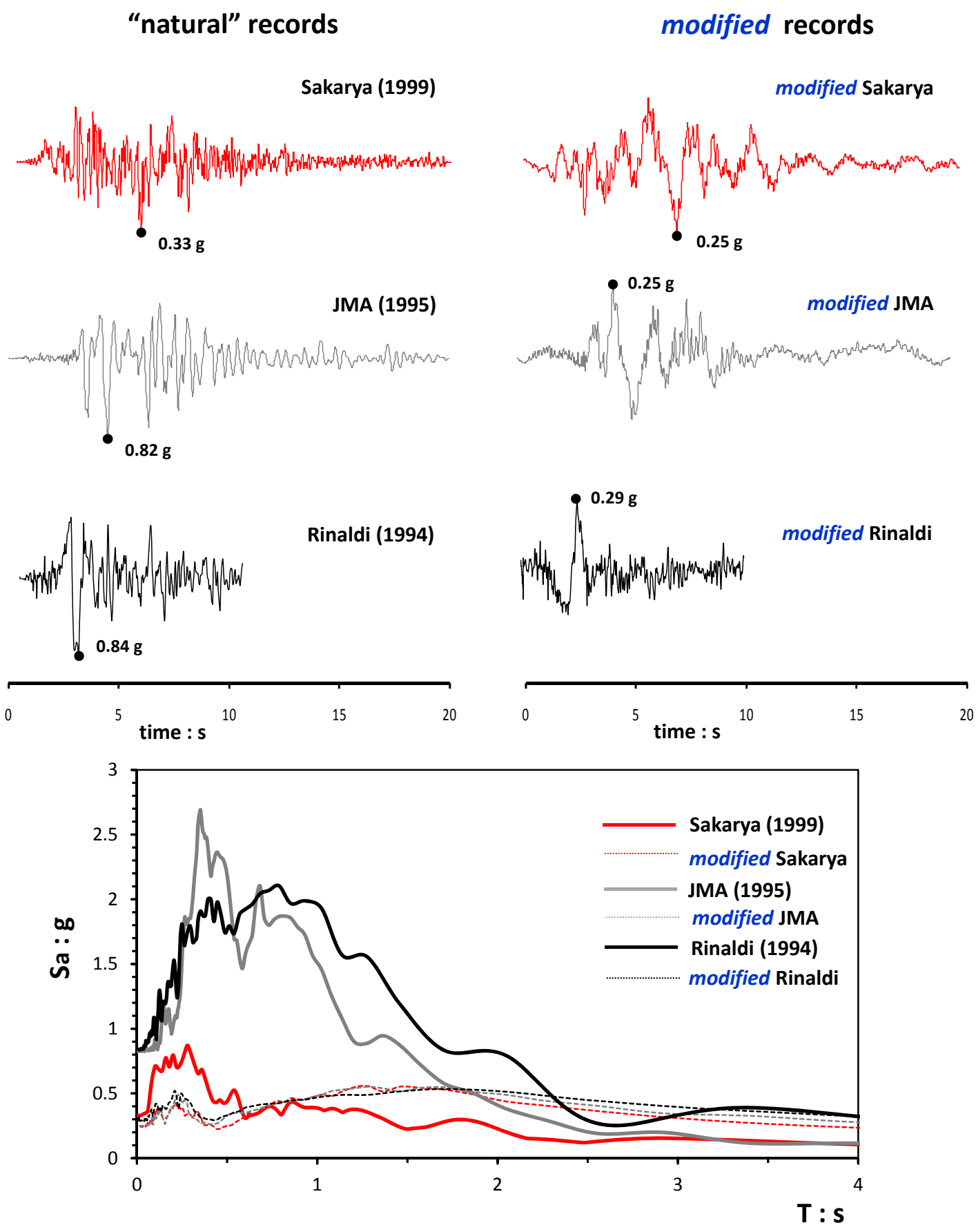

Fig. 4.13 "Natural" and corresponding *modified* (according to the methodology depicted in Figs 11, 12) acceleration time histories used as base excitation, along with their elastic response spectra.

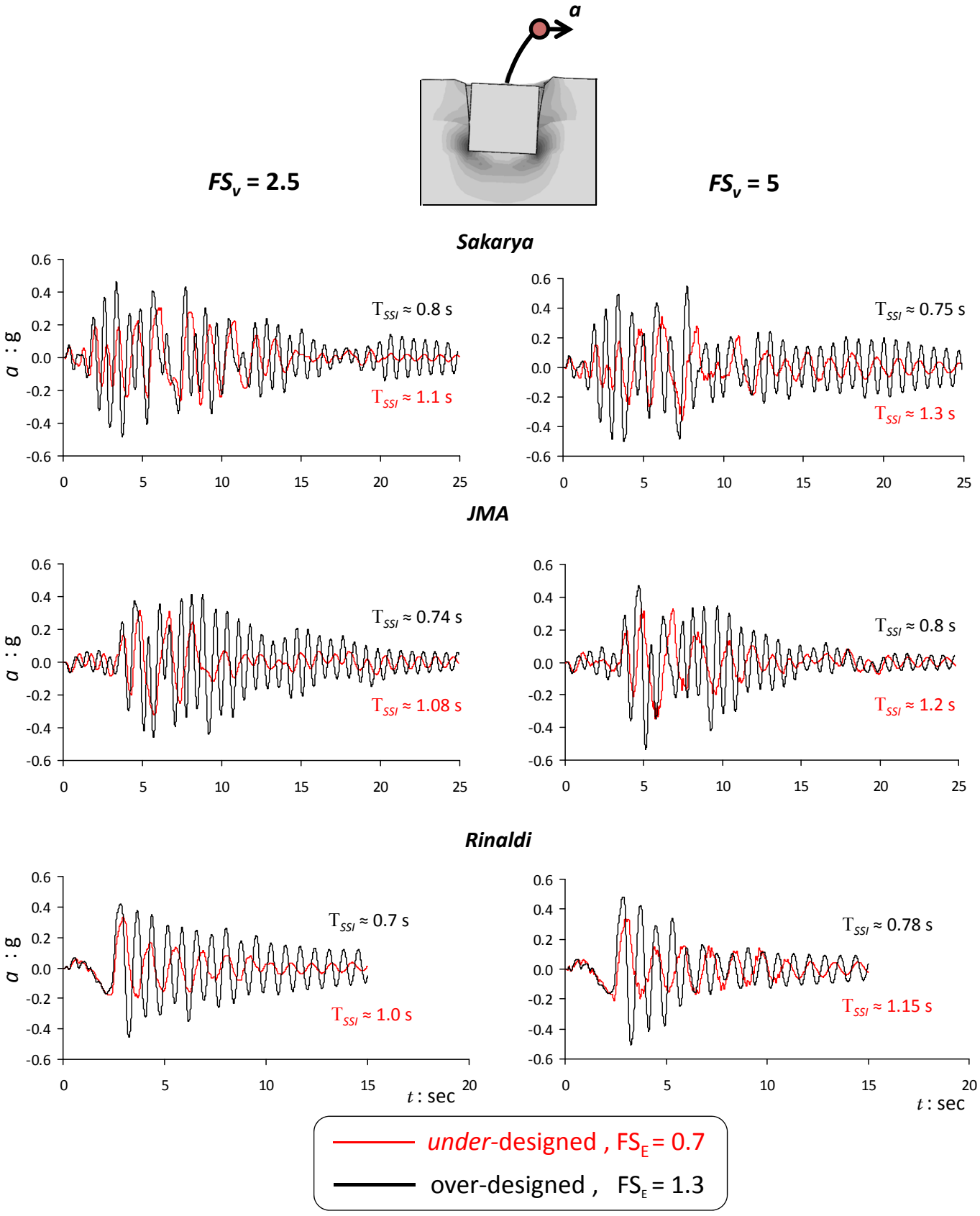

Fig. 4.14 Response in terms of acceleration time histories at the deck mass. The respective effective periods, T_{SSI}, are also given.

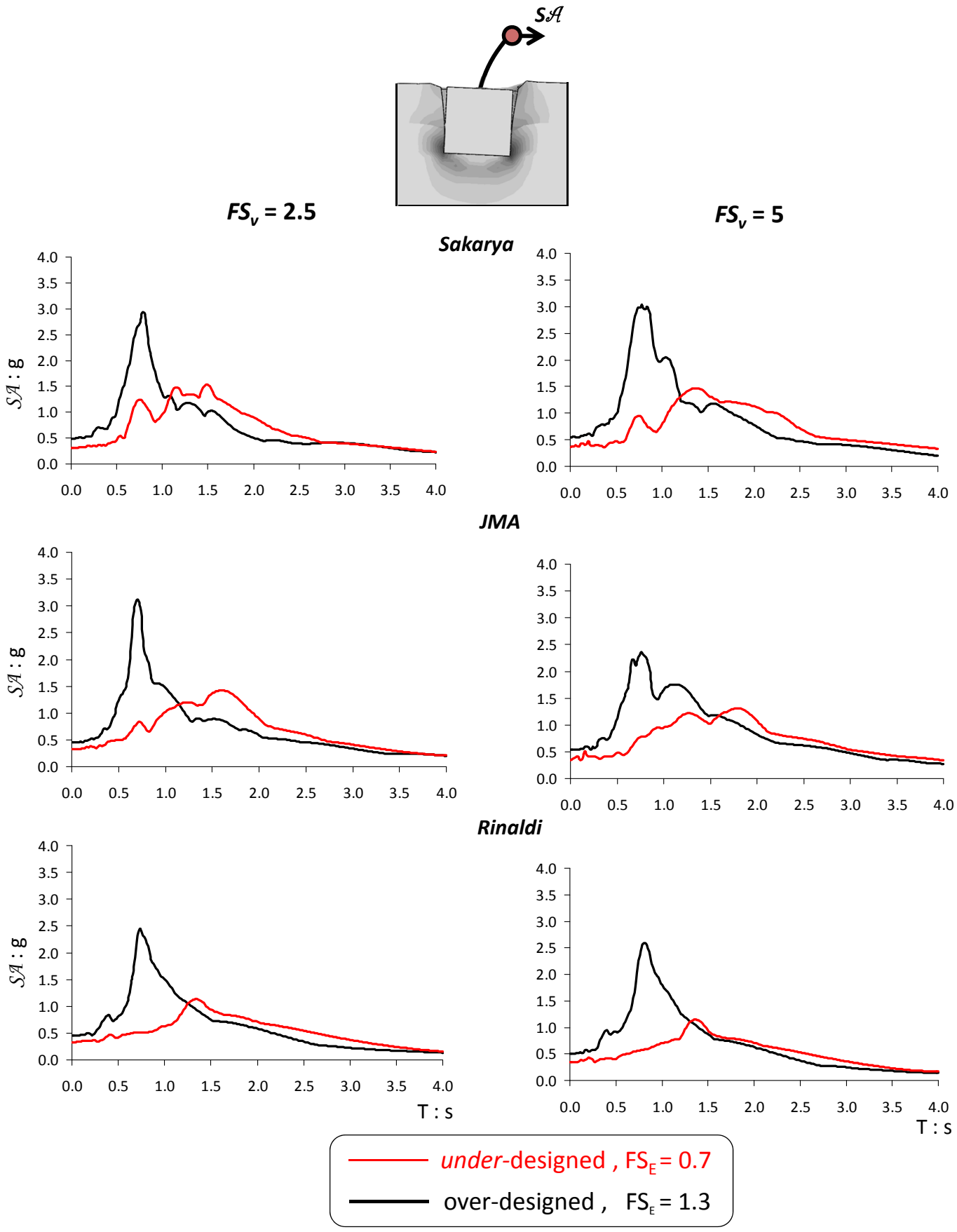

Fig. 4.15 Response in terms of *floor* response spectra at the deck mass.

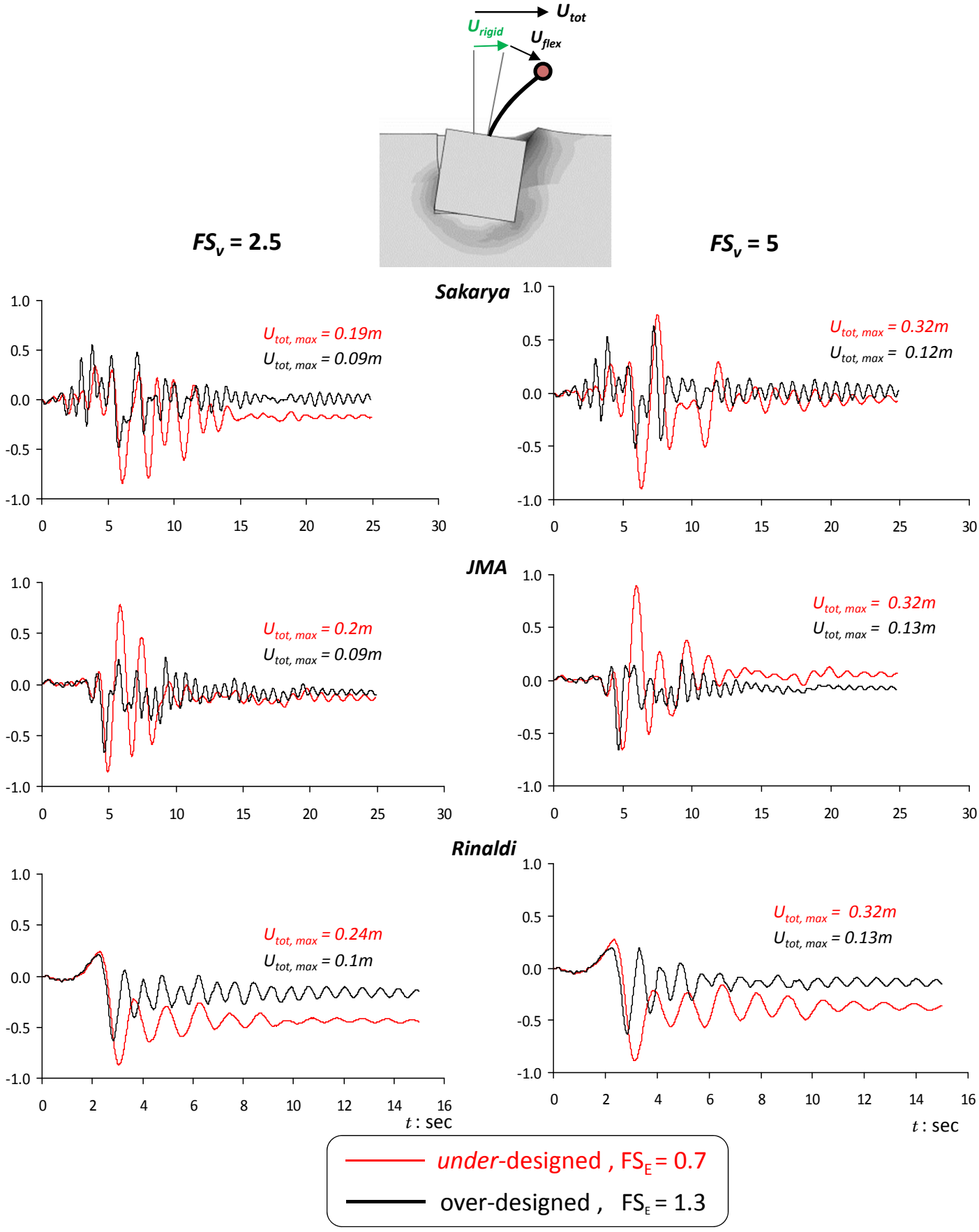

Fig. 4.16 Response in terms of time histories of the deck drift (horizontal displacement) due to **rigid-body** displacement of the pier (U_{rigid}), normalized with the respective maximum horizontal displacement ($U_{tot, max}$).

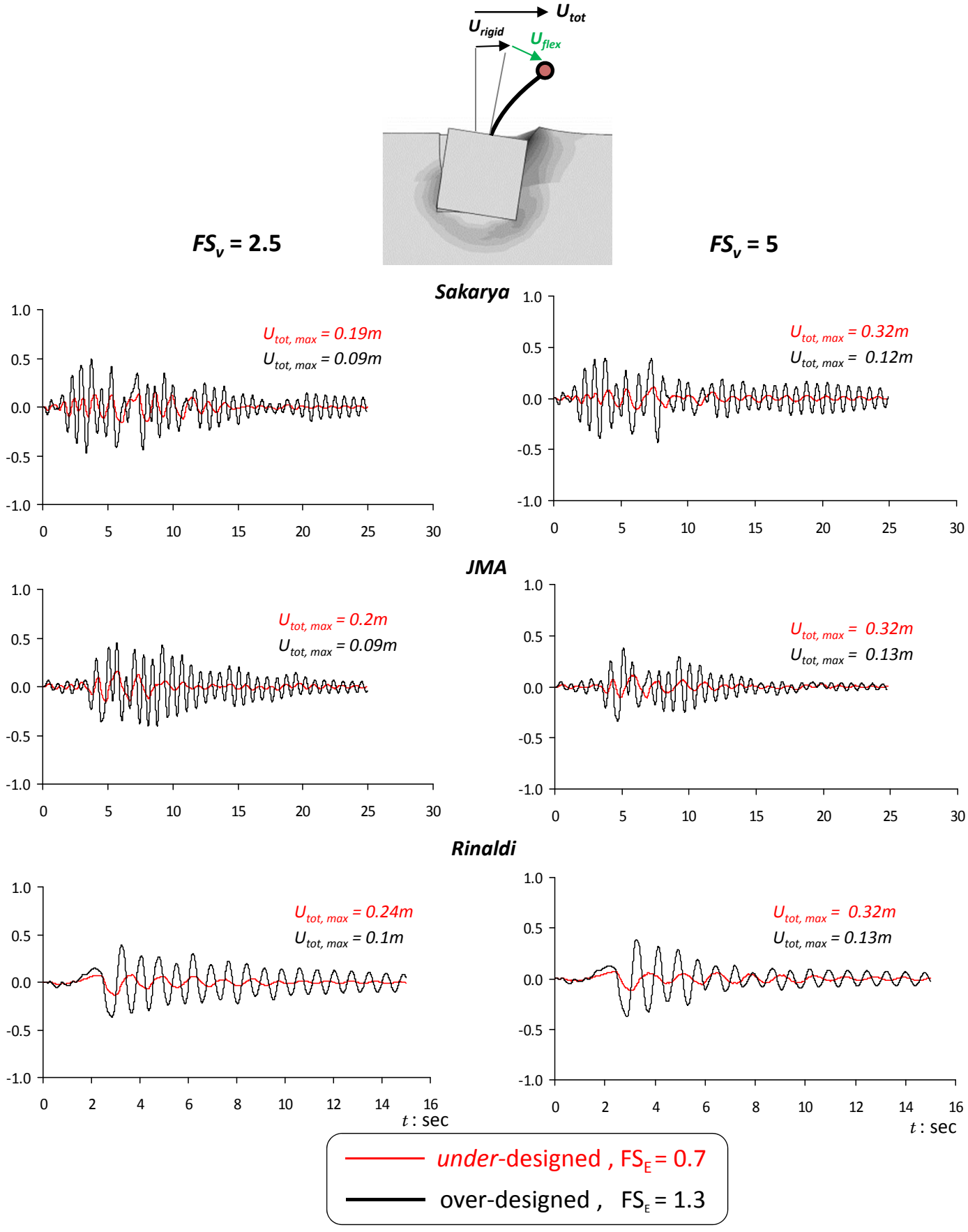

Fig. 4.17 Response in terms of time histories of the deck drift (horizontal displacement) due to **flexural** displacement (bending) of the pier (U_{flex}), normalized with the respective maximum horizontal displacement ($U_{tot, max}$).

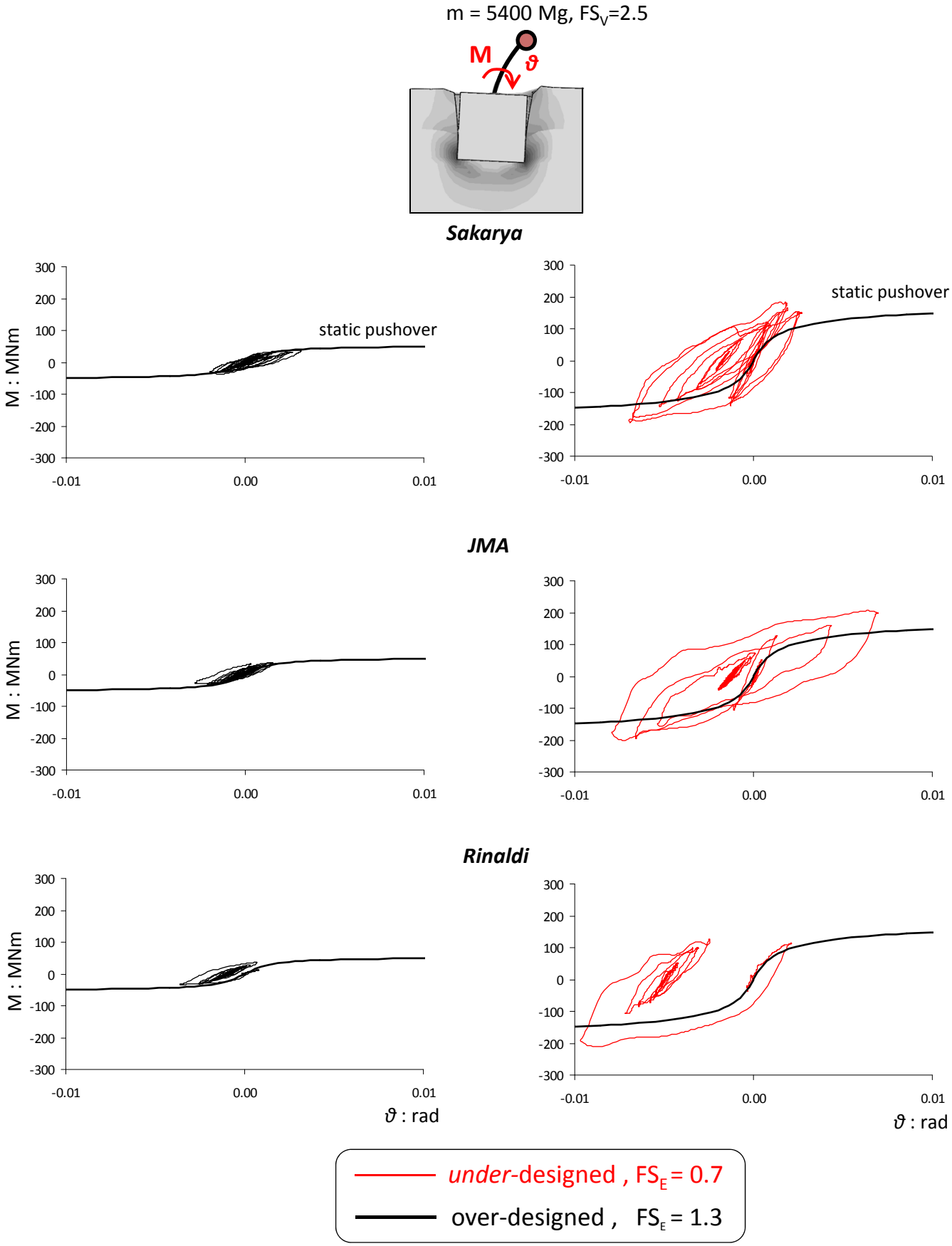

Fig. 4.18 Response of the heavily loaded caissons (**FS$_V$ = 2.5)**, in terms of overturning moment–rotation loops (M–ϑ) at the head of the caisson.

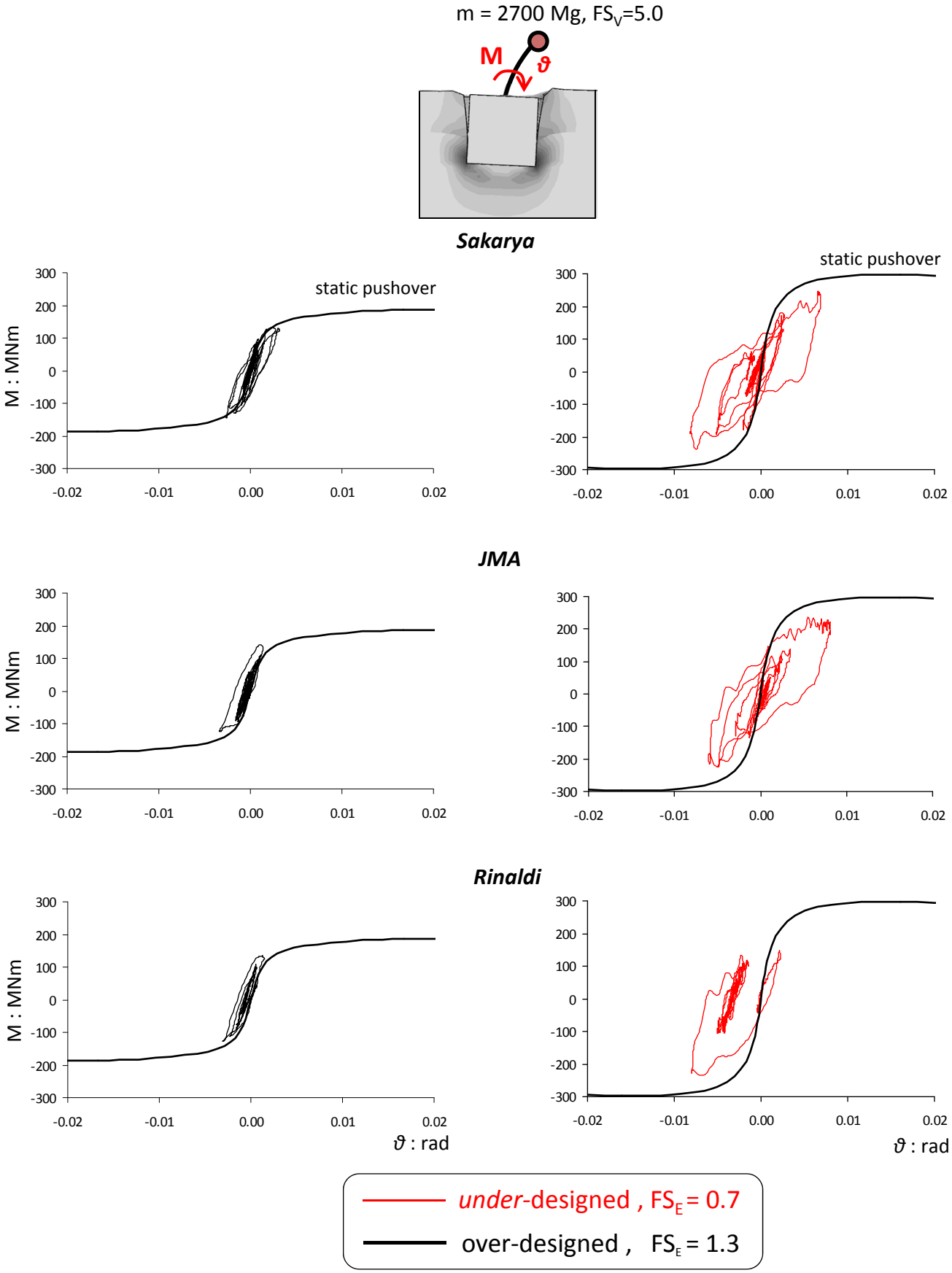

Fig. 4.19 Response of the lightly loaded caissons (**FS$_V$ = 5)**, in terms of overturning moment–rotation loops (M–ϑ) at the head of the caisson.

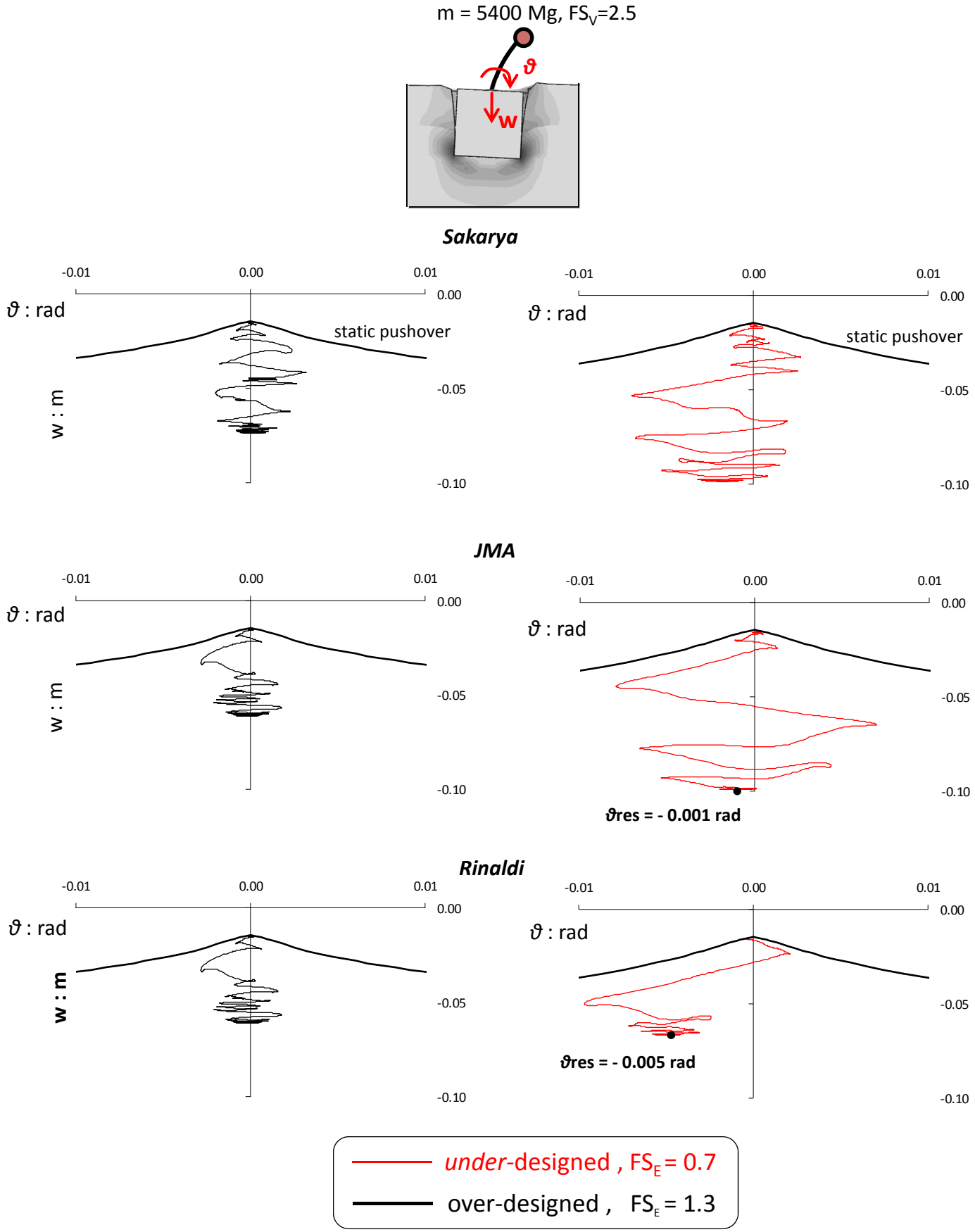

Fig. 4.20 Response of the heavily loaded caissons (**FS$_V$ = 2.5)**, in terms of settlement–rotation (w–ϑ) curves at the head of the caisson.

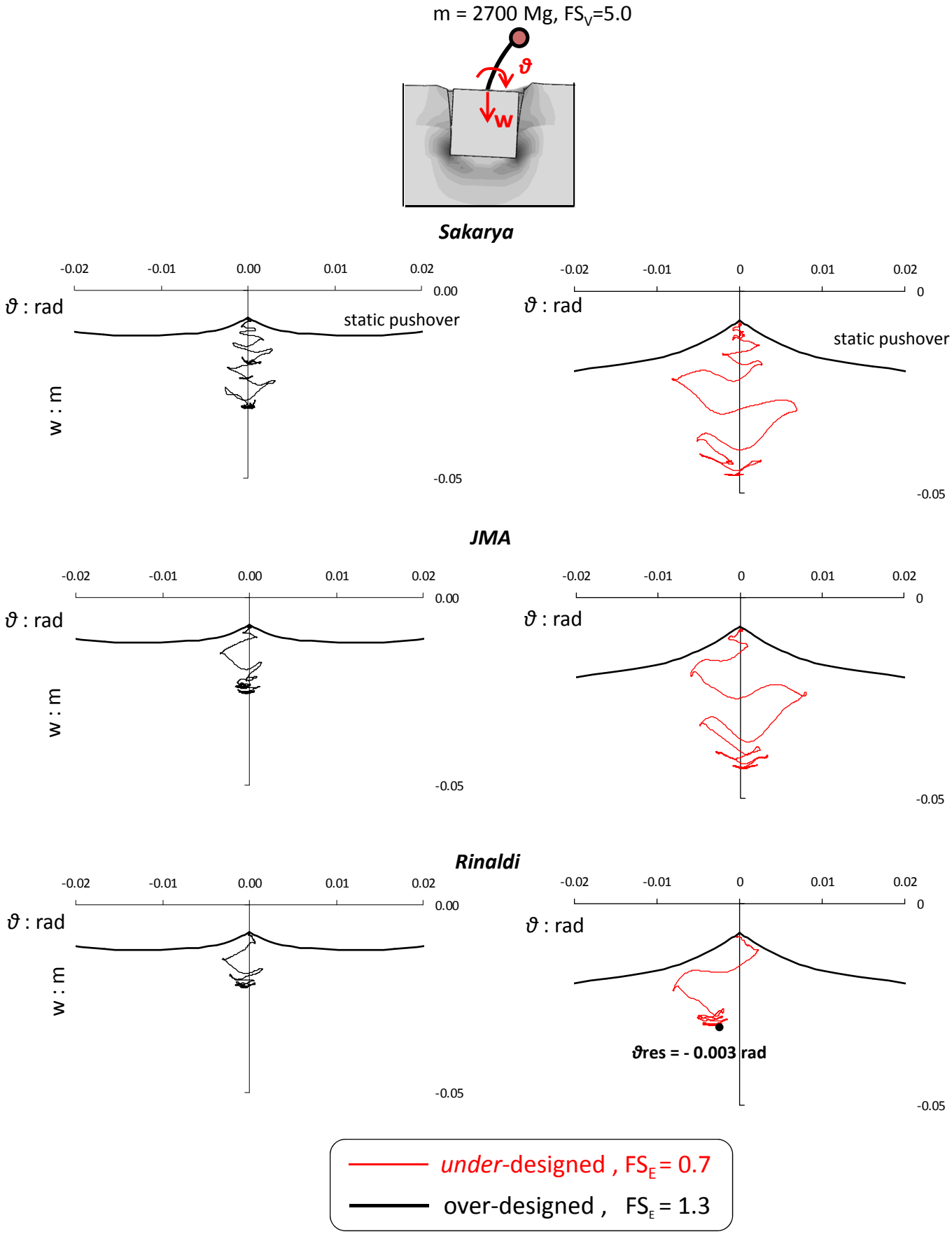

Fig. 4.21 Response of the lightly loaded caissons (**FS$_V$ = 5)**, in terms of settlement–rotation (w–ϑ) curves at the head of the caisson.

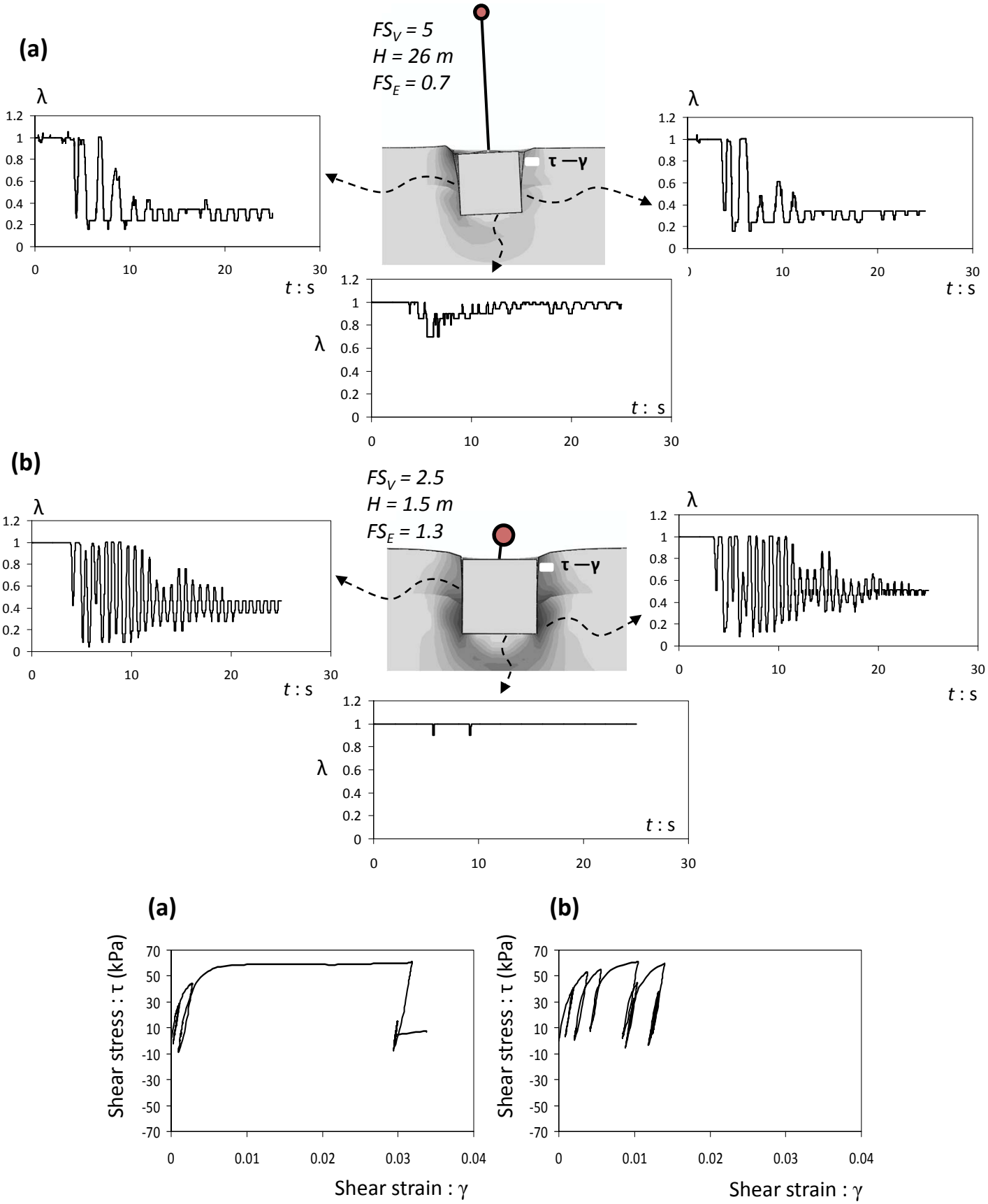

Fig. 4.22 Time histories of the fraction of the area of the caisson that is in contact with the soil (at the respective side) and shear stress−strain loops calculated at the caisson-soil interface near the surface, for the two extreme cases examined: **(a)** lightly loaded (FS_V = 5) *under*-designed and **(b)** heavily loaded (FS_V = 2.5) *over*-designed caisson. Record: *modified* JMA.

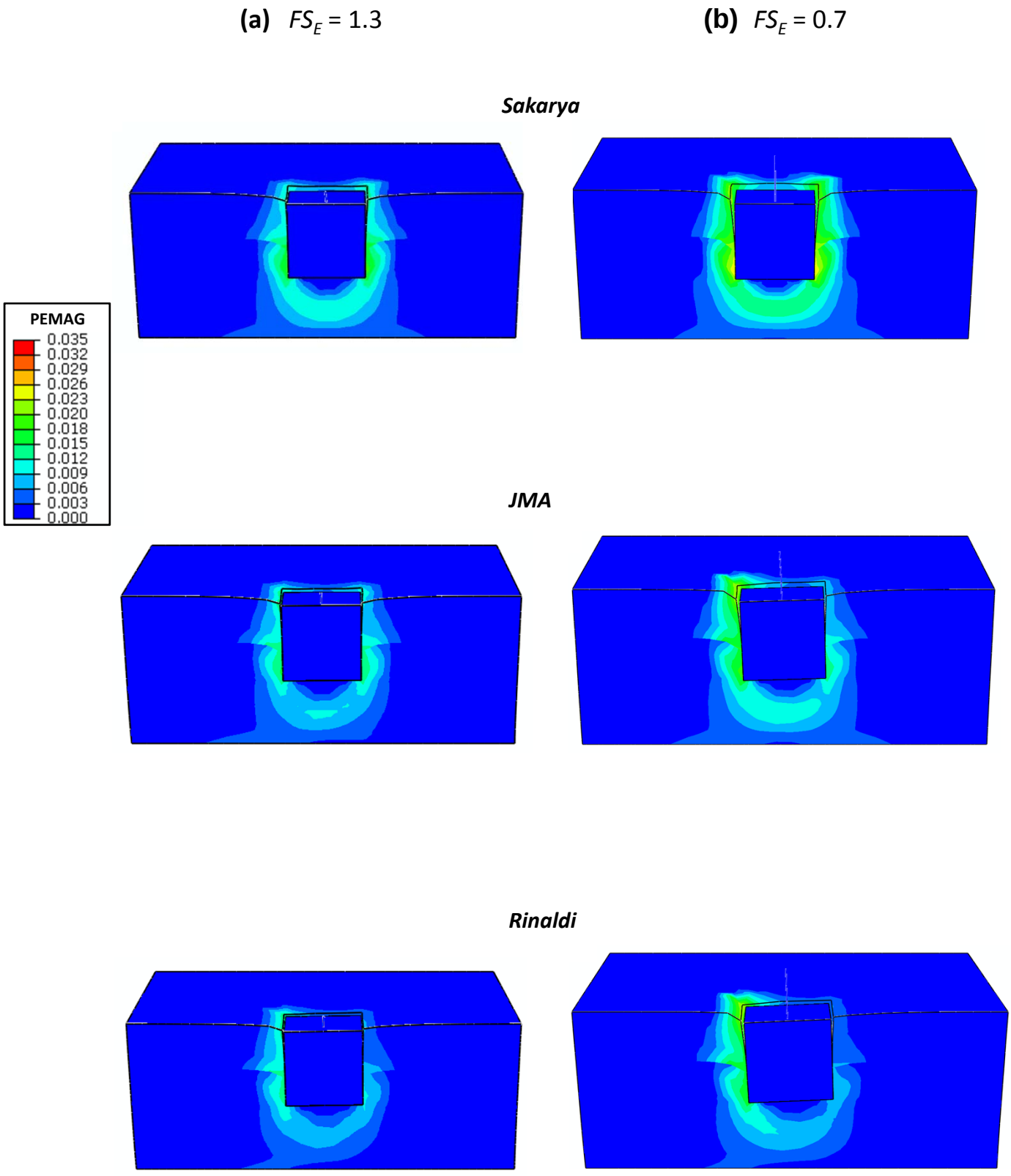

Fig. 4.23 Response of the heavily loaded caissons (**FS_V = 2.5)**, in terms of plastic strain magnitude (deformed mesh exaggerated ×20 times).

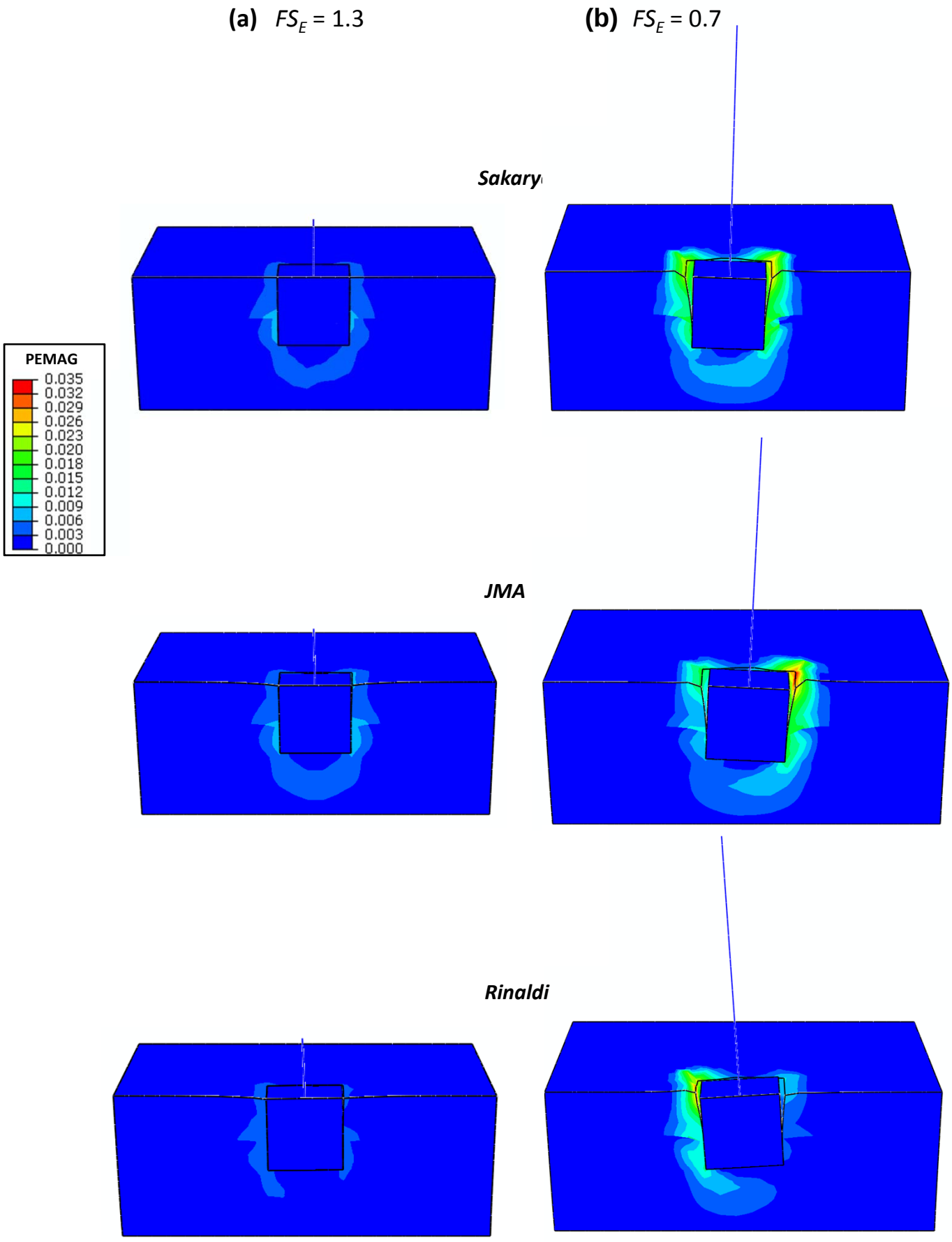

Fig. 4.24 Response of the lightly loaded caissons (**FS_V = 5)**, in terms of plastic strain magnitude (deformed mesh exaggerated ×20 times).

Incremental dynamic analysis of caisson-pier interaction

A B S T R A C T

This paper presents a 3D finite-element Incremental Dynamic Analysis (IDA) study of caisson foundations carrying single-degree-of-freedom (SDOF) structures on clayey soil. The emphasis is given to the interplay between the nonlinearities developed above (superstructure) and, mainly, below ground surface, either of material (soil plasticity) or of geometric (caisson-soil interface gapping and slippage) origin. The study is performed with respect to the static (F_S) and the seismic (F_E) safety factor of the foundation and involves SDOF oscillators of varying mass (to account for vertical loading, F_S) and height (relating to moment loading, F_E) founded on similar rigid cubic caissons. Structural nonlinearity is considered through a simplified moment-curvature law and the yield strength is deliberately chosen so that the following three configurations are obtained: (a) a lightly loaded (F_S=5) seismically *under*-designed (as compared to the superstructure) caisson, (b) a lightly loaded seismically *over*-designed caisson, and (c) a heavily loaded (F_S=2.5) seismically *under*-designed caisson. The analysis is performed with several earthquake records, each scaled to multiple levels of intensity. IDA curves are produced for a single intensity measure, (peak ground acceleration, PGA), and appropriate engineering demand parameters (EDP) describing both the maximum and the residual response of the system. The results emphasize a potentially beneficial role of foundation nonlinearities on reducing the seismic

demands on the superstructure, but at the cost of residual foundation settlements and rotations.

5.1. Introduction

The seismic design of deeply embedded caisson foundations has been based either on solutions for shallow embedded foundation [7, 8, 12, 26, 33, 35, 42, 43], (mostly cylindrical), or on solutions for pile (e.g., [28, 41]). Gerolymos and Gazetas [16, 17, 18] proposed a multi spring model for the static, cyclic, and dynamic response of massive caisson foundations embedded in nonlinear layered or inhomogeneous soil and loaded at the top, taking into account for soil and interface nonlinearities. In a recent related work, Varun et al. [47] developed a dynamic Winkler model that accounts for the multitude of soil resistance mechanisms mobilized at the base and the circumference of laterally loaded caissons, thus retaining the advantages of Winkler-type models while allowing for realistic representation of the complex soil–structure interaction effects.

Current seismic design of structures is based on the so-called "capacity design" approach, in which the structural response is presumed ductile. In essence, it dictates the hierarchy of failure, ensuring that the critical components of a joint (column/pier-to-foundation or beam-to-column) which are the foundation and the columns respectively, are not designed by their own action effects but to exceed, by an appropriate capacity factor, the available resistance of the "sacrificial" components, the latter designed by their nominal earthquake loading coefficient. Structurally-elastic behaviour of the foundation, for the case of deep embedded and caisson foundations, indicates that passive and shear failure along the sides and the base are undesirable. Although such restrictions may, at first, appear reasonable (the inspection and rehabilitation of foundation damage after a strong earthquake is not a trivial task), they may lead to economically conservative designs; elastic foundation response might prove a rather expensive solution. Moreover, neglecting the aforementioned nonlinear phenomena prohibits the exploitation of the substantial ductility capacity offered by the failure mechanisms developed below ground surface in dissipating the seismic energy. In fact, recent research on shallow [e.g. 2, 9, 10, 14, 15, 22, 27, 36, 38, 39] and

pile [20] foundations suggests that soil compliance and subsequent development of nonlinearities and inelasticity in the soil–foundation system may be beneficial for the superstructure and should be considered in the analysis and perhaps allowed in the design. However, the consequences of allowing for plasticity below ground surface include transient and permanent deformations which must be realistically assessed in design.

The impact of nonlinear soil-foundation-structure interaction (SFSI) on the seismic response of caisson foundations was illustrated in a recent numerical comparative study by the authors [49]. The study comprised similar rigid cubic caissons carrying elastic single degree of freedom (SDOF) structures, of varying mass and height, in clay. Four different configurations were examined, with respect to the static (F_V) and seismic (F_E) safety factor of the foundation, corresponding to lightly (F_V=5) and heavily loaded (F_V=2.5) seismically *over*- (F_E>1) and *under*-designed (F_E<1) caissons. It was shown that seismically *under*-designing a caisson foundation, thus deliberately *allowing* for plastic deformations to develop below ground level, generally leads to:

- Reduction in "*floor*" response and spectral accelerations.
- Significant reduction in flexural structural deformations.
- Increased dynamic settlements and rotations but minimal residual displacements and tilting.

Overall, the paper highlighted the effectiveness of interface nonlinearities, prevalent in the response of the *under*-designed foundations, in damping the seismic energy, owing to the large ductility capacity of the soil mass.

Incremental Dynamic Analysis is a tool to assess the global and local capacity of structures by subjecting the structural model to several ground motion records, each scaled to multiple levels of intensity. Though introduced and well documented by Vamvatsikos and Cornell [44], the concept of seismic load scaling had been formerly used by several authors to assess the performance of structural frames in buildings [3, 31, 34]. This method of analysis provides several insights regarding the dynamic characteristics of a structural system as well as useful input for applications of performance-based evaluation. In a recent relevant publication, Pecker and Chatzigogos [40] presented results of IDA for a simple bridge pier founded on stiff clay

with a shallow circular foundation considering soil and geometric nonlinearities. They deduced that, on a whole, consideration of nonlinear SSI appears beneficial in drastically reducing the ductility demand in the structure, while stressing out that this positive effect is counterbalanced by larger displacement and rotation of the foundation.

In this framework, the present study further extends the investigation on the seismic response of *under*-designed caisson foundations through 3-D IDA. Similar rigid cubic caissons under three different loading conditions, with respect to the static (F_S) and the seismic (F_E) safety factor of the foundation, are examined. Since the paper aspires to characterize the global foundation-superstructure response in performance based design terms, structural nonlinearity is also accounted for, in order to capture the complex interplay between the main sources of nonlinearities; namely those above and below ground level. The main focus, however, is on the nonlinear phenomena developed at the foundation level. Therefore, structural nonlinearity is considered through a simplified moment-curvature law. The yield strength of the columns is deliberately chosen so that the following idealized configurations are obtained: (*a)* a 12 m and a 46 m tall column, corresponding to a seismically *over*-designed and a seismically *under*-designed (as compared to the superstructure) foundation, respectively, carrying a "light" superstructure (F_S = 5), and (*b*) a 18 m tall column corresponding to a seismically *over*-designed foundation carrying a "heavy" superstructure (F_S = 2.5). Given that IDA covers the full spectrum of the dynamic capacity of the soil-caisson-superstructure system, conclusions of more general validity are expected.

As a final remark, it should be stated that although computationally demanding and challenging, the 3D analysis was preferred to more simplified approaches, e.g. Winkler-based models, due to the fact that while the latter models are, in theory, capable of capturing any observed interface behaviour, their success lies on the appropriate calibration of their parameters which, unfortunately, could not be known *a priori* for each specific case. To the authors' best knowledge, a thorough calibration procedure for Winkler-based modeling of soil-caisson interface response is still missing in the literature.

5.2. Problem definition and analysis methodology

5.2.1 Problem definition

The studied problem is portrayed in **Fig. 1**: A mass-and-column structure is founded through a rigid cubic caisson of side h = 10 m in a 20 m thick 2-layer cohesive soil stratum. The soil is considered to be undrained with S_u = 65 kPa at the upper 6 m and S_u = 130 kPa at the lower 14 m and constant stiffness to strength ratio E/S_u = 1500. The mass-and-column superstructures are modeled as single degree of freedom (SDOF) oscillators. The concentrated oscillator mass, *m*, is given parametrically the values of 5400 and 2700 Mg, corresponding to a static factor of safety F_S = 2.5 ("heavy" superstructure) and F_S = 5 ("light" superstructure) respectively. For each case of F_S, different column heights are calculated; one for the former and two for the latter. In total, a set of three structural configurations are analysed.

The height and strength of the superstructures are calculated according to the following two-step procedure:

(1) A series of finite element static pushover-type of analyses are carried out to derive the bearing strength surfaces of the caisson−soil system in moment (*M*)−horizontal load (*Q*) space. Two envelopes are produced, depicted in **Fig. 2**, one for each case of vertical load applied from the mass weight. The results are normalized with respect to the pure moment capacity M_u (with no horizontal loading) and the pure horizontal capacity Q_u (no moment loading) of the caisson−soil system. The verification of the aforementioned entities is given in **Fig. 3** in terms of Q-u and M-ϑ curves along with the respective contours of plastic strain magnitude at failure.

(2) Using the strength envelopes derived at the first step, the height of the superstructure is deliberately calculated to match a "*target*" critical (yielding) acceleration ($\mathbf{A_{c,\,f}}$), applied at the superstructure mass level, associated with bearing capacity of the foundation. Structural yielding is then either prevented (*under*-designed foundation) or pursued (*over*-designed foundation) by designing the superstructure for a critical acceleration ratio

$$\frac{A_{c,\,f}}{A_{c,\,str}} < 1 \qquad (1)$$

or

$$\frac{A_{c,\,f}}{A_{c,\,str}} > 1 \tag{2}$$

respectively, where $\mathbf{A_{C,\,str}}$ is the critical (at yield) spectral acceleration of the structure. Since the superstructure is modeled as SDOF oscillator, the horizontal force at the top of the caisson is related to the overturning moment as: $M = Q \cdot H$.

It should be noted at this point that since this work comprises a theoretical study on the SFSI of the same caisson under various loading cases and does not intend to propose specific design guidelines, any value of $\mathbf{A_{C,\,f}}$ that stems from the strength envelopes and any value of $\mathbf{A_{C,\,str}}$ that satisfies condition (1) or (2), should suffice for our parametric study. In this paper, values for $\mathbf{A_{C,\,f}}$ and $\mathbf{A_{C,\,str}}$ are arbitrarily chosen so that the critical acceleration ratio, $\mathbf{r_{max}}$, defined as:

$$r_{max} = \frac{\max\left\{A_{c,\,f}\,,\,A_{c,\,str}\right\}}{\min\left\{A_{c,\,f}\,,\,A_{c,\,str}\right\}} \tag{3}$$

is kept constant for all cases considered. Assuming $\mathbf{A_{C,f}}$ = 0.3 g and $\mathbf{A_{C,str}}$ = 0.8 g for the seismically *under*-designed caissons, (3) leads to $\mathbf{A_{C,f}}$ = 0.8 g and $\mathbf{A_{C,str}}$ = 0.3 g for the seismically *over*-designed caisson.

Fig. 2 schematically illustrates the process for calculating the column heights for both the seismically *over*- and *under*-designed foundations. The three model configurations are summarized in **Table 1**:

Table 1 Summary of the model configurations used for the dynamic analysis

model	**m (Mg)**	**F_S**	**H (m)**	**A_c : critical spectral acceleration**	**Foundation**
1	2700	5.0	46	*0.3* g (foundation) 0.8 g (superstructure)	***under***-designed
2	2700	5.0	12	0.8 g (foundation) *0.3* g (superstructure)	*over*-designed
3	5400	2.5	18	*0.3* g (foundation) 0.8 g (superstructure)	***under***-designed

5.2.2 Numerical modelling aspects

The problem is analysed with the finite element code ABAQUS (**Fig. 4**). Both caisson and soil are modeled with 3D 8-noded solid elements, assuming elastic behavior for the former and nonlinear for the latter. The superstructure is modeled with 3D nonlinear Timoshenko beam elements. The caisson is connected to the soil with special contact surfaces, allowing for realistic simulation of the possible detachment and sliding at the soil-caisson interfaces. The mesh for the soil-caisson consists of 12500 elements. The analyses were performed in a Core i-7 desktop processor, 2.8 GHz and 8 GB RAM. Depending on the severity of the input seismic motion, each analysis lasted approximately 16 to 24 hours. To improve the computational cost without jeopardizing the accuracy of the analysis, the surface-to-surface contact interaction was modeled by exponential ("softened") pressure-overclosure relationship through the direct constraint enforcement method that makes use of Lagrange multipliers. For more details on the contact interaction algorithm the reader is referred to ABAQUS manual [1].

The location and type of lateral boundaries is an important consideration in the dynamic modelling. It is known from the literature that whereas under monotonic and cyclic static loading these boundaries can be placed fairly close to the foundation (just outside the “pressure bulb”) and they can be of any “elementary” type (from “free” to “fixed”), under dynamic loading waves emanating from the footing–soil interface cannot propagate to infinity unless special transmitting boundaries are placed at suitably large distances. “Elementary” boundaries may cause spurious reflections, thereby contaminating the wave field below the foundation and reducing or even eliminating the radiation damping. In this particular case, however, even "elementary" boundaries placed at a “reasonably–large” distance from the foundation might suffice, for the following reasons:

1) Under low frequency dynamic loading, waves emitted from symmetrically–opposite points of the foundation contact surface, being out-of-phase, "interfere destructively" and thus limit substantially the radiation of wave energy [13, 25, 30, 48]. Therefore, even in an (infinite) halfspace, boundaries placed at short distances from the loaded surface would hardly be “seen” by the waves emitted from the caisson.

2) The geometric properties of the superstructures were appropriately calculated so that the elastic fixed-base period T_{str} = 0.6 sec, for all cases, is deliberately larger than the first natural period, T = 0.41 sec, of the soil profile. In this way spurious reflections at the boundaries of the model are limited as a result of a destructive interference (existence of a cut-off period for radiation damping equal to the first natural period of the soil profile) of the outward spreading waves [12, 13]. "Elementary" boundaries placed at relatively short distances (a few widths) would therefore suffice.

3) In most cases analysed, soil inelasticity is activated, mobilizing bearing capacity failure mechanisms. The presence of the associated localized failure surfaces (at small distances from the caisson), has the effect of creating a softer zone inside the (stiffer) soil; this zone would reflect the incident waves, thus further reducing the amount of wave energy transmitted (“leaking”) into the surrounding soil. Borja et al [4, 5] thoroughly examined the aforementioned phenomenon for the case of surface footings.

In the absence of a cut-off frequency for the radiation damping, then the "elementary" boundaries should be placed at far distances from the loaded surface, e.g. at approximately L = 10 B [37], increasing prohibitively the computational cost. The use of appropriate wave energy transmitting boundaries would alleviate the cost of analysis even if placed at relatively short distances. However, to the authors' knowledge, special boundaries that can absorb accurately all types of body and surface waves at all angles of incidence and all frequencies, consistent with a predefined acceleration time history (input motion) at the base of the model, does not exist in the literature.

A distance of L = 5 B was therefore adopted in all studied cases. Moreover, appropriate kinematic constraints are imposed to the lateral edges of the model, allowing it to move in horizontal shear as the free field [19, 21]. The nodes at the bottom of the finite element mesh are fixed in the vertical direction and they follow the horizontal motion imposed by the seismic records.

5.2.3 Constitutive modelling

5.2.3.1 Soil

For the total stress analysis under undrained conditions soil behavior is modeled through a nonlinear constitutive law [18] which is a slight modification of one incorporated in ABAQUS. It uses the Von Mises failure criterion with yield stress σ_y related to the undrained shear strength S_u as

$$\sigma_y = \sqrt{3} \cdot S_u \tag{4}$$

along with a nonlinear kinematic and isotropic hardening law, and an associative plastic flow rule. The model parameters are calibrated to fit published G–γ curves of the literature. **Figs 5(a)** and **5(b)** illustrate the validation of the kinematic hardening model (through simple shear finite element analysis) against published G–γ and ξ–γ curves by Ishibashi and Zhang [24]. Mass and stiffness proportional Rayleigh damping, representing material damping, is taken equal to 5% between the eigenfrequency of the soil deposit and the dominant frequency of the earthquake ground motion.

5.2.3.2 Superstructure

In their previous work the authors considered elastic superstructures, thus focusing solely on the role of soil and interface nonlinearities in the response. However, as aforementioned, the engineering motivation of this paper has arisen from the recent developments of performance based design approaches, which aim at characterizing the structural behavior in terms of displacement, rotation, distortion and drift rather than in terms of strength criteria. Since both superstructure and soil-foundation can be potential sources of nonlinearities and energy dissipation during a strong earthquake, they should be both characterized by nonlinear models, allowing to capture their complex nonlinear interplay, and giving a reliable estimate of system deformation, both at the foundation and the superstructure level [6, 9]. Therefore, structural nonlinearity is introduced. A simple hyperbolic backbone moment (M)–curvature (κ) curve describes this nonlinear behavior of the column:

$$\kappa = \frac{M_y}{EI} \cdot \left(\frac{M}{M_y - M} \right) \quad \text{for } M < M_y \tag{5}$$

where EI the initial structural bending stiffness and M_y the bending moment yield strength associated with the critical acceleration ($\mathbf{A_{C,\,str}}$). **Fig. 6** shows the respective nonlinear $M-\kappa$ curves of the examined systems. Regarding the elastic fixed-base period (T_{str}=0.6 sec) of the columns, the choice was deliberate so the comparison of their effective response, namely the T_{SSI}, is performed on a *fair* basis; that is from the same starting point. Furthermore, given that the determination of shear strength and especially of shear deformation characteristics of (e.g. reinforced concrete) structures are still controversial issues [32], the interplay between shear-flexure in the inelastic regime is not taken into account and the controlled mode of failure is assumed to be flexure-dominated.

5.3. Static Pushover Analysis

Prior to the dynamic analysis, we investigate the response in terms of monotonic loading: the static "*pushover*" test. Displacement controlled horizontal loading is applied atop the superstructure mass. To investigate the level of nonlinear SSI effects developed in the seismically *over*- and *under*-designed caissons, the tests involved: (a) fixed-base superstructures (no SSI effects), and (b) complete soil-structural models considering elastic superstructures, in order to determine the pure lateral capacity of the caisson. As illustrated in **Fig. 7,** in terms of load–displacement relation at the structure mass, SSI effects are virtually absent in the seismically *over*-designed foundation (*model 2*), where structural inelasticity governs entirely the system response. Notice the negative slope of the force-displacement curve, attributed to P-δ effects and not to stiffness degradation of the material of the superstructure. Structural collapse occurs when the curve reaches the point of zero horizontal load. It can be observed, however, that the aforementioned behavior, also qualitatively similar to the results by Hutchinson et al [23] and Lignos et al [29], becomes prevalent at rather large displacements. In stark contrast, plasticity that developed below ground level in the seismically *under*-designed foundations (*models 1*, *3*), reduces significantly the structural demand, by approximately 30 % in *model 1* and 50 % in *model 3*.

5.4. Incremental Dynamic Analysis

Incremental Dynamic Analysis (IDA) offers thorough seismic demand and capacity prediction capability [44, 45]. A series of nonlinear dynamic analyses is conducted using a scaled ensemble of ground motion records, aiming at covering the entire range of response, from elasticity to collapse, having selected an Intensity Measure (IM), to represent the seismic intensity and proper Engineering Demand Parameters (EDPs) to characterize the structural response. The output is a plot of a selected IM versus a selected EDP. Similarly, an IDA *curve set* is a collection of IDA curves of the same structural model under different records that have been parameterized on the same IM. While each curve, given the soil-structure model and the ground motion record, is a completely defined deterministic entity, a probabilistic characterization can be brought into play by defining the 16 %, 50 % and 84 % probability level curves (fractiles) for each IDA curve set, displaying the evolution of the effectiveness (median values) and efficiency (dispersion) of the analysis methodology.

5.4.1 Record suite

An ensemble of 10 real acceleration time histories has been chosen for the incremental dynamic analyses. The seismic records are imposed in a single horizontal direction at the base ("within" motion) of the finite element models. In terms of severity, the selection ranges from medium intensity (e.g. Kalamata, Aegion) to stronger (e.g. Lefkada-2003, Imperial Valley), and to very strong accelerograms characterized by forward-rupture directivity effects, or large number of significant cycles, or fling-step effects (e.g. Takatori, JMA, TCU). Note that since the scope of this study was to examine the nonlinear response of the caisson foundations in a wide range of exciting intensities, frequencies, and kinematic characteristics, selection criteria that are commonly used in the design of actual projects, such as specific soil class, Magnitude, source-to-site distance R, duration etc, were not applied.

The unscaled records are outlined in **Table 2** and given along with the corresponding elastic response spectra in **Fig. 8**.

Table 2 Selected records for incremental dynamic analysis

No	Event	Year	Station	Component	Soil†	M_w	R§ (km)	PGA (g)	CAV	Arias Intensity (m/sec)
1	Aegion	1995	Aegion-rock	—	A	6.1	8	0.359	247.449	0.517
2	ChiChi	1999	TCU	68°	C,D	7.6	0.2	0.353	1599.58	3.018
3	Kocaeli	1999	Duzce	180°	D	7.2	9	0.312	1257.38	2.654
4	Imperial Valley	1979	El Centro #4	140°	C,D	6.6	28	0.485	658.099	1.301
5	Kobe	1995	JMA	000°	B	6.9	2	0.83	1943.28	8.358
6	Kalamata	1986	Nomarxia	EW	C	6	4	0.24	367.488	0.554
7	Lefkada	2003	Hospital	W325N	C	6.4	8	0.426	1460.91	3.972
8	Northridge	1994	Rinaldi	228°	B	6.7	5	0.837	1464.88	7.156
9	Kocaeli	1999	Sakarya	EW	B	7.2	3	0.33	771.243	1.158
10	Kobe	1995	Takatori	000°	D	6.9	4	0.611	2317.8	8.592

† USGS, Geomatrix soil class.
§ Closest distance to fault rupture.

The scaling of the ten real records was performed with due consideration on the role of the soil on the response of the caisson, which is two-fold:

1) It acts as a medium that amplifies (or de-amplifies) the seismic load and transmit it into the foundation. Most certainly, very strong motions may lead to soil failure during the nonlinear wave propagation prior to any possible failure of the foundation—superstructure system; a clear deviation from the scope of this work.
2) It offers the resistance mechanisms that contribute to the bearing capacity of the caisson.

In an effort to reduce the number of parameters that affect the response of the studied systems, only the second property of the foundation soil is taken into consideration. The effect of soil amplification has been deliberately eliminated by predetermining the input motion at surface level through 1-D deconvolution analysis. More specifically, all accelerograms were deconvoluted to the base of the model so that five target PGA values of free-field motion, namely 0.1 g, 0.2 g, 0.3 g, 0.4 g and 0.6 g, are calculated at the top of the soil profile. In total, 200 dynamic analyses were

performed. The authors concluded that by limiting the scaling of the records to the specific five PGA values at the free-field: (a) the total computational cost is significantly reduced, while (b) gaining a clear insight into the physical phenomenon.

To elaborate on this argument, **Fig. 9** compares the PGA at ground surface as a function of the maximum input acceleration at the base of the model computed through 1-D linear and 3-D nonlinear analysis, for the TCU-068ns record. At low to moderate base acceleration levels (less than about 0.3 g) soil nonlinearity has an insignificant effect on the soil response. At higher base acceleration levels, however, there is a significant de-amplification of the ground accelerations compared to linear response analysis. Observe that the effect of nonlinearity becomes prominent for PGAs larger than 0.4 g to 0.6 g. Therefore, to avoid excessive soil inelasticity (or even soil failure) due to seismic wave propagation, the maximum input PGA was set equal to 0.6 g.

The IDA curves, however, were based on the actually computed PGA values and not on the targeted ones. The deconvolution technique was used as a crude approximation of the PGA at the surface and the deviation from the targeted values was certainly not a restriction in our methodology.

Admittedly, simply scaling an acceleration time history to various PGA values representing the severity of an earthquake is not necessarily correct. Obviously, this is not the case for Aegion record which can be satisfactorily approximated by a single sinusoidal pulse.

5.4.2 Intensity measure

Different options are available for the IM to be used in the IDA curves. In this paper, however, a single convenient IM is used, PGA of ground surface motion. Though the PGA is among those exhibiting the less satisfactory statistical correlation with the EDPs [11], in this study it was considered as the most appropriate intensity measure, since the analyses were performed with records deconvoluted to a specific PGA at the surface of the free-field. Furthermore, it still remains the most commonly used parameter in the seismic codes for describing earthquake hazard and seismic loading.

5.4.3 Engineering demand parameters

Selecting an EDP is application-specific; for example, the peak floor accelerations are correlated with damage to contents and other non-structural elements damage. The maximum drift ratio, Y_{max}, is known to relate well to global dynamic instability and several structural performance limit-states upon which we intend to focus [45, 46,]. In this paper, the following EDPs are considered:

- The maximum total horizontal drift of the oscillator, Y_{max}

$$Y_{max} = \max\left[\frac{u^{mass} - u^{structure\ base}}{H}\right] \quad (6)$$

- The maximum ductility demand: μ_δ.

The global (displacement) ductility demand, μ_δ, including the SSI effects, is the maximum ratio of the induced flexural distortion of the superstructure (free of any rigid-body motion) divided by a characteristic displacement, designated as yield displacement, u_y :

$$\mu_\delta = \max\left[\frac{u^{mass} - (u^{structure\ base} + \theta H)}{u_y}\right] \quad (7)$$

where, as schematically depicted in **Fig. 10**, θ is the caisson rotation and H the structure height. The yield displacement u_y is assessed through the static push-over analyses of the systems, considering fixed-base structures, according to the following procedure, also adopted by Gerolymos et al [20]: At the mass of the superstructure, a horizontal load is progressively applied and the load–displacement curve (P–u) is calculated. Then, the P–u curve is approximated by an equivalent bilinear elastic–perfectly plastic curve, in which the linear section is defined as the secant line corresponding to 60 % of the maximum horizontal load (P_y) and the second section by the tangent line on the post-yielding section of the load–displacement curve. The intersection of these two lines defines the yield displacement u_y (**Fig. 11**).

- The maximum caisson rotation, θ_{max}
- The residual caisson rotation, θ_{res}

Since both θ_{res} and θ_{max} are strongly associated with phenomena such as separation and slippage between soil–caisson interface and caisson base uplifting (geometric nonlinearities), greater values are expected for the *under*-designed foundations (*models 1* and *3*).

5.5. Analysis: Results and Discussion

Figures 12 - 19 compare the performance of all three examined systems through the IDA curves. To assist in the interpretation of these graphs, the respective 16%, 50% and 84% fractile curves are given alongside each curve set. The IDA curves were approximated by spline interpolation, while the fractile curves were derived considering the available EDP values corresponding to each IM value. The calculation process is terminated when the number of available curves corresponding to the specific IM is:

- less than 9, for the 16% fractiles
- less than 5, for the 50% fractiles
- less than 2, for the 84% fractiles

At first, to facilitate the understanding and explanation of results, it is fruitful to give a brief description of the mobilized impedance mechanisms that govern the response of the studied systems [49]. That is :

(a) Soil inelasticity and bearing capacity failure mobilization that generate hysteretic damping. This type of impedance mechanism dominates the response of *over*-designed foundations.

(b) Radiation damping due to the outward---emitted from the caisson-soil interface---spreading waves (only marginal in our case due to the existence of a cut-off period).

(c) Geometric nonlinearities: uplift and sliding at the caisson-soil interfaces, that lead to a threshold value (*cutoff*) for the maximum transmitted seismic forces. This type of impedance mechanism is the most influential one to the response of the *under*-designed foundations.

The IDA curves for the maximum horizontal drift, Y_{max}, a measure of structural distress, are given in **Fig. 12** and the corresponding fractile-specific curves in **Fig. 13**. Interestingly, the lightly loaded systems (*models 1* and *2*) exhibit a quite similar response with the *under*-designed heavily loaded foundation (*model 3*) and especially *model 2* (F_S = 5, *over*-designed caisson) and *model 3*. Undoubtedly, however, the most advantageous response concerning structural demand is exhibited by the *under*-designed lightly loaded *model* 1. The latter exhibits minimal drift—a clear evidence of the beneficial geometric nonlinearities governing the response.

At this point the following remarks should be made:

- Concerning the scaled record suite, observe that no seismic record, with the exception of one, produces PGA at the free-field greater than 0.6 g. The remarkable TCU-068 record (from Chi-Chi 1999), however, proves the severity of the near-fault ground motions bearing fling-step, by reaching 0.71 g after propagating through the nonlinear soil stratum, even though scaled for 0.6 g in a 1-D equivalent linear analysis. It is furthermore obvious that the *IM* used in the analyses (PGA at the free-field) cannot be predicted *a priori*.
- Note that from the analyses no 'flatlines' [44, 45, 46] were produced, which would indicate a rapid increase of the EDP towards 'infinite' values for small changes in the IM, thus signaling global dynamic instability. The explanation lies in the definition of the problem and the selection of the IM, since, as justified previously, the maximum PGA at the free-field to which the seismic records were scaled was 0.6 g.
- The aforementioned observations may explain why in this study the widely used tracing algorithms, such as the *Hunt & Fill* or the *constant IM-step* algorithms [45, 46] could not be implemented for the generation of the IDA curves.

The IDA curves for the maximum displacement ductility demand (μ_δ) are portrayed in **Figs. 14** and **15**. Once more, the beneficial influence of geometric nonlinearities, dominant in the response of the seismically *under*-designed foundations (*models 1* and *3*), on the distress of the superstructure is evident. While the *over*-designed *model 2* exhibits ductility demands $\mu_\delta \geq 1$ for most of the seismic motions, the respective demand on the columns founded on the *under*-designed caissons is $\mu_\delta \leq 1$. This may be attributed to the fact that although the *over*-designed caissons generally develop smaller displacements, their corresponding rotations as well as yield displacements u_y are also significantly decreased. The net effect was a trend towards larger displacement ductility demands. The opposite statements are true for the *under*-designed foundations—the maximum displacements were larger, but the rotations and the yield displacements are also increased, resulting in a trend towards smaller displacement ductility demands. The fractile curves in **Fig. 15** highlight once again the exceptional performance of the *under*-designed lightly loaded *model* 1, exhibiting minimal structural distress, as opposed to the largest demands experienced by its *over*-designed counterpart (*model 2*).

Figs. 16-19 present the IDA curves for the maximum and the residual caisson rotation, θ_{max} and θ_{res}. The latter, θ_{res}, is determined at the end of each dynamic calculation, which, in all analyses, is continued for 5 seconds after the main motion has ended in order to establish an equilibrium state. The performance does not seem to deviate from any rational intuitive expectation: the seismically *under*-designed caissons demonstrate substantially larger rotations than the *over*-designed counterpart, as a result of the intense caisson-soil interface separation, gapping and soil inelastic action. Notice again the tremendous demand imposed by the large velocity pulse (2.6 m/s) of huge duration (6.3 s) of the TCU-068 record on the *under*-designed caissons, causing global instability and system failure of the lightly loaded *model* 1 at PGA = 0.7 g. Nevertheless, it is remarkable that with the exception of the performance under the TCU record at high PGA levels (which incidentally are 2 times higher than the actual record), the *under*-designed caissons can avoid collapse sustaining rather tolerable rotations and displacements. This observation is consistent with the results presented by the authors in [49], in which it was shown that in the *over*-designed foundations the

developed *drift* is mainly due to flexural distortion, whereas in the *under*-designed ones the *drift* is mainly due to foundation rotation.

Worthy of note are the irregularities exhibited in the IDA curves for the θ_{res} in the *under*-designed caissons, as depicted in **Figs. 18-19**. Observe the instabilities followed by regain at higher levels, consistent with the variability of the response as a function of the individual records, but especially with the random nature of this EDP.

5.5.1. IDA curves of maximum acceleration at mass level

In **Fig. 20** the comparison is performed for the maximum acceleration at mass level as the Earthquake Demand Parameter. It is immediately evident that all systems exhibit a threshold at $a_{max} \approx 0.3$ g. However, the mechanisms for this acceleration *cut-off* differ with respect to the seismic safety factor of the foundation:

a) In the *under*-designed foundations, it is the geometric nonlinearities and soil inelasticity that dominate the response and control the value that cannot be exceeded by the transmitted seismic force thus providing a type of seismic isolation for the superstructure ($A_{C,\,f} = 0.3$ g).
b) In the *over*-designed foundation it is the structural inelasticity that sets an acceleration plateau at $A_{C,\,str} = 0.3$ g, stemming from the bending moment capacity at the base of the column.

The results once again emphasize the favorable performance exhibited by the *under*-designed caissons in terms of structural demand, which become more prominent when combined with a conservative *static* design: for a given PGA level, smaller accelerations are transmitted to the *under*-designed lightly loaded *model 1* than the other two systems.

To further elucidate the effect of structural inelasticity on the seismic response, **Fig. 21** compares the acceleration time-histories and the corresponding "*floor*" response spectra at the mass level of the over-designed *model* 2 considering both elastic and inelastic superstructure. Excitation: JMA-000 record, down-scaled at a *free-field* PGA = 0.4 g, is used. As expected, an elastic superstructure allows a large inertia force to develop at the mass, whereas column inelasticity provides a *cut-off* for the transmitted accelerations.

5.5.2. Some detailed results of dynamic analysis

To get a detailed insight into the nonlinear response mechanisms, typical results of the analyses are portrayed in **Figs 22–23** in terms of acceleration time–histories at the mass level, and moment–rotation and settlement–rotation loops at the head of the caisson. Shaking: JMA-000 record, down-scaled at a *free-field* PGA = 0.4 g.

The strong contribution of geometric nonlinearities in de-amplifying the seismic motion is again evident in both the lightly and the heavily loaded systems (**Figs. 22a1, 23a3**). Yet, intense interface gapping does not provide only a threshold for the transmitted accelerations to the superstructure, but also affects the frequency content of the motions: note the long-period motions calculated at the structures founded on the *under*-designed caissons (*models 1, 3*) as opposed to the higher-frequency motion developed at the *over*-designed *model 2* (**Fig. 22a2)**.

The moment–rotation (M–ϑ) curves at caisson head for F_S = 2.5 and F_S = 5.0 are presented in **Fig. 22b1–b2** and **Fig. 23b3** respectively. P-δ effects were considered in the calculations. Respecting their design principles, the *over*-designed foundation (*model* 2) experiences limited inelasticity, while the *under*-designed ones (*models* 1 *and* 3) behave strongly inelastic. Once more, the advantageous contribution of the interface (**Fig. 22b1–Fig. 23b3**) rather than the material (**Fig. 22b2**) and structural nonlinearities in damping the seismic energy is apparent. The shape of the loops in **Fig. 22b1** and **Fig. 23b3** reflects the successive detachments/re-attachments of the caisson from the surrounding soil. Another noteworthy observation from the M–ϑ loops of both heavily and lightly loaded structures is that they do not exhibit significant strength degradation, indicating minor P-δ effects.

However, this favorable performance is not attainable at zero cost: in this case an increase of foundation settlements is expected. Studying the settlement–rotation (w–ϑ) response of the seismically *over*- and *under*-designed caissons for F_S = 5 ("light" superstructure), presented in **Fig. 22c1–c2**, the *over*-designed caisson experiences practically elastic settlement $w \approx 2$ cm. Remarkably, the *under*-designed alternative experiences only marginally larger and quite tolerable seismically induced settlement, $w \approx 2.5$ cm and minimal residual rotation.

As anticipated, the heavily loaded (F_S = 2.5) *model 3* exhibits larger accumulated settlements than the lightly loaded counterparts: $w \approx 5.5$ cm, as portrayed in **Fig. 23c3**. An interesting observation that may be extracted from the (w–ϑ) loops is that the low F_S system not only sustains larger residual rotations than the high F_S systems, but also the forward directivity pulse carried by the JMA record determines its response.

5.6. Summary and Conclusions

The present study compares the dynamic response of seismically *over*− and seismically *under*−designed caisson foundations and evaluates the effect of the nonlinear phenomena developed below ground surface on the seismic demand of the superstructures. SDOF structures of varying mass weight, simulating heavily or lightly loaded structures founded through similar rigid cubic caissons on a 2-layer soil stratum are used as examples. The investigation is performed considering soil and structural nonlinearity through 3D finite element incremental dynamic analysis (IDA) with 8-noded solid elements to represent the soil domain. An ensemble of 10 earthquake motions ranging from medium intensity to very strong, scaled at different PGAs of ground surface motion, was used as base excitation. IDA curves were generated for the maximum horizontal drift, the maximum global ductility demand, the maximum caisson rotation and the residual caisson rotation. The maximum acceleration developed at the superstructure mass was introduced as an *ad hoc* Engineering Demand Parameter.

From the study, the following conclusions could be inferred:

- In terms of structural distress, there is a distinct predominance in the performance of the structures founded on the *under*-designed caissons (*models* 1 and 3) developing significantly reduced horizontal drifts and ductility demands, as opposed to the one founded on the *over*-designed caisson; clear evidence that the mechanism of interface nonlinearities acts as a "*fuse*" for the superstructure.

- Concerning the accelerations developed at the structure mass level, both mechanisms of geometric nonlinearities and structural inelasticity, prevalent in the response of the seismically *under*- and *over*-designed foundations

respectively, provide a plateau for the maximum transmitted accelerations. Due to the strongly nonlinear soil-structure interaction effects present in the former mechanism, however, the superstructure experiences a longer-period motion as compared to the one filtered by the localized plasticity in the column.

- In terms of system performance, the *under*-designed foundations experienced increased dynamic settlements and rotations as compared to the *over*-designed one. Strikingly, however, they sustained only minimal residual displacements and tilting, owing much to the massive weight of the caisson which acts as a restraining force.

Overall, the study highlighted the efficacy of *under*-designed caisson foundations with high static factor of safety, providing a low-cost foundation solution with a high seismic isolation potential.

References

[1] ABAQUS, Inc. ABAQUS Analysis User's Manual, Version 6.8, Providence, RI, USA, 2008.

[2] Anastasopoulos I, Gazetas G, Loli M, Apostolou M, Gerolymos N. Soil failure can be used for seismic protection of structures. *Bull of Earthquake Eng* 2010; 8: 309-326.

[3] Bertero VV. Strength and deformation capacities of buildings under extreme environments. *Structural Engineering and Structural Mechanics*, K. S. Pister, ed., Prentice Hall, Englewood Cliffs, NJ, 211–215, 1977.

[4] Borja RI, Wu WH, Smith HA. Nonlinear response of vertically oscillating rigid foundations. *Journal of Geotechnical and Geoenvironmental Engineering*, ASCE 1993; 119(5): 893-911.

[5] Borja RI, Wu WH, Amies AP, Smith HA. Nonlinear lateral, rocking, and torsional vibrations of rigid foundations. *Journal of Geotechnical and Geoenvironmental Engineering*, ASCE 1994; 94(3): 491-513.

[6] Chatzigogos CT, Figini R, Pecker A, Salençon J. A macroelement formulation for shallow foundations on cohesive and frictional soils. *International Journal for Numerical and Analytical Methods in Geomechanics 2011*; 35 (8): 902-931.

[7] Dominguez J. *Dynamic stiffness of rectangular foundations*. Research report, R78-20, MIT, 1978.

[8] Elsabee F, Morray JP. *Dynamic behavior of embedded foundations*. Research report, R77-33, MIT, 1977.

[9] Figini R, Paolucci R, Chatzigogos CT. A macro-element model for non-linear soil–shallow foundation–structure interaction under seismic loads: theoretical development and experimental validation on large scale tests. *Earthquake Engineering & Structural Dynamics 2012*; 41 (3): 475-493.

[10] Gajan S, Kutter BL, Phalen JD, Hutchinson TC, Martin GR. Centrifuge modeling of load-deformation behavior of rocking shallow foundations. *Soil Dynamics and Earthquake Engineering 2005*; 25: 773–783.

[11] Garini E, Gazetas G. *Destructiveness of Earthquake Ground Motions: Intensity Measures Versus Sliding Displacement*. *Proceedings of 2nd International Conference on Performance-Based Design in Earthquake Geotechnical Engineering*, May 28-30 2012, Taormina, Italy: 886-899.

[12] Gazetas G. Analysis of machine foundation vibrations: state of the art. *Soil Dynamics and Earthquake Engineering 1983*; 2: 2–42.

[13] Gazetas G. Simple physical methods for foundation impedances. *Dynamics of Foundations and Buried Structures*. Benerjee PK and Butterfield R, editors, Elsevier Applied Science 1987; Chapter 2: 44-90.

[14] Gazetas G, Apostolou M, Anastasopoulos I. Seismic Uplifting of Foundations on Soft Soil, with Examples from Adapazari (Izmit 1999, Earthquake). *Foundations: Innovations, Observations, Design & Practice*. British Geotechnical Association; 2003:37–50.

[15] Gelagoti F, Kourkoulis R, Anastasopoulos I, Gazetas G. Rocking isolation of low-rise frame structures founded on isolated footings. *Earthquake Engineering & Structural Dynamics 2012*; 41 (7): 1177-1197.

[16] Gerolymos N, Gazetas G. Winkler model for lateral response of rigid caisson foundations in linear soil. *Soil Dynamics and Earthquake Engineering 2006*; 25(5):347–61.

[17] Gerolymos N, Gazetas G. Development of Winkler model for static and dynamic response of caisson foundations with soil and interface nonlinearities. *Soil Dynamics and Earthquake Engineering 2006*;26(5):363–76.

[18] Gerolymos N, Gazetas G. Static and dynamic response of massive caisson foundations with soil and interface nonlinearities—validation and results. *Soil Dynamics and Earthquake Engineering 2006*; 26(5):377–94.

[19] Gerolymos N, Giannakou A, Anastasopoulos I, Gazetas G. Evidence of beneficial role of inclined piles: Observations and summary of numerical analyses. *Bull of Earthquake Eng 2008*; 6 (4); 705-722.

[20] Gerolymos N, Drosos V, Gazetas G. Seismic response of single-column bent on pile: Evidence of beneficial role of pile and soil inelasticity. *Bull of Earthquake Eng 2009*; 7 (2); 547-573.

[21] Giannakou A, Gerolymos N, Gazetas G, Tazoh T, Anastasopoulos I. Seismic behavior of batter piles: Elastic response. *Journal of Geotechnical and Geoenvironmental Engineering*, ASCE 2010; 136 (9); 1187-1199.

[22] Harden CW, Hutchinson TC. Beam-on-Nonlinear-Winkler-Foundation Modeling of Shallow, Rocking-Dominated Footings. *Earthquake Spectra 2009*; 25(2): 277–300.

[23] Hutchinson TC, Boulanger RW, Chai YH, Idriss IM. Inelastic Seismic Response of Extended Pile Shaft Supported Bridge Structures. PEER Report 2002/14. Department of Civil and Environmental Engineering University of California, Irvine, Department of Civil and Environmental Engineering University of California, Davis.

[24] Ishibashi I, Zhang X. Unified dynamic shear moduli and damping ratios of sand and clay. *Soils & Foundations 1993*; 33(1): 12−191

[25] Kausel E. *Forced vibrations of circular foundations on layered media*. Research Report R74-11, MIT, 1974.

[26] Kausel E, Roesset JM. Dynamic stiffness of circular foundations. *Journal of the Engineering Mechanics Division*, ASCE 1975; 101 (6): 770–85.

[27] Kawashima K, Nagai T, Sakellaraki D. Rocking seismic isolation of bridges supported by spread foundations. In: Proc. 2nd Japan–Greece workshop on seismic design, observation, and retrofit of foundations, Tokyo, Japan, April 3–4 2007: 254–265.

[28] Lam IP, Chaudhury D. *Modeling of drilled shafts for seismic design*. NCEER Report II2D-2.5, The National Center for Construction Education and Research, 1997.

[29] Lignos DG, Krawinkler H, Whittaker AS. Prediction and validation of sidesway collapse of two scale models of a 4-story steel moment frame. *Earthquake Engineering and Structural Dynamics 2011*; 40 (7): 807-825

[30] Luco JE, Westman RA. Dynamic response of circular footings. *Journal of the Engineering Mechanics Division*, ASCE 1971; 97(5): 1381–1395.

[31] Luco N, Cornell CA. Effects of connection fractures on SMRF seismic drift demands, *Journal of Geotechnical and Geoenvironmental Engineering*, ASCE 2000;126: 127–136.

[32] Mergos PE, Kappos AJ. Seismic damage analysis including inelastic shear–flexure interaction. *Bull Earthquake Eng* 2010; 8: 27–46.

[33] Mita A, Luco JE. Dynamic response of a square foundation embedded in an elastic halfspace. *Soil Dynamics and Earthquake Engineering* 1989; 8 (2): 54–67.

[34] Nassar AA, Krawinkler H. *Seismic demands for SDOF and MDOF systems*. Research Report No. 95; 1991, The John A. Blume Earthquake Engineering Center, Stanford University.

[35] Novak M, Beredugo YO. Vertical vibration of embedded footings. *Journal of the Soil Mechanics and Foundations Division*, ASCE 1972; 98 (SM12): 1291–310.

[36] Paolucci R. Simplified evaluation of earthquake induced permanent displacement of shallow foundations. *Journal of Earthquake Engineering 1997*; 1(3): 563–579.

[37] Panagiotidou AI, Gazetas G, Gerolymos N. Pushover and Seismic Response of Foundations on Stiff Clay: Analysis with P-Δ Effects. *Earthquake Spectra* 2012; 28 (4): 1589-1618..

[38] Pecker A. Capacity Design Principles for Shallow Foundations in Seismic Areas, *Proceedings of the 11th European Conference on Earthquake Engineering*, 1998: 303-316.

[39] Pecker A. A seismic foundation design process, lessons learned from two major projects : the Vasco de Gama and the Rion Antirion bridges. *ACI International Conference on Seismic Bridge Design and Retrofit*, University of California at San Diego, 2003, La Jolla, USA.

[40] Pecker A, Chatzigogos CT. Non Linear Soil Structure Interaction: Impact on the Seismic Response of Structures. *Geotechnical, Geological, and Earthquake Engineering* (17); *Earthquake Engineering in Europe 2010*: 79-103.

[41] Suarez V, Kowalsky MJ. Displacement-based seismic design of drilled shaft bents with soil-structure interaction. *Journal of Earthquake Engineering 2007*; 11(6): 1010-1030

[42] Tajirian FF, Tabatabaie M. Vibration analysis of foundations in layered media. *Vibration problems in geotechnical engineering*, ASCE 1985; 27-46.

[43] Tassoulas JL. Elements for the numerical analysis of wave motion in layered media. Research report, R81-2, MIT, 1981.

[44] Vamvatsikos D, Cornell CA. Incremental dynamic analysis. *Earthquake Engineering and Structural Dynamics 2002*; 31(3):491–514.

[45] Vamvatsikos D, Cornell CA. Applied Incremental Dynamic Analysis. *Earthquake Spectra 2004*; 20(2): 523-553.

[46] Vamvatsikos D, Cornell CA. Tracing and post-processing of IDA curves: Theory and software implementation. Report No. RMS-44, RMS Program, Stanford University, Stanford, 2001.

[47] Varun, Assimaki D, Gazetas G. A simplified model for lateral response of large diameter caisson foundations-Linear elastic formulation. *Soil Dynamics and Earthquake Engineering 2009*; 29(2):268-291.

[48] Vetetsos AS, Wei YT. Lateral and rocking vibration of footings. *Journal of the Soil Mechanics and Foundations Division*, ASCE 1971; 97: 1227–1248.

[49] Zafeirakos A, Gerolymos N, Gazetas G. The role of soil and interface nonlinearities on the seismic response of caisson supported bridge piers. *Proceedings of the 5th International Conference on Geotechnical Earthquake Engineering*, 2011, Santiago, Chile.

Chapter 5

Figures

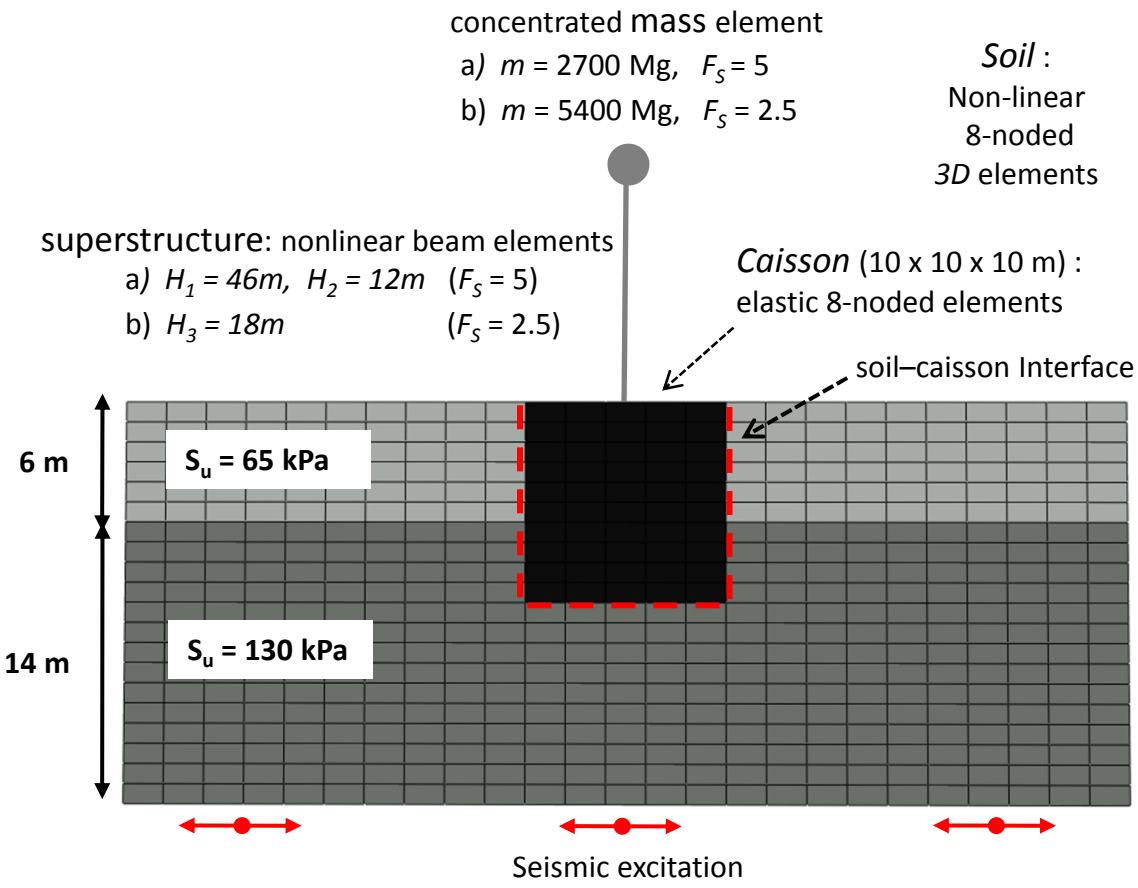

Fig. 5.1. Overview of the 3D finite element model with the parameters used in the analysis.

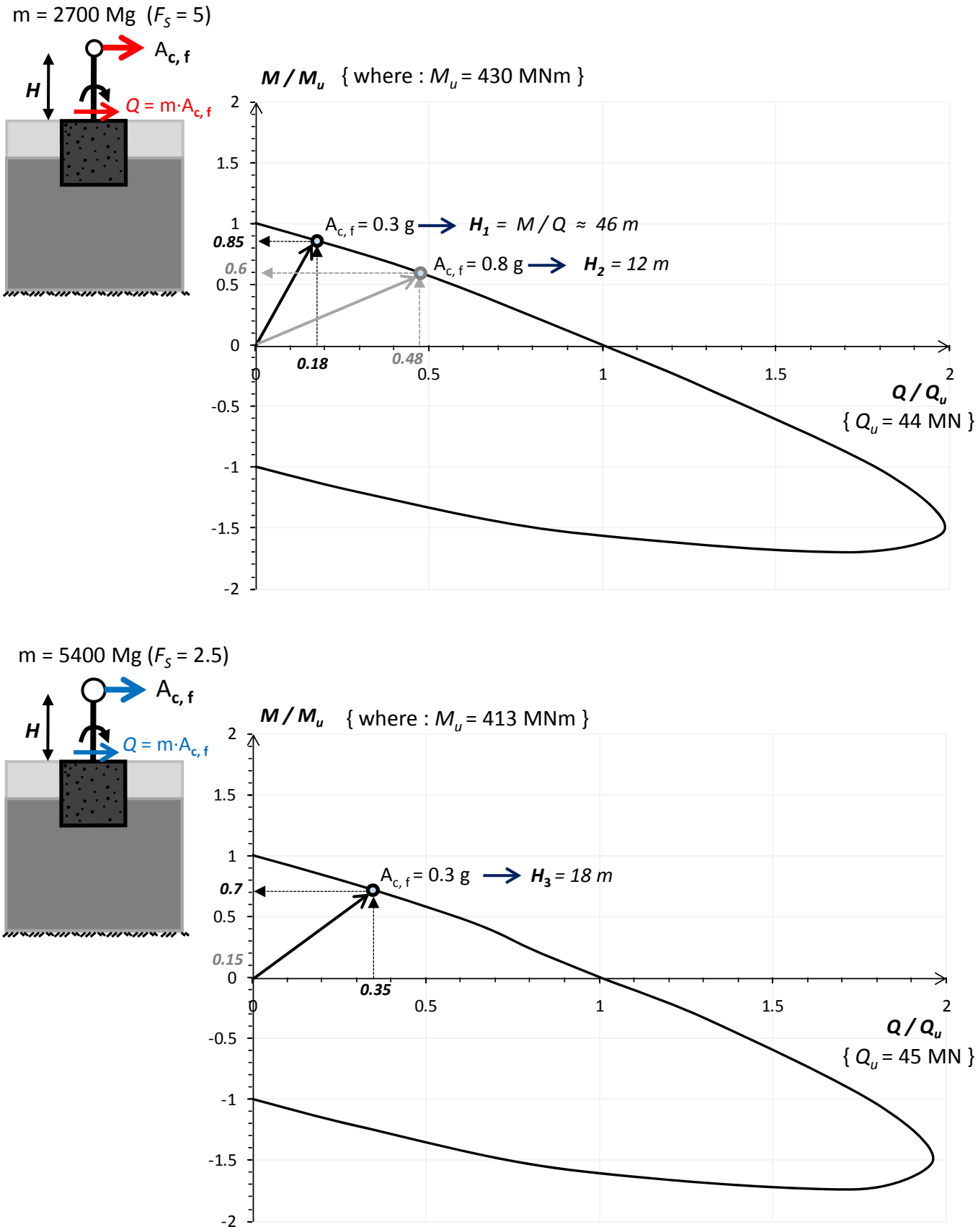

Fig. 5.2 Normalized M-Q Interaction diagrams for **F_S=5** (top) and **F_S=2.5** (bottom)**:** Calculation of the column heights for the seismically *over*-designed ($A_{C,f}$ = 0.8 g) and *under*-designed ($A_{C,f}$ = 0.3 g) foundations.

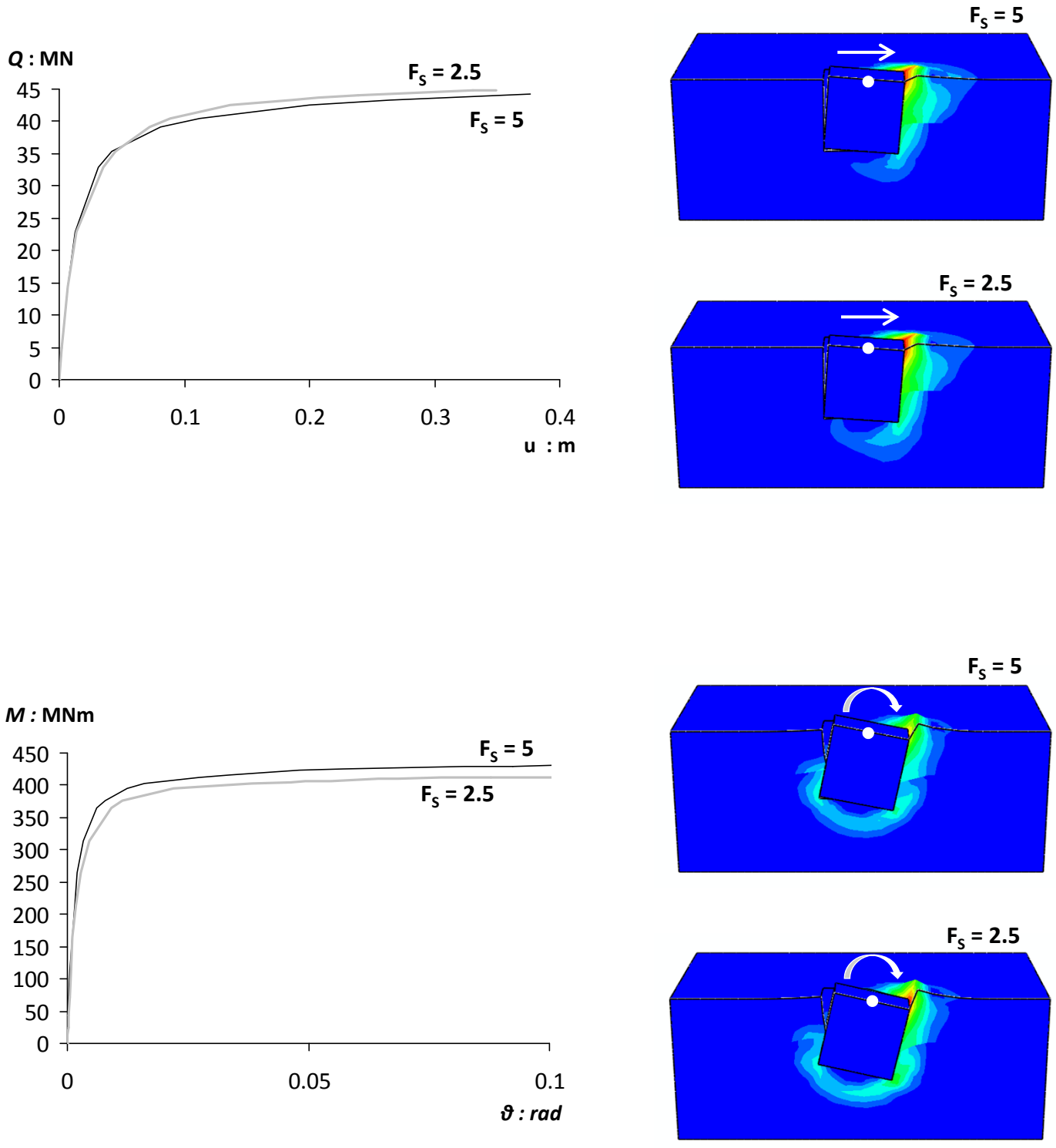

Fig. 5.3 Q-u and M-ϑ curves corresponding to monotonic loading at the top of the caisson along with the respective contours of plastic strain magnitude at failure, for F_S**=5** and **F_S=2.5**.

model : 1
m = 2700 Mg
F_S = 5
H = 46 m
under-designed caisson

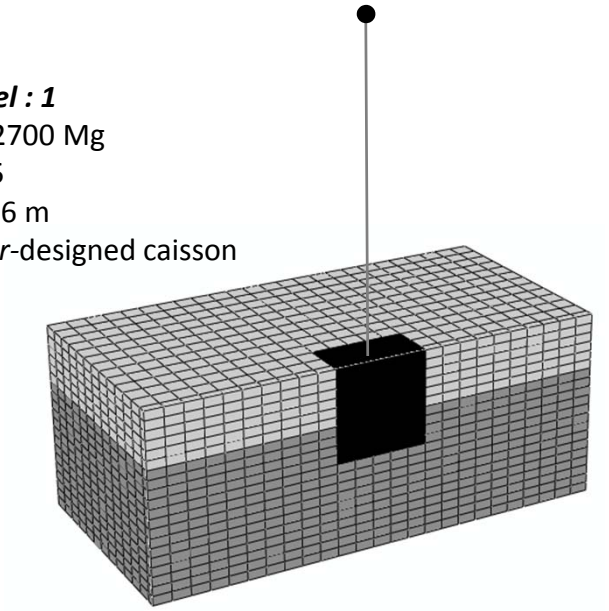

model : 2
m = 2700 Mg
F_S = 5
H = 12 m
over-designed caisson

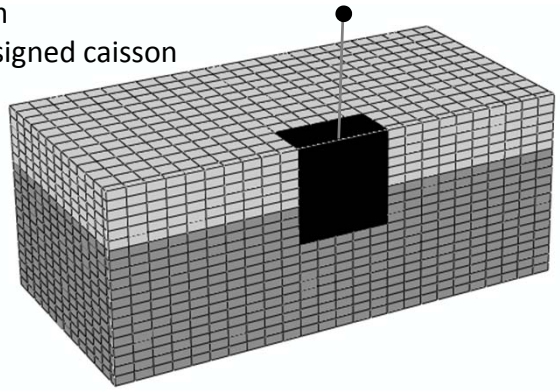

model : 3
m = 5400 Mg
F_S = 2.5
H = 18 m
under-designed caisson

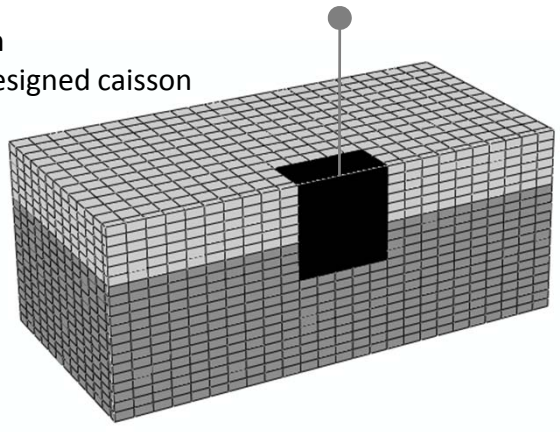

Fig. 5.4 Finite element discretisation of the three configurations analyzed (column heights not in scale).

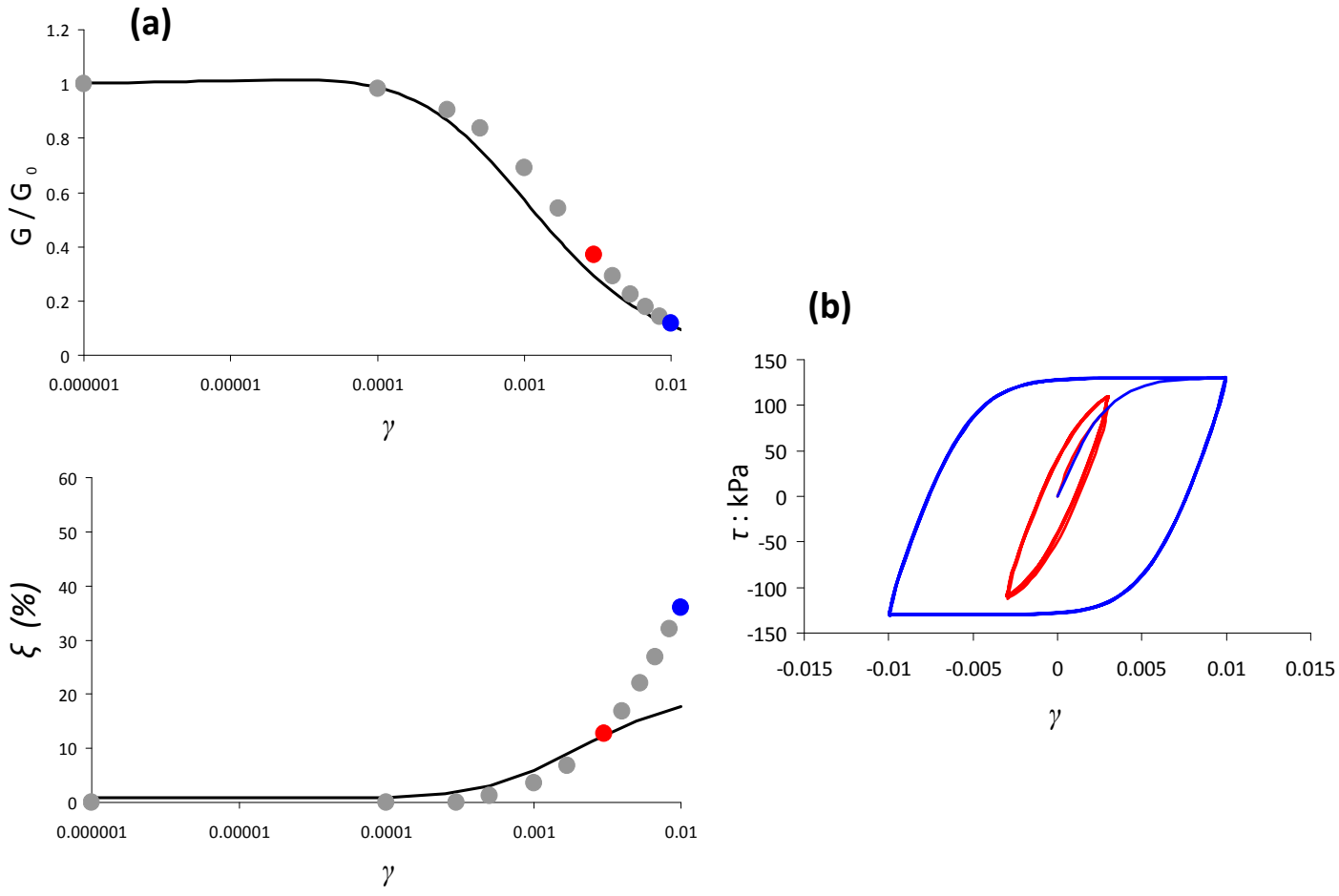

Fig. 5.5 (a) Calibration of kinematic hardening model for soil (stiff clay, Su =130 kPa, G_0 = 500 Su) against published *G*–*γ* and *ξ*–*γ* (PI = 30, σ_v = 200 kPa) curves (Ishibashi and Zhang 1993). **(b)** Shear stress−strain loops corresponding to the designated points in (**a**).

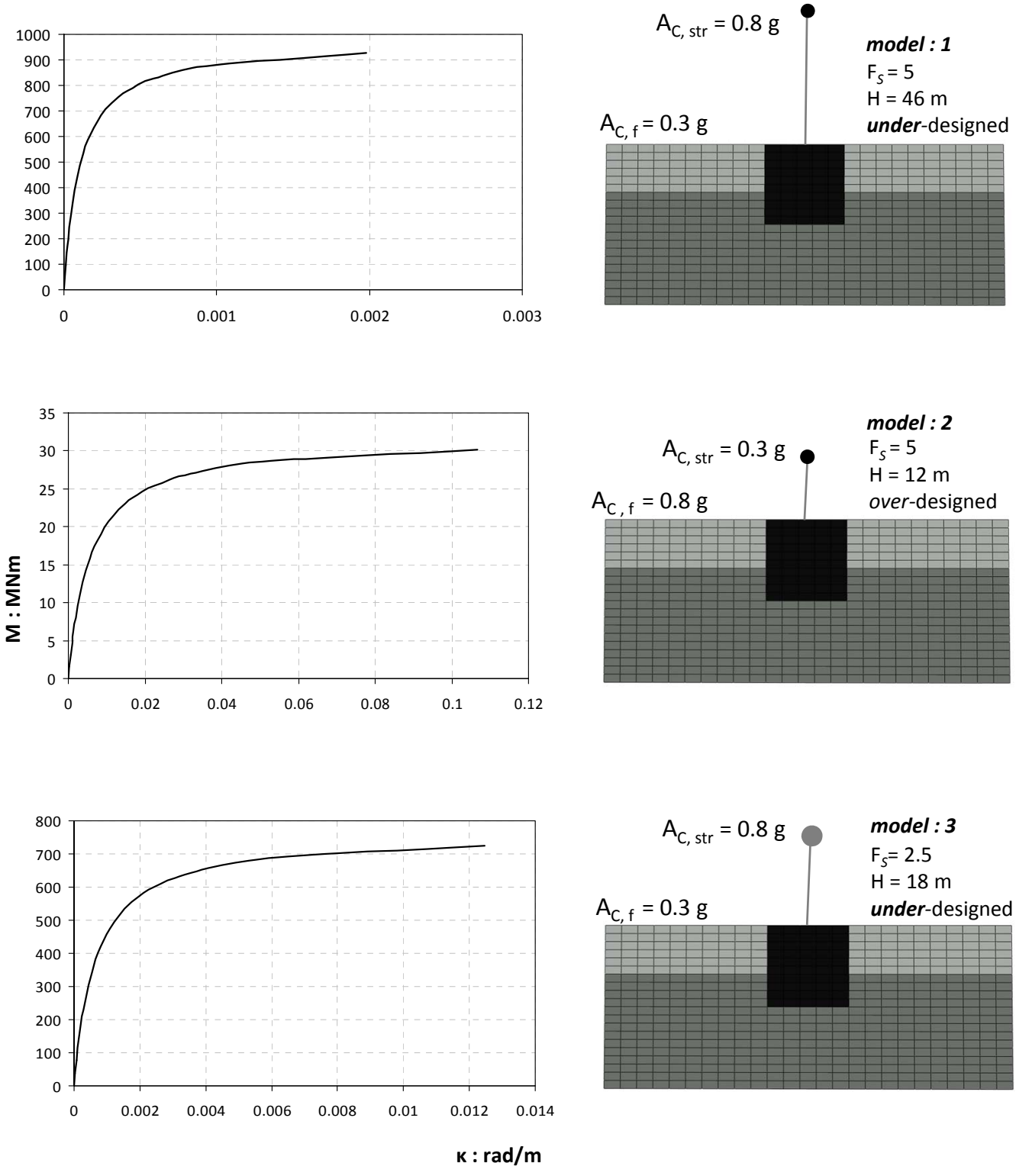

Fig. 5.6 Predefined moment–curvature relations used for superstructure inelasticity (column heights not in scale).

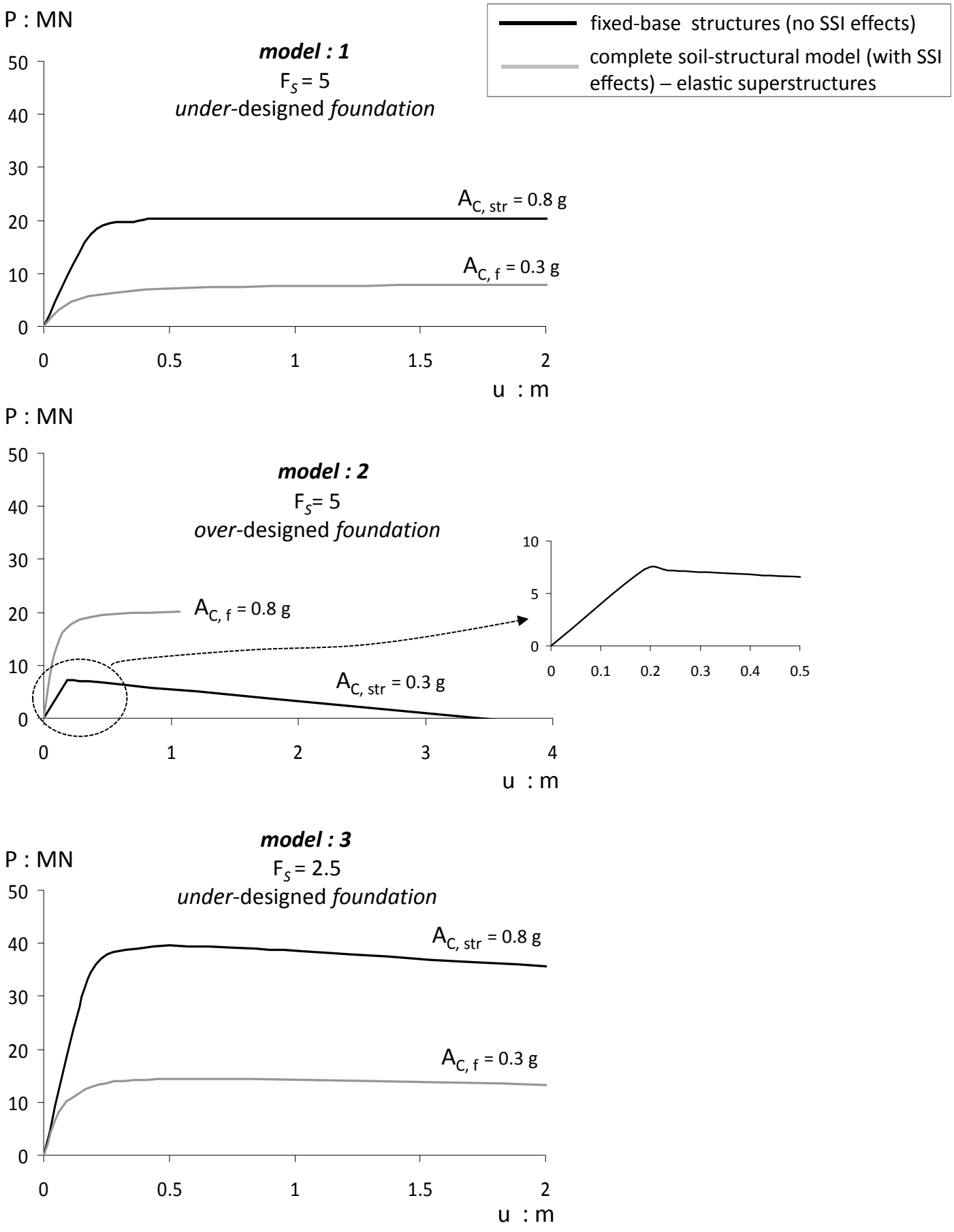

Fig. 5.7 Load-displacement pushover curves for horizontal loading of all examined systems.

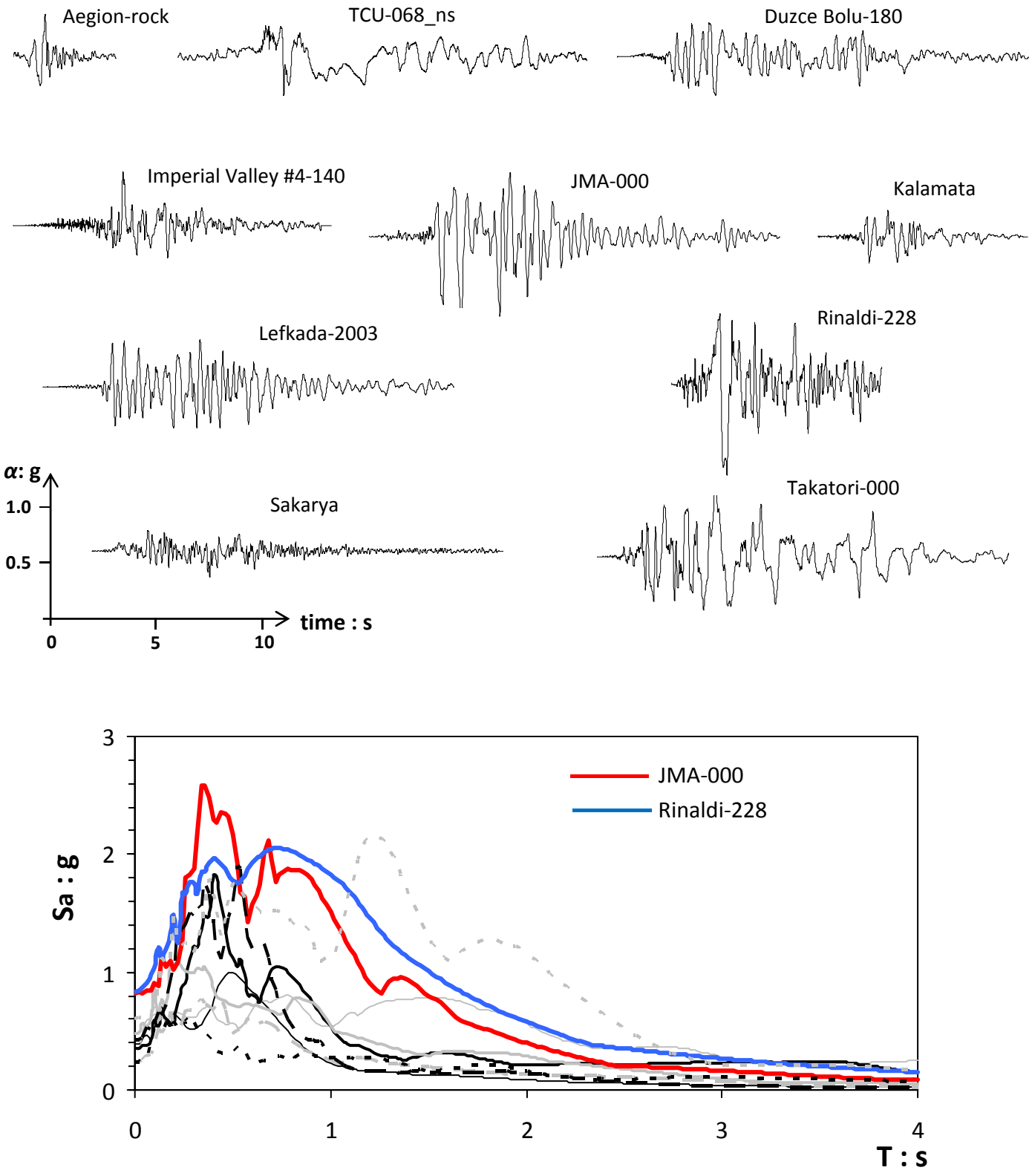

Fig. 5.8 Real earthquake records used for the analysis, along with their elastic spectra.

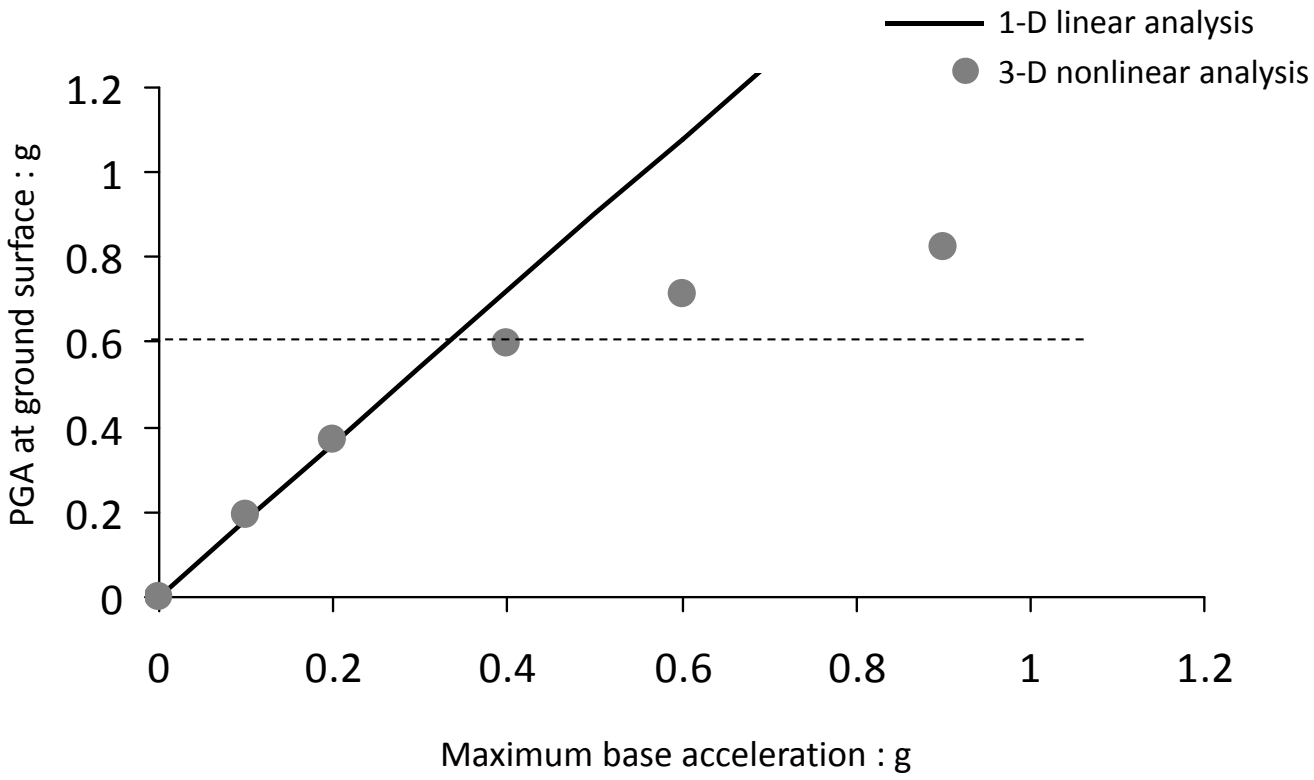

Fig. 5.9 Computed PGA at ground surface versus the maximum base acceleration, through 1-D linear and 3-D nonlinear analysis. Excitation: *TCU-068_ns.*

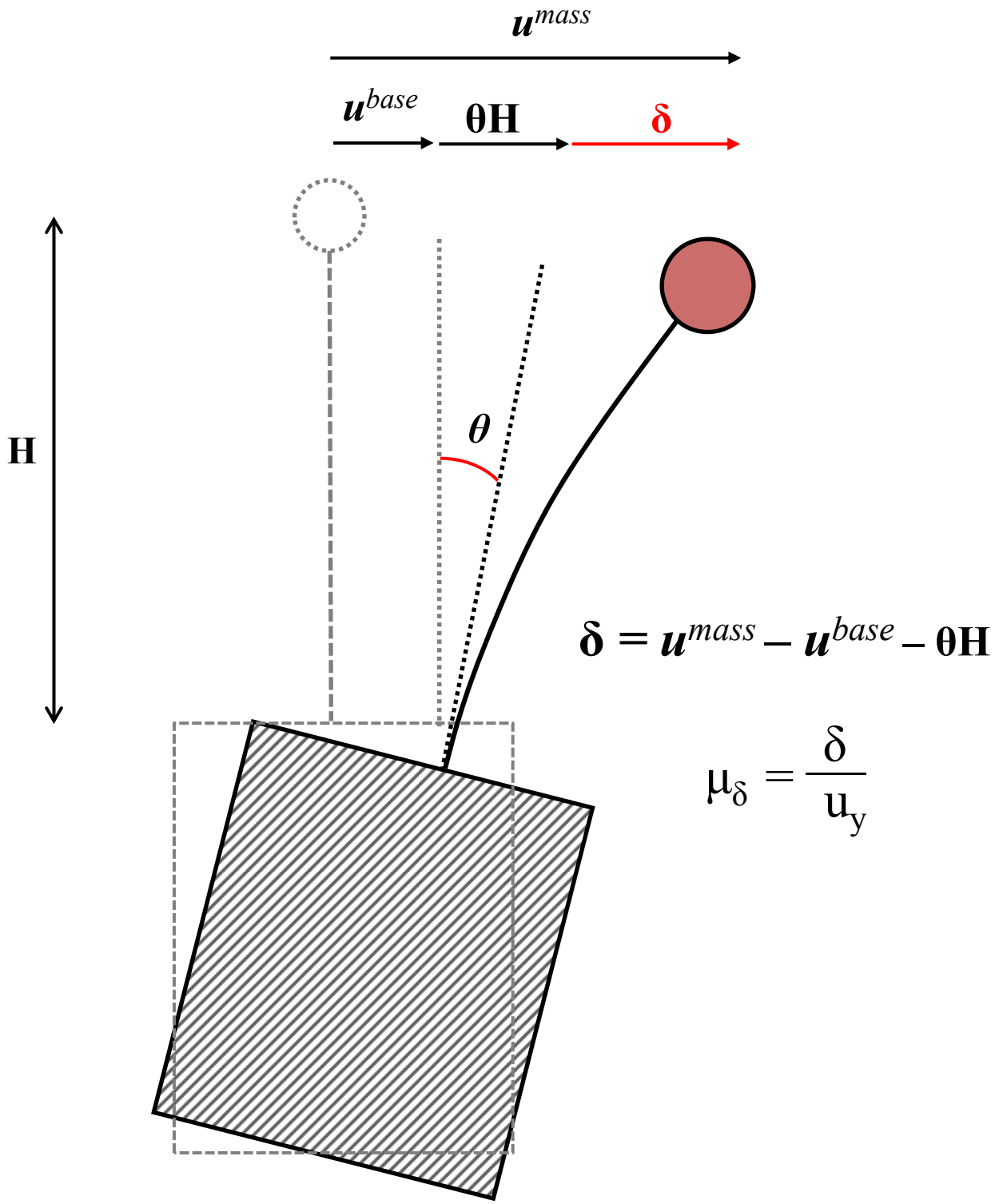

Fig. 5.10 Definition of the global displacement ductility demand, μ_δ.

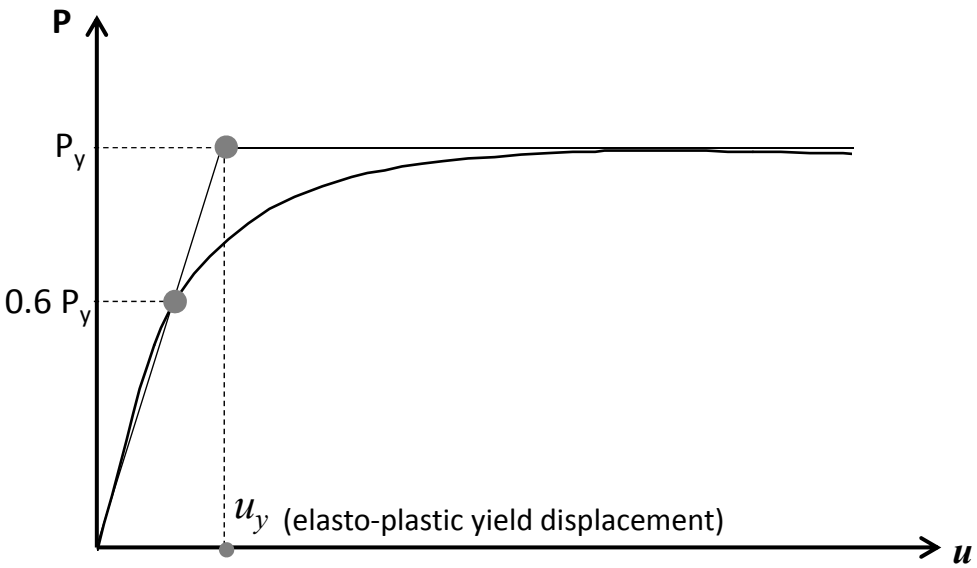

Fig. 5.11 Definition of yield displacement of the soil-structure system.

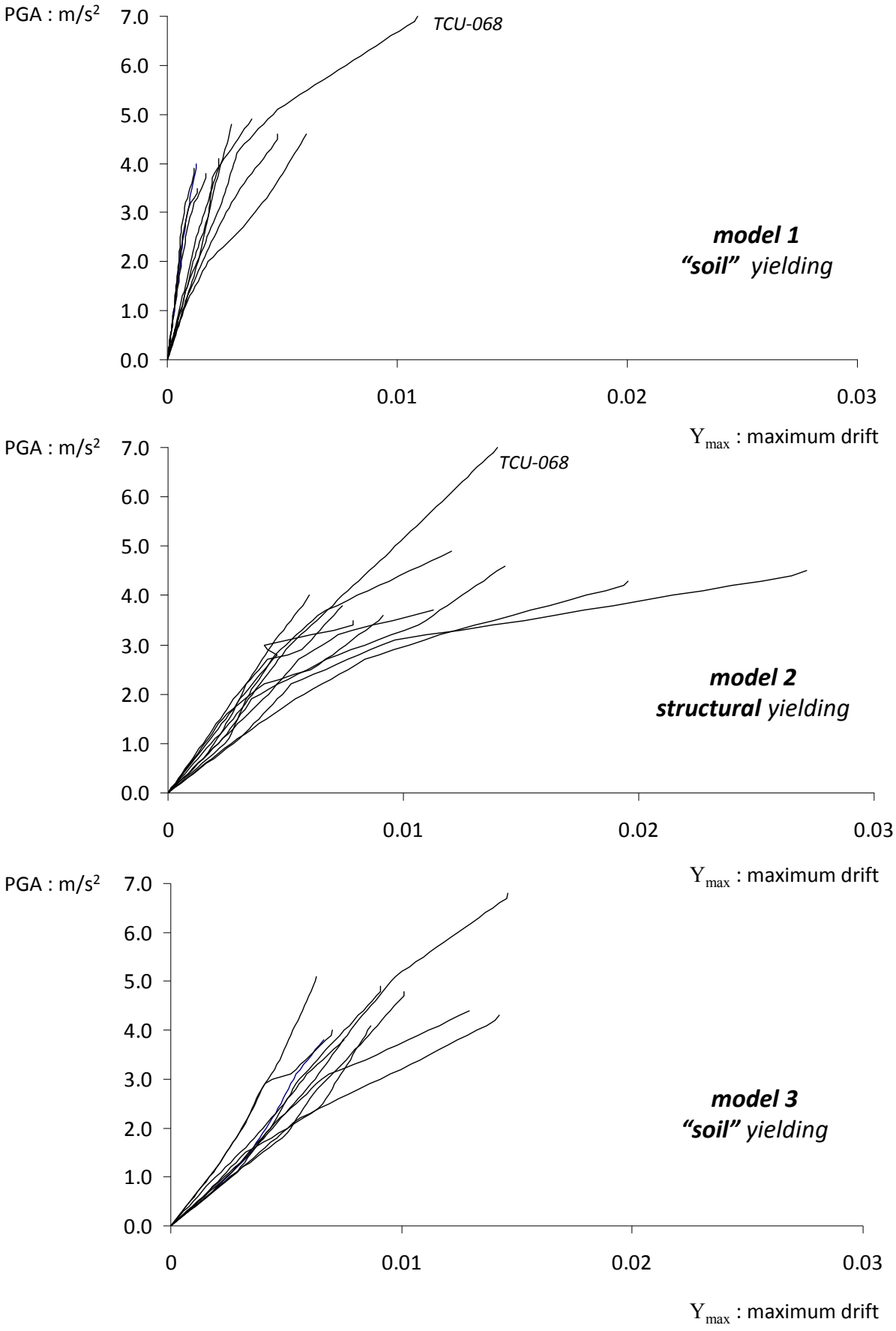

Fig. 5.12 IDA curves: $\mathbf{Y_{max}}$ **(maximum drift)** versus the free-field PGA for the three models.

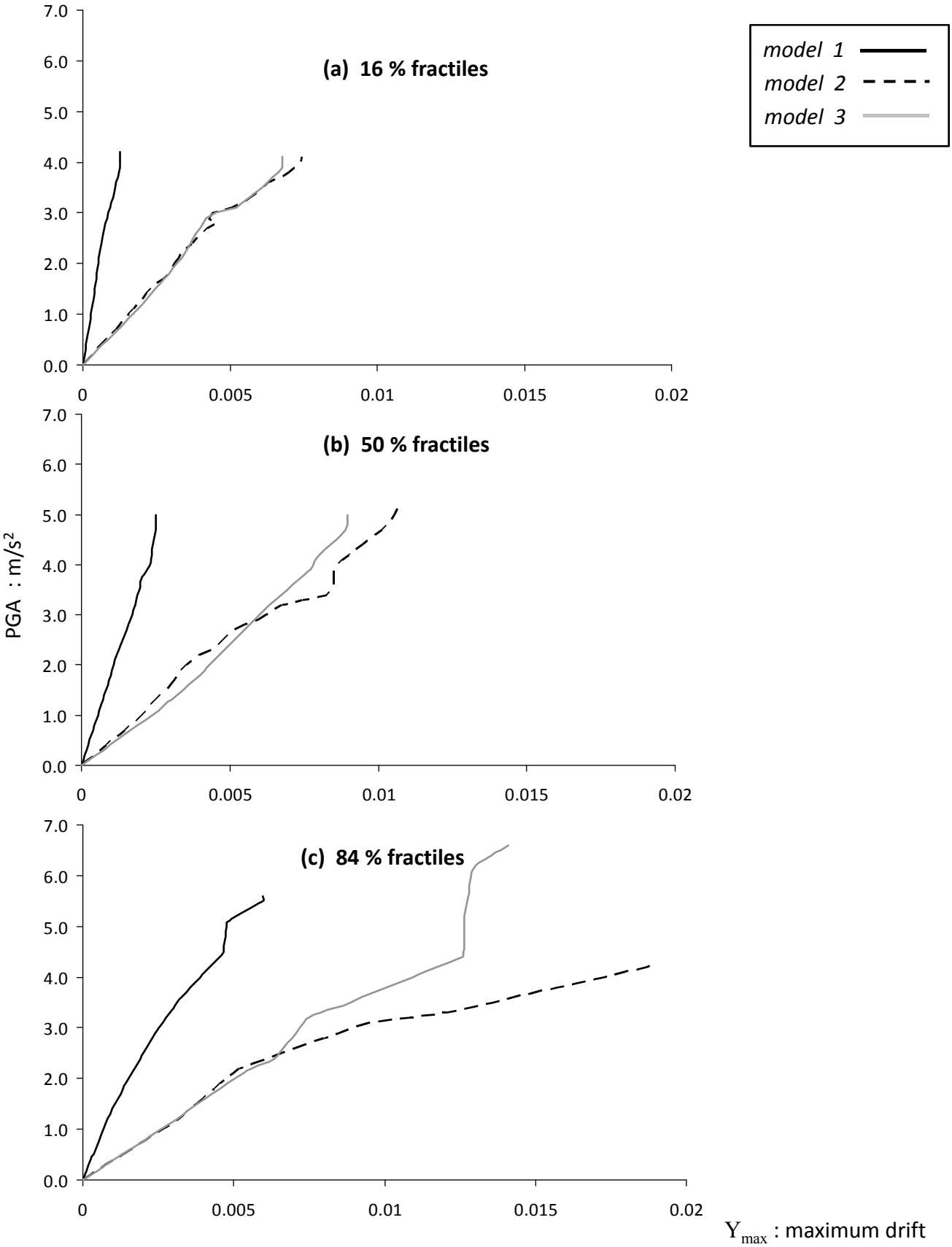

Fig. 5.13 Summarized IDA curves : $\mathbf{Y_{max}}$ **(maximum drift)** for the three models: (a) 16% fractiles, (b) 50% fractiles, (c) 84% fractiles.

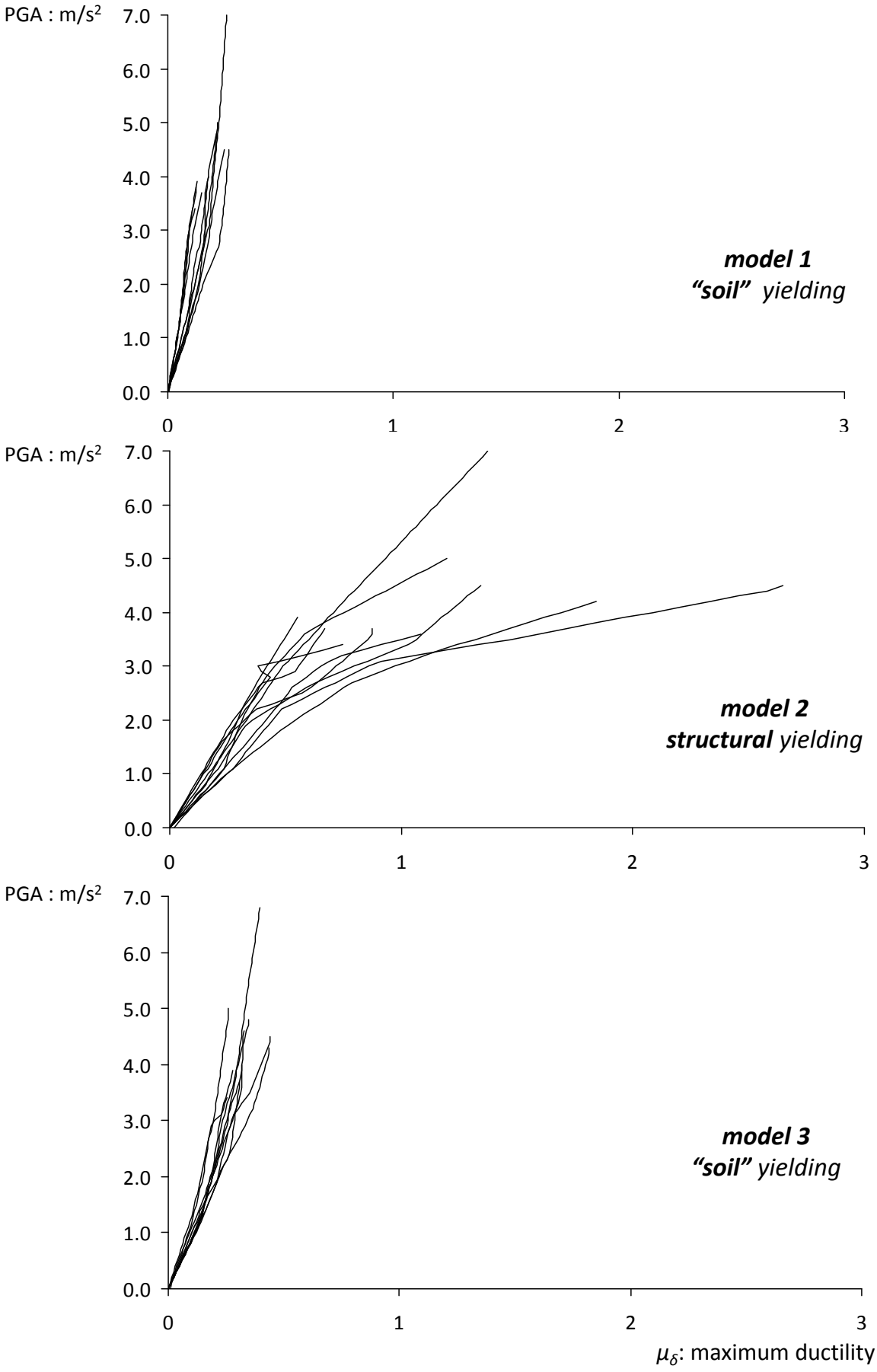

Fig. 5.14 IDA curves: μ_δ **(maximum ductility)** versus the free-field PGA for the three models.

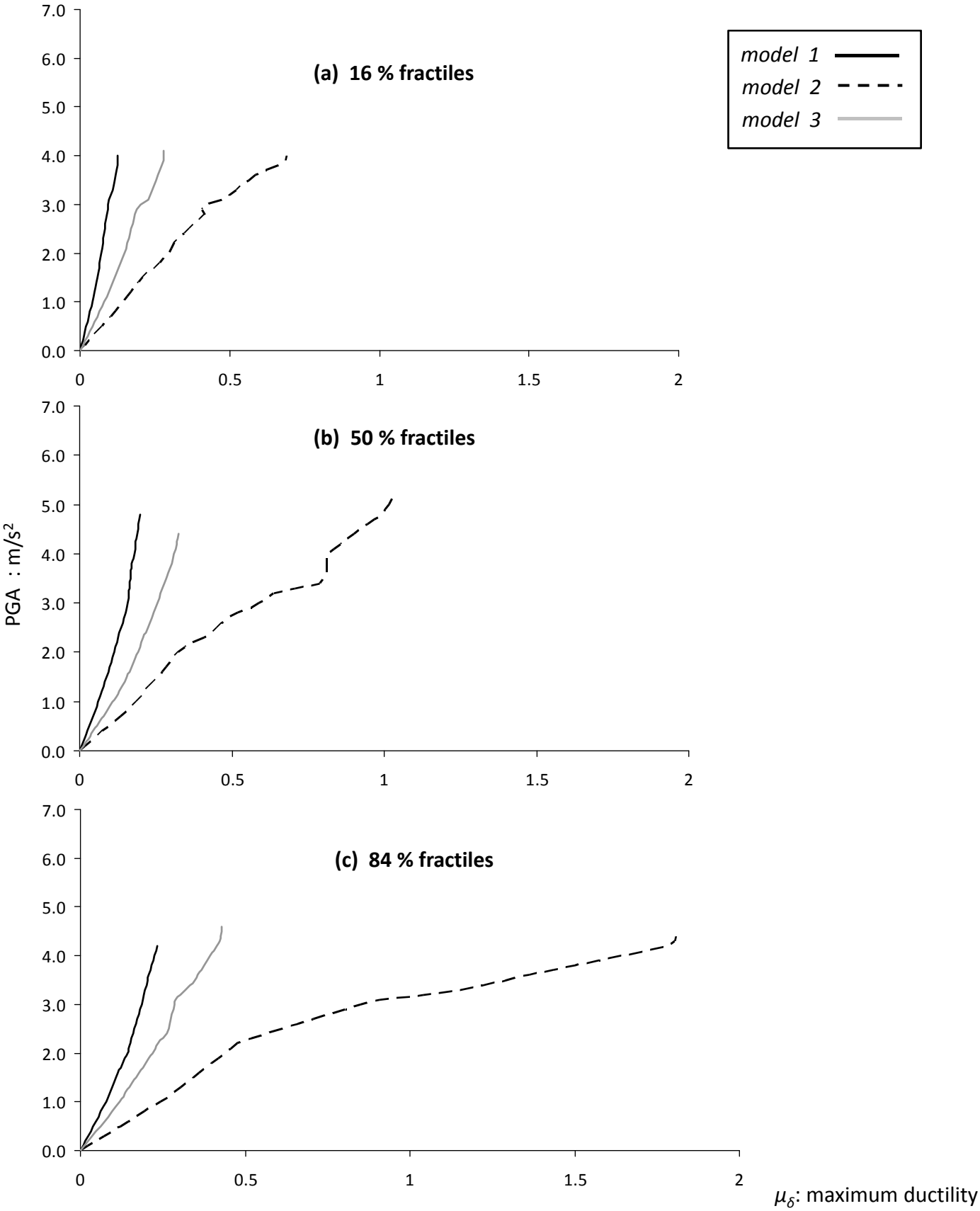

Fig. 5.15 Summarized IDA curves : μ_δ **(maximum ductility)** for the three models: (a) 16% fractiles, (b) 50% fractiles, (c) 84% fractiles.

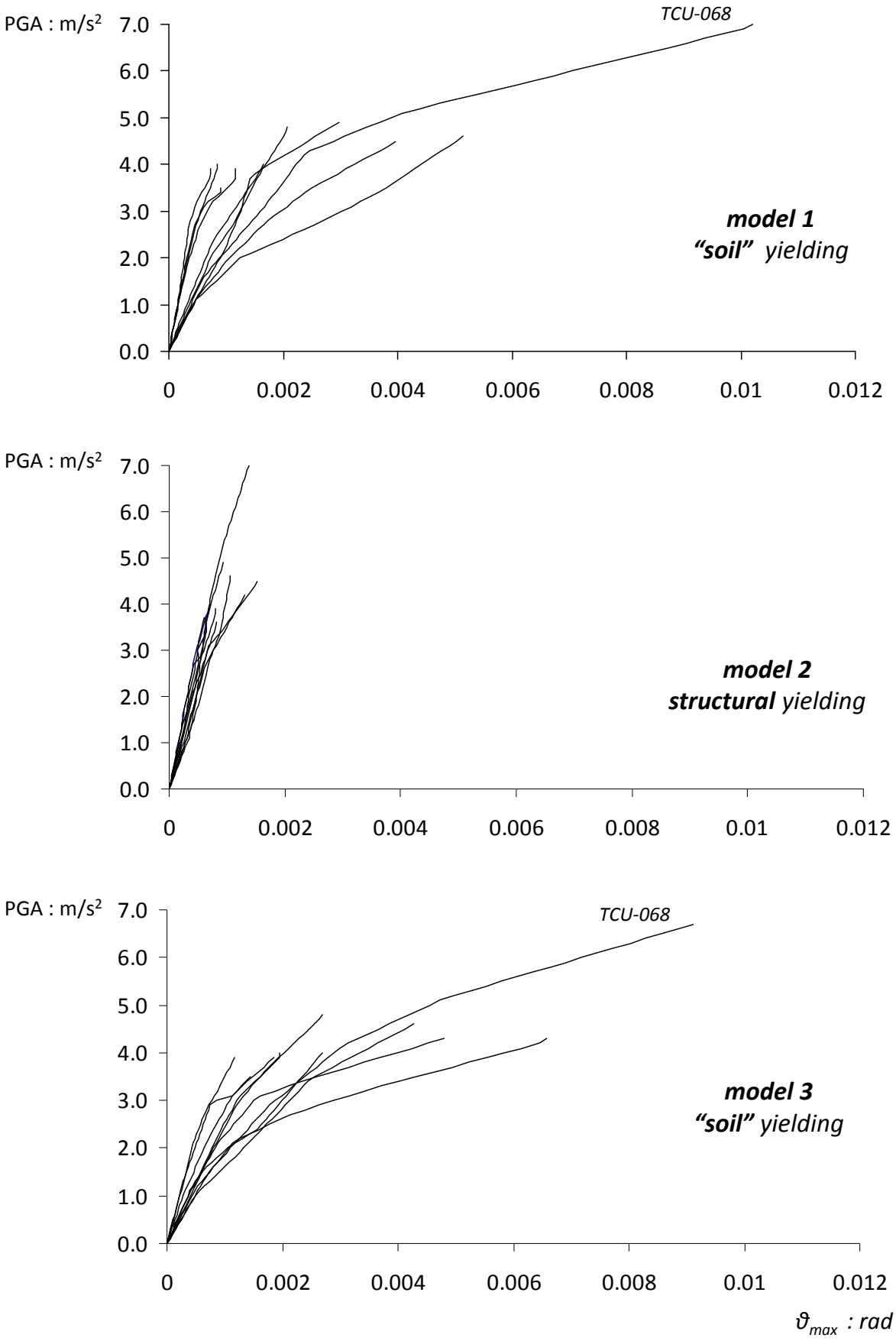

Fig. 5.16 IDA curves : ϑ_{max} **(maximum caisson rotation)** versus the free-field PGA for the three models.

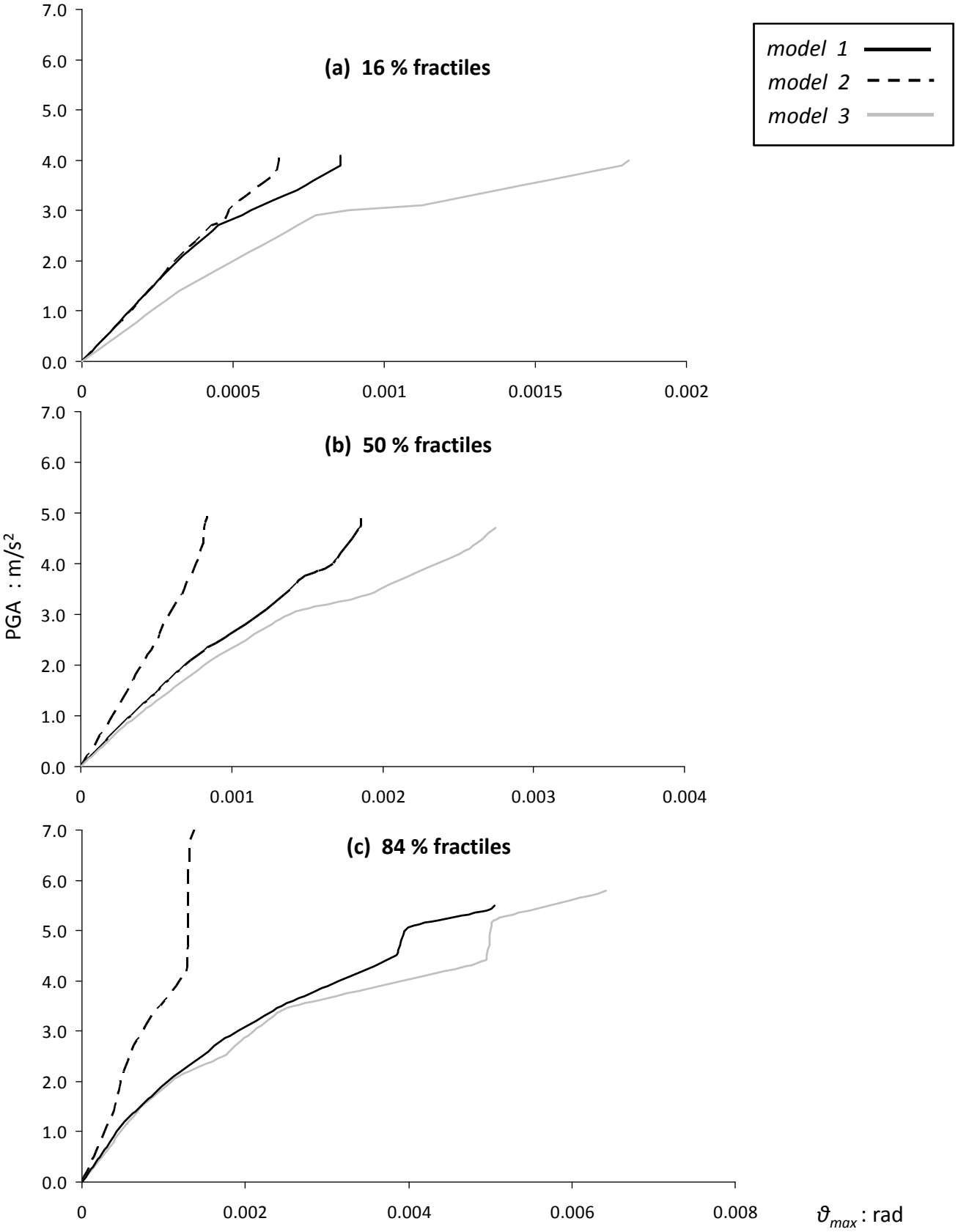

Fig. 5.17 Summarized IDA curves : ϑ_{max} **(maximum caisson rotation)** for the three models: (a) 16% fractiles, (b) 50% fractiles, (c) 84% fractiles.

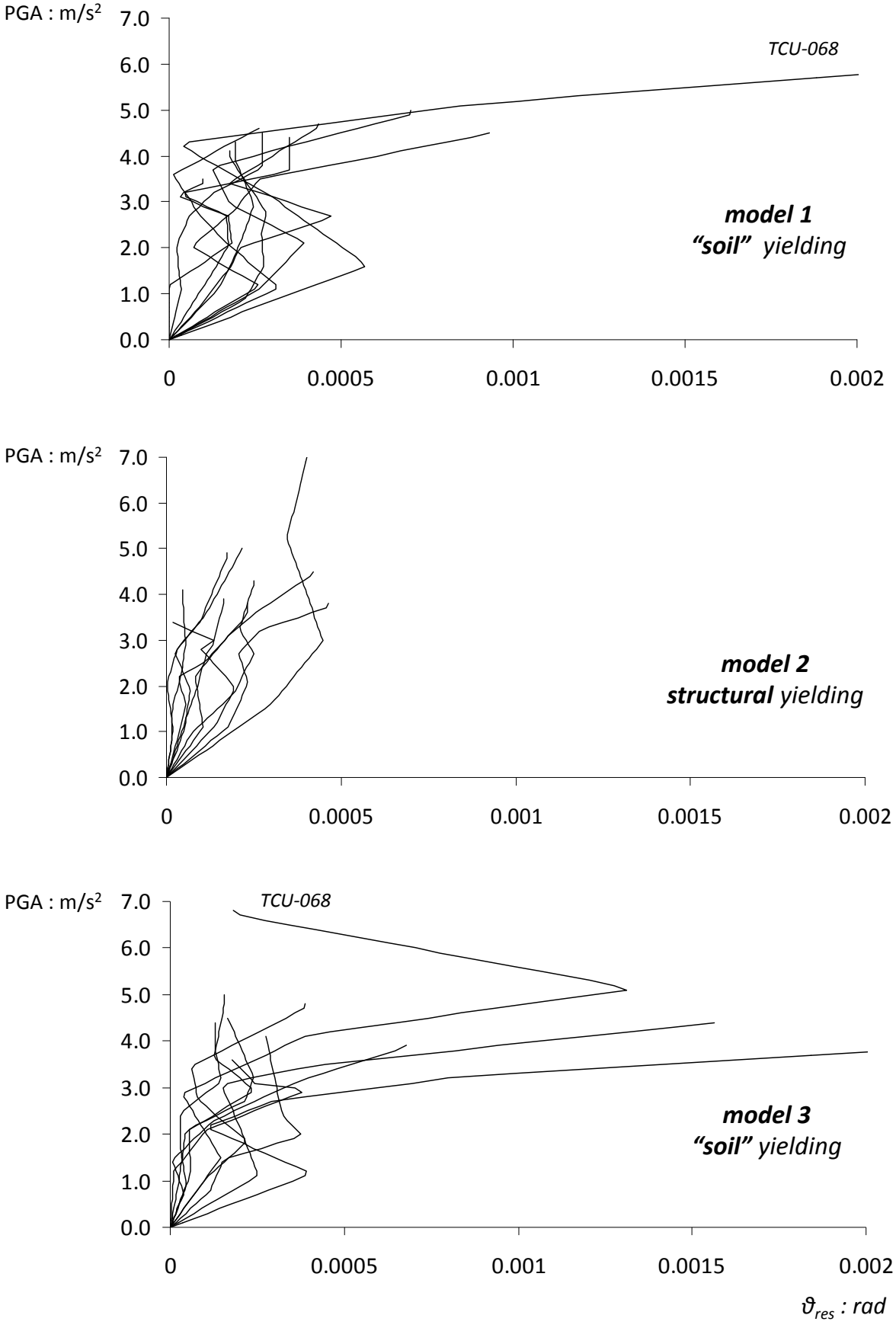

Fig. 5.18 IDA curves : ϑ_{res} **(residual caisson rotation)** versus the free-field PGA for the three models.

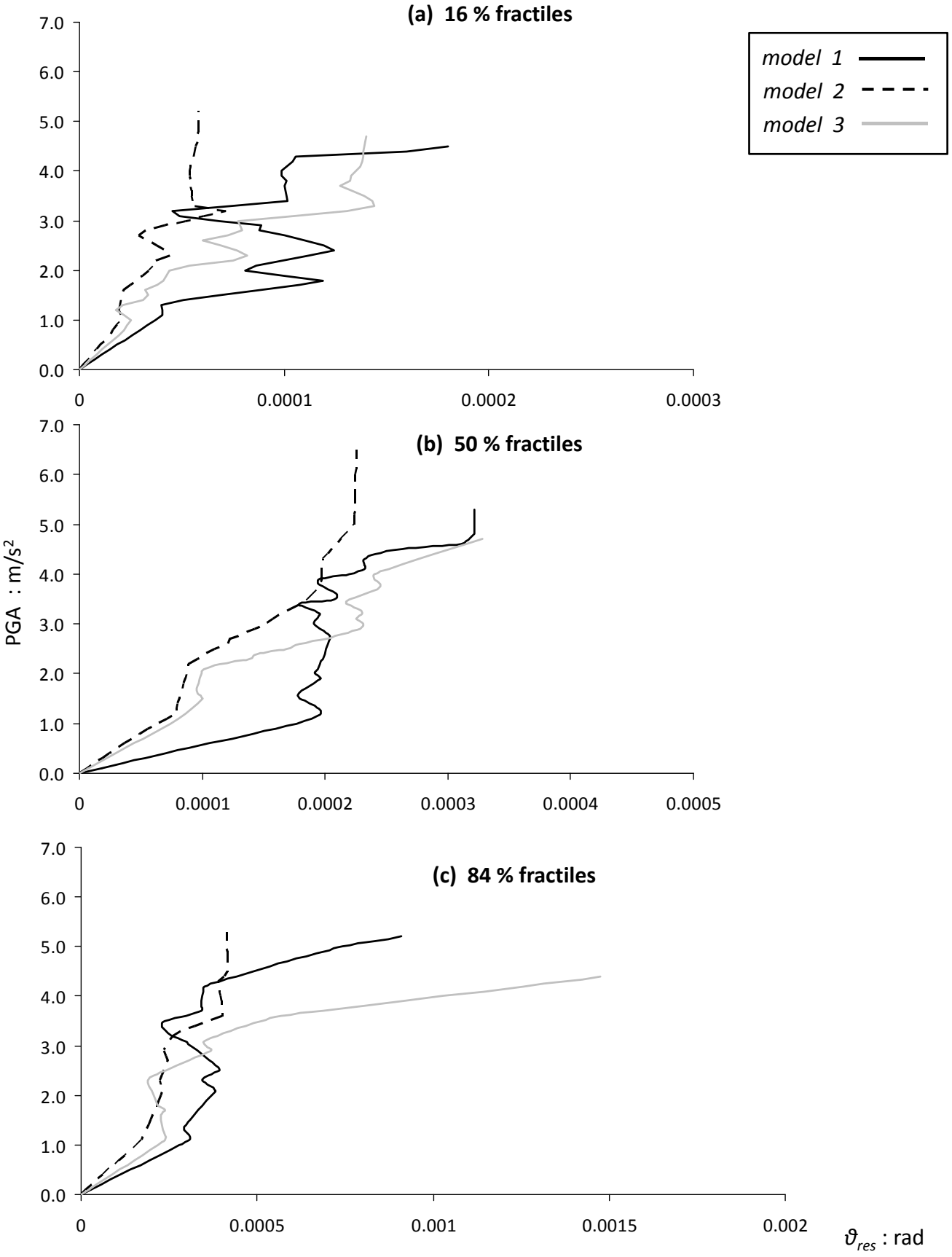

Fig. 5.19 Summarized IDA curves : ϑ_{res} **(residual caisson rotation)** for the three models: (a) 16% fractiles, (b) 50% fractiles, (c) 84% fractiles.

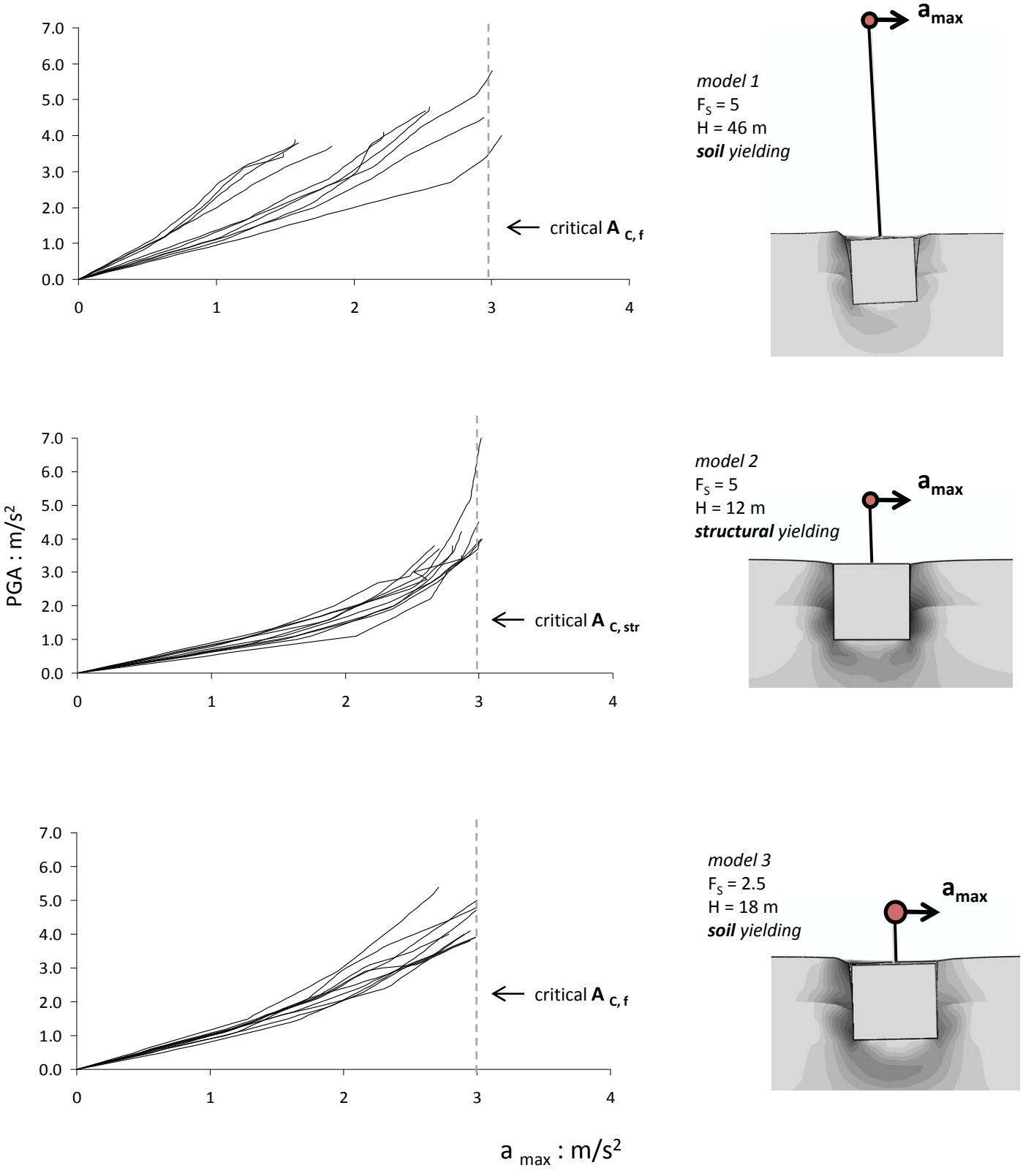

Fig. 5.20 IDA curves of $\mathbf{a}_{max}$ **(maximum acceleration at the structure mass)** for the three models.

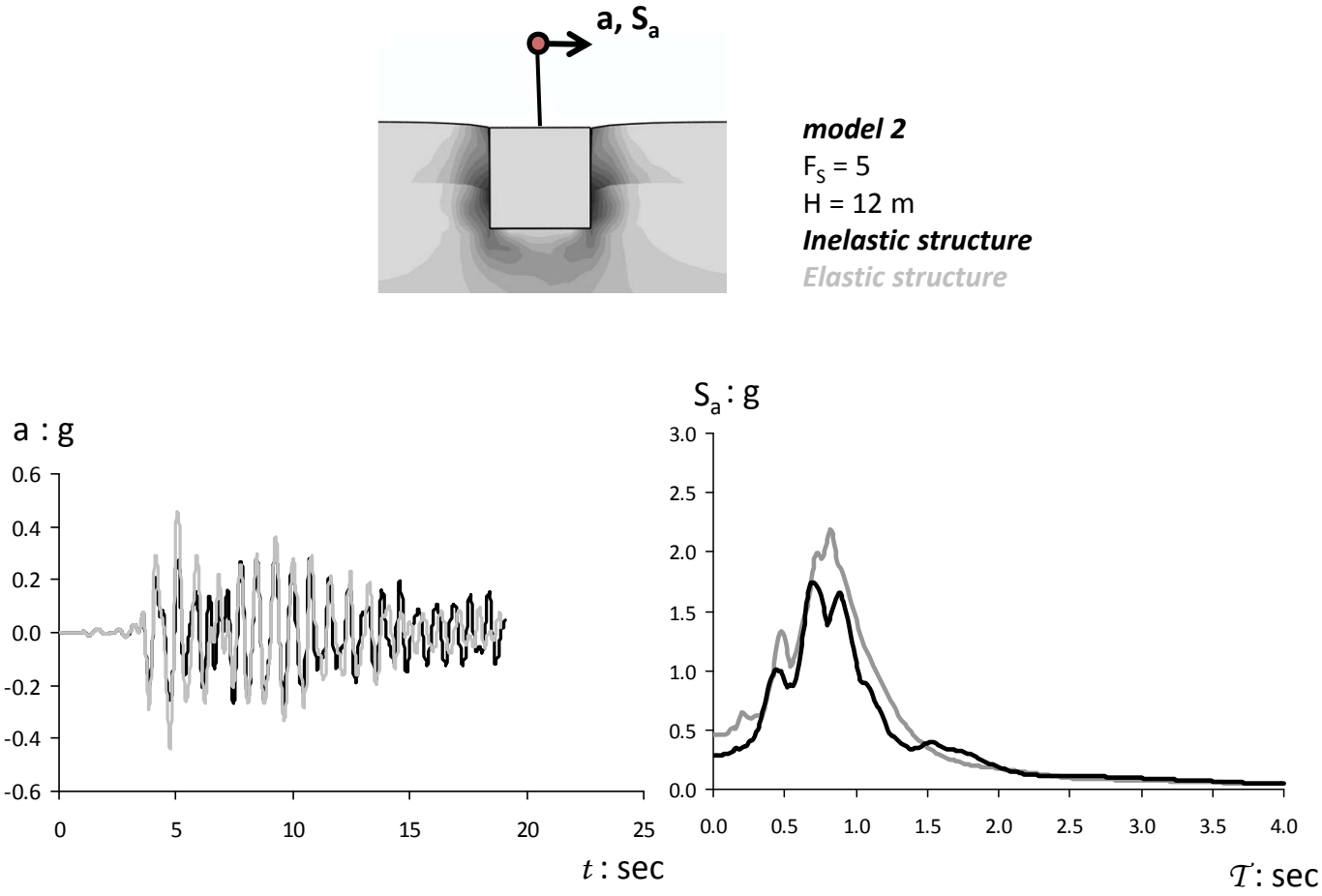

Fig. 5.21 Acceleration time-histories and "*floor*" response spectra comparison at the mass level for the *over*-designed *model 2* considering (a) **inelastic** and (b) **elastic** superstructure. Record: JMA-000, scaled at *free-field* **PGA** = 0.4 g.

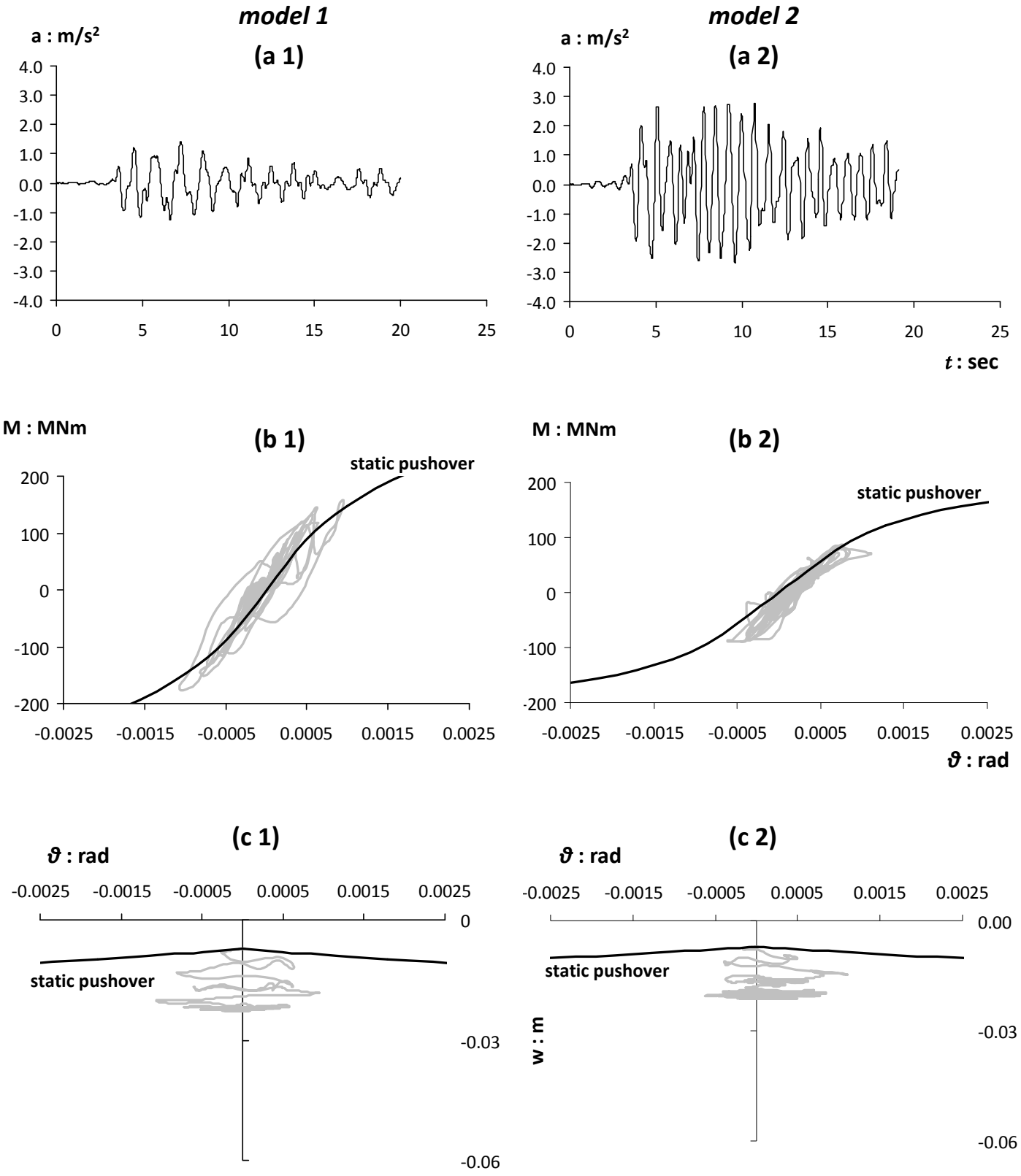

Fig. 5.22 Typical dynamic response comparison for the systems with $\mathbf{F_S=5}$ (light structure) in terms of : (a) acceleration time-history at the mass level, (b) moment-column base rotation, (c) caisson settlement-column base rotation. 1) *under*-designed foundation, 2) *over*-designed foundation. Record: JMA-000, scaled at *free-field* **PGA** = 0.4 g.

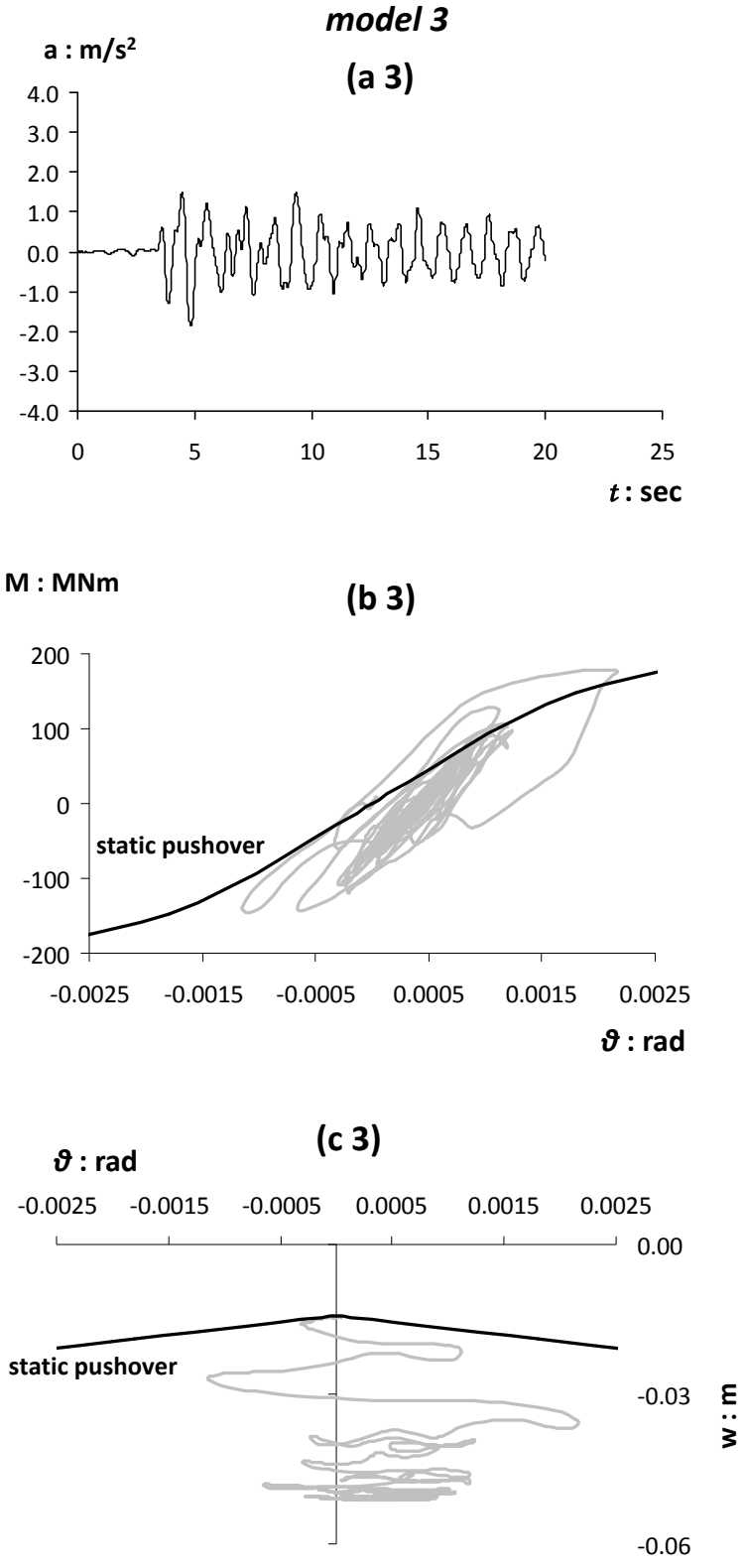

Fig. 5.23 Typical dynamic response comparison for the *under*-designed heavily loaded foundation (**F_S=2.5**) in terms of : (a) acceleration time-history at the mass level, (b) moment-column base rotation, (c) caisson settlement-column base rotation. Record: JMA-000, scaled at *free-field* **PGA** = 0.4 g.

Conclusions

The final section presents the main conclusions of the study in a chapter-wise order.

Chapter 2 investigated the response of rigid caisson foundations, with D / B ≥ 1, in cohesive and frictional soils under combiner N-M-Q loading, by an extensive series of 3-D finite element analyses. The analysis accounted for soil and interface nonlinearities, and examined parametrically the effect of the (a) embedment ratio D/B, (b) level of vertical loading χ and (c) caisson-soil interface friction coefficient μ, on the response. Emphasis was given to the physical and geometrical interpretation of the kinematic mechanisms that accompany failure and, in particular, the location of the rotation pole, z_p, under various loading combinations. Three-dimensional bearing strength surfaces (failure envelopes) were presented, either in normalized or in dimensionless form. It was shown that the bearing strength surface can be viewed as a locus, on which certain types of failure are mobilized, with respect to the M/Q loading ratio. The effects of interface and soil nonlinearities due to vertical loading (expressed by the factor χ) are reflected in the loss of symmetry of the mechanisms and thus the slight change in the position of the rotation pole. Of particular interest is the evolution of the kinematic mechanisms around the apex of the surface, where within a very narrow load ratio region, the depth of the rotation pole changes from to $z_p \rightarrow \infty$ to $z_p = 0$. At the apex, the mechanism governing the response of deeply embedded foundations (D/B ≥ 2) is not formed along continuous failure planes, but rather appears "*diffused*" within the soil mass. Interesting conclusions were also drawn for the ultimate uniaxial capacities, M_u and Q_u, with respect to soil and, especially, interface nonlinearities: while under fully-bonded interface these are found to be decreasing functions of χ, when interface nonlinearities develop (either

in the form of gapping, in cohesive soil, or sliding, in frictional soil), an increase is initially observed for low to moderate levels of χ, followed then by a decrease until bearing failure. For all cases, closed-form expressions for M_u and Q_u were derived to fit the numerical results. All the aforementioned findings were employed to develop a generalized failure criterion-expression for the bearing strength surface of deeply embedded foundations (1 ≤ D / B ≤ 3) in N-M-Q space, capable of capturing all aspects of the response. Most importantly, it was shown that, from a macroelement perspective, the plastic potential function is practically coincident with the failure envelops (the normality conditions are satisfied at any point on the surface), verifying thus the associated plastic flow rule assumption.

Chapter 3 aimed to qualitatively and quantitatively express the nonlinear *SFSI* effects in the case of rigid caisson foundations supporting bridge piers subjected to lateral loading. A series of finite element analysis in 3D was therefore employed to assess the performance, with respect to the combined M-Q loading at the foundation, of similar rigid cubic caissons carrying a column-mass superstructure. The pier height (H) and the pier-to-deck joint rigidity (K_R) varied parametrically, with the latter being modeled by a rotational spring at the deck level. The foundation-superstructure systems were then subjected to lateral monotonic and slow-cyclic loading at the deck level. Throughout the loading, the resulting M-Q load paths at the caisson were constantly monitored and plotted on the normalized of M/M_u-Q/Q_u space, along with the failure envelope of the foundation. To evaluate the effects of the interplay between foundation and structural nonlinearities on the load path, the latter was also introduced, by means of bi-linear moment-rotation and moment-curvature laws for the spring and the pier, respectively. It was found out that:

- Contrary to conventional design, in which uncoupled springs are used to model the foundation elements, accurate prediction of the foundation response can be achieved only if the nonlinear coupling between the horizontal and the rotational degrees of freedom is accounted for.

- Due to the pier-to-deck joint stiffness and the nonlinear coupling between the rotational and translational degrees of freedom at the foundation, that trigger the "*negative effective height*" effect, the loading at the caisson follows a nonlinear path in M-Q space. This load-path was found to display certain characteristics, such as a particular "overstrength" in bearing capacity that can be mobilized by the foundation, irrespective of the stiffness properties and constraints at the superstructure system. From the analysis results, a closed-form expression for the load path was formulated and validated in all examined cases.

- The load paths under slow-cyclic pushover loading track the respective monotonic path with striking agreement, justifying thus the use of the latter as a "backbone" curve for seismic analysis.

The analysis results motivated the development of a methodology to be used as a preliminary seismic capacity design of caisson foundations, accounting for nonlinear response of the foundation and the pier-to-deck superstructure system.

Chapter 4 shed light on the seismic performance of caisson foundations supporting bridge piers, by means of a series of parametric 3D finite element nonlinear dynamic analyses. The emphasis was given on the inelastic response of the soil and caisson-soil interface. Prior to embarking on the parametric investigation, the finite element model was verified in static and dynamic loading conditions and the employed soil constitutive model was validated against available related experimental data. The analysis was performed considering similar caissons supporting elastic SDOF structures. The mass and height of the superstructure was varied to correspond to heavily and lightly loaded, seismically *over*- ($FS_E > 1$) and *under*-designed ($FS_E < 1$) caisson. A series of modified seismic records was used as base excitation. It was found out that seismically *under*-designing a caisson foundation generally leads to:

- Reduction in superstructure response and spectral accelerations.
- Significant reduction in flexural deformations (structural demand).

- Increased dynamic settlements and rotations but minimal residual displacements and tilting.

It was observed that the response of heavily loaded caissons is determined by excessive material (soil) inelasticity, whereas intense caisson−soil interface separation and gapping prevails in the response of lightly loaded foundations. Furthermore, the mobilization of caisson-soil interface nonlinearities provides a threshold for the transmitted seismic forces to the superstructure. Finally, it may be inferred that the seismically *under*-designed foundations combined with a high static safety factor (as usually the case in routine design) are more advantageous compared to the seismically *over*-designed heavily loaded caissons, in both static and dynamic terms, providing a low-cost solution with high seismic isolation potential.

Chapter 5 compared the dynamic response of seismically *over*− and seismically *under*−designed caisson foundations by means of 3D finite element incremental dynamic analysis (IDA), and evaluated the effect of the nonlinear phenomena developed below ground surface on the seismic demand of the supported superstructures. SDOF structures of varying mass weight, simulating heavily or lightly loaded structures founded through similar rigid cubic caissons on a 2-layer soil stratum were used as examples. The investigation was performed considering soil and structural nonlinearity. An ensemble of 10 earthquake motions ranging from medium intensity to very strong, scaled at different PGAs of ground surface motion, was used as base excitation. IDA curves were generated for the maximum horizontal drift, the maximum global ductility demand, the maximum caisson rotation and the residual caisson rotation. The maximum acceleration developed at the superstructure mass was introduced as an *ad hoc* Engineering Demand Parameter. The results revealed that in terms of structural distress, there is a distinct predominance in the performance of the structures founded on the *under*-designed caissons developing significantly reduced horizontal drifts and ductility demands, as opposed to the one founded on the *over*-designed caisson; clear evidence that the mechanism of interface nonlinearities acts as a "*fuse*" for the superstructure.

Regarding the accelerations developed at the structure mass level, both mechanisms of geometric nonlinearities and structural inelasticity, prevalent in the response of the seismically *under*- and *over*-designed foundations respectively, provide a plateau for the maximum transmitted accelerations. Due to the strongly nonlinear soil-structure interaction effects present in the former mechanism, however, the superstructure experiences a longer-period motion as compared to the one filtered by the localized plasticity in the column. In terms of system performance, the *under*-designed foundations experienced increased dynamic settlements and rotations as compared to the *over*- designed one. Strikingly, however, they sustained only minimal residual displacements and tilting, owing much to the massive weight of the caisson which acts as a restraining force. Overall, the study highlighted the efficacy of *under*-designed caisson foundations with high static factor of safety, providing a low-cost foundation solution with a high seismic isolation potential.